NMR studies on the nucleosome and chromatin factors

Vincenzo Romano Lobbia

ISBN 978-90-393-7526-6

Doctoral thesis
NMR studies on the nucleosome and chromatin factors

Vincenzo R. Lobbia

Utrecht university, NMR Spectroscopy Research Group,
Bijvoet Center for Biomolecular Research
Department of Chemistry, Faculty of Science
Utrecht University, the Netherlands
December 2022

Cover design: Vincenzo R. Lobbia   PDBid: 1KX5
Layout design: Vincenzo R. Lobbia & Proefschriftenprinten.nl

NMR studies on the nucleosome and chromatin factors

NMR studies van het nucleosoom en chromatine factoren
(met een samenvatting in het Nederlands)

Proefschrift

ter verkrijging van de graad van doctor aan de
Universiteit Utrecht
op gezag van de
rector magnificus, prof.dr. H.R.B.M. Kummeling,
ingevolge het besluit van het college voor promoties
in het openbaar te verdedigen op

woensdag 14 december 2022 des middags te 12.15 uur

door

Vincenzo Romano Lobbia

geboren op 10 februari 1993
te Delft

Promotor:

Prof. dr. M. Baldus

Copromotor:

Dr. H. van Ingen

Beoordelingscommissie:

Prof. dr. T. Baubec
Prof. dr. J. Lipfert
Prof. dr. M. Ubbink
Prof. dr. P. van der Wel
Prof. dr. F. Mueller-Planitz

Table of Contents

1. Introduction 6

2. Beyond the nucleosome: nucleosome-protein interactions and higher order chromatin structure 21

3. Methyl-TROSY NMR at 1.2 GHz: exploiting resolution and magnetic field alignment 56

4. Methyl-TROSY NMR observation of ionic strength dependent nucleosome clustering 93

5. Conformational dynamics in ISWI and the nucleosome upon their interaction 127

6. General discussion 165

7. English summary 175

8. Nederlandse samenvatting 177

9. Acknowledgement 179

10. Curriculum vitae 182

11. List of Publications 182

1

Introduction

Chromatin is vital to compaction and regulation of the DNA in eukaryotes and is intimately involved in DNA expression, replication, and repair. As one of the cell's biggest polymers, chromatin forms a multi-scale structure consisting of DNA and protein. At the largest level chromatin forms heterochromatin, which is highly compacted, and euchromatin, which is more open and readily accessible to the protein machinery that operates on the DNA[1,2]. At the smallest level, the nucleosome forms the repeating unit of chromatin[3]. A central question in chromatin biology is how chromatin, DNA binding proteins and chromatin factors work together regulate all DNA-mediated processes. The underlying molecular mechanisms not only involve interactions between the smallest units, e.g. proteins and the nucleosome, but also the interplay of the complex higher-order organization of chromatin and these molecular interactions. These aspects converge in the case of chromatin remodelers. These enzymes interact with nucleosomes to alter higher-order chromatin structure directly, by reshuffling the position of nucleosomes in the genome. This thesis examines in detail how one such remodeler enzyme, ISWI, interacts with nucleosomes, explores the relationship between nucleosome interactions and higher-order chromatin structure, and elaborates on approaches to study nucleosome structure and dynamics using nuclear magnetic resonance (NMR) spectroscopy.

Nucleosome structure

The nucleosome is formed by wrapping 147 base pairs (bp) of DNA around two copies of each of the four histones proteins: H2A, H2B, H3 and H4 (Fig. 1.1). Each histone contains a core composed of three a-helices connected by loops L1 and L2 (Fig. 1.1a)[3,4]. The histones form dimers, H2A-H2B and H3-H4, in which loop L1 of one histone interacts with L2 of the other together with multiple interactions between their α-helices of the histones, forming a handshake motif (Fig. 1.1b). Two copies of each dimer combine to form the octamer structure (Fig. 1.1c). The two H3-H4 dimers interact through a four-helix bundle consisting of the α2 and α3-helix of H3. The H2A-H2B dimers combine with both H3-H4 dimers though a four-helix bundle formed by H2B and H4 and extensive interactions between H2A and H3-H4. The DNA in the nucleosome is bound to the histones though interaction of α1-α2 patches of the dimers with the phosphate backbone of DNA and insertion of histone arginine residues in the minor groove of DNA. The nucleosome consists of a globular core, and flexible tails. The globular core consists of the structured parts of the histones and DNA, while the flexible tails consist of the N-terminal ends of the histones and the C-terminus of H2A, which protrude from the globular nucleosome core. The surface of the globular histone core contains an acidic patch consisting of aspartic and glutamic acids of H2A and H2B, which is used by many proteins as a binding surface to interact with the nucleosome[5]. The histone tails, that are positively charged, are important for the wrapping of the nucleosome DNA ends and influence nucleosome stability and compaction[6–9]. The tails also contain most histone post-translational modification (PTM) sites which are essential in regulating nucleosome-protein and nucleosome-nucleosome interactions[10–12].

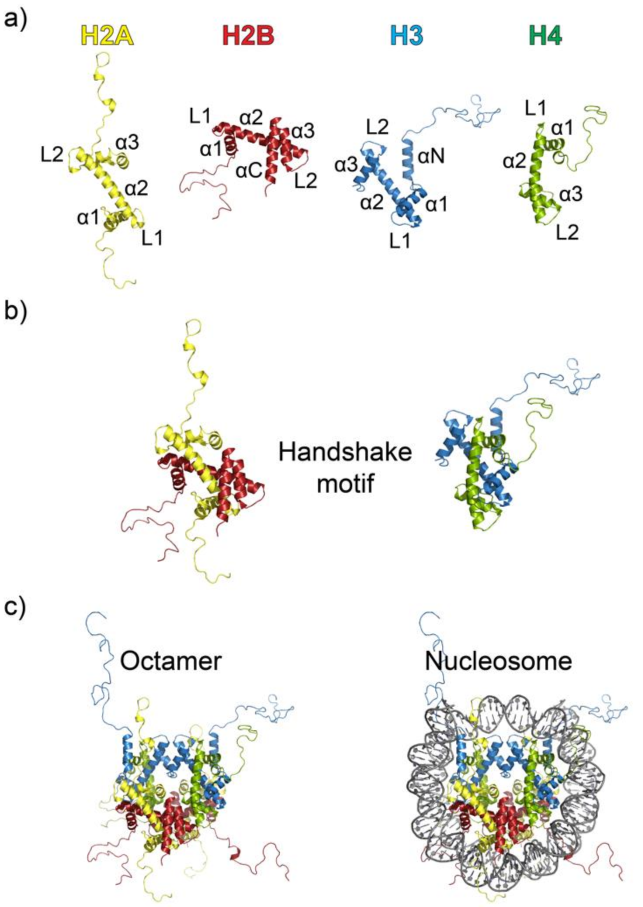

Figure 1.1: Structure of the nucleosome. a) Canonical histone proteins that are part of the nucleosome. Each histone contains an α1, α2 and α3 helix. b) Combination of H2A and H2B or H3 and H4 results a histone dimer where the three a-helices of both proteins fold together to form a handshake motif. c) Two copies of each dimer combine to form an octamer (left). The octamer is then wrapped with approximately 147 bp DNA to form a nucleosome core particle (right).

The nucleosome is formed from highly negatively charged DNA and highly positively charged histone proteins, thus forming a charged polymer held together primarily by electrostatic interactions. Nucleosomes have a net negative charge which in principle cause mutual repulsion between nucleosomes[13]. The presence of monovalent and divalent cations can thus have a pronounced effect on the structure of the nucleosome as well as the binding or activity of proteins interacting with the nucleosome[14]. In the absence of ions the nucleosomal DNA is thought to be stably and fully bound to the histone core with the histone tails bound to DNA[15,16]. Increase of ionic strength will promote unwrapping of DNA ends[17–19] and increase the accessibility of histone tails[20–22]. At a certain ionic concentrations, depending on the DNA length, the repulsive forces between nucleosomes will switch to an attractive force, thus favoring inter-nucleosome interactions[22,23]. When ionic concentrations increase even further DNA can unwrap from the histone core and the histone core will dissociate[6,24–26].

Higher-order chromatin structure

Nucleosomes can form higher order structures through inter-nucleosome interactions, in particular considering that many nucleosomes are present on one DNA duplex in chromatin[27,28]. Folding of such nucleosome array occurs through inter-nucleosome contacts mediated by interactions between either the globular core and the flexible tails, the globular core and DNA or the flexible tails and DNA. The acidic patch can bind N-terminal H4 tail of the nucleosome and is thought to play an important role in the formation of higher order nucleosome structures[29,30]. Similar observations have been made with the H3 nucleosome tail[31,32]. Also, here ionic strength plays an important role in modulating the electrostatic forces that govern packing of nucleosomes in arrays. Ions can drive higher order compaction of nucleosomes[33,34] with compaction depending on the concentration of ions, the valency of the ion and DNA linker length[35]. Monovalent cations efficiently compact nucleosome arrays and can even compact mononucleosomes under physiological ionic concentrations[36,37] if there is a sufficiently high concentration of mononucleosomes[38]. Divalent cations compact both arrays and mononucleosomes, with higher efficiency for arrays[23,39]. Divalent cations behave differently in combination with different monovalent salts. When Mg^{2+} is used to compact nucleosome arrays, Na^+ will improve compaction while K^+ will either decrease or revert part of the compaction[34]. Without Mg^{2+} both Na^+ and K^+ ions cause compaction of arrays. This highlights the importance of the buffer conditions used in studying nucleosomes, as the absence or different concentration of an ion can influence the experimental outcome.

The textbook picture of higher-order chromatin structure is that of a well-defined packing of nucleosomes in a 30nm chromatin fiber[40]. This is in contrast with recent experimental studies that suggest a heterogenous and dynamic arrangement of nucleosomes without distinct long-range order[41–43]. Recent findings demonstrate that chromatin can condense through liquid-liquid phase separation, at least in vitro[44–46]. Liquid-liquid phase separation is a reversible process in which a liquid fluid de-mixes into two distinct liquid-phases with intrinsically different physical properties: one condensed phase and one diluted phase[47–50]. Phase separation has been observed in combination with heterochromatin associated proteins[44–46] and in actively transcribed chromatin[51–53]. Phase separation is driven by multivalent interactions between proteins and/or nucleic acids, often involving intrinsically disordered proteins or regions, forming a close interacting network of molecules [49,54–58]. The underlying microscopic affinities between the interacting molecules can be weak, resulting in dynamic assemblies without strong long-range ordering. As many nucleosome-binding proteins contain disordered acidic or basic tails to match the charge of either DNA or histones, weak electrostatic and multivalent interactions are abundant within chromatin. These works suggest a model were phase separation compartmentalizes distinct functional processes in the nucleus[46,49,59–61].

Chromatin remodelers

The chromatin landscape is dynamic. Replication of DNA requires a new copy of the nucleosome to be placed on the new DNA strand with the same modifications and spacing as the original one. Upon DNA damage the chromatin is remodeled during the process of DNA repair, giving repair proteins access to DNA, and restoring the chromatin afterwards[62]. While DNA is transcribed, nucleosomes are removed to allow RNA polymerase to have access to the DNA[63]. Transcription of genes is regulated by applying various changes to chromatin, like posttranslational modifications on various locations of histones, incorporation of histone variants, eviction, or incorporation of nucleosomes and by changing the position or spacing of nucleosomes[5,62,63].

A family of proteins that is involved in many of these processes are the ATP-dependent chromatin remodelers. This family consists of four subfamilies including the SWI/SNF (SWItch/Sucrose Non-Fermentable), INO80, CHD (chromodomain helicase DNA-binding) and ISWI (Imitation SWItch) remodelers[64]. All these remodelers have in common a structurally conserved ATPase domain that consists of two lobes each containing a part of an ATP catalytic site and that is required for its motor function. Each family has specialized domains that regulate the motor domain and change the behavior of the remodeler.

The ISWI family is capable of remodeling nucleosomes into a regularly spaced nucleosome array with approximately 20 base pair of DNA in between each nucleosome[65]. ISWI consists of five main functional regions, namely the ATPase domain, the NTR (N terminal region), NegC, HSS (HAND-SANT-SLIDE) and APB (acidic patch binding) (Fig. 1.2a). The NTR region negatively regulates the ATPase domain, preventing ATP hydrolysis when it is not bound to a nucleosome[66,67]. In its inactive form the NTR region binds both lobes of the ATPase domain in a conformation where the ATP catalytic regions of both lobes are separated[67,68] (Fig. 1.2b). While DNA only slightly activates ATP hydrolysis, full activation is only observed when the H4 tail of the nucleosome is bound, which is thought to compete with the L3 loop of the NTR region for a binding site on one of the ATPase lobes[66,67,69–71]. The NegC region disconnects the motor function of the ATPase domain from ATP hydrolysis until NegC is inactivated by the HSS domain[66]. The HSS domain can bind approximately 20 base pair of DNA and is thought to act as a ruler to measure the distance between nucleosomes[65,70,72]. Only when nucleosomes are spaced by more than 20 base pairs is remodeling activity stimulated and NegC inhibition relieved[66,70]. Lastly, the APB is a motif just before the HSS domain capable of binding the acidic patch on the nucleosome and is required for nucleosomes remodeling[73].

Over the last few decades, a large quantity of structural information has been obtained by biochemical assays and solving the structures of free[68,74] and nucleosome bound forms of ISWI[75–77]. Together these studies have highlighted the conformation changes within ISWI that are necessary to activate the remodeler upon nucleosome binding (Fig. 1.2b). In addition, these structures have given extraordinary insight into the molecular mechanism of the ATPase motor. Binding of ISWI causes local deformation in the nucleosomal DNA at its binding site of the superhelix 2 (Fig. 1.2b). In the ADP-bound state of ISWI, the DNA is locally untwisted resulting in the effective translocation of 1 bp for one of two DNA strands[77]. When ISWI is bound to the ATP mimic ADP-BeF$_x$ this deformation of the DNA is not observed[75–77], suggesting that in the ATP-bound state the strain in the DNA generated by ISWI binding can be released. This nucleotide-state dependent deformation is thus thought to underlie the mechanism by which DNA can be translocated along the nucleosome. Yet, several key questions remain. One of the defining features of ISWI is that it translocates the DNA without disrupting the nucleosome, meaning that overall, the nucleosome remains intact and thus histone-DNA contacts are only transiently disrupted during remodeling. At what point during remodeling these contacts are broken and how the local DNA deformation is translated into a global altered pattern of histone-DNA contacts is unclear. In addition, there is a hot debate on the whether the histone core plays a role in facilitating remodeling by transient deformations[77–80]. A few studies using solution based NMR and crosslinking mass-spectrometry approaches have suggested that ISWI binding induces significant histone deformations and that these are essential to allow remodeling[78,81]. In the static high-resolution cryo-EM structures none such deformations are however visible, highlighting the challenges in bringing the different perspectives afforded by different techniques together.

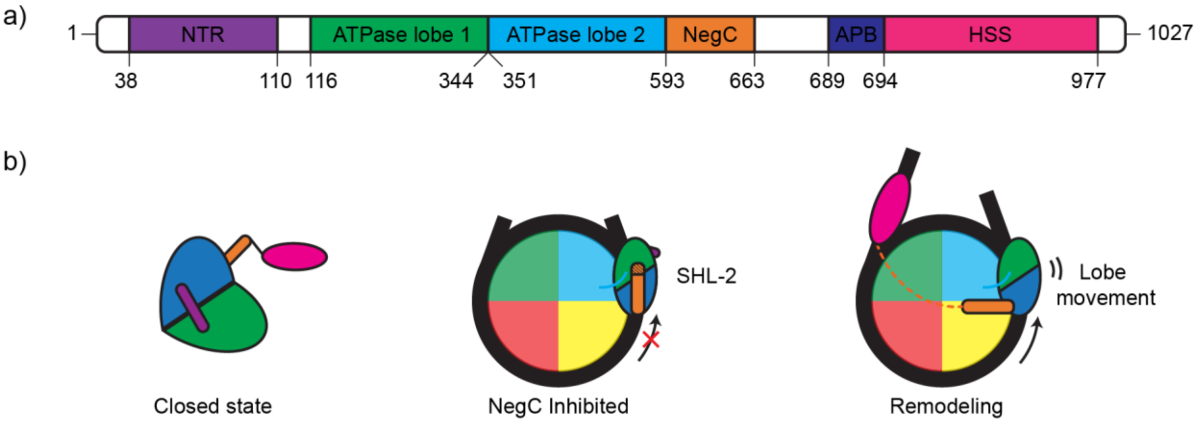

Figure 1.2: ISWI mechanism of action. a) Cartoon overview of the defined regions of ISWI include the N terminal region (NTR), the ATPase domain consisting of two lobes, the regulatory domain NegC, the Acidic patch binding region (ABP) and the Hand Sand Slide (HSS) domain. b) Cartoon overview of the remodeling mechanism. In the closed state The NTR locks the two lobes of the ATPase domain in an inactive conformation preventing ATP hydrolysis. ISWI binds on the super helix 2 (SHL-2) position on the nucleosome. ATP hydrolysis is activated by

release of the NTR through binding of nucleosomal DNA and the H4-tail. NegC inhibition to remodeling is released when the HSS domain can bind sufficiently long DNA linkers.

Study of the nucleosome by NMR

While perhaps not the most obvious structural biology technique in the context of chromatin, NMR has been successfully used in the last decades to study multiple components within chromatin[12]. A particular strength of NMR is that it can give information at residue-specific level on intrinsically disordered regions (IDRs) in proteins, on protein motions in general, and on binding interfaces for both strong and very weak interactions. In this light, NMR offers unique opportunities to study IDRs in histones and chromatin factors, nucleosome-protein interactions and the dynamics of nucleosome such as in remodeling.

An important advancement to allow such studies is the development of methyl-TROSY (transverse relaxation-optimized spectroscopy) solution NMR[82]. Methyl-TROSY NMR allows for the selection of optimal relaxation pathways in specifically isotope-labeled proteins, greatly expanding the size limit[82–91]. It has been successfully applied to study protein complexes up to 1 MDa [84,87,92], including the nucleosome with binding partners[78,92–95]. Within the context of nucleosomes, the methyl-TROSY technique has been mostly applied to the histone proteins and nucleosome binding proteins, due to the relative ease with which protein methyl groups can be specifically labeled. Application to DNA is possible either using the thymine methyl groups (Thesis Clara van Emmerik, Chapter 5[96]) or by selective cytosine methyl-labeling[97]. For both approaches specialized sample preparation schemes are required which are not routinely available.

With the availability of higher and higher magnetic fields, an indirect manner of studying nucleosomal DNA conformation and dynamics may become available. Most recently a high-resolution NMR machine operating at 28.2 T equivalent to a ^{1}H resonance frequency of 1.2 GHz (1200 MHz) became available. At this ultra-high magnetic field, the effects of magnetic field alignment will be amplified as they depend on the square of the magnetic field. Nucleic acids have a large magnetic susceptibility anisotropy (χ_a) causing a slight orientation dependence in the overall magnetic energy of the molecule. As a result, a DNA helix will tend to align orthogonal to the magnetic field due to the nearly colinear arrangement of the aromatic bases within the helix[98–101]. The net alignment of the molecule causes incomplete averaging of the dipolar interactions and hence result in residual dipolar couplings (RDCs). For the nucleosome, like any protein-DNA complex, it can be expected that the alignment generated by the DNA component gives sizeable RDCs that can be measured on the histone protein signals. These RDCs depend on the bond-vector orientations corresponding to the observed protein NMR signal within the alignment frame, which is determined largely by the DNA conformation. Thus, methyl-TROSY NMR at 1.2 GHz also offers exciting new potential to probe the conformational dynamics of the nucleosomal DNA and could in general be an extremely powerful tool to study nucleosome-protein and protein-DNA complexes.

Scope of the thesis

The studies in this thesis focus on dynamic interactions within and between nucleosomes, observed through an NMR perspective. These interactions are altered in higher-order chromatin structure, can be controlled using ionic conditions and manipulated by the ISWI remodeler.

Chapter 1 provides a short introduction on chromatin and the nucleosome. It provides a brief review of the chromatin remodeler ISWI and the highlights the study of nucleosomes by NMR.

Chapter 2 provides an overview of nucleosomes-protein interactions in the context of higher order chromatin structures that nucleosomes can form. Nucleosome-protein interactions in mononucleosome and oligonucleosome structures are reviewed and mechanisms of condensation of chromatin are discussed.

Chapter 3 investigates the nucleosome structure and dynamics at the recently available highest magnetic NMR field of 1.2 GHz. At this higher field we observe significant alignment of nucleosomes with the magnetic field, asymmetries within the nucleosome core and find the nucleosome DNA ends to be partially unwrapped despite the low ionic strength conditions.

Chapter 4 examines the influence of cationic ions on the nucleosome through the eyes of NMR at a molecular level. We observe an ion-dependent decrease in NMR signal which is reasoned to be caused by inter-nucleosome interactions. Using paramagnetic manganese ions, a specific binding sites for divalent ions near the acidic patch is revealed.

Chapter 5 present a study on the dynamics of ISWI remodeler in its free state, its activation upon nucleosome binding and the impact of ISWI binding on the histone core. We find that there is pervasive dynamics in the free ISWI and that upon nucleosome binding ISWI induces large scale alterations in histone-histone and histone-DNA contacts.

Chapter 6 provides a general discussion of all findings of the previous chapters and gives an outlook on future research of the nucleosome and chromatin remodelers.

References

1. Lieberman-Aiden, E. *et al.* Comprehensive Mapping of Long-Range Interactions Reveals Folding Principles of the Human Genome. *Science (80-.).* **326**, 289–293 (2009).
2. van Steensel, B. & Belmont, A. S. Lamina-Associated Domains: Links with Chromosome Architecture, Heterochromatin, and Gene Repression. *Cell* **169**, 780–791 (2017).
3. Luger, K., Mäder, A. W., Richmond, R. K., Sargent, D. F. & Richmond, T. J. Crystal structure of the nucleosome core particle at 2.8 A resolution. *Nature* **389**, 251–60 (1997).
4. Davey, C. A., Sargent, D. F., Luger, K., Maeder, A. W. & Richmond, T. J. Solvent mediated interactions in the structure of the nucleosome core particle at 1.9 A resolution. *J. Mol. Biol.* **319**, 1097–1113 (2002).
5. Lobbia, V. R., Trueba Sanchez, M. C. & van Ingen, H. Beyond the Nucleosome: Nucleosome-Protein Interactions and Higher Order Chromatin Structure. *J. Mol. Biol.* **433**, 166827 (2021).
6. Toth, K. *et al.* Histone- and DNA Sequence-Dependent Stability of Nucleosomes Studied by Single-Pair FRET. *Cytom. Part A* **83A**, 839–846 (2013).
7. Brower-toland, B. *et al.* Specific Contributions of Histone Tails and their Acetylation to the Mechanical Stability of Nucleosomes. *J. Mol. Biol.* **346**, 135–146 (2005).
8. Iwasaki, W. *et al.* Contribution of histone N-terminal tails to the structure and stability of nucleosomes. *FEBS Open Bio* **3**, 363–369 (2013).
9. Li, Z. & Kono, H. Distinct Roles of Histone H3 and H2A Tails in Nucleosome Stability. *Sci. Rep.* **6**, 31437 (2016).
10. Bannister, A. J. & Kouzarides, T. Regulation of chromatin by histone modifications. *Cell Res.* **21**, 381–395 (2011).
11. Bowman, G. D. & Poirier, M. G. Post-translational modifications of histones that influence nucleosome dynamics. *Chem. Rev.* **115**, 2274–2295 (2015).
12. van Emmerik, C. L. & van Ingen, H. Unspinning chromatin: Revealing the dynamic nucleosome landscape by NMR. *Prog. Nucl. Magn. Reson. Spectrosc.* **110**, 1–19 (2019).
13. Clark, D. J. & Kimura, T. Electrostatic mechanism of chromatin folding. *J. Mol. Biol.* **211**, 883–896 (1990).
14. Andreeva, T. V. *et al.* Na+and K+Ions Differently Affect Nucleosome Structure, Stability, and Interactions with Proteins. *Microsc. Microanal.* 1–11 (2021) doi:10.1017/S1431927621013751.
15. CARY, P. D., MOSS, T. & BRADBURY, E. M. High-Resolution Proton-Magnetic-Resonance Studies of Chromatin Core Particles. *Eur. J. Biochem.* **89**, 475–482 (1978).
16. Walker, I. O. Differential dissociation of histone tails from core chromatin. *Biochemistry* **23**, 5622–5628 (1984).
17. Chien, F. T. & Van Der Heijden, T. Characterization of nucleosome unwrapping within

chromatin fibers using magnetic tweezers. *Biophys. J.* **107**, 373–383 (2014).

18. Gansen, A. *et al.* High precision FRET studies reveal reversible transitions in nucleosomes between microseconds and minutes. *Nat. Commun.* **9**, 1–13 (2018).

19. Bilokapic, S., Strauss, M. & Halic, M. Histone octamer rearranges to adapt to DNA unwrapping. *Nat. Struct. Mol. Biol.* **25**, 101–108 (2018).

20. Rodriguez, Y., Duan, M., Wyrick, J. J. & Smerdon, M. J. A cassette of basic amino acids in histone H2B regulates nucleosome dynamics and access to DNA damage. *J. Biol. Chem.* **293**, 7376–7386 (2018).

21. Mutskov, V. *et al.* Persistent Interactions of Core Histone Tails with Nucleosomal DNA following Acetylation and Transcription Factor Binding. *Mol. Cell. Biol.* **18**, 6293–6304 (1998).

22. Mangenot, S., Leforestier, A., Vachette, P., Durand, D. & Livolant, F. Salt-induced conformation and interaction changes of nucleosome core particles. *Biophys. J.* **82**, 345–356 (2002).

23. De Frutos, M., Raspaud, E., Leforestier, A. & Livolant, F. Aggregation of nucleosomes by divalent cations. *Biophys. J.* **81**, 1127–1132 (2001).

24. Böhm, V. *et al.* Nucleosome accessibility governed by the dimer/tetramer interface. *Nucleic Acids Res.* **39**, 3093–3102 (2011).

25. Yager, T. D., McMurray, C. T. & van Holde, K. E. Salt-Induced Release of DNA from Nucleosome Core Particles. *Biochemistry* **28**, 2271–2281 (1989).

26. Tokuda, J. M., Pabit, S. A. & Pollack, L. Protein–DNA and ion–DNA interactions revealed through contrast variation SAXS. *Biophys. Rev.* **8**, 139–149 (2016).

27. Kalashnikova, A. A., Porter-Goff, M. E., Muthurajan, U. M., Luger, K. & Hansen, J. C. The role of the nucleosome acidic patch in modulating higher order chromatin structure. *J. R. Soc. Interface* **10**, (2013).

28. Pepenella, S., Murphy, K. J. & Hayes, J. J. Intra- and inter-nucleosome interactions of the core histone tail domains in higher-order chromatin structure. *Chromosoma* **123**, 3–13 (2014).

29. Dorigo, B., Schalch, T., Bystricky, K. & Richmond, T. J. Chromatin fiber folding: Requirement for the histone H4 N-terminal tail. *J. Mol. Biol.* **327**, 85–96 (2003).

30. Wakamori, M. *et al.* Intra- and inter-nucleosomal interactions of the histone H4 tail revealed with a human nucleosome core particle with genetically-incorporated H4 tetra-acetylation. *Sci. Rep.* **5**, 1–16 (2015).

31. Zheng, C., Lu, X., Hansen, J. C. & Hayes, J. J. Salt-dependent intra- and internucleosomal interactions of the H3 tail domain in a model oligonucleosomal array. *J. Biol. Chem.* **280**, 33552–33557 (2005).

32. Kan, P.-Y., Lu, X., Hansen, J. C. & Hayes, J. J. The H3 Tail Domain Participates in Multiple Interactions during Folding and Self-Association of Nucleosome Arrays. *Mol. Cell. Biol.* **27**, 2084–2091 (2007).

33. Widom, J. Physicochemical studies of the folding of the 100 Å nucleosome filament into the 300 Å filament. *J. Mol. Biol.* **190**, 411–424 (1986).

34. Allahverdi, A., Chen, Q., Korolev, N. & Nordenskiöld, L. Chromatin compaction under mixed salt conditions: Opposite effects of sodium and potassium ions on nucleosome array folding. *Sci. Rep.* **5**, (2015).

35. Bass, M. V., Nikitina, T., Norouzi, D., Zhurkin, V. B. & Grigoryev, S. A. Nucleosome spacing periodically modulates nucleosome chain folding and DNA topology in circular nucleosome arrays. *J. Biol. Chem.* **294**, 4233–4246 (2019).

36. Milo, R., Jorgensen, P., Moran, U., Weber, G. & Springer, M. BioNumbers The database of key numbers in molecular and cell biology. *Nucleic Acids Res.* **38**, 750–753 (2009).

37. Palmer, L. G. & Civan, M. M. Distribution of Na+, K+ and Cl- between nucleus and cytoplasm in Chironomus salivary gland cells. *J. Membr. Biol.* **33**, 41–61 (1977).

38. Hammonds, E. F. *et al.* Histone H3 and H4 tails play an important role in nucleosome phase separation. *Biophys. Chem.* **283**, 106767 (2022).

39. Blacketer, M. J., Feely, S. J. & Shogren-Knaak, M. A. Nucleosome interactions and stability in an ordered nucleosome array model system. *J. Biol. Chem.* **285**, 34597–34607 (2010).

40. Horn, P. J. & Peterson, C. L. Molecular biology: Chromatin higher order folding: Wrapping up transcription. *Science (80-.).* **297**, 1824–1827 (2002).

41. Hansen, J. C. *et al.* The 10-nm chromatin fiber and its relationship to interphase chromosome organization. *Biochem. Soc. Trans.* **46**, 67–76 (2018).

42. Luger, K., Dechassa, M. L. & Tremethick, D. J. New insights into nucleosome and chromatin structure: an ordered state or a disordered affair? *Nat. Rev. Mol. Cell Biol.* **13**, 436–447 (2012).

43. Lakadamyali, M. & Cosma, M. P. Visualizing the genome in high resolution challenges our textbook understanding. *Nat. Methods* **17**, 371–379 (2020).

44. Larson, A. G. *et al.* Liquid droplet formation by HP1alpha suggest a role for phase separation in heterochromatin. *Nat. Publ. Gr.* **547**, 236–240 (2017).

45. Strom, A. R. *et al.* Phase separation drives heterochromatin domain formation. *Nature* **547**, 241–245 (2017).

46. Gibson, B. A. *et al.* Organization of Chromatin by Intrinsic and Regulated Phase Separation. *Cell* **179**, 470-484.e21 (2019).

47. Banani, S. F., Lee, H. O., Hyman, A. A. & Rosen, M. K. Biomolecular condensates: Organizers of cellular biochemistry. *Nat. Rev. Mol. Cell Biol.* **18**, 285–298 (2017).

48. Hyman, A. A., Weber, C. A. & Jülicher, F. Liquid-liquid phase separation in biology. *Annu. Rev. Cell Dev. Biol.* **30**, 39–58 (2014).

49. Peng, A. & Weber, S. C. Evidence for and against liquid-liquid phase separation in the nucleus. *Non-coding RNA* **5**, (2019).

50. Sabari, B. R., Dall'Agnese, A. & Young, R. A. Biomolecular Condensates in the Nucleus. *Trends Biochem. Sci.* **45**, 961–977 (2020).

51. Boehning, M. *et al.* RNA polymerase II clustering through carboxy-terminal domain phase separation. *Nat. Struct. Mol. Biol.* **25**, 833–840 (2018).

52. Lu, H. *et al.* Phase-separation mechanism for C-terminal hyperphosphorylation of RNA polymerase II. *Nature* **558**, 318–323 (2018).

53. Boija, A. *et al.* Transcription Factors Activate Genes through the Phase-Separation Capacity of Their Activation Domains. *Cell* **175**, 1842-1855.e16 (2018).

54. Boeynaems, S. *et al.* Protein Phase Separation: A New Phase in Cell Biology. *Trends Cell Biol.* **28**, 420–435 (2018).

55. Frank, L. & Rippe, K. Repetitive RNAs as Regulators of Chromatin-Associated Subcompartment Formation by Phase Separation. *J. Mol. Biol.* **432**, 4270–4286 (2020).

56. Martin, E. W. & Mittag, T. Relationship of Sequence and Phase Separation in Protein Low-Complexity Regions. *Biochemistry* **57**, 2478–2487 (2018).

57. Li, P. *et al.* Phase transitions in the assembly of multivalent signalling proteins. *Nature* **483**, 336–340 (2012).

58. Zhu, L. & Brangwynne, C. P. Nuclear bodies: The emerging biophysics of nucleoplasmic phases. *Curr. Opin. Cell Biol.* **34**, 23–30 (2015).

59. Wang, L. *et al.* Histone Modifications Regulate Chromatin Compartmentalization by Contributing to a Phase Separation Mechanism. *Mol. Cell* **76**, 646-659.e6 (2019).

60. Strom, A. R. & Brangwynne, C. P. The liquid nucleome – phase transitions in the nucleus at a glance. *J. Cell Sci.* **132**, 1–7 (2019).

61. Cramer, P. Organization and regulation of gene transcription. *Nature* **573**, 45–54 (2019).

62. Gsell, C., Richly, H., Coin, F. & Naegeli, H. A chromatin scaffold for DNA damage recognition: How histone methyltransferases prime nucleosomes for repair of ultraviolet light-induced lesions. *Nucleic Acids Res.* **48**, 1652–1668 (2020).

63. Venkatesh, S. & Workman, J. L. Histone exchange, chromatin structure and the regulation of transcription. *Nat. Rev. Mol. Cell Biol.* **16**, 178–189 (2015).

64. Clapier, C. R., Iwasa, J., Cairns, B. R. & Peterson, C. L. Mechanisms of action and regulation of ATP-dependent chromatin-remodelling complexes. *Nat. Rev. Mol. Cell Biol.* **18**, 407–422 (2017).

65. Lieleg, C. *et al.* Nucleosome Spacing Generated by ISWI and CHD1 Remodelers Is Constant Regardless of Nucleosome Density. *Mol. Cell. Biol.* **35**, 1588–1605 (2015).

66. Clapier, C. R. & Cairns, B. R. Regulation of ISWI involves inhibitory modules antagonized by nucleosomal epitopes. *Nature* **492**, 280–284 (2012).

67. Racki, L. R. *et al.* The histone H4 tail regulates the conformation of the ATP-binding pocket in

the SNF2h chromatin remodeling enzyme. *J. Mol. Biol.* **426**, 2034–2044 (2014).

68. Yan, L., Wang, L., Tian, Y., Xia, X. & Chen, Z. Structure and regulation of the chromatin remodeller ISWI. *Nature* **540**, 466–469 (2016).

69. Clapier, C. R., Längst, G., Corona, D. F. V., Becker, P. B. & Nightingale, K. P. Critical Role for the Histone H4 N Terminus in Nucleosome Remodeling by ISWI. *Mol. Cell. Biol.* **21**, 875–883 (2001).

70. Dang, W., Kagalwala, M. N. & Bartholomew, B. Regulation of ISW2 by Concerted Action of Histone H4 Tail and Extranucleosomal DNA. *Mol. Cell. Biol.* **26**, 7388–7396 (2006).

71. Ludwigsen, J. *et al.* Concerted regulation of ISWI by an autoinhibitory domain and the H4 N-terminal tail. *Elife* **6**, 1–24 (2017).

72. Yamada, K. *et al.* Structure and mechanism of the chromatin remodelling factor ISW1a. *Nature* **472**, 448–453 (2011).

73. Dao, H. T., Dul, B. E., Dann, G. P., Liszczak, G. P. & Muir, T. W. A basic motif anchoring ISWI to nucleosome acidic patch regulates nucleosome spacing. *Nat. Chem. Biol.* **16**, 134–142 (2020).

74. Grüne, T. *et al.* Crystal structure and functional analysis of a nucleosome recognition module of the remodeling factor ISWI. *Mol. Cell* **12**, 449–460 (2003).

75. Armache, J. P. *et al.* Cryo-EM structures of remodeler-nucleosome intermediates suggest allosteric control through the nucleosome. *Elife* **8**, 1–26 (2019).

76. Chittori, S., Hong, J., Bai, Y. & Subramaniam, S. Structure of the primed state of the ATPase domain of chromatin remodeling factor ISWI bound to the nucleosome. *Nucleic Acids Res.* **47**, 9400–9409 (2019).

77. Yan, L., Wu, H., Li, X., Gao, N. & Chen, Z. Structures of the ISWI–nucleosome complex reveal a conserved mechanism of chromatin remodeling. *Nat. Struct. Mol. Biol.* **26**, 258–266 (2019).

78. Sinha, K. K., Gross, J. D. & Narlikar, G. J. Distortion of histone octamer core promotes nucleosome mobilization by a chromatin remodeler. *Science (80-.).* **355**, (2017).

79. Gamarra, N. & Narlikar, G. J. Histone dynamics play a critical role in SNF2h-mediated nucleosome sliding. *Nat. Struct. Mol. Biol.* **28**, 548–551 (2021).

80. Li, L., Yan, L. & Chen, Z. Reply to: Histone dynamics play a critical role in SNF2h-mediated nucleosome sliding. *Nat. Struct. Mol. Biol.* **28**, 552–553 (2021).

81. Hada, A. *et al.* Histone Octamer Structure Is Altered Early in ISW2 ATP-Dependent Nucleosome Remodeling. *Cell Rep.* **28**, 282-294.e6 (2019).

82. Tugarinov, V., Hwang, P. M., Ollerenshaw, J. E. & Kay, L. E. Cross-correlated relaxation enhanced 1H-13C NMR spectroscopy of methyl groups in very high molecular weight proteins and protein complexes. *J. Am. Chem. Soc.* **125**, 10420–10428 (2003).

83. Huang, C., Rossi, P., Saio, T. & Kalodimos, C. G. Structural basis for the antifolding activity of a molecular chaperone. *Nature* **537**, 202–206 (2016).

84. Gelis, I. *et al.* Structural Basis for Signal-Sequence Recognition by the Translocase Motor SecA as Determined by NMR. *Cell* **131**, 756–769 (2007).

85. Pervushin, K., Riek, R., Wider, G. & Wüthrich, K. Attenuated T2 relaxation by mutual cancellation of dipole-dipole coupling and chemical shift anisotropy indicates an avenue to NMR structures of very large biological macromolecules in solution. *Proc. Natl. Acad. Sci. U. S. A.* **94**, 12366–12371 (1997).

86. Fiaux, J., Bertelsen, E. B., Horwich, A. L. & Wüthrich, K. NMR analysis of a 900K GroEL-GroES complex. *Nature* **418**, 207–211 (2002).

87. Sprangers, R. & Kay, L. E. Quantitative dynamics and binding studies of the 20S proteasome by NMR. *Nature* **445**, 618–622 (2007).

88. Tugarinov, V., Choy, W. Y., Orekhov, V. Y. & Kay, L. E. Solution NMR-derived global fold of a monomeric 82-kDa enzyme. *Proc. Natl. Acad. Sci. U. S. A.* **102**, 622–627 (2005).

89. Robson, S. A. *et al.* Mixed pyruvate labeling enables backbone resonance assignment of large proteins using a single experiment. *Nat. Commun.* **9**, 2–3 (2018).

90. Arthanari, H., Takeuchi, K., Dubey, A. & Wagner, G. Emerging solution NMR methods to illuminate the structural and dynamic properties of proteins. *Curr. Opin. Struct. Biol.* **58**, 294–304 (2019).

91. Schütz, S. & Sprangers, R. Methyl TROSY spectroscopy: A versatile NMR approach to study challenging biological systems. *Prog. Nucl. Magn. Reson. Spectrosc.* **116**, 56–84 (2020).

92. Kato, H. *et al.* Architecture of the high mobility group nucleosomal protein 2-nucleosome complex as revealed by methyl-based NMR. *Proc. Natl. Acad. Sci.* **108**, 12283–12288 (2011).

93. Horn, V. *et al.* Structural basis of specific H2A K13/K15 ubiquitination by RNF168. *Nat. Commun.* **10**, 1–12 (2019).

94. Sanulli, S. *et al.* HP1 reshapes nucleosome core to promote phase separation of heterochromatin. *Nature* **575**, 390–394 (2019).

95. Kitevski-Leblanc, J. *et al.* The rnf168 paralog rnf169 defines a new class of ubiquitylated histone reader involved in the response to dna damage. *Elife* **6**, 1–31 (2017).

96. Emmerik, C. van. *Computational, biochemical and NMR-driven structural studies on nucleosomal DNA.*, ISBN: 978-94-6380-673-2

97. Abramov, G., Velyvis, A., Rennella, E., Wong, L. E. & Kay, L. E. A methyl-TROSY approach for NMR studies of high-molecular-weight DNA with application to the nucleosome core particle. *Proc. Natl. Acad. Sci. U. S. A.* **117**, 12836–12846 (2020).

98. Maret, G., Schickfus, M. V., Mayer, A. & Dransfeld, K. Orientation of Nucleic Acids in High Magnetic Fields. *Phys. Rev. Lett.* **35**, 397–400 (1975).

99. Bastiaan, E. W. & MacLean, C. Molecular Orientation in High-Field High-Resolution NMR. in *NMR at Very High Field* vol. 25 17–43 (Springer Berlin Heidelberg, 1990).

100. Brandes, R. & Kearns, D. R. Magnetic ordering of DNA liquid crystals. *Biochemistry* **25**, 5890–

5895 (1986).

101. Kung, H. C., Wang, K. Y., Goljer, I. & Bolton, P. H. Magnetic Alignment of Duplex and Quadruplex DNAs. *J. Magn. Reson. Ser. B* **109**, 323–325 (1995).

2

Beyond the nucleosome: nucleosome-protein interactions and higher order chromatin structure

Based on the review article: **Lobbia, V. R.**, Trueba Sanchez, M. C. & van Ingen, H. Beyond the Nucleosome: Nucleosome-Protein Interactions and Higher Order Chromatin Structure. *J. Mol. Biol.* **433**, 166827 (2021).

Abstract

The regulation of chromatin biology ultimately depends on the manipulation of its smallest subunit, the nucleosome. The proteins that bind and operate on the nucleosome do so, while their substrate is part of a polymer embedded in the dense nuclear environment. Their molecular interactions must in some way be tuned to deal with this complexity. Due to the rapid increase in the number of high-resolution structures of nucleosome-protein complexes and the increasing understanding of the cellular chromatin structure, it is starting to become more clear how chromatin factors operate in this complex environment. In this review, we analyze the current literature on the interplay between nucleosome-protein interactions and higher-order chromatin structure. We examine in what way nucleosomes-protein interactions can affect and can be affected by chromatin organization at the oligonucleosomal level. In addition, we review the characteristics of nucleosome-protein interactions that can cause phase separation of chromatin. Throughout, we hope to illustrate the exciting challenges in characterizing nucleosome-protein interactions beyond the nucleosome.

Introduction

As one of the cell's biggest polymers, chromatin structure is inherently a multi-scale structure. At the lowest level is the well-known structure of the nucleosome[1], while at the largest level is the division between the A and B-compartments, corresponding to the compacted heterochromatin and more open euchromatin[2,3]. In recent years the picture of what is in between these extremes has tilted dramatically, from a well-defined packing of nucleosomes in a 30nm chromatin fiber[4] to a heterogenous and dynamic arrangement of nucleosomes without distinct long-range order[5–7]. Super-resolution light-microscopy and cryo-electron tomography studies have demonstrated an irregular in situ chromatin structure where nucleosomes were found to compact together into so called clutches or blobs with densities and sizes dependent on histone modifications[8–14]. Still, higher-order chromatin structures may be present, either as large, mobile domains (~150nm)[15], or as a canonical 30nm fiber present within an overall heterogenous population of metaphase chromatin[16].

A second shift in our understanding of chromatin organization has come from the recent demonstration that chromatin is able to condense through liquid-liquid phase separation (LLPS)[17–19]. LLPS is a reversible process in which a liquid fluid de-mixes into two distinct liquid-phases with intrinsically different physical properties: one condensed phase and one diluted phase and is excellently covered in several reviews[20–23]. The ability of chromatin to phase separate was first established for heterochromatin, with heterochromatin Protein 1 (HP1) as the main driver of condensate formation[17,18]. Later, Gibson and colleagues demonstrated that phase separation is an intrinsic property of chromatin, i.e. a string of nucleosomes, modulated by the linker DNA length, the presence of linker histone H1, and the presence of histone modifications and reader proteins[19]. Together with the discovery of condensate formation in actively transcribed chromatin driven by RNA Polymerase II[24,25], and transcription factors[26], these works have led to the model that phase separation can create distinct functional chromatin compartments within the nucleus, enabling epigenetic processes, covalent modifications, regulation of gene transcription and maintenance of chromatin states[19,22,27–29].

Phase separation is driven by multivalent interactions between proteins and/or nucleic acids, often involving intrinsically disordered proteins or regions, forming a close interacting network of molecules[22,30–34]. The underlying microscopic affinities between the interacting molecules can be weak, resulting in dynamic assemblies without strong long-range ordering. Thus, the lack of large-scale chromatin ordering, mirrored in the observation of polymer-melt or liquid-like properties of chromatin[35–38], and chromatin's ability to phase separate could be two sides of the same coin, consistent with the polymeric and polyionic nature of chromatin. As many nucleosome-binding proteins contain disordered acidic or basic tails to match the charge of either DNA or histones, weak electrostatic and multivalent interactions are abundant within chromatin.

After a brief overview of the interactions in nucleosome-protein complexes, we examine in the first part of this review in what way nucleosomes-protein interactions can affect and can be affected by higher-order chromatin organization, focusing on the oligonucleosomal level. In the second part, we review some of the nucleosome-protein interactions that haven been shown to be responsible for phase separation of chromatin.

Meta-analysis of nucleosome protein interactions

As a starting point to understand the potential impact between nucleosome-protein interactions and chromatin structure, we analyzed all current published structures of unique nucleosome-protein complexes available in the Protein Data Bank (PDB) (107 structures of 44 unique proteins or unique complexes, see Supplemental Table S2.1). Not included in this analysis are the many interactions to the histone tails.

By visualizing the center of mass of the interacting protein chains a remarkably large volume around the nucleosome is revealed (Fig. 2.1a,b). In most cases the occupied space is incompatible with close packing of nucleosomes. For several proteins, the interaction seems compatible with close nucleosome packing. This includes the linker histones that bind the dyad region and transcription factors SOX2 and OCT4 that bind the nucleosomal DNA[39,40] . In other cases, such as for chromatin factor PSIP1 that binds the H3 N-terminal tail and the nucleosomal DNA[41,42], it is harder to assess whether the nucleosome binding mode is compatible with compacted chromatin as the structures contain only parts of the protein or the proteins could be part of larger complexes.

Hotspots emerge where many proteins contact the nucleosome (Fig. 2.1c,d). These include the well-known acidic patch and the area around the H3 α1 helix, as also seen in a recent nucleosome interactome screen[43], and on the DNA near super-helical location (SHL) 2, SHL 6, the dyad and linker DNA. The nucleosome surface formed by the H3 α3- and H4 α2-helices shows very few protein contacts (Fig. 2.1d). Interestingly, this region also has a slightly positive electrostatic potential (Fig. 2.1e).

For histone tail binding proteins, which are not part of the analysis in Figure 1, the effect of close nucleosome packing will depend on the availability of the histone tail. Within the context of mononucleosomes, histone tail-DNA binding has been observed to inhibit protein binding[44]. On the other hand, proximity of DNA or other tails may promote association, which also has been observed within the context of mononucleosomes[41].

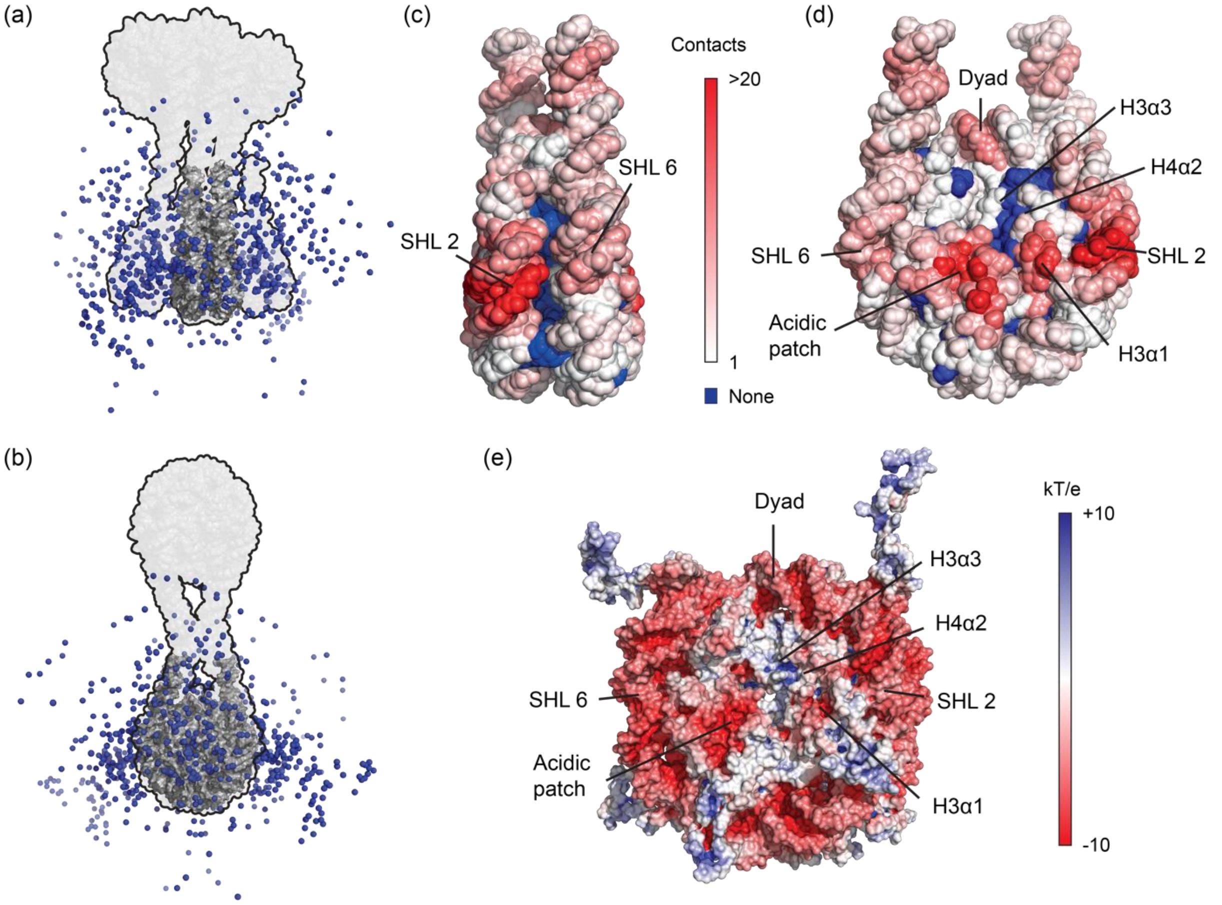

Figure 2.1: Overview of the nucleosome-protein contact interface. (a, b) Visualization of the protein-interaction space around the nucleosome, showing a side (a) and front (b) view. Blue spheres represent the center of mass from all protein chains in all structures of nucleosome-protein complexes deposited in the Protein Data Bank (PDB). Nucleosome structure (model based on PDB 1KX5 extended to 167bp DNA) is shown in dark grey, the hexanuclesome structure (PDB 6HKT) is shown in light gray. (c, d) Visualization of the protein contact surface on the nucleosome, showing side (c) and front (d) view. Color coding and position of key structural elements are indicated in the figure. SHL is superhelical location. (e) Electrostatic potential on the nucleosome surface (PBD: 1KX5), color coding indicated.

Oligonucleosomal structure and nucleosome-protein interactions

To account for the polymer nature of chromatin, nucleosome protein interactions should be considered within the context of oligonucleosomal substrates. The finding that small clusters of and short-range contacts between nucleosomes are observed in situ[8,45,46], suggests that zig-zag arranged oligonucleosomal structures may form relevant functional units of chromatin[47,48]. Akin to the hierarchical description of proteins structure, two secondary structure types for the packing of nucleosomes in a tetra-nucleosome have been proposed as fundamental units of chromatin structure based on a detailed analysis of Hi-C data[49]. The closely packed tetranucleosome structure as seen in the crystal structure[50] and the 30nm cryo-electron microscopy (cryo-EM) fiber structure[51] may represent the ideal packing or a ground-state chromatin structure. Whatever the precise arrangement, data obtained on mononucleosomes indicate that many proteins will interfere with close packing of nucleosomes and, vice versa, that their binding may be impeded by close nucleosome packing. On the other hand, other proteins such as HP1 and linker histones promote inter-nucleosomal interactions, inducing chromatin compaction and possibly long-range ordering.

General factors influencing oligonucleosomal structure

Before going into the possible impact of nucleosome-binding proteins, we describe some important general factors that determine structure and dynamics of oligonucleosomes, as the background in which these proteins operate. First, the relative orientation between two neighboring nucleosomes depends strongly on the length of the DNA linker between them, or in other words the nucleosome repeat length. A DNA molecule of 90 bp, the maximum DNA linker length found in vivo, and approximately 30nm long, behaves as a stiff rod due to the long persistence length of DNA (50 nm). This means that in principle the relative orientation between two nucleosomes changes by 36° for every bp of linker DNA, strongly affecting the way nucleosome can pack. In vivo, preference for linker lengths that make an integral number of complete turns, i.e. DNA linker length corresponding to 10*n*, as well as preference for linkers imposing a 180° rotation, lengths corresponding to 10*n*+5, have been reported[19,52]. Combined with the length of linker DNA, the rotational positioning is a main determinant of oligonucleosomal folding[53–55].

Second, the positive charge of the histone is insufficient to compensate for the negative charge of the nucleosomal DNA. The net negative charge of the nucleosome and the unscreened charge of the linker DNA make that folding of an array of nucleosomes is intrinsically electrostatically driven[56,57] and thus very sensitive to amount and type of mono- and divalent cations[58]. At physiological ionic strengths and in presence of divalent ions, the screening of the negative charge is sufficient to allow for favorable inter-nucleosome interactions.

Third, the dominant inter-nucleosome interaction in folding of oligonucleosomal arrays is the interaction between the H4 tail basic patch and the H2A/H2B acidic patch[59–62]. This interaction is required for compaction[61] and mediates the packing of tetranucleosomal building blocks in the structure of 30nm fiber[51]. Since deacetylation of K16 in the H4 tail is required for chromatin compaction in mitosis[63], this inter-nucleosomal interaction is expected to be relevant in vivo as well. Other inter-nucleosomal interactions are possible as well[51,64] and may be especially relevant for long-range inter-nucleosomal interactions.

Finally, nucleosomes and oligonucleosomes are intrinsically dynamic structures, subject to spontaneous breathing motions that alter DNA wrapping, nucleosome packing and octamer arrangement, as recently reviewed[65,66].

Possible effects of nucleosome-protein binding on oligonucleosome structure

In the following we will describe seven scenarios for the impact of nucleosome-protein interactions on oligonucleosomal structure, that either involve binding to single or multiple nucleosomes. These are schematically depicted in Fig. 2.2. Interactions that involve only one nucleosome can influence higher-order structure by promoting compaction or decompaction of the linker DNA, promoting wrapping or unwrapping of nucleosomal DNA, repositioning nucleosomes, and evicting or assembling nucleosomes. Proteins or protein complexes that can bind at least two nucleosomes could bridge nucleosomes either short-range (between nucleosomes relatively close on the DNA sequence) or long-range (between distant parts of the fiber). Such protein could also orient nucleosomes or promote stacking or unstacking of nucleosomes.

Importantly, nucleosome-binding proteins could exert these effects directly or indirectly, through binding the nucleosomal or linker DNA, the histone core and/or the histone tails. For example, linker histones bind nucleosomal and linker DNA to compact the linker segments directly (see next section). For transcription factor Sox2 it was recently shown that by binding to the nucleosomal DNA it can move the H4 tail to a position that is incompatible with the H4 tail-acidic patch interaction between nucleosomes[39]. Vice versa, interactions between nucleosomes could occlude protein-binding interfaces on DNA, histone core and tails or create new binding surfaces. For instance, proximity of linker DNA segments within interdigitated fibers can create new binding sites for linker histones (see next section), whereas increased interaction of histone tails with DNA in a dense fiber may impede binding of many regulatory proteins.

Below we discuss general features of these scenarios and highlight relevant examples from the literature with a particular focus on linker DNA (de)compaction and nucleosome bridging.

Linker DNA (de)compaction

Since the two linker DNA arms that protrude from the nucleosome core are the connectors to the neighboring nucleosomes, their relative orientation is a crucial factor in higher-order chromatin structure. Unlike the nucleosomal DNA, the linker DNA is not screened by the core histone proteins, resulting in electrostatic repulsion when the two linkers are brought close together. The main factors in stabilizing a compacted linker DNA conformation are the linker histones. Linker histones are able to condense chromatin and are important in many biological processes, including apoptosis, cell cycle progression, transcription, and DNA repair[67,68]. Other nucleosome binding proteins antagonize linker histone function, by competing either directly for the nucleosome binding site as in the case of FoxA [69], or indirectly interfering with linker histone function as in the case of HMGN proteins[70].

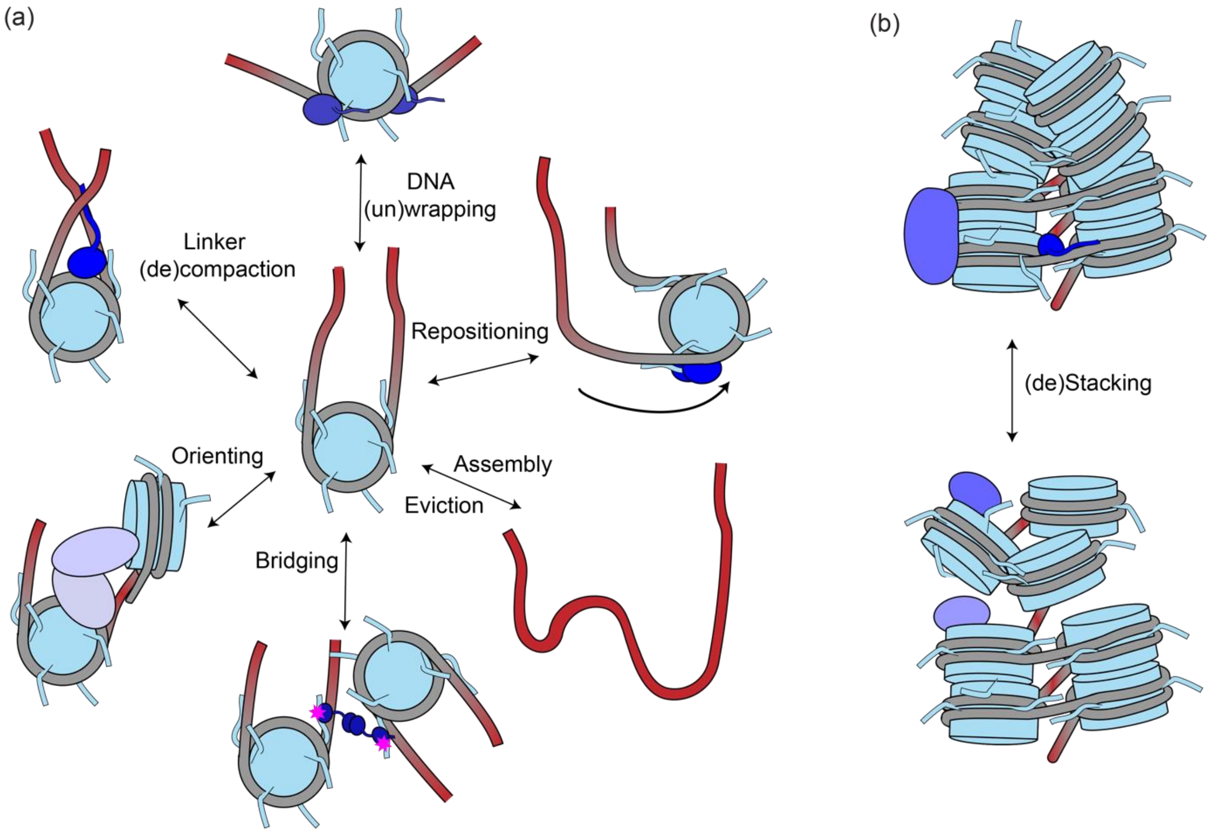

Figure *2.2*: Possible effects of nucleosome protein interactions on chromatin structure. (a,b) Schematic view of the ways in which proteins can alter nucleosome structure and influence inter-nucleosome interactions (a) and packing of nucleosome arrays (b). Histones are shown light blue, nucleosomal DNA in gray, linker and free DNA in red to indicate the larger net negative charge.

Mammals have several isoforms of linker histones that consist of a globular winged-helix domain, a short intrinsically disordered N-terminal tail (NTD) and a long basic C-terminal domain (CTD). Several structures of linker histone bound to a mononucleosome have been solved[71–73], as also reviewed recently[74,75]. The linker histone globular domain binds the nucleosomal DNA right at or slightly away from the central base-pair in-between the linker DNA arms, the so-called on-dyad or off-dyad mode (the on-dyad mode is depicted in Fig. 2.3a,b). These different binding modes are linker histone isoform specific as substitution of DNA binding residues between isoforms can alter the dyad binding mode[76]. Notably, on-dyad binding showed higher compaction than off-dyad binding[71], indicating the importance of linker histone isoform in the higher-order structure in chromatin. Recently, a third binding mode of the globular domain was discovered[73]. In this so-called non-dyad mode, the linker histone does not position itself at the dyad but on the DNA of neighboring nucleosomes in interacting fibers, in an overall configuration that is very similar to on-dyad binding (Fig. 3d,e).

The study by Bednar et al. showed that the CTD can bind to one of the DNA linkers, rationalizing how linker histones can stabilize the repulsion between linker DNA arms[77]. A systematic study by the Bai lab revealed that the CTD of different linker histone isoforms compacts linker DNA to different degrees, with compactness correlated with the charge and amount of T/SPKK motifs present in the CTD[72] (Fig. 2.3c). As of yet, there is no experimental data on the structural role of the linker histone NTD in nucleosome binding. Computational modelling studies predicted that the NTD becomes helical upon binding, enhancing the binding affinity[78]. Linker histone isoforms with higher helicity for the NTD showed increased binding affinities in the simulations[78].

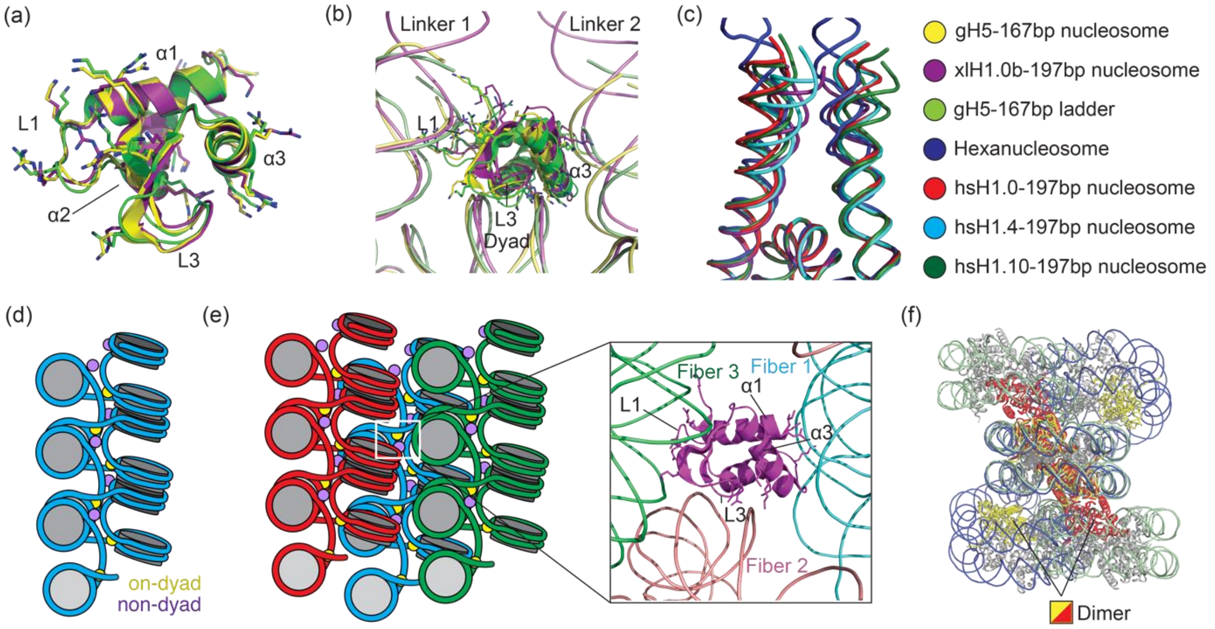
(a)
α1
L1
α3
α2
L3
(b)
Linker 1
Linker 2
L1
α3
L3
Dyad
(c)
gH5-167bp nucleosome
xlH1.0b-197bp nucleosome
gH5-167bp ladder
Hexanucleosome
hsH1.0-197bp nucleosome
hsH1.4-197bp nucleosome
hsH1.10-197bp nucleosome
(d)
on-dyad
non-dyad
(e)
Fiber 3
Fiber 1
α1
L1
α3
L3
Fiber 2
(f)
Dimer

Figure *2.3*: Linker DNA compaction by linker histones. (a) Overlay of linker histone globular domain structures observed in different on-dyad nucleosome complexes, with DNA binding lysine and arginine residues shown as sticks. Color coding indicated next to panel (c). (b) As (a), but with structures superimposed on the nucleosome, showing small variations in positioning on the dyad and linker DNA conformation. (c) Overlay of dyad and linker DNA of various linker histone-nucleosome complexes. Color coding indicated on the right-hand side. (d, e) Schematic view of a single (d), or three interdigitated fibers (e) with linker histones in on- and non-dyad positions. The inset shows the non-dyad binding mode in more detail. Color coding indicated in the panels. (f) Comparison of nucleosome stacking in the hexanuclesome-H1.0 structure (blue) and the proposed H5-nucleosome array structure (green). The H2A/H2B dimers are colored red and yellow, respectively, to highlight the different handedness and inter-nucleosomal contacts.

Comparing the various “on-dyad” linker-histone-nucleosome complexes, clear differences in linker arm position can only be observed when the CTD was included in the linker histone construct (Fig. 2.3b,c). Structures of oligonucleosome complexes with linker histones show even more variation. Song et al. solved the cryo-EM structure of a crosslinked compacted 12-mer nucleosomal array with linker histone H1.4, showing clearly a zig-zag packing of nucleosomes as tetranucleosomal units in a helix with ~30nm diameter[51]. While the resolution of this structure (11 Å) did not permit to pinpoint the position or conformation of the CTD, the structure showed that the globular domain of H1.4 was bound in an off-dyad position. Experiments performed without cross-linking showed that H1.4 was bound on-dyad, illustrating the sensitivity of the H1-oligonucleosome complex to experimental conditions[72,79]. An even more striking example of this sensitivity was observed by Garcia-Saez et al. in a study of H1.0-bound hexanucleosomes, an array of six nucleosomes[80]. The crystal structure obtained under physiological conditions without crosslinker did not show clear electron density for the linker histone, indicating either a heterogenous or a highly dynamic binding. The linker DNA in the hexanucleosome structure is more strongly bent compared to the linker DNA of mononucleosomes, but nevertheless still compatible with linker histone-DNA contacts as observed with mononucleosomes (Fig. 2.3c). Interestingly, the nucleosomes in this structure are packed in a zig-zag ladder-like arrangement, i.e. as an untwisted helix. In solution, both unfolded, ladder-like and Song-type 30nm fiber structures were found to coexist at the same time. Strikingly, a small increase in Mg^{2+}-concentration, from 0.3 to 0.6 mM, was sufficient to predominantly obtain a twisted helical structures[80]. Another type of ladder-like arrangement was proposed for ~172bp-arrays compacted by linker histone H5, based on the crystal packing of H5-bound mononucleosomes[79]. In this arrangement, the stacking of nucleosome follows the opposite handedness compared to the 187bp-array ladders seen for the hexanucleosome structure, resulting in different inter-nucleosomal interactions between the two structures (Fig 2.3f). The flexibility in oligonucleosomal structure upon linker histone binding underscores that it may be better to consider linker histone complexes as ensembles of different conformations that are particular sensitive to the fine characteristics of the systems and environmental conditions[74,75]. Nevertheless, the precise binding mode is important also for other nucleosome-protein interactions because the different higher-order structures obscure and expose different parts of the nucleosome. In addition, binding and compaction of nucleosomes by linker histones decreased the dynamics of the H2A C-terminal and H3 N-terminal tail, likely by promoting their binding to DNA[72]. This can affect subsequent protein binding, as was shown for the ATP-dependent chromatin remodeler ISWI[72]. Finally, destabilization of nucleosome-nucleosome contacts in either arrangement may cause large-scale changes in structure, just as an H4R23A mutant caused untwisting of the 30nm-helix to a ladder-like arrangement[51].

Nucleosome (un)wrapping, eviction/reassembly and repositioning

Similar to linker DNA length decompaction, unwrapping of the nucleosomal DNA can be expected to have profound impact on nucleosome packing, leading to a more open chromatin structure. A recent exciting example is the demonstration that binding of the pioneer transcription factor Sox alone or in complex with partner Oct4 to the nucleosomal DNA can cause DNA unwrapping from entry/exit site to the transcription factor binding site[39,40]. This opening effect may in part explain their gene-activating function.

Nucleosome remodelers, often aided by histone chaperones[81], are the main group of proteins that reposition, completely evict, or partially unwrap nucleosomes. Remodelers can both enhance or decrease accessibility to genomic sites by interfering or promoting chromatin packing. Nucleosome remodelers have been extensively reviewed elsewhere[82], detailing the different structures[83] and interactions[84], possible translocation mechanisms[85], impact on nucleosome positioning[86], and their role in nucleosome unwrapping to facilitate transcription factors[87].

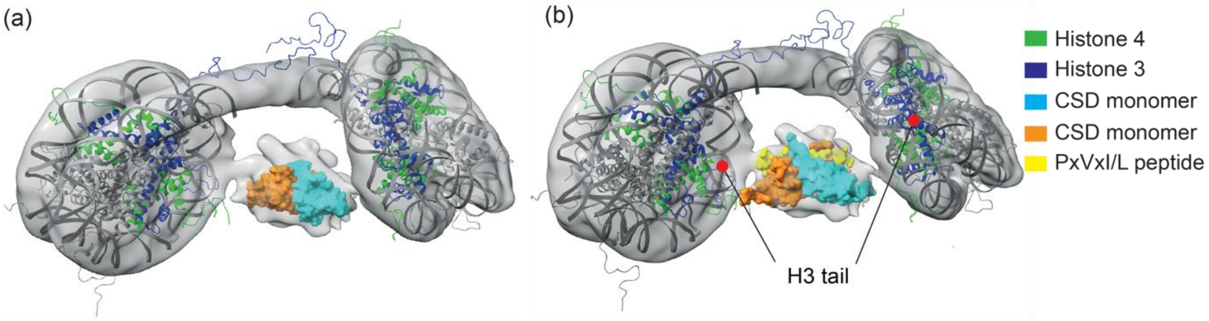

Figure *2*.4: Nucleosome bridging by heterochromatin protein HP1. (a,b) Cryo-electron microscopy density map of HP1 bound to a dinucleosome (EMDB 6738) superimposed with the nucleosome structure (PDB 1KX5) and the structure of the HP1 chromoshadow domain (CSD) dimer (PDB 3P7J/5T1I). The density map (light gray) fits two nucleosomes surrounding a central density that fits well to the CSD dimer structure in the free state (PDB 3P7J) and to the complex of the CSD dimer with a H3.1 tail peptide containing a PxVxI/L motif (PDB 5T1I).

Nucleosome bridging and orienting

Many chromatin-binding proteins have multiple nucleosome binding domains, often for a specific post-translational modification on one of the histone tails. As a result of this multivalency, these proteins can in principle bind multiple nucleosomes simultaneously. Such bridging effect may be important in compacting or stabilizing a certain chromatin configuration or in simply sequestering nucleosomal substrates for further modification. In theory, bridging of nucleosomes could also result in imposing or stabilizing a specific relative orientation between nucleosomes. The resulting structure could subsequently form a specific binding epitope for chromatin binding protein. However, in many of these multivalent proteins the nucleosome-binding domains are separated by flexible linker regions, thus allowing them to adapt to different nucleosome orientations.

A prime example of a flexible, multivalent protein that can bridge nucleosome is HP1. HP1 is highly conserved dimeric protein that is present in different isoforms with each slightly different functions and localization[88]. HP1a proteins drive and expand chromatin condensation[89–91], which is essential for the function of heterochromatin in gene silencing[92]. HP1 proteins consist of two folded domains, a chromodomain (CD) and a chromoshadow domain (CSD), that are connected by a flexible linker or hinge region and extended at the N- and C-terminus with a disordered tail (see also Fig. 2.5 below). The CD is a specific reader of the H3K9me2 and H3K9me3 epigenetic marks[93] and thus essential for recruitment of HP1 to heterochromatin. Due to the CSD-CSD dimerization[94–96], HP1a is a bivalent reader protein capable of binding two H3K9me3 histone tails. Recently, a cryo-EM structure from the Kurumizaka lab demonstrated that HP1 is indeed able to bridge two nucleosomes[97]. Using dinucleosomes connected by a 15bp linker and decorated with thioether mimics of H3K9me3, three types of structures could be resolved, with all three showing distinct density for the HP1a dimer in between the two nucleosomes. The path of the linker DNA and thus the relative orientation of the two nucleosomes differed, indicating a flexibility in the binding mode. Dinucleosomes with longer linker lengths (48 and 58 bp) also resulted in HP1-mediated nucleosome bridging. As longer linker lengths decrease binding specificity for the H3K9me mark[90], it is not clear whether both H3K9me3 tails were bound in these complexes. The resolution of the resulting structures was unfortunately insufficient to create an atomistic model. The observed density for the HP1 dimer roughly matches the dimensions of the CSD-CSD dimer (Fig. 2.4). Density for the chromodomain is not apparent, suggesting a flexible linkage of the CD-H3K9me3 complex. Thus, it remains unclear how the different parts of HP1 cooperate in bridging nucleosomes and to what extent this is impacted by presence of DNA linker between the nucleosomes.

Another clear example of how proteins can make use of nucleosome bridging for their function is the polycomb repressive complex 2 (PRC2). PRC2 is a methyltransferase that is able to methylate H3K27 leading to gene silencing[98]. Besides the catalytic domain, PRC2 also contains a H3K27me3-binding domain, allowing propagation of the H3K27me3 mark. PRC2 is thus a multivalent nucleosome-binding protein. Interestingly, PRC2 shows higher activity on dinucleosomes compared to mononucleosomes[99]. A recent cryo-EM structure using a specially crafted dinucleosomal substrate containing one H3K37me3 nucleosome and one unmodified nucleosome showed how PRC2 sits between the two nucleosomes, binding to both the modified and unmodified tail and the nucleosomal DNA[100]. Within the complex, the unmodified H3K27 tail is positioned on the surface of the catalytic domain. The increased DNA binding sites on dinucleosomes and the positioning of the substrate are most likely what increase the binding affinity and activity of PRC2 on dinucleosomes compared to mononucleosomes. Strikingly, PRC2 is able to adapt to different linker lengths and different orientations between the two nucleosomes due to a flexible hinge in one of the subunits[100]. A similar preference for di-nucleosomal substrates has been observed for several other proteins, including ZMET2, a DNA methyltransferase that recognizes methylated H3K9[101], and Rpd3S, a histone deacetylase complex recruited by RNA polymerase II[102].

Nucleosome (de)stacking

From the analysis in Figure 1 it will be clear that many proteins that bind to the histone octamer surface, for example via the acidic patch, are incompatible with close nucleosome stacking. However, even compacted nucleosomal arrays show spontaneous and dynamic opening allowing transient access and binding of chromatin factors[66]. To what extent acidic patch binding proteins would subsequently destabilize nucleosome packing and alter higher-order structure will also depend on their residence times in the bound states. The Fierz lab demonstrated that pioneer transcription factor Rap1 can transiently invade and disrupt stacking of neighboring nucleosomes without drastically altering nucleosome conformation, while requiring the cooperation of RSC remodeler for stable binding[103]. Both linker histones and HP1 are proteins that stabilize the stacking of nucleosomes. Linker histone stabilizes compacted conformations of the compacting linker DNA, thereby removing a barrier for proximity of nucleosomes and formation of favorable inter-nucleosome interactions. By bridging neighboring nucleosomes in an oligonucleosomal array HP1 can transiently stabilize stacking of nucleosomes[104]. Whether a protein exists that tightly clamps packed nucleosomes together remains to be seen.

Protein-protein interactions in chromatin condensates

The formation of a dynamically cross-linked network of biomolecules in condensates impacts the formation of protein-protein or protein-nucleic acid interactions at several levels[105]. First, the internal crowding and the confinement of interaction partners in the condensate will affect the binding affinity. On one hand diffusion rates will be reduced due to the increased viscosity, potentially lowering binding affinities. Indeed, diffusion of both H1 and HP1 are reduced roughly two-fold in heterochromatin condensates[18]. This effect, however, is in general overshadowed by the reduced available free volume in a condensate that promotes intermolecular interactions due to depletion interactions[106,107]. Also, the high local protein concentrations in the condensate, with reports of up to 30 mM in vitro[108], will promote the formation of protein complexes. For chromatin, the nucleosome concentration in cells has been estimated by Weidemann et al. to average to 140 μM, with maxima around 250 μM, corresponding to an average packing density of nucleosome of ~10%[109]. This would mean that a nucleosome binding protein with dissociation constant K_D of 0.2-0.3 mM would still be bound for 50% of the time when inside a dense chromatin region, supporting the importance of weak interactions in chromatin organization[110]. Second, the network of interacting molecules in a condensate may work as a sieve or filter, either preventing molecules above a certain size to enter[111] or enriching for binding partners[112]. A sieve-like barrier has been proposed for dense chromatin domains[113], and a recent study of HP1-heterochromatin condensates showed exclusion of TFIIB in vitro[27]. However, in-cell studies show that even dense heterochromatin regions are accessible to proteins of 500-600 kDa and dextran polymers with radius of gyration of 10 nm[114], which is aided by intrinsic chromatin dynamics[115]. The boundary of heterochromatin domains was recently shown to strongly reduce diffusion of an inert probe[18]. Thus, the specific characteristics of a protein (affinity for a certain chromatin state, including histone modifications and associated proteins) may be critical for enrichment within specific condensates. A third general factor is that the constituent proteins in a condensate may impose a distinct physiochemical environment influencing molecular stability, activity or folding. For example, the hydrophobic environment of Ddx4 condensates was shown to be able to melt double-strand DNA[116]. Recently, it was found that the proteins required for H2B mono-ubiquitination form a specialized droplet that resulted in an increased rate of ubiquitination compared to a non-phase separated state[117].

The protein interactions that drive condensate formation in chromatin-related systems, i.e. the scaffold proteins, in many cases involve a combination of a well-defined ‘anchoring’ interaction and dynamic interactions from an intrinsically disordered region[26,118–120]. Intrinsically disordered regions are well known to form multivalent cation-pi, pi-pi or charge-charge interactions in phase separation[32,121–123]. In the next section we will focus on the phase separation promoting interactions from intrinsically disordered regions in the core histones, linker histones and HP1 (Fig. 2.5).

Inter-nucleosome interactions in phase separation

The work from the Rosen lab showed that histone tails are responsible for the intrinsic phase separation of nucleosomal arrays, in particular the H4 tail, and that lysine acetylation by p300 can reverse condensate formation[19]. Interestingly, the interaction between H4 tail and the H2A/H2B acidic patch, which promotes nucleosome packing, was not involved in driving phase separation. This indicates that the tails mediate interactions between arrays, most likely by binding DNA.

All histone tails are known to bind DNA by virtue of their overall high positive charge, formed by patches of positive residues interspersed with neutral residues and near absence of negatively charge residues (Fig 2.5a). The affinities of the histone tail-DNA interactions within the nucleosome have been probed by measuring the accessibility of tail cysteine mutants for chemical attack[125,126]. These experiments showed that at 150 mM NaCl, the H2B is bound to the DNA 90-95% of the time with a 15/0.4 sec lifetime of the bound/unbound state[125], and that the H3 tail is 90% bound[126]. Extensive molecular dynamics simulations showed that lysine and arginines in the tails bind mainly to the DNA minor groove, in many different conformations[127]. As such the histone tails can be considered as an electrostatic glue[128].

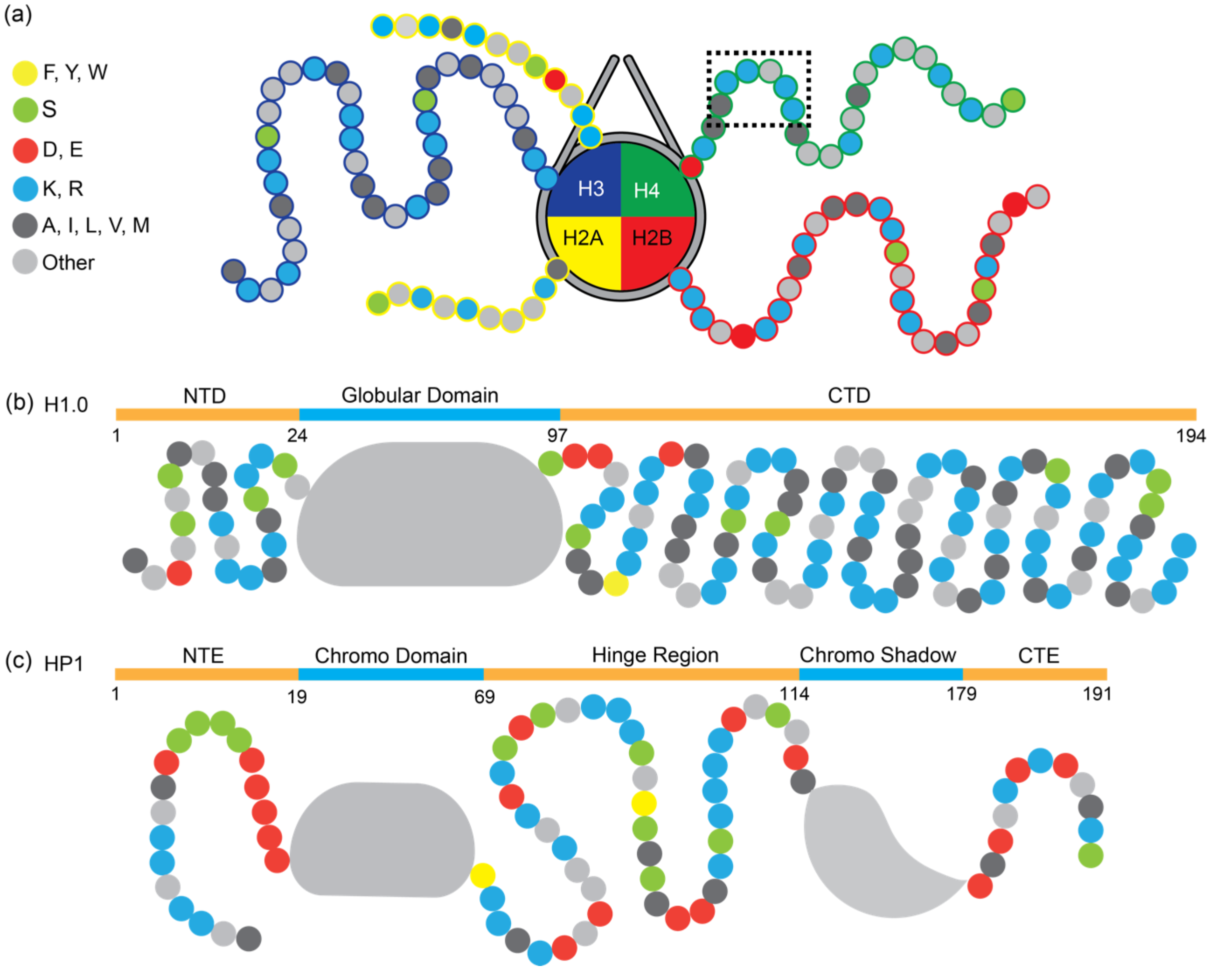

Figure 2.5: Amino acid composition in the intrinsically disordered regions of the core histones, linker histone H1 and HP1. Each small circle indicates one residue in the tail regions of human core histones (a), human H1.0 (b) and human HP1α (c). Folded domains are represented as grey blobs. The core histone tails have a net positive charge. Residues K16, R17, R19, and K20 in the H4 tail are boxed. The H1.0 NTD and CTD have a high density of positively charged residues while lacking negatively charged residues. N-terminal domain (NTD), C-terminal domain (CTD), N-terminal tail (NTE), C-terminal tail (CTE). Figure (c) was adapted from ref. [124].

While the affinities of inter-nucleosomal tail-DNA interactions are not known, their role in array oligomerization has been probed. While only the H4 tail is required for folding of arrays[59], all histone tails and in particular the H3 and H4 tails are required for salt induced array oligomerization[129,130]. The inter-array interactions of the H4 tail are not dependent on the acidic patch, indicating DNA binding instead[131,132]. Thus it is likely that in the phase-separated droplets of nucleosomal arrays both H3 tail-DNA and H4 tail-DNA interactions contribute to forming a dynamic network of arrays, consistent with experimental findings[19].

To get a clearer picture on how these inter-array tail-DNA interactions would influence the condensation and arrangement of the arrays in the droplet, it is important to consider two factors. First, phase separation was readily induced in arrays with linker DNA lengths corresponding to 10*n*+5, and much less so in arrays with 10*n* linkers. While 10*n* arrays can fold into compact 30nm-fibre structures[51], 10*n*+5 arrays are less compact and show less nucleosomes stacking[53]. The more open structure of the 10*n*+5 array could promote the formation of inter-array contacts. Second, the phase separated droplets were found to have a 10,000x fold enrichment in nucleosome concentration over the solution, reaching a concentration of 340 μM in the droplet[19]. This compares favorably with the observed cellular range[109]. Furthermore, following the ideas of Weidemann et al., we can estimate that the packing density of nucleosomes in the droplet is ca. 30%. This is based on the volume per nucleosome in the most compacted state for linked nucleosomes, the 30-nm structure, resulting in a maximum nucleosome concentration of 1.2 mM[109]. The 30% packing density translates into 1 to 2 inter-array contacts per 12-mer array. Also, it can be estimated that the average distance between arrays is ~75nm, when accounting for the fact that arrays must contact each other. Together the nucleosome arrangement in the phase-separated droplet can be imagined as in Figure 2.6. Inter-nucleosomal, inter-array interactions dynamically link one array to the next, resulting in an overall rather open, fluctuating network.

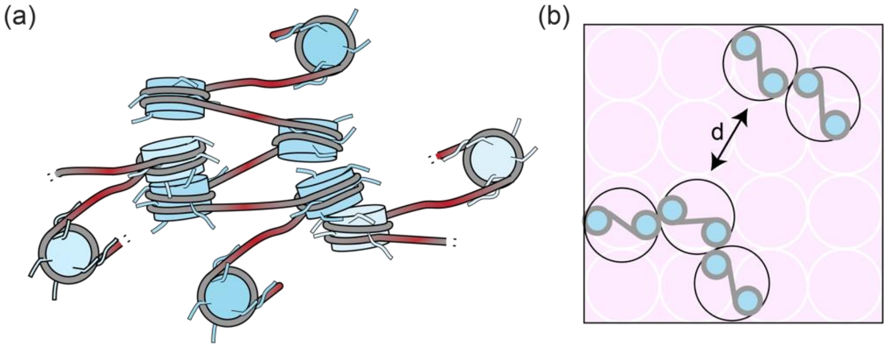

Figure 2.6. Schematic representation of a possible nucleosome arrangement in a chromatin droplet. (a) Packing and interdigitation of three fibers. The arrangement of the main fiber in darker blue is based on the model for 183bp arrays from Bass et al.[53], here using a longer linker to account for the 46bp linker used in Gibson et al.[19]. The number of inter-array contacts is based on the experimentally observed nucleosome concentration as outlined in the text (1-2 contact per 12-mer, here only 6 of the 12mer-are shown). Inter-nucleosomal interactions are here shown as head-to-tail face-to-face nucleosome stacks, stabilized by H4-tail DNA contacts. Other arrangements are possible. (b) Schematic to illustrate the nucleosome density in the droplet, assuming each array occupies a cylinder of 30nm diameter, and an overall packing density of 30%. The average distance between array, *d*, is 75 nm. The white circles in the background indicate 16 theoretical positions of compact fibers in a maximally packed state. At 30% packing ca. 5 of these 16 positions are occupied.

Linker histone in chromatin phase separation

The work by Gibson et al. also established that linker histone H1.4 promotes the phase separation of nucleosome arrays, lowering the salt concentration required to induce phase separation[19]. They also found that the linker histone decreased the overall dynamics within the separated phase. Both findings suggest increased inter-array interaction due to linker histones. A previous study showed that the C-terminal tail (CTD) of H1 can phase separate together with DNA[133]. The CTD domain of linker histones is highly basic (Fig. 2.5b) and electrostatic interactions most likely play an important role in linker histone phase separation[133]. Several residues in the CTD are post-translationally modified in linker histone regulation[134], some introducing negative charges that decrease DNA binding affinity[133]. The CTD is known to be dynamic in structure[135] and remains dynamic and unstructured upon binding of DNA[133]. The CTD is expected to be the driving factor of the linker histone-nucleosome interaction as removal of the CTD causes a 10 to 200x drop in affinity for either DNA or nucleosomes (See Table 2.1 and S2.2). Interestingly, the CTD is required for increased density of and reduced internal diffusion in phase separated nucleosome arrays[19]. Moreover, this effect is independent of the presence of the globular domain as a fusion of the CTD to the LANA peptide, targeting the CTD to the acidic patch, showed similar effects. This indicates that the linker histone can bridge different arrays by anchoring on one nucleosome in the first array with its globular domain and binding to the linker DNA in the second array through the CTD. The electrostatic screening of the linker DNA by the CTD also explains how linker histones can condense arrays with long linker DNA lengths to similar high densities as arrays with short linker length[19]. It should be noted that the impact of linker histones on nucleosome array phase separation was studied in this work within the context of 10*n*+5 arrays. It would be interesting to see if linker histones can also promote phase separation of nucleosome arrays with 10*n* linker DNA lengths. In this case the formation of inter-array bridging interactions of the CTD may be in competition with formation of intra-array interactions that stabilize the folding of the array.

A recent study showed that H1 was found to colocalize with HP1 and compact DNA, condensing in an average of 10 puncta in the cell nucleus of Hela cells during the interphase[136]. These puncta were found to be dynamic and able to coalesce when they come into contact, supporting phase separation within the nucleus of live cells. However, the authors also observed that these puncta where not always spherical and further found that H1-nucleosome array condensates were irregular in shape in vitro. It should be noted that these experiments used arrays isolated from nuclear extracts and can thus be expected to be heterogenous in terms of nucleosome positioning and histone tail modifications. Still, this may be a sign that phase separation of nucleosomal arrays and chromatin in general is not purely an LLPS process, as that should result in spherical droplets. As a polymer with intrinsic affinity between its subunits, chromatin phase separation may be better described by a polymer-polymer-phase separation (PPPS) or other mixed liquid/polymer models[137,138]. Such mechanisms are also in-line with the absence of a strong boundary-based exclusion effect to other protein factors. The irregular droplet shape observed points to reduced internal dynamics of the array and increased inter-array contacts. This could be the result of 'maturation' of initially liquid droplets to more dense gels or solids, which will alter the material properties of the condensate[30]. In the cell, the degree of long range chromatin contacts needs to be regulated as there is both a requirement for liquid like properties to allow access for diverse protein machineries[115], as well as a need for structural support of the nucleus through dense chromatin domains[139,140].

Table *2*.1: Affinities of H1-nucleosome interaction.

Type	**Domain**	**Low [I] (<100mM)[a]**	**High [I] (>100mM)[a]**
DNA	CTD[b]	19 nM	101-133 nM
	Globular	n/a	1446 nM
	Full length	10-18 nM	([c]7) 140-313 nM
Mononucleosome	Globular	n/a	[c]123-1300nM
	Full length	2nM	[c]0.013nM
Dinucleosome	Full length	7.4nM	n/a
Trinucleosome	Full length	n/a	[c]0.046 nM

[a] Affinity depends strongly on ionic strength of the buffer, dropping with higher ionic strength. References are listed in Table S2.2.

[b] C-terminal domain.

[c] Measured using a fluorescence-based methods to probe short lived, high affinity interactions.

Heterochromatin HP1 in phase separation

The work of Strom *et al.* showed that the establishment of heterochromatin domains in Drosophila embryos proceeds through a phase separation mechanism driven by HP1[18]. As mentioned above, the HP1 dimer can bridge nucleosomes due to its bivalent reading of the histone H3K9me mark. Thus, HP1 proteins can be expected to be able to promote formation of a dynamic chromatin network which would be required for phase separation. Indeed, mutations in the dimerization domain abolish phase separation of HP1a proteins with chromatin[17,18,141]. In contrast to the tight, but highly dynamic, H1 chromatin interaction, the interaction of HP1 with the H3K9me site on the nucleosome is rather weak, with K_D 's in the micromolar range (Table 2.2 and S2.3). This anchoring interaction relies on intermolecular β-sheet formation and capture of the methylated K9 sidechain in an aromatic cage[142]. In addition, the hinge region in HP1 can bind DNA through a basic region (see Figure 5(c)) with micromolar affinity, increasing the effective chromatin affinity[143]. The modular nature of these weak interactions render HP1 proteins sensitive to regulation by post-translational modifications and interactions with additional protein factors as reviewed in[144,145].

Table *2.2*: Affinities of the HP1-nucleosome interaction.

Type	**Domain**	**Mm /Dm /Hs**[a]	**Sc**[a]
Anchoring	CD[b]-H3K9me3	2 µM	10-12 µM
	CD-H3K9me2	2-6 µM	n/a
	CD-H3K9me0	n/a	170 µM
Dimerization	CSD[c]-CSD	3 µM	< 17 nM
	CD-CD (closed state)	n/a	50 nM / 110 µM
DNA binding	HP1-DNA	0.4 µM	15 µM
Additional interactions	NTE[d]-H3K9me3	2 µM	n/a
	CSD-H3 tail	60 µM	n/a

[a] Sc and higher eukaryotes are presented separately since there are key differences in their structure and in their phase separation behavior. References are listed in Table S2.3.

[b] Chromodomain

[c] Chromoshadow domain

[d] N-terminal extension

The relatively low affinities are in line with the observed highly dynamic mode of chromatin binding by HP1a both in vitro and in vivo[104,146–148]. Notably, Strom *et al.* also identified a significant fraction (up to 50%) of immobile HP1a upon maturation of the heterochromatin domain in cells[18]. This may reflect the intrinsic phase separation property of HP1a[17,18], promoting the formation of a dense network HP1a through HP1-nucleosome as well as HP1-HP1 interactions. To what extent HP1-driven phase separation also promotes inter-nucleosomal interactions, for example whether there are increased H4 tail-DNA contacts in the condensate, remains yet unclear. Work by the Fierz lab showed that HP1a can transiently stabilize nucleosome stacking in nucleosomal arrays[104]. Possibly, HP1 could also stabilize long-range “inter-array” contacts in condensates, as schematically illustrated in Figure 2.6. The abundance of such long-range contacts could be a decisive difference between the more liquid and more immobile heterochromatin regions.

Recently, the yeast paralog of HP1, Swi6, was found to induce a conformational change in the nucleosome upon binding[141]. This “reshaping” event increased solvent exposure of buried histone octamer regions, likely by weakening histone-histone and histone-DNA interactions. Weakening of these intra-nucleosomal contacts would be the effect of the tripartite Swi6-nucleosome interaction: the CD can bind to H3K9me3, the hinge to DNA, and the CSD to H2B α1-helix. Notably, the CSD-H2B interaction would involve unfolding of the H2B α1 helix which is positioned close to the nucleosomal DNA. A possibly related reshaping event has also been suggested for mammalian HP1a, where the CSD domain bind the H3 αN helix which is also close to nucleosomal DNA[149,150]. In either case, the increased exposure of histone proteins due to reshaping could result in an increased repertoire of inter-nucleosomal or HP1-nucleosome binding modes and thus critically contribute to phase separation.

The CSD domain of HP1 proteins also provides the interactions surface for a wide variety of factors, via a hydrophobic surface on the CSD-CSD dimer surface. Recently, it was shown that both a HP1 scaffolding protein (TRIM28) and the H3K9me2/3-writer enzyme (Suv39H1) are enriched in HP1 foci in cells and that these proteins enhance condensate formation in vitro[27]. Together with the hydrophobic CD-H3K9me2/3 interaction, these interactions could explain the sensitivity of HP1a droplets in cells to treatment with hexane-diol, a compound that interferes with hydrophobic interactions[18]. Notably, both Suv39H1 and TRIM28 effectively enhance the multivalency of HP1 by sequestering multiple copies of HP1 dimers in one complex and this effect was shown to be responsible for the enhanced phase separation[27]. Another intriguing finding is that AuroraB, which also binds the CSD-CSD dimer, can be enriched in HP1 droplets[17]. AuroraB phosphorylates H3S10 during mitosis and thereby disrupts the CD-H3K9me3 interaction[151]. Thus, both heterochromatin promoting (Suv39H1) and inhibiting proteins (AuroraB) can be recruited to HP1/heterochromatin condensates, illustrating how the intricate balance of opposing activities can regulate condensate formation[152]. Finally, HP1α and H1 have been found to interact through the linker domain of HP1α[153,154]. To what extent they enforce each other in promoting phase separation is yet unclear.

Conclusion

When looking beyond the nucleosome, chromatin structure and the way proteins interact with it becomes significantly more complex. Structural studies on mono-nucleosomes lay the foundation for our understanding these interactions. To understand the interplay between chromatin binding factors and chromatin as an array of nucleosomes, there is a need for structural studies of nucleosome-protein complexes with a di- or oligo-nucleosomal complex. For such studies in vitro, the experimenter faces many difficult questions, on top of the stiff challenge to prepare homogenous samples. The studies on linker histones have illustrated the pronounced sensitivity of nucleosomal arrays to choices on DNA linker length and salt conditions, and the increased dynamics of the bound protein. As of yet only few structures at the oligonucleosomal level have been solved, but with the continuous advances in cryo-EM and sample preparation, we expect to see more of these structures in the future. One of the biggest challenges will be to capture the structural details of the interactions occurring in (hetero)chromatin droplets, due to their intrinsic dynamics. Especially in these cases, integration throughout the structural, biophysical and cell biological range is needed to bring these critical mechanisms into focus. It may seem like a hopelessly complicated endeavor, but at the same time the challenges can also be taken as motivation. It is through rigorous studies as those highlighted here that we increase our understanding.

References

1. Luger, K., Mäder, A. W., Richmond, R. K., Sargent, D. F. & Richmond, T. J. Crystal structure of the nucleosome core particle at 2.8 A resolution. *Nature* **389**, 251–60 (1997).

2. Lieberman-Aiden, E. *et al.* Comprehensive Mapping of Long-Range Interactions Reveals Folding Principles of the Human Genome. *Science (80-.).* **326**, 289–293 (2009).

3. van Steensel, B. & Belmont, A. S. Lamina-Associated Domains: Links with Chromosome Architecture, Heterochromatin, and Gene Repression. *Cell* **169**, 780–791 (2017).

4. Horn, P. J. & Peterson, C. L. Molecular biology: Chromatin higher order folding: Wrapping up transcription. *Science (80-.).* **297**, 1824–1827 (2002).

5. Hansen, J. C. *et al.* The 10-nm chromatin fiber and its relationship to interphase chromosome organization. *Biochem. Soc. Trans.* **46**, 67–76 (2018).

6. Luger, K., Dechassa, M. L. & Tremethick, D. J. New insights into nucleosome and chromatin structure: an ordered state or a disordered affair? *Nat. Rev. Mol. Cell Biol.* **13**, 436–447 (2012).

7. Lakadamyali, M. & Cosma, M. P. Visualizing the genome in high resolution challenges our textbook understanding. *Nat. Methods* **17**, 371–379 (2020).

8. Ricci, M. A., Manzo, C., García-Parajo, M. F., Lakadamyali, M. & Cosma, M. P. Chromatin fibers are formed by heterogeneous groups of nucleosomes in vivo. *Cell* **160**, 1145–1158 (2015).

9. Nozaki, T. *et al.* Dynamic Organization of Chromatin Domains Revealed by Super-Resolution Live-Cell Imaging. *Mol. Cell* **67**, 282-293.e7 (2017).

10. Trzaskoma, P. *et al.* Ultrastructural visualization of 3D chromatin folding using volume electron microscopy and DNA in situ hybridization. *Nat. Commun.* **11**, 1–9 (2020).

11. Ou, H. D. *et al.* ChromEMT: Visualizing 3D chromatin structure and compaction in interphase and mitotic cells. *Science (80-.).* **357**, (2017).

12. Otterstrom, J. *et al.* Super-resolution microscopy reveals how histone tail acetylation affects DNA compaction within nucleosomes in vivo. *Nucleic Acids Res.* **47**, 8470–8484 (2019).

13. Xu, J. *et al.* Super-Resolution Imaging of Higher-Order Chromatin Structures at Different Epigenomic States in Single Mammalian Cells. *Cell Rep.* **24**, 873–882 (2018).

14. Cai, S., Song, Y., Chen, C., Shi, J. & Gan, L. Natural chromatin is heterogeneous and self-associates in vitro. *Mol. Biol. Cell* **29**, 1652–1663 (2018).

15. Maeshima, K., Tamura, S., Hansen, J. C. & Itoh, Y. Fluid-like chromatin: Toward understanding the real chromatin organization present in the cell. *Curr. Opin. Cell Biol.* **64**, 77–89 (2020).

16. Wako, T. *et al.* Human metaphase chromosome consists of randomly arranged chromatin fibres with up to 30-nm diameter. *Sci. Rep.* **10**, 1–6 (2020).

17. Larson, A. G. *et al.* Liquid droplet formation by HP1alpha suggest a role for phase separation in heterochromatin. *Nat. Publ. Gr.* **547**, 236–240 (2017).

18. Strom, A. R. *et al.* Phase separation drives heterochromatin domain formation. *Nature* **547**, 241–245 (2017).

19. Gibson, B. A. *et al.* Organization of Chromatin by Intrinsic and Regulated Phase Separation. *Cell* **179**, 470-484.e21 (2019).

20. Banani, S. F., Lee, H. O., Hyman, A. A. & Rosen, M. K. Biomolecular condensates: Organizers of cellular biochemistry. *Nat. Rev. Mol. Cell Biol.* **18**, 285–298 (2017).

21. Hyman, A. A., Weber, C. A. & Jülicher, F. Liquid-liquid phase separation in biology. *Annu. Rev. Cell Dev. Biol.* **30**, 39–58 (2014).

22. Peng, A. & Weber, S. C. Evidence for and against liquid-liquid phase separation in the nucleus. *Non-coding RNA* **5**, (2019).

23. Sabari, B. R., Dall'Agnese, A. & Young, R. A. Biomolecular Condensates in the Nucleus. *Trends Biochem. Sci.* **45**, 961–977 (2020).

24. Boehning, M. *et al.* RNA polymerase II clustering through carboxy-terminal domain phase separation. *Nat. Struct. Mol. Biol.* **25**, 833–840 (2018).

25. Lu, H. *et al.* Phase-separation mechanism for C-terminal hyperphosphorylation of RNA polymerase II. *Nature* **558**, 318–323 (2018).

26. Boija, A. *et al.* Transcription Factors Activate Genes through the Phase-Separation Capacity of Their Activation Domains. *Cell* **175**, 1842-1855.e16 (2018).

27. Wang, L. *et al.* Histone Modifications Regulate Chromatin Compartmentalization by Contributing to a Phase Separation Mechanism. *Mol. Cell* **76**, 646-659.e6 (2019).

28. Strom, A. R. & Brangwynne, C. P. The liquid nucleome – phase transitions in the nucleus at a glance. *J. Cell Sci.* **132**, 1–7 (2019).

29. Cramer, P. Organization and regulation of gene transcription. *Nature* **573**, 45–54 (2019).

30. Boeynaems, S. *et al.* Protein Phase Separation: A New Phase in Cell Biology. *Trends Cell Biol.* **28**, 420–435 (2018).

31. Frank, L. & Rippe, K. Repetitive RNAs as Regulators of Chromatin-Associated Subcompartment Formation by Phase Separation. *J. Mol. Biol.* **432**, 4270–4286 (2020).

32. Martin, E. W. & Mittag, T. Relationship of Sequence and Phase Separation in Protein Low-Complexity Regions. *Biochemistry* **57**, 2478–2487 (2018).

33. Li, P. *et al.* Phase transitions in the assembly of multivalent signalling proteins. *Nature* **483**, 336–340 (2012).

34. Zhu, L. & Brangwynne, C. P. Nuclear bodies: The emerging biophysics of nucleoplasmic phases. *Curr. Opin. Cell Biol.* **34**, 23–30 (2015).

35. Maeshima, K., Imai, R., Tamura, S. & Nozaki, T. Chromatin as dynamic 10-nm fibers.

Chromosoma **123**, 225–237 (2014).

36. Maeshima, K., Ide, S., Hibino, K. & Sasai, M. Liquid-like behavior of chromatin. *Curr. Opin. Genet. Dev.* **37**, 36–45 (2016).

37. Eltsov, M., MacLellan, K. M., Maeshima, K., Frangakis, A. S. & Dubochet, J. Analysis of cryo-electron microscopy images does not support the existence of 30-nm chromatin fibers in mitotic chromosomes in situ. *Proc. Natl. Acad. Sci. U. S. A.* **105**, 19732–19737 (2008).

38. McDowall, A. W., Smith, J. M. & Dubochet, J. Cryo-electron microscopy of vitrified chromosomes in situ. *EMBO J.* **5**, 1395–1402 (1986).

39. Dodonova, S. O., Zhu, F., Dienemann, C., Taipale, J. & Cramer, P. Nucleosome-bound SOX2 and SOX11 structures elucidate pioneer factor function. *Nature* **580**, 669–672 (2020).

40. Michael, A. K. *et al.* Mechanisms of OCT4-SOX2 motif readout on nucleosomes. *Science (80-.).* **368**, 1460–1465 (2020).

41. Van Nuland, R. *et al.* Nucleosomal DNA binding drives the recognition of H3K36-methylated nucleosomes by the PSIP1-PWWP domain. *Epigenetics and Chromatin* **6**, 1 (2013).

42. Wang, H., Farnung, L., Dienemann, C. & Cramer, P. Structure of H3K36-methylated nucleosome–PWWP complex reveals multivalent cross-gyre binding. *Nat. Struct. Mol. Biol.* **27**, 8–13 (2020).

43. Skrajna, A. *et al.* Comprehensive nucleosome interactome screen establishes fundamental principles of nucleosome binding. *Nucleic Acids Res.* **48**, 1–18 (2020).

44. Morrison, E. A., Bowerman, S., Sylvers, K. L., Wereszczynski, J. & Musselman, C. A. The conformation of the histone H3 tail inhibits association of the BPTF PHD finger with the nucleosome. *Elife* **7**, 1–35 (2018).

45. Hsieh, T. H. S. *et al.* Mapping Nucleosome Resolution Chromosome Folding in Yeast by Micro-C. *Cell* **162**, 108–119 (2015).

46. Risca, V. I., Denny, S. K., Straight, A. F. & Greenleaf, W. J. Variable chromatin structure revealed by in situ spatially correlated DNA cleavage mapping. *Nature* **541**, 237–241 (2017).

47. Moraru, M. & Schalch, T. Chromatin fiber structural motifs as regulatory hubs of genome function? *Essays Biochem.* **63**, 123–132 (2019).

48. Krietenstein, N. & Rando, O. J. Mesoscale organization of the chromatin fiber. *Curr. Opin. Genet. Dev.* **61**, 32–36 (2020).

49. Ohno, M. *et al.* Sub-nucleosomal Genome Structure Reveals Distinct Nucleosome Folding Motifs. *Cell* **176**, 520-534.e25 (2019).

50. Schalch, T., Duda, S., Sargent, D. F. & Richmond, T. J. X-ray structure of a tetranucleosome and its implications for the chromatin fibre. *Nature* **436**, 138–141 (2005).

51. Song, F. *et al.* Cryo-EM study of the chromatin fiber reveals a double helix twisted by tetranucleosomal units. *Science (80-.).* **344**, 376–380 (2014).

52. Valouev, A. *et al.* Determinants of nucleosome organization in primary human cells. *Nature* **474**, 516–522 (2011).

53. Bass, M. V., Nikitina, T., Norouzi, D., Zhurkin, V. B. & Grigoryev, S. A. Nucleosome spacing periodically modulates nucleosome chain folding and DNA topology in circular nucleosome arrays. *J. Biol. Chem.* **294**, 4233–4246 (2019).

54. de Jong, B. E., Brouwer, T. B., Kaczmarczyk, A., Visscher, B. & van Noort, J. Rigid Basepair Monte Carlo Simulations of One-Start and Two-Start Chromatin Fiber Unfolding by Force. *Biophys. J.* **115**, 1848–1859 (2018).

55. Correll, S. J., Schubert, M. H. & Grigoryev, S. A. Short nucleosome repeats impose rotational modulations on chromatin fibre folding. *EMBO J.* **31**, 2416–2426 (2012).

56. Clark, D. J. & Kimura, T. Electrostatic mechanism of chromatin folding. *J. Mol. Biol.* **211**, 883–896 (1990).

57. Korolev, N. *et al.* Electrostatic origin of salt-induced nucleosome array compaction. *Biophys. J.* **99**, 1896–1905 (2010).

58. Allahverdi, A., Chen, Q., Korolev, N. & Nordenskiöld, L. Chromatin compaction under mixed salt conditions: Opposite effects of sodium and potassium ions on nucleosome array folding. *Sci. Rep.* **5**, (2015).

59. Dorigo, B., Schalch, T., Bystricky, K. & Richmond, T. J. Chromatin fiber folding: Requirement for the histone H4 N-terminal tail. *J. Mol. Biol.* **327**, 85–96 (2003).

60. Sinha, D. & Shogren-Knaak, M. A. Role of direct interactions between the histone H4 tail and the H2A core in long range nucleosome contacts. *J. Biol. Chem.* **285**, 16572–16581 (2010).

61. Shogren-Knaak, M. *et al.* Histone H4-K16 Acetylation Controls Chromatin Structure and Protein Interactions. *Science (80-.).* **311**, 844–847 (2006).

62. Chen, Q., Yang, R., Korolev, N., Liu, C. F. & Nordenskiöld, L. Regulation of Nucleosome Stacking and Chromatin Compaction by the Histone H4 N-Terminal Tail–H2A Acidic Patch Interaction. *J. Mol. Biol.* **429**, 2075–2092 (2017).

63. Wilkins, B. J. *et al.* A cascade of histone modifications induces chromatin condensation in mitosis. *Science (80-.).* **343**, 77–80 (2014).

64. Korolev, N., Lyubartsev, A. P. & Nordenskiöld, L. A systematic analysis of nucleosome core particle and nucleosome-nucleosome stacking structure. *Sci. Rep.* **8**, 1–14 (2018).

65. Armeev, G. A., Gribkova, A. K., Pospelova, I., Komarova, G. A. & Shaytan, A. K. Linking chromatin composition and structural dynamics at the nucleosome level. *Curr. Opin. Struct. Biol.* **56**, 46–55 (2019).

66. Fierz, B. & Poirier, M. G. Biophysics of Chromatin Dynamics. *Annu. Rev. Biophys.* **48**, 321–345 (2019).

67. Hergeth, S. P. & Schneider, R. The H1 linker histones: multifunctional proteins beyond the nucleosomal core particle. *EMBO Rep.* **16**, 1439–1453 (2015).

68. Kijima, M. *et al.* Histone H1 quantity determines the efficiency of chromatin condensation in both apoptotic and live cells. *Biochem. Biophys. Res. Commun.* **512**, 202–207 (2019).

69. Cirillo, L. A. *et al.* Opening of Compacted Chromatin by Early Developmental Transcription Factors HNF3 (FoxA) and GATA-4. *Mol. Cell* **9**, 279–289 (2002).

70. Postnikov, Y. & Bustin, M. Regulation of chromatin structure and function By HMGN proteins. *Biochim. Biophys. Acta - Gene Regul. Mech.* **1799**, 62–68 (2010).

71. Zhou, B. R. *et al.* Structural Mechanisms of Nucleosome Recognition by Linker Histones. *Mol. Cell* **59**, 628–638 (2015).

72. Zhou, B.-R. *et al.* Distinct Structures and Dynamics of Chromatosomes with Different Human Linker Histone Isoforms. *Mol. Cell* 1–17 (2020) doi:10.1016/j.molcel.2020.10.038.

73. Adhireksan, Z., Sharma, D., Lee, P. L. & Davey, C. A. Near-atomic resolution structures of interdigitated nucleosome fibres. *Nat. Commun.* **11**, 1–13 (2020).

74. Zhou, B. R. & Bai, Y. Chromatin structures condensed by linker histones. *Essays Biochem.* **63**, 75–87 (2019).

75. Öztürk, M. A., Cojocaru, V. & Wade, R. C. Toward an Ensemble View of Chromatosome Structure: A Paradigm Shift from One to Many. *Structure* **26**, 1050–1057 (2018).

76. Zhou, B. R. *et al.* A Small Number of Residues Can Determine if Linker Histones Are Bound On or Off Dyad in the Chromatosome. *J. Mol. Biol.* **428**, 3948–3959 (2016).

77. Bednar, J. *et al.* Structure and Dynamics of a 197 bp Nucleosome in Complex with Linker Histone H1. *Mol. Cell* **66**, 384-397.e8 (2017).

78. Sridhar, A., Orozco, M. & Collepardo-Guevara, R. Protein disorder-to-order transition enhances the nucleosome-binding affinity of H1. *Nucleic Acids Res.* **48**, 5318–5331 (2020).

79. Zhou, B. R. *et al.* Revisit of Reconstituted 30-nm Nucleosome Arrays Reveals an Ensemble of Dynamic Structures. *J. Mol. Biol.* **430**, 3093–3110 (2018).

80. Garcia-Saez, I. *et al.* Structure of an H1-Bound 6-Nucleosome Array Reveals an Untwisted Two-Start Chromatin Fiber Conformation. *Mol. Cell* **72**, 902-915.e7 (2018).

81. Hammond, C. M., Strømme, C. B., Huang, H., Patel, D. J. & Groth, A. Histone chaperone networks shaping chromatin function. *Nat. Rev. Mol. Cell Biol.* **18**, 141–158 (2017).

82. Clapier, C. R., Iwasa, J., Cairns, B. R. & Peterson, C. L. Mechanisms of action and regulation of ATP-dependent chromatin-remodelling complexes. *Nat. Rev. Mol. Cell Biol.* **18**, 407–422 (2017).

83. Kobayashi, W. & Kurumizaka, H. Structural transition of the nucleosome during chromatin remodeling and transcription. *Curr. Opin. Struct. Biol.* **59**, 107–114 (2019).

84. Sundaram, R. & Vasudevan, D. Structural Basis of Nucleosome Recognition and Modulation. *BioEssays* **42**, 1–16 (2020).

85. Yan, L. & Chen, Z. A Unifying Mechanism of DNA Translocation Underlying Chromatin

Remodeling. *Trends Biochem. Sci.* **45**, 217–227 (2020).

86. Prajapati, H. K., Ocampo, J. & Clark, D. J. Interplay among ATP-Dependent Chromatin Remodelers Determines Chromatin Organisation in Yeast. *Biology (Basel).* **9**, 190 (2020).

87. Brahma, S. & Henikoff, S. Epigenome Regulation by Dynamic Nucleosome Unwrapping. *Trends Biochem. Sci.* **45**, 13–26 (2020).

88. Canzio, D., Larson, A. & Narlikar, G. J. Mechanisms of functional promiscuity by HP1 proteins. *Trends Cell Biol.* **24**, 377–386 (2014).

89. Azzaz, A. M. *et al.* Human heterochromatin protein 1α promotes nucleosome associations that drive chromatin condensation. *J. Biol. Chem.* **289**, 6850–6861 (2014).

90. Canzio, D. *et al.* Chromodomain-Mediated Oligomerization of HP1 Suggests a Nucleosome-Bridging Mechanism for Heterochromatin Assembly. *Mol. Cell* **41**, 67–81 (2011).

91. Teif, V. B., Kepper, N., Yserentant, K., Wedemann, G. & Rippe, K. Affinity, stoichiometry and cooperativity of heterochromatin protein 1 (HP1) binding to nucleosomal arrays. *J. Phys. Condens. Matter* **27**, (2015).

92. Janssen, A., Colmenares, S. U. & Karpen, G. H. Heterochromatin: Guardian of the Genome. *Annu. Rev. Cell Dev. Biol.* **34**, 265–288 (2018).

93. Jacobs, S. A. & Khorasanizadeh, S. Structure of HP1 Chromodomain Bound to a Lysine 9 – Methylated Histone H3 Tail. *Science (80-.).* **295**, 2080–2084 (2002).

94. Cowieson, N. P., Partridge, J. F., Allshire, R. C. & McLaughlin, P. J. Dimerisation of a chromo shadow domain and distinctions from the chromodomain as revealed by structural analysis. *Curr. Biol.* **10**, 517–525 (2000).

95. Thiru, A. *et al.* Structural basis of HP1/PXVXL motif peptide interactions and HP1 localisation to heterochromatin. *EMBO J.* **23**, 489–499 (2004).

96. Nishibuchi, G. & Nakayama, J. I. Biochemical and structural properties of heterochromatin protein 1: Understanding its role in chromatin assembly. *J. Biochem.* **156**, 11–20 (2014).

97. Machida, S. *et al.* Structural Basis of Heterochromatin Formation by Human HP1. *Mol. Cell* **69**, 385-397.e8 (2018).

98. Cao, R. *et al.* Role of histone H3 lysine 27 methylation in polycomb-group silencing. *Science (80-.).* **298**, 1039–1043 (2002).

99. Martin, C., Cao, R. & Zhang, Y. Substrate preferences of the EZH2 histone methyltransferase complex. *J. Biol. Chem.* **281**, 8365–8370 (2006).

100. Poepsel, S., Kasinath, V. & Nogales, E. Cryo-EM structures of PRC2 simultaneously engaged with two functionally distinct nucleosomes. *Nat. Struct. Mol. Biol.* **25**, 154–162 (2018).

101. Stoddard, C. I. *et al.* A Nucleosome Bridging Mechanism for Activation of a Maintenance DNA Methyltransferase. *Mol. Cell* **73**, 73-83.e6 (2019).

102. Huh, J. W. *et al.* Multivalent di-nucleosome recognition enables the Rpd3S histone

deacetylase complex to tolerate decreased H3K36 methylation levels. *EMBO J.* **31**, 3564–3574 (2012).

103. Mivelaz, M. *et al.* Chromatin Fiber Invasion and Nucleosome Displacement by the Rap1 Transcription Factor. *Mol. Cell* **77**, 488-500.e9 (2020).

104. Kilic, S. *et al.* Single-molecule FRET reveals multiscale chromatin dynamics modulated by HP1α. *Nat. Commun.* **9**, 235 (2018).

105. Zhang, Y., Narlikar, G. J. & Kutateladze, T. G. Enzymatic Reactions inside Biological Condensates. *J. Mol. Biol.* (2020) doi:10.1016/j.jmb.2020.08.009.

106. Zimmerman, S. B. & Minton, A. P. Macromolecular Crowding: Biochemical, Biophysical, and Physiological Consequences. *Annu. Rev. Biophys. Biomol. Struct.* **22**, 27–65 (1993).

107. Zosel, F., Soranno, A., Buholzer, K. J., Nettels, D. & Schuler, B. Depletion interactions modulate the binding between disordered proteins in crowded environments. *Proc. Natl. Acad. Sci. U. S. A.* **117**, 13480–13489 (2020).

108. Ryan, V. H. *et al.* Mechanistic View of hnRNPA2 Low-Complexity Domain Structure, Interactions, and Phase Separation Altered by Mutation and Arginine Methylation. *Mol. Cell* **69**, 465-479.e7 (2018).

109. Weidemann, T. *et al.* Counting nucleosomes in living cells with a combination of fluorescence correlation spectroscopy and confocal imaging. *J. Mol. Biol.* **334**, 229–240 (2003).

110. Kantidze, O. L. & Razin, S. V. Weak interactions in higher-order chromatin organization. *Nucleic Acids Res.* **48**, 4614–4626 (2020).

111. Wachsmuth, M., Caudron-Herger, M. & Rippe, K. Genome organization: Balancing stability and plasticity. *Biochim. Biophys. Acta - Mol. Cell Res.* **1783**, 2061–2079 (2008).

112. Ditlev, J. A., Case, L. B. & Rosen, M. K. Who's In and Who's Out—Compositional Control of Biomolecular Condensates. *J. Mol. Biol.* **430**, 4666–4684 (2018).

113. Cremer, T. & Cremer, C. Chromosome territories, nuclear architecture and gene regulation in mammalian cells. *Nat. Rev. Genet.* **2**, 292–301 (2001).

114. Verschure, P. J. *et al.* Condensed chromatin domains in the mammalian nucleus are accessible to large macromolecules. *EMBO Rep.* **4**, 861–866 (2003).

115. Hihara, S. *et al.* Local Nucleosome Dynamics Facilitate Chromatin Accessibility in Living Mammalian Cells. *Cell Rep.* **2**, 1645–1656 (2012).

116. Nott, T. J., Craggs, T. D. & Baldwin, A. J. Membraneless organelles can melt nucleic acid duplexes and act as biomolecular filters. *Nat. Chem.* **8**, 569–575 (2016).

117. Gallego, L. D. *et al.* Phase separation directs ubiquitination of gene-body nucleosomes. *Nature* **579**, 592–597 (2020).

118. Sabari, B. R. *et al.* Coactivator condensation at super-enhancers links phase separation and gene control. *Science (80-.).* **361**, eaar3958 (2018).

119. Kilic, S. *et al.* Phase separation of 53BP1 determines liquid-like behavior of DNA repair compartments. *EMBO J.* **38**, 1–17 (2019).

120. Shrinivas, K. *et al.* Enhancer Features that Drive Formation of Transcriptional Condensates. *Mol. Cell* **75**, 549-561.e7 (2019).

121. Watson, M. & Stott, K. Disordered domains in chromatin-binding proteins. *Essays Biochem.* **63**, 147–156 (2019).

122. Martin, E. W. *et al.* Valence and patterning of aromatic residues determine the phase behavior of prion-like domains. *Science (80-.).* **367**, 694–699 (2020).

123. Peran, I. & Mittag, T. Molecular structure in biomolecular condensates. *Curr. Opin. Struct. Biol.* **60**, 17–26 (2020).

124. Ackermann, B. E. & Debelouchina, G. T. Heterochromatin Protein HP1α Gelation Dynamics Revealed by Solid-State NMR Spectroscopy. *Angew. Chemie - Int. Ed.* **58**, 6300–6305 (2019).

125. Wang, X. & Hayes, J. J. Site-specific binding affinities within the H2B tail domain indicate specific effects of lysine acetylation. *J. Biol. Chem.* **282**, 32867–32876 (2007).

126. Gatchalian, J. *et al.* Accessibility of the histone H3 tail in the nucleosome for binding of paired readers. *Nat. Commun.* **8**, (2017).

127. Shaytan, A. K. *et al.* Coupling between Histone Conformations and DNA Geometry in Nucleosomes on a Microsecond Timescale: Atomistic Insights into Nucleosome Functions. *J. Mol. Biol.* **428**, 221–237 (2016).

128. Olins, D. E. & Olins, A. L. Epichromatin and chromomeres: A ‘fuzzy’ perspective. *Open Biol.* **8**, (2018).

129. Gordon, F., Luger, K. & Hansen, J. C. The core histone N-terminal tail domains function independently and additively during salt-dependent oligomerization of nucleosomal arrays. *J. Biol. Chem.* **280**, 33701–33706 (2005).

130. Kan, P.-Y., Lu, X., Hansen, J. C. & Hayes, J. J. The H3 Tail Domain Participates in Multiple Interactions during Folding and Self-Association of Nucleosome Arrays. *Mol. Cell. Biol.* **27**, 2084–2091 (2007).

131. Chodaparambil, J. V. *et al.* A charged and contoured surface on the nucleosome regulates chromatin compaction. *Nat. Struct. Mol. Biol.* **14**, 1105–1107 (2007).

132. Kan, P.-Y., Caterino, T. L. & Hayes, J. J. The H4 Tail Domain Participates in Intra- and Internucleosome Interactions with Protein and DNA during Folding and Oligomerization of Nucleosome Arrays. *Mol. Cell. Biol.* **29**, 538–546 (2009).

133. Turner, A. L. *et al.* Highly disordered histone H1−DNA model complexes and their condensates. *Proc. Natl. Acad. Sci. U. S. A.* **115**, 11964–11969 (2018).

134. Andrés, M., García-Gomis, D., Ponte, I., Suau, P. & Roque, A. Histone h1 post-translational modifications: Update and future perspectives. *Int. J. Mol. Sci.* **21**, 1–22 (2020).

135. Bradbury, E. M. *et al.* Studies on the Role and Mode of Operation of the Very-Lysine-Rich

Histone H1 (F1) in Eukaryote Chromatin. The Conformation of Histone H1. *Eur. J. Biochem.* **52**, 605–613 (1975).

136. Shakya, A., Park, S., Rana, N. & King, J. T. Liquid-Liquid Phase Separation of Histone Proteins in Cells: Role in Chromatin Organization. *Biophys. J.* **118**, 753–764 (2020).

137. Erdel, F. & Rippe, K. Formation of Chromatin Subcompartments by Phase Separation. *Biophys. J.* **114**, 2262–2270 (2018).

138. Erdel, F. Biophysical mechanisms of chromatin patterning. *Curr. Opin. Genet. Dev.* **61**, 62–68 (2020).

139. Pitman, M., Melters, D. P. & Dalal, Y. Job Opening for Nucleosome Mechanic: Flexibility Required. *Cells* **9**, 580 (2020).

140. Stephens, A. D., Banigan, E. J., Adam, S. A., Goldman, R. D. & Marko, J. F. Chromatin and lamin A determine two different mechanical response regimes of the cell nucleus. *Mol. Biol. Cell* **28**, 1984–1996 (2017).

141. Sanulli, S. *et al.* HP1 reshapes nucleosome core to promote phase separation of heterochromatin. *Nature* **575**, 390–394 (2019).

142. Nielsen, P. R. *et al.* Structure of the HP1 chromodomain bound to histone H3 methylated at lysine 9. *Nature* **416**, 103–107 (2002).

143. Nishibuchi, G. *et al.* N-terminal phosphorylation of HP1α increases its nucleosome-binding specificity. *Nucleic Acids Res.* **42**, 12498–12511 (2014).

144. Larson, A. G. & Narlikar, G. J. The Role of Phase Separation in Heterochromatin Formation, Function, and Regulation. *Biochemistry* **57**, 2540–2548 (2018).

145. Kumar, A. & Kono, H. Heterochromatin protein 1 (HP1): interactions with itself and chromatin components. *Biophys. Rev.* **12**, 387–400 (2020).

146. Kilic, S., Bachmann, A. L., Bryan, L. C. & Fierz, B. Multivalency governs HP1α association dynamics with the silent chromatin state. *Nat. Commun.* **6**, 7313 (2015).

147. Festenstein, R. *et al.* Modulation of Heterochromatin Protein 1 Dynamics in Primary Mammalian Cells. *Science (80-.).* **299**, 719–721 (2003).

148. Cheutin, T. *et al.* Maintenance of stable heterochromatin domains by dynamic HP1 binding. *Science (80-.).* **299**, 721–725 (2003).

149. Richart, A. N., Brunner, C. I. W., Stott, K., Murzina, N. V. & Thomas, J. O. Characterization of chromoshadow domain-mediated binding of Heterochromatin Protein 1α (HP1α) to histone H3. *J. Biol. Chem.* **287**, 18730–18737 (2012).

150. Liu, Y. *et al.* Peptide recognition by heterochromatin protein 1 (HP1) chromoshadow domains revisited : Plasticity in the pseudosymmetric histone binding site of human HP1. *J. Biol. Chem.* **292**, 5655–5664 (2017).

151. Fischle, W. *et al.* Regulation of HP1-chromatin binding by histone H3 methylation and phosphorylation. *Nature* **438**, 1116–1122 (2005).

152. Söding, J., Zwicker, D., Sohrabi-Jahromi, S., Boehning, M. & Kirschbaum, J. Mechanisms for Active Regulation of Biomolecular Condensates. *Trends Cell Biol.* **30**, 4–14 (2020).

153. Nielsen, A. L. *et al.* Heterochromatin Formation in Mammalian Cells. *Mol. Cell* **7**, 729–739 (2001).

154. Daujat, S., Zeissler, U., Waldmann, T., Happel, N. & Schneider, R. HP1 binds specifically to Lys26-methylated histone H1.4, whereas simultaneous Ser27 phosphorylation blocks HP1 binding. *J. Biol. Chem.* **280**, 38090–38095 (2005).

Supplementary information

Table S2.1. PDB codes of structures used for Figure 2.2.

Access code	What	Access code	What
6MUO	CENP-A CENP-C CENP-N	6NE3	SNF2H
6MUP	CENP-A CENP-C CENP-N	6PWF	ISWI
6SEE	CENP-A CENP-C	6IRO	ISWI
6SEF	CENP-A CENP-C	6JYL	ISWI
6SE6	CENP-A CENP-C	6K1P	ISWI
6C0W	CENP-N CENP-A	6UXW	SWI-SNF
6BUZ	CENP-A CENP-N	5X0X	snf2
6QLD	CCAN-Cenp-A	5X0Y	snf2
6OM3	Orc1 BAH	5Z3V	snf2
3MVD	RCC1	5Z3O	snf2
4JJN	Sir3	5Z3U	snf2
3TU4	Sir3 BAH	5Z3L	snf2
4KUD	Sir3 BAH D205N	6IY3	snf2
4LD9	BAH domain of Sir3	6IY2	snf2
4R8P	PRC1 ubiquitylation module	6GEN	SWR1 complex
4ZUX	SAGA DUB module	6GEJ	SWR1 complex
6T9L	SAGA DUC module	6KW3	RSC
6J99	Dot1L	6KW4	RSC
6O96	Dot1L	6V92	RSC
6NN6	Dot1L	6TDA	RSC
6JM9	Dot1L	6FML	INO80 core
6JMA	Dot1L	6HTS	INO80 complex
6NOG	Dot1L-H2Bub	6R8Y	UV-DDB
6NJ9	Dot1L-H2Bub	6R8Z	UV-DDB
6NQA	Dot1L-H2Bub	6R90	UV-DDB
5HQ2	Set8	6R92	UV-DDB

6PX3	Set2	6R91	UV-DDB
6NZO	Set2	5KGF	53BP1
6UGM	COMPASS	6T7B	Sox2
6UH5	COMPASS	6T7A	Sox2
6VEN	COMPASS	6T7D	Sox2
6PWX	MLL1 complex	6T7C	Sox2
6PWW	MLL1 complex	6T90	OCT4-SOX2
6PWV	MLL1 complex	6YOV	OCT4-SOX2
6KIX	MLL1 or MLL3 complex	6INQ	RNA pol II
6KIZ	MLL1 or MLL3 complex	6A5R	RNA pol II
6KIW	MLL1 or MLL3 complex	6A5U	RNA pol II
6KIU	MLL1 or MLL3 complex	6A5T	RNA pol II
6KIV	MLL1 or MLL3 complex	6A5L	RNA pol II
6VYP	LSD1-CoREST	6A5O	RNA pol II
6R25	LSD2-NPAC-linker	6A5P	RNA pol II
6R1U	LSD2-NPAC-linker	6IR9	RNA pol II
6S01	LEDGF PWWP domain	6J4Y	RNA pol II
6G0L	chd1	6J4X	RNA pol II
6FTX	chd1	6J4Z	RNA pol II
5O9G	chd1	6J51	RNA pol II
6RYU	CHD4	6J4W	RNA pol II
6RYR	CHD4	6J50	RNA pol II
6I84	transcribing RNA pol II	5MLU	PFV GAG CBS
6upk	FACT_subnucleosome	5E5A	cytomegalovirus IE1 protein
6UPL	FACT_subnucleosome	5WCU	Chromatosome
5GTC	DMAP-SH LANA conjugate	5NL0	Chromatosome
1ZLA	LANA peptide	4QLC	Chromatosome
6RNY	PFV intasome		

T

Table S2.2. Reported binding affinities of linker histone-nucleosome interactions

Interaction	[I](mM)	Species	Method	Kd (nM)	Ref
LH -DNA					
H1	60	Calf	Gel retardation	10	(Nightingale, Pruss and Wolffe, 1996)
H1	60	Calf	Gel retardation	18	(Ura, Nightingale and Wolffe, 1996)
H1.0	163	-	ITC	140	(Machha *et al.*, 2013)
H1 (1-193) H1 (1-121) gH1 (1-96)	150	mouse	FRET	7 70 1446	(White, Hieb and Luger, 2016)
H1.1	163	Mouse	ITC	159	(Machha *et al.*, 2014)
H1.4	163	Mouse	ITC	313	(Machha *et al.*, 2014)
CTD H1.0	163	-	ITC	133	(Machha *et al.*, 2013)
CTD H1.11L – 20bp	160	Chicken	ITC	101	(Turner *et al.*, 2018)
CTD H1.11L – 20bp	10	Chicken	ITC	43 (1st event) 19 (2nd event)	(Turner *et al.*, 2018)
CTD H1.11L-P – 20bp	10	Chicken	ITC	260 (1st event) 48 (2nd event)	(Turner *et al.*, 2018)
LH-mononucleosome					
gH5 (22-102) H5(22-142)	112	Chicken	ITC	350 230	(Zhou *et al.*, 2015b)
gH5	-	Chicken	ITC	300	(Zhou *et al.*, 2016)
gH5 (R47L/R74S/ K97A/V80K/V87K)	112	Chicken	ITC	1300	(Zhou *et al.*, 2016)
gH1	112	Drosophila	ITC	1300	(Zhou *et al.*, 2016)
H1(1-193) H1(1-121) gH1(1-96) (30bp linker)	150	mouse	Competition assay	0.0177 1.850 123	(White, Hieb and Luger, 2016)

H1.0 H1.1 H1.4	180	Human	Biolayer interferometry	0.0135 0.0131 0.0244	(Osunsade *et al.*, 2019)
H1 (237bp)	60	Calf	Gel retardation	2 (1st LH) 10 (2nd LH)	(Nightingale, Pruss and Wolffe, 1996)
LH-dinucleosomes					
H1-dinucleosome	60	Calf	Gel retardation	7.4	(Ura, Nightingale and Wolffe, 1996)
LH-trinucleosomes					
H1(1-121) H1(1-193) (30&60bp linker)	150	mouse	fluorescence (de)quenching	0.047 0.046	(White, Hieb and Luger, 2016)

Table S2.3. Reported binding of affinities of HP1-nucleosome interactions

Classification	Interaction	Paralog	Affinity	Method	Reference
Anchoring interaction	CD-H3K9me0	Swi6	Kd=170±5μM	Fluorescence anisotropy	(Isaac et al., 2017)
	CD – H3K9me2	dHP1	FL* Kd=4±1.0μM CD Kd=6.9±0.2 μM	ITC	(Jacobs and Khorasanizadeh, 2002)
		mHP1β	CD Kd=1.94±0.65 μM	Trp fluorescence	(Nielsen *et al.*, 2002)
	CD – H3K9me3	mHP1β	CD- Kd=1.9 μM	Trp fluorescence	(Nielsen *et al.*, 2002)
		dHP1	FL Kd= 2.5±0.1 μM	ITC	(Jacobs and Khorasanizadeh, 2002)
		Swi6	FL Kd =12±2μM	Fluorescence anisotropy	(Canzio *et al.*, 2013)*
		Swi6	FL Kd= 10±1.4	Fluorescence anisotropy	(Isaac et al., 2017)
		Phos-hHP1α	Kd = 8.3 μM	Binding energy simulation	(Machado, Dans and Pantano, 2010)
Dimerization interaction	CSD self-association	Swi6	Kd<17 nM	Cross-linking based approach and ITC	(Canzio, Evelyn Y Chang, *et al.*, 2011)
		dHP1	Kd=3.0±0.2 μM	Analytical ultracentrifugation (AUC)	(Mendez *et al.*, 2011)
Additional self-interactions	NTE – H3K9me3	mHP1	Kd=1.77 μM	ITC	(Shimojo *et al.*, 2016)
	CSD tetramer	hHp1	n.a	Survive molecular dynamics	(Li *et al.*, 2012)
	CSD-HR	n.a	n.a	n.a	(Larson et al., 2018)
	CD-HR	n.a	n.a	n.a	(Larson et al., 2018)
Heteroprotein interactions	CSD-H3	hHP1	Kd=58±7 μM	NMR fast exchange	(Richart *et al.*, 2012)
		Swi6	Kd<1mM	Fluorescence polarization and SV-AUC	(Isaac et al., 2017)
	CSD-Sgo1	hHP1β	Kd=0.18 μM	ITC	(Kang et al., 2011)
		Swi6	Kd=6.6±2.1 μM	Fluorescence anisotropy	(Isaac et al., 2017)
	CSD dimer-CAF-1 peptide	mHP1	n.a	NMR and structure calculation	(Thiru *et al.*, 2004)

	CSD-dimer EMSY	hHP1	n.a	Crystallography	(Huang, Myers and Xu, 2006)
Closed State	CTE-CTE	hHP1	n.a.	n.a.	(Larson et al., 2018)
	CD-CD	Swi6 (30 °C)	Dimerization Kd=48±11 nM	Sedimentation Velocity AUC	(Canzio *et al.*, 2013)*
			Isodesmic Association Kd= 110 ±2.1 μM		
		Swi6 (24°C)	Dimerization Kd<6nM		
			Isodesmic Association Kd=151 μM		
Naked DNA interactions	HP1- DNA	hHP1α	Kd=0.48 μM	EMSA titration	(Nishibuchi and Nakayama, 2014)
		Swi6	WT Kd=15±0.04μM	Fluorescence anisotropy	(Canzio *et al.*, 2013)*
			WT+H3K9 Kd=23±2.0μM		
			WT+H3K9me3 Kd=5±0.3μM		

3

Methyl-TROSY NMR at 1.2 GHz: exploiting resolution and magnetic field alignment

Based on the manuscript: **Lobbia, V. R.** & van Ingen, H. Methyl-TROSY NMR at 1.2 GHz: exploiting resolution and magnetic field alignment. *in preparation*

Abstract

The range of protein assemblies that can be studied by NMR has greatly expanded both by increases in magnetic field strength and by development of new NMR approaches, such as methyl-group specific transverse relaxation optimized spectroscopy (methyl-TROSY). Recently, a new generation of NMR magnets operating at 1.2 GHz has become available, offering the highest resolution for biomolecular NMR. The high magnetic field will however also cause increased relaxation due to the chemical shift anisotropy (CSA) of the nuclear spins which will negatively affect sensitivity. The ultra-high magnetic field may also offer new opportunities as the effects of magnetic field induced alignment will be significantly increased. Here, we investigated the performance of methyl-TROSY NMR at 1.2 GHz, using the nucleosome, a 200 kDa protein-DNA complex, as a test sample. We find that the increased resolution of the 1.2 GHz system allows to resolve small asymmetries in sidechain conformation between symmetry-related copies of the histone proteins. Enhanced CSA relaxation effectively increases ^{13}C transverse relaxation rates by 20% at 1200 compared to 900 MHz. We further observe significant magnetic field alignment of the nucleosome at 1.2 GHz, giving rise to methyl ^{1}H-^{13}C residual dipolar couplings (RDCs) that can be used for assignment and structural characterization. We show that these histone methyl group RDCs can be used to aid assignment and to determine the overall conformation of the nucleosomal DNA, revealing a significant unwrapping of the DNA from the histone core. We expect that 1.2 GHz NMR will be very advantageous for studies of large biomolecular assemblies, in particular for protein-DNA complexes.

Introduction

With availability of higher magnetic fields, the increased resolution and sensitivity have enabled NMR spectroscopists to study more and more complex systems. Next to these instrumental factors, the development of new labeling approaches and transverse-relaxation optimized spectroscopy (TROSY), and in particular methyl-TROSY, have greatly expanded the size limit of the system that can be studied using solution NMR[1–10]. Thanks to development of high-temperature superconducting materials, the leading commercial manufacturer in NMR spectrometers has been able to build a high-resolution NMR machine operating at 28.2 T or 1H resonance frequency of 1.2 GHz. The performance of NMR at this ultra-high field has been discussed in a few recent papers[11,12]. Here, we focus on the implications of the high magnetic field for methyl-TROSY NMR, and in particular for large protein-DNA complexes.

Methyl-TROSY NMR relies on favorable properties of ^{1}H,^{13}C-labeled methyl groups in a perdeuterated protein. Due to its fast internal rotation and three—fold symmetry, the interference between intra-methyl ^{1}H-^{13}C dipolar interactions can be exploited to select slowly decaying signals for optimum sensitivity[6,13]. As the methyl-TROSY effect is based on dipolar-dipolar cross-correlations, it is field independent. However, the ^{13}C spin in a methyl group has a small, but non negligible chemical shift anisotropy (CSA)[14], causing a field-dependent increase to the transverse relaxation rate[15]. In addition, methyl-TROSY spectra can be recorded using the SOFAST fast-pulsing approach[16,17] to further optimize sensitivity per measurement time. In this approach the sensitivity gain depends on the longitudinal relaxation rate of the ^{1}H spins, which will decrease slightly with increased magnetic field. Both the increased transverse ^{13}C relaxation and the reduced longitudinal ^{1}H relaxation will negatively affect the methyl-TROSY experiment at 1.2 GHz, leaving open the question to what degree methyl-TROSY NMR at the ultra-high field will outperform that at more widely available fields such as 600 or 900 MHz.

Next to affecting relaxation rates, the increased magnetic field will also increase the effects of magnetic field alignment. When molecules with an anisotropic magnetic susceptibility are placed in a magnetic field, the induced magnetic moment will depend on their orientation with respect to the field, causing them to align in such a way that the induced magnetic moments are minimal[18,19]. Nucleic acids are well known to have a large magnetic susceptibility anisotropy (χ_a) due to the nearly colinear arrangement of the aromatic bases, and thus show pronounced magnetic field alignment[18,20,21]. The net alignment of the molecule causes incomplete averaging of the dipolar interactions and hence result in residual dipolar couplings (RDCs) which can be used to determine structure[22–25]. Proteins show less magnetic field alignment compared to nucleic acids as they in general have few aromatic residues which will be not colinear. Yet, even for ubiquitin at moderate magnetic field strength of 750 MHz small magnetic field induced RDCs (fiRDCs) have been measured.[26] As the alignment depends on the square of the magnetic field, significant fiRDCs for both proteins and nucleic acids can be expected at 1.2 GHz. These fiRDCs will add to the regular J-coupling splitting and “traditional” RDC splittings when using anisotropic solutions, as has been evaluated in detail for nucleic acids[27]. Importantly, as magnetic susceptibility anisotropy can be predicted quite accurately from the structure of a molecule[28], fiRDCs can be used for structure determination[22–25,29]. Thus, methyl-TROSY NMR at 1.2 GHz also offers exciting new potential for structure determination of large protein-DNA complexes, such as the nucleosome.

Here, we compared methyl-TROSY spectra recorded at 600, 900 and 1200 MHz in terms of sensitivity, resolution and extracted fiRDCs. We find that methyl-TROSY spectra at the 1200 MHz system are ~20% less sensitive than at 900 MHz, in line with the expected increase in ^{13}C CSA relaxation. At 1200 MHz, resonances for several isoleucine, leucine and valine (ILV) methyl groups show clearly resolved splittings that correlate with asymmetric rotamer states in many nucleosome crystal structures. Further, we observe large fiRDCs of up to 8 Hz at 1200 MHz. We show that these can be used to obtain stereospecific assignments of nearly all methyl groups. Importantly, the experimental fiRDCs can be used to determine the conformation of the linker DNA in the nucleosome, revealing significant unwrapping of the nucleosomal DNA from the histone core.

Materials and Methods

Expression and purification of isotope labelled histones

The histones, H2A, H2B, H3 and H4, from *Xenopus laevis* (*Xl.)* were transformed into BL21(DE3) pLysS cells using pET3a derived plasmids encoding histones (Uniprot P06897, P02281, P84233, P62799). Histones were perdeuterated using an adapted protocol of Marley et al[30]. In short, cells were grown at 37 °C in Luria-Bertani (LB) medium to optical density (OD) 1.5, then spun down and washed twice in D_2O-based M9 medium without glucose and NH_4Cl. Cell pellets were resuspended in D_2O M9 with deuterated glucose, and $^{15}NH_4Cl$ for labeled histones or $^{14}NH_4Cl$ for fully deuterated histones to an OD of ~0.6 and incubated for 1–2 hours at 37 °C. To obtain perdeuterated ^{15}N,{^{1}H-^{13}C}-ILV labeled H2B, 60 mL/L α-ketobutyric acid (4-^{13}C,3,3-2d) and 80 mg/L α-ketoisovalerate (3-(methyl-d3),4-^{13}C,3-d) sodium salt (Sigma-Aldrich) were added to the culture and incubated for another hour, while for H2B with {^{1}H-^{13}C}-labeling of both LV methyl groups (2MeLV), 80 mg/L 2-Keto-(3-methyl-^{13}C)-butyric-4-^{13}C,3d acid (Sigma-Aldrich) was added. All histones were expressed overnight with 1 mM IPTG at 37 °C.

Histones were purified as described previously in Klinker et al.[31]. Briefly, cell pellets were resuspended in lysis buffer (50 mM Tris, 100 mM NaCl, 1% triton, pH 7.5) with lysozyme, then lysed using one freeze-thaw cycle and sonication. The inclusion bodies were collected and unfolded using unfolding buffer (6 M Guanidinium-HCl, 50 mM Tris, 100 mM NaCl, pH 7.5). Unfolded histones were purified using first size-exclusion chromatography (SEC) over a superdex 75 column (GE Healthcare) in denaturing buffer (7 M urea, 50 mM KPi, 1 mM EDTA, 150 mM NaCl, pH 7.5) and then using ion-exchange chromatography (IEX) over a combined HiTrap Q and HiTrap SP column (Cytiva) in denaturing buffer, where the HiTrap Q column was removed before eluting the histones from the SP column using a salt gradient (0.15 – 1 M NaCl in denaturing buffer). Fractions were analyzed using SDS-PAGE, histone containing fractions were pooled and concentrated to 3 mg/mL, supplemented with 1 mM lysine, and stored at -20°C for further use.

DNA production

A pUC19 plasmid containing 12 x 167 base pair repeats was used to produce 167 base pair 601 Widom DNA[32]. Plasmids were produced using DH5alpha in 2xYT medium with an overnight culture at 37 °C. Plasmids were isolated using alkaline lysis[33] followed by isopropanol and ethanol precipitation and redissolved in TE buffer (10 mM Tris, 1 mM EDTA, pH 8.0). Plasmids were purified using IEX over HiTrap Q column (Cytiva) with a 0-1 M NaCl gradient in TE buffer. Purified plasmids were digested in TE buffer supplemented with 10x Cutsmart buffer (New England Biolabs) to 1x final concentration using 700U ScaI-HF (New England Biolabs) per 10 mg plasmid DNA for 72 hours at 1mg/mL plasmid concentration. Completion of the restriction was monitored using PAGE. Then 167 bp DNA fragments were purified using anion exchange (HiTrap Q column 5 mL), ethanol precipitated and resuspended in TE buffer to a concentration of ~2.4 mg/mL before storage at -20 °C.

Histone octamer refolding and reconstitution of nucleosomes

The histone octamer was refolded as described in Dyer et al[33]. In brief, histones were mixed in equimolar ratio in denaturing buffer (7 M urea, 50 mM Tris, 100 mM NaCl, pH 7.5) at 1 mg/mL protein concentration, using absorbance at 280 nm to determine their concentrations. The histone octamer mixture was dialyzed in three steps for 16, 8, and 16 hours to high salt buffer (2 M NaCl, 10 mM Tris, 1 mM EDTA) at 4 °C using 3 kDa MWCO membrane and then purified using SEC over a superdex 200 column (120 mL, GE Healthcare) in high salt buffer. Peak fractions were analyzed using SDS PAGE. The histone octamer eluted at 64 mL, with a yield of ~70%. Fractions containing pure octamers were pooled and concentrated to ~4 mg/mL and stored at 4 °C before immediate use.

Nucleosomes were reconstituted from 601 DNA and perdeuterated histones and ILV-labeled H2B according to the protocol described by Dyer et al.[33]. Briefly, stock-solution of 601 DNA was adjusted with 4 M NaCl to a final salt concentration 2 M and ~3 mg/mL DNA. Equimolar amounts of histone octamer (in high salt buffer) and 601 DNA were mixed at 4 °C and diluted to 0.7 mg/mL protein concentration using high salt buffer, incubated for 2 hours, and then dialyzed using a 16-hour gradient to low salt buffer (0.25 M KCl, 10 mM Tris, pH 7.5, 1 mM EDTA). The soluble fractions containing nucleosomes (ca. 70% yield based on DNA absorbance) was then buffer exchanged to NMR buffer (20 mM KPi, pH 6.2, 0.01% NaN_3, 100% D_2O) and concentrated to ~13.6 mg/mL over a 30kDa MWCO centrifugal concentration device. Analysis by SDS-PAGE and native PAGE confirmed that the obtained nucleosomes are free of significant amounts of free DNA (Supplementary Figure S1). Nucleosomes were stored at 4 °C before use.

NMR spectroscopy

All NMR experiments were recorded on Bruker Avance spectrometers, using either an Avance III 600 MHz spectrometer with 5 mm room-temperature probe, an Avance III 900 MHz spectrometer with a 5 mm cryo-probe, or an Avance NEO 1200 MHz spectrometer with a 3 mm cryo-probe. Samples were measured in a 5 mm thin-wall Shigemi tube (600, 900 MHz) or a 3 mm thin-wall tube (1200 MHz), in all cases containing 64.3 μM nucleosomes in 300 μL NMR buffer (20 mM KPi, pH 6.2, 0.01% NaN_3, 100% D_2O). All experiments were recorded at 45 °C. NMR data were processed using Bruker Topspin using forward linear prediction in the indirect dimension(s) and cosine-squared window functions, and subsequently analyzed using NMRFAM-SPARKY[34], except where noted otherwise.

To compare resolution and sensitivity, methyl-TROSY HMQC experiments were recorded at 600, 900 and 1200 MHz. Experiments used the SOFAST fast-pulsing method[17] with a 6 ms PC9-shaped methyl selective pulse with 120° flip angle (band width 6 ppm), a recycle delay of 0.5 s, and acquisition times of 66.5 ms (^{1}H) and 42.4 ms (^{13}C), and 3.3 kHz WALTZ64 decoupling during acquisition. Total measurement time was 2 hours for all three spectra. Peak intensities and noise levels were determined using the built-in functions of NMRFAM-SPARKY.

Resonance assignment Xl. H2B ILV methyl groups

Initial assignments of the ILV methyl group resonances in *Xenopus leaevis (Xl.)* H2B were based on assignment transfer from the available *Drosophila melanogaster* (*Dm.*) chemical shifts[35]. To confirm and complete the assignments, 3D methyl-TROSY (h)CCH NOESY were recorded with acquisition times $t_{1,\max}$ 8 ms, $t_{2,\max}$ 8 ms and $t_{3,\max}$ 67 ms, total measurement time 3 days, and with 200 (50) ms NOESY mixing time on nucleosome sample with ILV (2MeLV)-labeled H2B. Spectra were processed with Bruker Topspin 3.2pl7 using forward linear prediction in both indirect dimensions and analyzed using NMRFAM-SPARKY 3.13. Assignments were made using MAGMA 1.2.3[36] and verified manually by comparing the experimental NOE network and to the methyl-methyl distances in the 1KX5 nucleosome crystal structure[37]. Stereospecific assignments could be transferred from the *Dm*. spectra based on conservation of NOE patterns for 16 of the 30 LV resonances (5 out of 6 Leu and 3 out of 9 Val residues). Comparison of the Leu ^{13}C δ1 and δ2 chemical shifts and the crystal structure rotamer conformation using the Sider program[38] confirmed the stereospecific assignments for all Leu residues, except L98 and L99, which were too dynamic.

ILV rotamer analysis

Nucleosome crystal and cryo-EM structures in the PDB were selected if they contained *Xl.* canonical histones and had a resolution below or equal to 3.5 Å. The side chain conformation of ILV residues were analyzed to determine their rotamer distributions. All nucleosome structures that contained all eight *Xl.* histones, two DNA strands and no other binding partners (excluding ions) were selected (21 structures, see Table S1). After adapting the H2B residue numbers for consistency, the H2B histone chains were extracted using PyMOL and subsequently all H2B structures were aligned on the backbone N, CA, CO atoms of each ILV residue, one at a time.

Relaxation measurements

The longitudinal relaxation rates (R_1) of methyl group ^{1}H spins were measured by implementing a saturation recovery element using either a 90° hard uniform or a 90° PC9-shaped selective excitation pulse (band width 6 ppm) before the methyl-TROSY experiment[39]. Spectra were recorded with an inter-scan delay of 6 sec and relaxation delay values of 50, 100, 150, 200, 800, 1200 and 3000 ms. The transverse relaxation rates (R_2) of methyl group ^{13}C spins were measured using a ^{13}C-^{1}H MQ Carr–Purcell–Meiboom–Gill (CPMG) relaxation dispersion experiment[40] with or without a constant CPMG relaxation time T_{relax} of 10 ms and CPMG pulsing rates ν_{CPMG} of 100 and 1000 Hz. Both datasets were processed using NMRPipe[41] with exponential line broadening and peak volumes were obtained by fitting the 2D peaks to a gaussian line shape in the program PINT[42]. To obtain the methyl ^{1}H R_1 rates, peak volumes were fit to Eq. [1]:

$$I(t) = A * (1 - e^{-t*R_1}) \qquad [1]$$

where $I(t)$ is the peak volume at relaxation delay t, A is a scaling factor. The methyl ^{13}C effective R_2 rates, $R_{2,eff}$, were calculated using Eq. 2:

$$R_{2,\mathrm{eff}}(\nu_{\mathrm{CPMG}}) = -\frac{\ln\left(\frac{I(\mathrm{CPMG})}{I_0}\right)}{\mathrm{T_{relax}}} \qquad [2]$$

where I_0 is the peak volume in the reference spectrum and $I(\nu_{CPMG})$ the peak volume obtained in the CPMG experiment with pulsing rate ν_{CPMG}. Error bars in the fitted relaxation rates were calculated using PINT, which were estimated using the jacknife method[42].

RDC measurement

The ^{1}H-^{13}C one-bond methyl fiRDCs (D) were derived from methyl-TROSY IPAP spectra that encode the $J + D$ peak splittings in the ^{1}H dimension[43]. Data were recorded at 600, 900 and 1200 MHz with FID resolution of 7 Hz and processed to spectra with digital resolution of 2.35 Hz (typical line width in the ^{1}H dimension was ~30 Hz). Spectra with either the inphase (IP) and antiphase (AP) doublets were added/subtracted to result in spectra with either the upfield or downfield doublet component. Peak positions of the upfield and downfield component were determined using the 'peak center' command in NMRFAM-SPARKY, and then subtracted as values in Hz to yield the peak splitting (Δ). The error in Δ (σ_Δ) was derived from the error in peak position using the error propagation (Table S2). The error in peak position was estimated to be LWHH/(S/N), where LWHH is the linewidth at half height and S/N the signal-to-noise ratio. Peaks with severe overlap (V38a, V108γ1, L42δ2a and L42δ2b) were excluded from the analysis. The fiRDCs were obtained by fitting peak splittings Δ using gnuplot 5.4[44] to Eq. [3]:

$$\Delta(B_0) = J_{CH} + c_{RDC} * B_0^2 \qquad [3]$$

where J_{CH} is the one-bond 1H-13C scalar coupling constant, $c_{RDC}*B_0^2$ is the fiRDC at magnetic field strength B_0, and c_{RDC} is a scaling coefficient that depends, amongst others, on the magnitude of the magnetic susceptibility anisotropy and the bond-vector orientation. The fiRDC at 1200 MHz was calculated as $c_{RDC}*B_0^2$, where B_0 is 28.2 T, and the error was set to at least 0.5 Hz or $\sigma_{cRDC}*B_0^2$, where σ_{cRDC} is the fit error on c_{RDC} (Table S3).

Determination of magnetic susceptibility tensor from experimental fiRDCs

The experimental fiRDCs at 1200 MHz were used to determine the magnitude and orientation of the alignment tensor using the DC program of NMRPipe as implemented on the webserver (https://spin.niddk.nih.gov/bax/nmrserver/dc/svd.html) in the following way. First, only the fiRDCs from resonances with known stereo-specific assignment without overlap (20 in total) were used to fit alignment tensor, using the H2B structure (single chain) from 1KX5[37], 3LZ0[45] or 7OHC[46]. Error on the fiRDCS was set to 1 Hz for all residues. Comparison of observed vs. calculated fiRDCs identified three outliers (from I58 and L98 methyl groups) in the fits using the 1KX5 and 7OHC structures. After removing these outliers, the best fit according to Q-factor was obtained for the 1KX5 structure. The calculated RDCs from this fit were used to assign the stereochemistry of the 6 LV residues (excluding V15 in the histone tail) without stereospecific assignment. For each of these residues, the measured RDCs were compared with the predicted RDCs for the two possible assignments, evaluating for each assignment possibility Eq. 4:

$$\frac{1}{\sigma * n}\sqrt{(RDC_a - RDC_1)^2 + (RDC_b - RDC_2)^2} \qquad [4]$$

where RDC_a and RDC_b are the observed fiRDC for the two methyl groups of the same residue, RDC_1 and RDC_2 the predicted RDCs, n the amount of measured RDCs per residue ($n = 1$ if RDCs are available for only one methyl group due to overlap or low S/N), and σ is the standard deviation of the measured set of RDCs. Confident assignments were made when the score of equation 4 was less than 4 and the difference between the score of the two possible assignments was more than one σ, resulting in stereospecific assignments for all 6 remaining residues. Eq. 4 was similarly used to determine stereospecific assignments when including only fiRDCs from Ile or Ile and Sider-predicted Leu in the fit.

The final list of 29 fiRDCs was used to calculate the alignment tensor using 1KX5. The final magnetic susceptibility tensor was calculated from the fitted alignment tensor by scaling the eigenvalues with $B_0^2/15kT$, corresponding to 82814 at 28.2 T and 45 °C. The error in the magnetic susceptibility tensor was estimated by adding noise to the residual dipolar couplings, or noise to the reference structure, and by random removal of residual dipolar couplings from the dataset using the default "advanced error analysis options" on the webserver[47]. The final reported error is calculated as the average error in the different methods.

Prediction of magnetic susceptibility tensor from structure

To calculate the magnetic susceptibility tensor from known 3D structures, we followed the approach of Bryce et al.[28], taking into account the contributions from both DNA and protein. The residue-specific magnetic susceptibility anisotropies for DNA bases and protein carbonyl groups and aromatic residues were set to their axial symmetric values and orientations as described in Bryce et al. The residue-specific contributions were added via tensor-summation to the overall molecular magnetic susceptibility anisotropy.

To determine the linker DNA conformation in the 167 bp 601-nucleosome, structural models were constructed by extending the 147 bp 601-nucleosome crystal structure (3LZ0) with linear B-DNA that was generated using the 3DNA webserver[48]. To generate models of 167 nucleosome with different conformations of the linker DNA, the linear DNA fragment was added to the 3LZ0 DNA at bp ±70 (closed linkers), ±60 (straight linkers), ±55 (open), and at bp ±70 for one arm and bp ±55 for the other arm (asymmetric linkers).

Results and discussion

For our study we used nucleosomes reconstituted in vitro from perdeuterated *Xenopus laevis (Xl.)* histones with ILV-labeled histone H2B and a 167 bp DNA fragment corresponding to the Widom 601 strong positioning sequence[32]. While our previous solution NMR studies of the nucleosome used *Drosophila* histones[35,49–51] we here used *Xenopus* histones as these are widely used in the study of interactions with various chromatin factors, including remodelers[52]. Reconstitution of the *Xl.* 601-nucleosome was efficient and yielded pure samples (Fig. S3.1) that gave highly resolved 2D $^1H^{13}C$ methyl-TROSY NMR spectra (Fig. S2) with the expected 36 cross peaks for each of the H2B Ile $\delta 1$, Leu $\delta 1/\delta 2$, and Val $\gamma 1/\gamma 2$ methyl groups. Peak assignments were transferred from the previous *Drosophila* chemical shifts assignments[35] where possible, resulting in the confident assignment of 27 methyl group signals. The assignments were completed through analysis of 3D NOESY experiments using the known nucleosome structure[37]. The transferred assignments and NOESY data also allowed to determine the stereospecific assignment of methyl groups in 5 out of 6 Leu and 3 out of 9 Val residues.

Resolution and sensitivity of methyl-TROSY NMR at 1.2 GHz

We recorded methyl-TROSY spectra at 600, 900 and 1200 MHz and evaluated the obtained resolution and sensitivity. Spectral comparison shows clearly that peak overlap that is present at 600 or 900 MHz is resolved at 1200 MHz (Fig. 3.1a and S3.2). More detailed analysis shows that when expressed in ppm, the line widths at 1200 MHz are decreased by 23% in the ^{1}H and 9% in the ^{13}C dimension compared to the line widths at 900 MHz. While the resolution increase in the ^{1}H dimension is close to that expected from the increase in magnetic field, the resolution increase in the ^{13}C dimension is significantly less. This becomes clearer when examining the line width in Hz, which shows that the ^{13}C linewidths are increased by a factor ~1.2 going from 900 to 1200 MHz, while the ^{1}H line widths only minimally increase (Fig. S3.3 and S3.4).

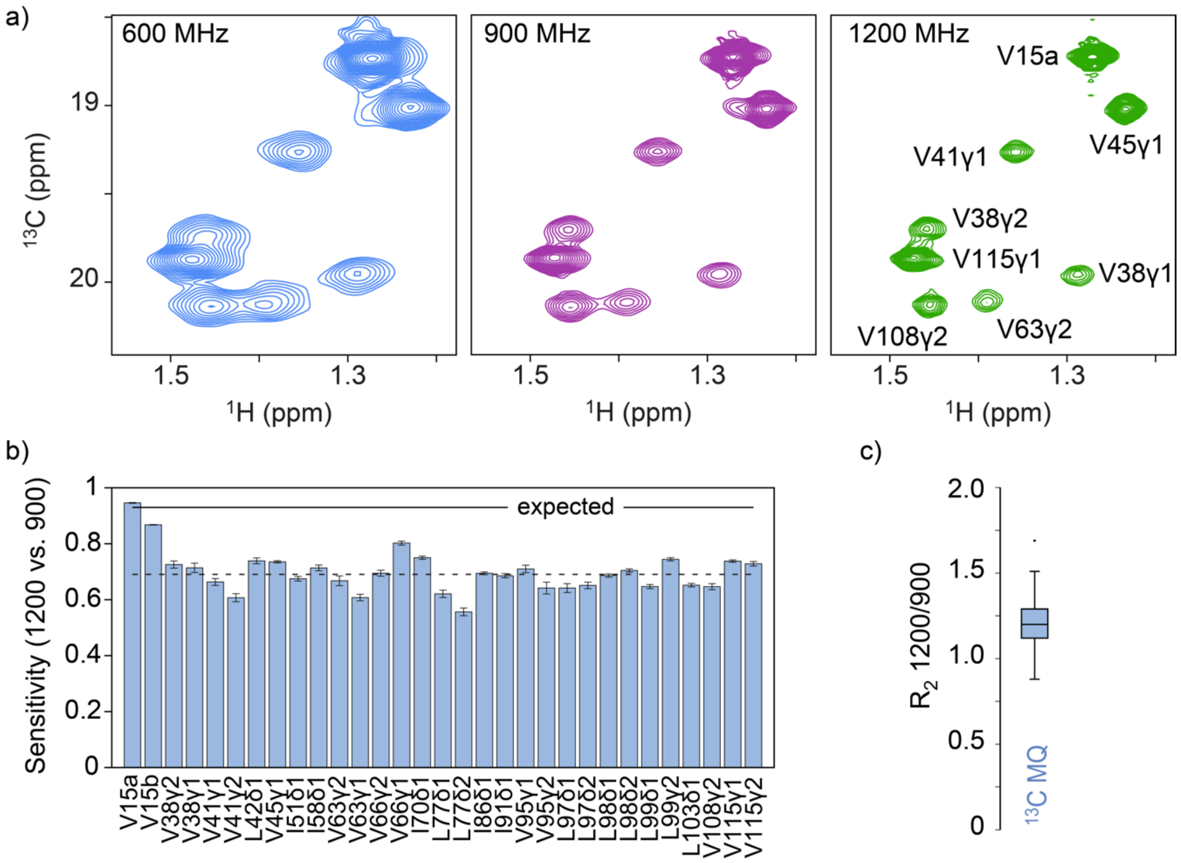

Figure 3.1: Resolution and sensitivity of methyl-TROSY NMR at 1.2 GHz. a) Zoom of methyl-TROSY spectra of nucleosomes with ILV-labeled H2B at indicated magnetic field strengths highlighting the increased resolution at 1.2 GHz. Assignments are shown on the 1.2 GHz spectrum only. Assignment V15a is not stereospecific. b) Relative sensitivity of methyl-TROSY signals of H2B ILV residues in the nucleosome at 1200 MHz in a 3 mm tube compared to 900 MHz in a 5 mm tube at constant concentration; solid line: expected sensitivity as extrapolated from the sucrose sensitivity standards and considering ionic strength and sample volumes; dashed line: average sensitivity

for all methyl signals from the nucleosome core. c) Box-plot of the ^{13}C-^{1}H MQ R_2 rates at 1200 MHz compared to 900 MHz, showing on average 1.2x increase.

To compare the sensitivity of the methyl-TROSY spectra, we focused on the 900 and 1200 MHz spectra as these were both recorded using cryo-probes. Notably, the 1.2 GHz system is equipped with a 3 mm probe, whereas the 900 MHz system has a 5 mm probe. As we used the nucleosome sample at the same concentration, the number of spins in the active volume of the 1.2 GHz is ca. 28% of that for the 900 MHz. Despite this, sucrose measurements showed that the 1.2 GHz offers same or up to 30% more sensitivity compared to the 900 MHz systems, depending on the ionic strength of the sample (Fig. S3.5). Extrapolating from these measurements, one would expect ca. 10% sensitivity increase at 1.2 GHz at the low ionic strength (I = 25 mM) of the nucleosome sample. Accounting for differences in the inner diameter of the tubes used for the sucrose measurements and our nucleosome sample, which result in relative number of active spins of 33% for sucrose and 28% for the nucleosome at 1.2 GHz, we expected a relative sensitivity at 1.2 GHz of ~93% (0.28/0.33*1.1). Indeed, for the methyl group resonances of V15 that are part of the highly flexible H2B histone tail, the experimental relative sensitivity of the 1.2 GHz matches closely the expected value (Fig. 3.1b). For methyl groups in the core of the nucleosome, sensitivities are however decreased by ~25%, on average (Fig. 3.1b). To explain this reduction in sensitivity, we measured ^{1}H and ^{1}H-^{13}C multiple-quantum (MQ) R_2 relaxation rates. On average, the ^{1}H-^{13}C MQ R_2 rates are 1.2 times higher at 1200 vs. 900 MHz (Fig. 3.1c), while there was no notable change in ^{1}H R_2 (Fig. S3.4). This is in-line with the expected impact of the CSA contribution to the transverse relaxation of methyl groups[15]. Studies on ubiquitin have shown that the ^{1}H CSA is very small, on the order of 1 ppm, while the ^{13}C CSA is sizable, with average value of 18 ppm for Leu/Val and 25 ppm for Ile methyl groups[14]. The increased ^{13}C CSA relaxation at 1.2 GHz thus explains most of the observed sensitivity loss.

The reduction in sensitivity could additionally be caused by differences in steady-state ^{1}H magnetization as we recorded these experiments using the SOFAST fast-pulsing approach[17]. To investigate this we measured methyl group ^{1}H longitudinal relaxation times (R_1) rates of the H2B ILV methyl groups in the nucleosome. We used both a methyl-selective ($R_{1,\mathrm{sel}}$) and a non-selective ^{1}H excitation pulse ($R_{1,\mathrm{uni}}$) at 900 MHz and then compared the $R_{1,\mathrm{sel}}$ different magnetic field strengths (Fig. 3.2a-c). Overall, the ^{1}H R_1 relaxation is more efficient when using the selective pulse, indicating a significant 'spin cooling' effect by keeping non-methyl protons in equilibrium (Fig. 3.2a, b). The I36 methyl group experiences the largest increase in relaxation rate which can be explained by its proximity to the protonated DNA. The other H2B methyl groups are however far from the DNA. For instance, V63 and V66 experience a large increase in relaxation rate but are in the core of the nucleosome at considerable distance from the DNA (12.5 and 19 Å, respectively). This indicates that enhancement of R_1 relaxation for the nucleosome core methyl groups is likely due to the presence of non-methyl ^{1}H spins within the histone and/or very efficient spin-diffusion throughout the histone ^{1}H-^{1}H network to the protonated DNA. Comparison of $R_{1,sel}$ rates at 600, 900 and 1200 MHz show a negligible increase with magnetic field (Fig. 3.2c), indicating that the degree of methyl-group polarization recovery during fast-pulsing experiments should be maintained at 1.2 GHz.

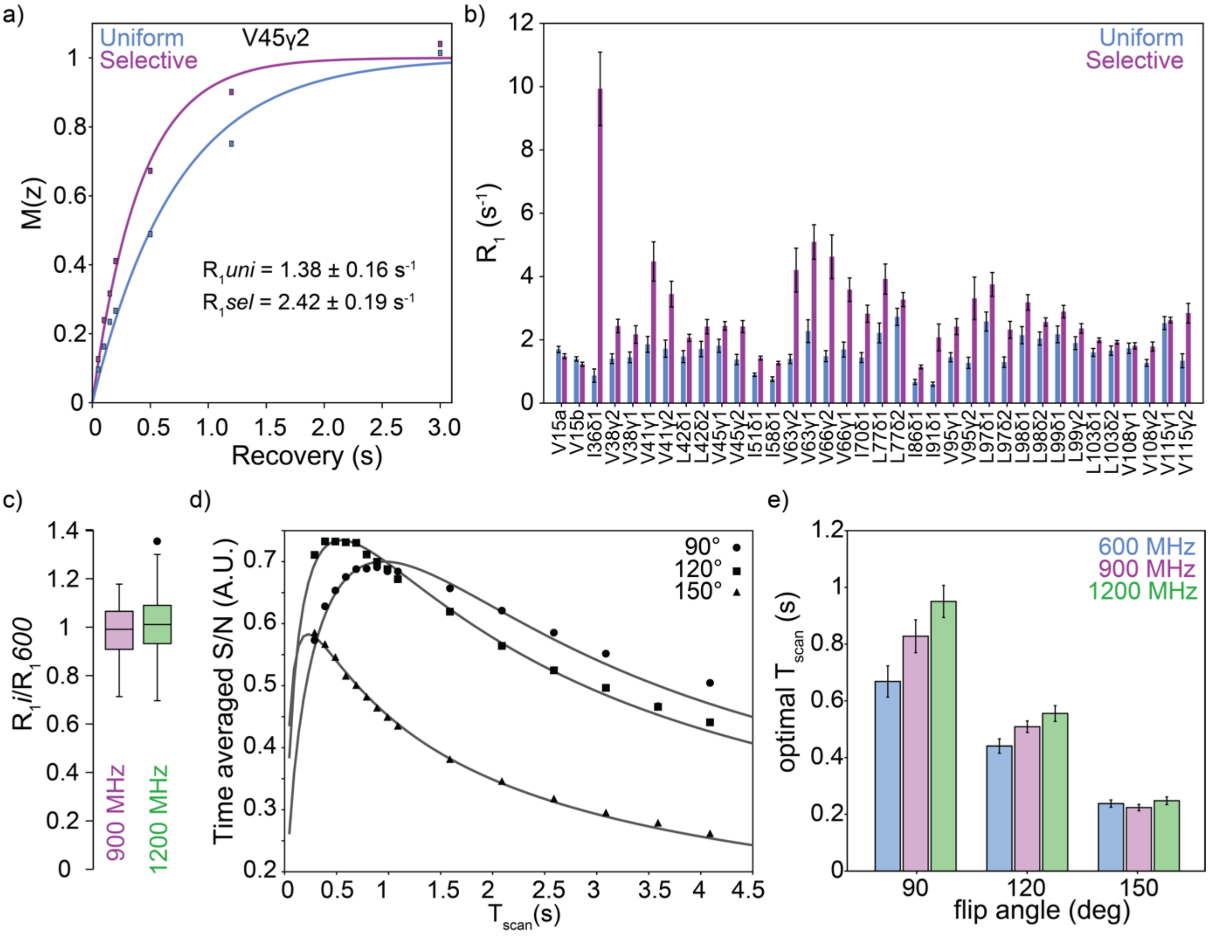

Figure 3.2: Methyl group 1H longitudinal relaxation rates and optimal flip-angle and scan time for SOFAST methyl-TROSY. a) Saturation recovery curve of V45γ2 methyl together with best fit and fitted 1H R_1 values upon either methyl-group selective or uniform excitation. b) Comparison of ^{1}H R_1 values obtained after methyl-selective ($R_{1,sel}$) or uniform excitation ($R_{1,uni}$) for all H2B ILV residues at 900 MHz. Most core residues have significantly larger $R_{1,sel}$. c) Box-plot of $R_{1,sel}$ values at 900 or 1200 MHz compared to 600 MHz. The outlier is V38γ2a. d) Sensitivity of the SOFAST methyl-TROSY experiment as function of total scan time T_{scan} for methyl-selective excitation with 90, 120 or 150° pulse, all at 1200 MHz. Solid lines show the best-fit of the data to expected sensitivity curves for SOFAST experiments[53] and was used to extract the optimum T_{scan}. e) Comparison of the optimal total scan time T_{scan} at 600, 900 and 1200 MHz when using a 90, 120 or 150 excitation pulse.

We also compared the sensitivity and optimal total scan time (T_{scan}) of the SOFAST methyl-TROSY experiment using three different pulse angles at 600, 900 and 1200 MHz (Fig. 3.2d, e). Optimal signal-to-noise was obtained using a 120° selective excitation pulse at all fields. The optimal T_{scan} time increases slightly with increasing field, in particular when using a 90° selective excitation pulse. Such a field-dependent optimal inter-scan delay has also been observed for SOFAST $^{1}H,^{15}N$-HSQC experiments[53]. We thus find that the optimal T_{scan} increases from 0.45 s at 600 MHz to 0.55 s at 1200 MHz. At the constant T_{scan} (0.5 s) used in the sensitivity comparison of Figure 1b the slight mis-setting of optimal T_{scan} contributes less than 1% to the decrease in sensitivity at 1.2 GHz.

Finally, magnetic field induced alignment (see below) will contribute only modestly to reduced sensitivity. As the histones are perdeuterated no ^{1}H-^{1}H RDCs can form and sensitivity loss is limited to reduced transfer efficiency (~1%) due to dispersion of the effective ^{1}H-^{13}C coupling values ($J + D$). We conclude that at 1.2 GHz the sensitivity of the methyl-TROSY experiment is reduced by the increased ^{13}C CSA relaxation to the transverse relaxation and not significantly affected by changes in longitudinal relaxation when using the fast-pulsing approach.

Ultra-high field NMR visualizes asymmetric histone side chain states

Careful comparison of the recorded methyl-TROSY spectra showed to our surprise that three cross peaks that are very broad at 600 MHz are resolved into two sharper peaks at 1200 MHz with close to 1:1 intensity ratio (Fig. 3.3a). For residues I36 and V45, the two peaks have slightly different ^{13}C chemical shifts, while for L103 the difference is in both ^{1}H and ^{13}C dimension. Previously, we observed peak splittings for residues in histones H3 and H2A that are in close contact with the nucleosomal DNA[35,51]. As the 601 DNA sequence we use is non-palindromic, residues in the DNA binding interface will experience two different chemical environments. This most likely also explains the double peak appearance for the H2B I36δ1 methyl group, which is close to the nucleosomal DNA.

For the other residues (V45 and L103), the peak splitting cannot be directly related to the DNA sequence as they are much further away. We can exclude that the splitting is caused by a J-coupling that is only resolved at 1200 MHz because 1) no J_{CC} couplings can be present due to the ILV labeling scheme; 2) J_{CN} couplings are only relevant for Val and are much smaller than the observed splittings (ca. 2 Hz[54]); 3) the splitting between the two peaks is not uniform; and 4) for L103 the split peaks are offset in both ^{13}C and ^{1}H dimension. Therefore, the split peak appearance indicates that the affected methyl groups experience two subtly different chemical environments, unrelated to the DNA sequence. As peak splitting is on the order of 20 Hz (125 rad s^{-1}), any interconversion between the two states occurs slowly, if at all, with approximate maximum exchange rate k_{ex} of 12 s^{-1}.

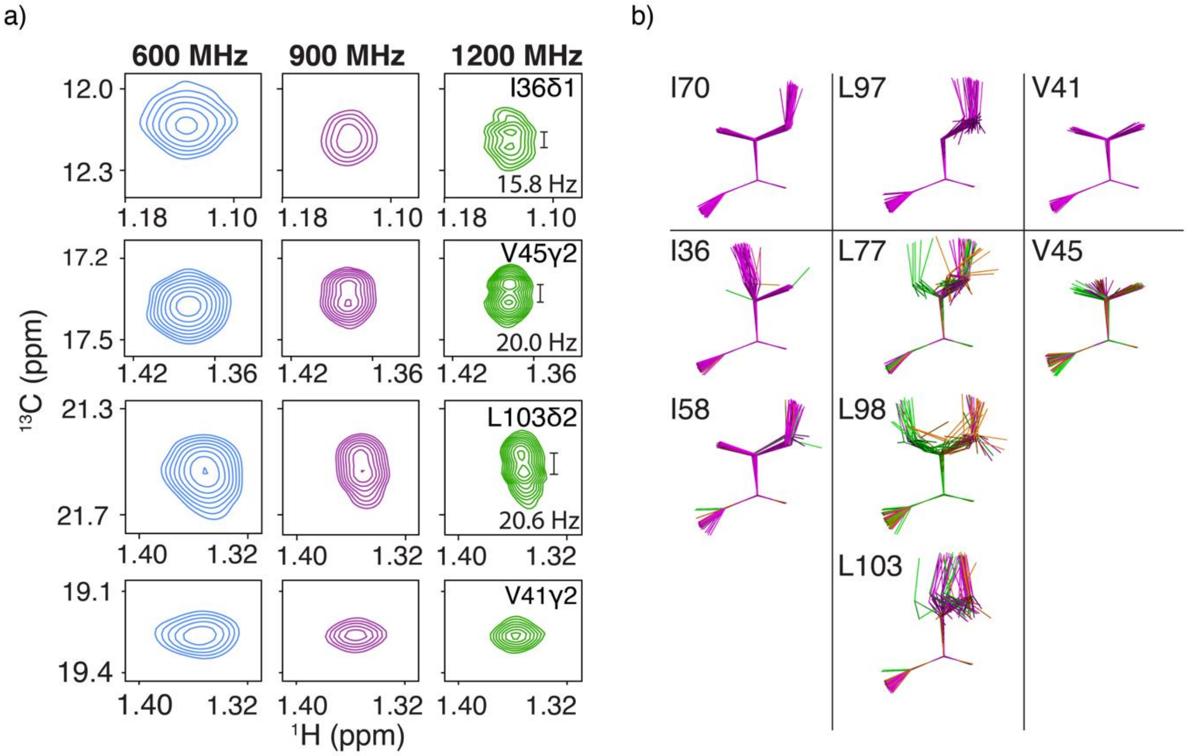

Figure 3.3: Asymmetry in the symmetric H2B histone copies of the nucleosome. a) Zoom on the peak shape for selected residues. At 1.2 GHz several residues I36δ1, V45γ2, L103δ2 show a split peak appearance, while most resonance such as V41γ2 have a normal peak shape. b) Heavy backbone atom superposition of selected Ile, Leu and Val side chains in 20 nucleosome crystal structures with Xl. histones (see Table S2). Side chains with difference in χ1/χ2 <= 30° between each H2B copy in a structure are color coded in magenta. Side chains for which the difference in χ1/χ2 > 30° are colored in green for one copy, and orange for the other copy.

Interestingly, comparison of the H2B ILV rotamers in twenty nucleosome structures containing *Xl.* histones shows that, while most residues have only a single side chain conformation, a few have multiple conformations (Fig. 3b). The residues with multiple conformations in the crystal or cryo-EM structures match with the residues whose resonances either show peak splitting (V45, L103), have more peak broadening compared to other residues (I58, L77, L98), or show a skewed peak shape (L98, L103) at 1200 MHz (Fig. S3.6). Moreover, these residues have different conformations for each H2B copy in many of the structures analyzed. In 65% of the structures analyzed, residue V45 is in the gauche– conformation in one H2B copy but in the trans or an eclipsed conformation in the other copy. Also, for L103, L77 and L98, there are significant differences in the χ_1 or χ_2 dihedral angles between the two H2B copies in respectively, 40, 60 and 75% of the analyzed structures. For I58 only a single structure in our analysis shows a different side chain conformation between the two H2B copies, although its conformation is variable between different structures. Together, this suggests that the asymmetry seen in some crystal structures is also present in solution, resulting in different (distributions of) side chain conformation of these residues between the two histone copies. This subsequently results in slight differences in chemical shifts. Of note, the NMR data further indicate that the residues with asymmetric side chain conformations are also affected by a dynamic conformational exchange. This is evident from the slight shift in peak position between the different fields, which is most visible for I36δ1 (Fig. 3a). At this point we cannot tell the origin of this process and how it is related to asymmetry in sidechain conformations for these residues. A recent solid-state NMR study suggested that the histone octamer contains several dynamic hotspots in H3 and H4 that could be connected in a dynamic network that extends from the DNA binding surface into the octamer interior[55]. The data here suggest that such dynamic network may also be present within the H2A-H2B dimer, or at least within H2B, as the identified residues are similarly distributed from the DNA binding site to the interior. Together, these data highlight the resolving power of methyl-TROSY NMR at 1200 MHz and provide further evidence for a role of the histone octamer core as an allosteric regulator.

Substantial magnetic field induced alignment of nucleosomes at 28.2 T

We next examined the degree of magnetic field induced alignment of the nucleosomes. At the magnetic field strengths used thus far such alignment effect would be difficult to pick up, but at 1.2 GHz the magnetic field alignment due to magnetic susceptivity anisotropy will be amplified. We thus first calculated the expected molecular magnetic susceptibility anisotropy $\Delta\chi_{\mathrm{mol}}$ for various model structures using residue-specific values of $\Delta\chi$ for the aromatic groups and the carbonyl backbone groups. To understand the alignment of the nucleosome, we first compared the $\Delta\chi_{\mathrm{mol}}$ tensor for linear DNA and DNA arranged in a super-helix, as in the archaeal hyper-nucleosome[56,57](Fig. 3.4). For linear DNA where the bases are stacked colinearly, the individual $\Delta\chi$ tensors add up almost perfectly, resulting in $\Delta\chi_{\mathrm{mol}}$ tensor with a main axis along the helical axis and thus a preferred molecular orientation orthogonal to the external magnetic field. When DNA is arranged in a super-helix, the main axis will be aligned with super helical axis (Fig. 3.4). As nucleosome core particle, which has 147 bp of DNA, has its DNA arranged in super-helix, we thus expect similar alignment with preferred orientation such that the super helical axis is orthogonal to external magnetic field. Using the crystal structure of the nucleosome core particle (1KX5) and considering both DNA and protein contributions, the predicted $\Delta\chi_{\mathrm{mol}}$ tensor has a main axial component of 105 10^{-27} J T^{-2} and low rhombicity (R = 0.07), resulting a significant degree of alignment (1.3 10^{-3}). This would subsequently result in ^{1}H-^{13}C fiRDCs of up to 18 Hz for a completely rigid methyl group.

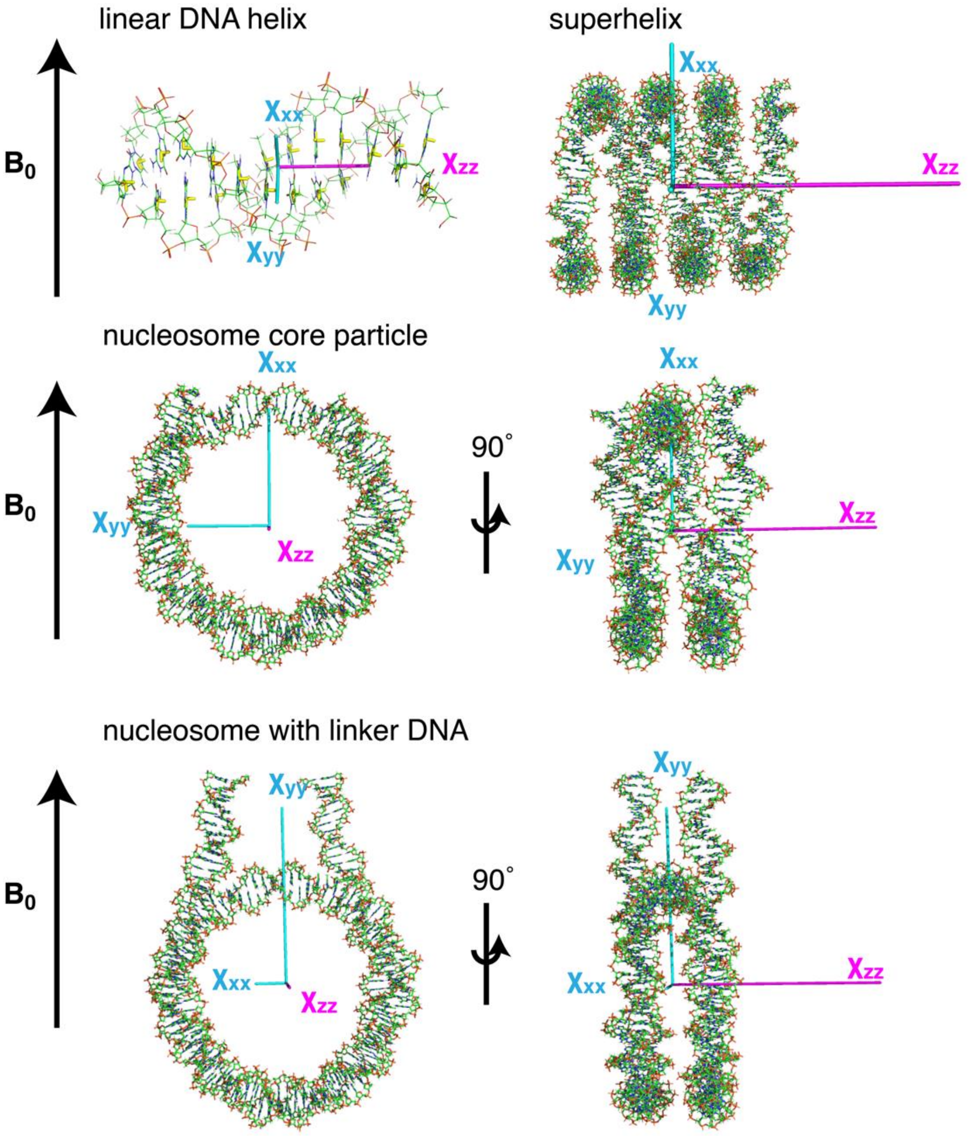

Figure 3.4: Predicted nucleosome alignment with magnetic field. For linear DNA the largest tensor is predicted along the helix of the DNA. For a superhelix of DNA, the largest tensor aligns along the super helical axis of the DNA. Both nucleosomes with and without linker DNA have the largest tensor along the super helical axis, like the superhelix (histone proteins not shown). Linker DNA of 2x 10bp have only a minor influence on the size of the Xzz tensor but have a large influence on the Xxx and Xyy tensor.

To experimentally determine the extent of magnetic field induced alignment of the nucleosome we recorded IPAP methyl-TROSY experiments[43] at 600, 900 and 1200 MHz. While at 600 MHz already small deviations from the expected 125 Hz $^{1}J_{CH}$ splitting are observed, this becomes particularly clear at 1200 MHz where the splitting ranges between 118.4 and 135.0 Hz (Fig. 3.5a). This indicates that there is a substantial contribution of fiRDC to the peak splitting, and thus magnetic field induced alignment of the nucleosome at 28.2 T / 1.2 GHz. For 33 out of 36 methyl group signals, peak splittings could reliable be measured at all three fields and fitted to extract the ^{1}H-^{13}C methyl fiRDC at 1200 MHz (Fig. 3.5b, c).

These fiRDCs range from -7.8 to +7.9 Hz. These values are ca. 44% of the predicted maximum fiRDC for the nucleosome core particle. The prediction did however not consider the presence of the additional linker DNA in our system, nor the presence of methyl group dynamics. Internal dynamics will downscale the RDC by the order parameter *S*, which is the degree of internal motions on nano to microsecond time scale of the methyl group symmetry axis. Previous relaxation measurements on nucleosomes with ILV-labeled H2B from *Dm*. showed that *S* is on average 0.5 for the core methyl groups, ranging from 0.16 to 0.94 (unpublished data). Assuming that the methyl dynamics in *Xl.* and *Dm.* H2B are similar, the magnitude of the experimental fiRDCs is in good agreement with that predicted. From the distribution of the fiRDCs, we can estimate that the alignment tensor has high rhombicity (Fig. 5d), which is in sharp contrast with predicted tensor based on the nucleosome core particle structure. This difference in rhombicity is caused the contribution of the linker DNA and, as we will show below, reflects the conformation of linker DNA.

Experimental fiRDCs match very well to nucleosomal H2B structure

We next evaluated the correspondence between the measured fiRDCs and the H2B structure as present in three representative nucleosome structures that have *Xl.* histones. We selected the structure with highest resolution (1KX5) and two high resolution structures that have the non-palindromic 601 DNA sequence that we also use, one determined by crystallography (3LZ0) and one by cryo-electron microscopy (cryo-EM) (7OHC). For each nucleosome structure, the fiRDCs for methyl groups in the histone core with a stereospecific assignment (20 in total) were fitted to the structure of one copy of H2B. The correlation plots of predicted *vs.* observed RDCs show that the best fits are obtained for the structures containing 601 DNA (Fig. 3.6a). Closer inspection shows that except for three outliers (I58 and L98), the best correlation is obtained using the 601-nucleosome structure determined by cryo-EM. As the conformation of I58 and L98 is very variable between different nucleosome structures (Fig. 3b), this suggests that the conformation of I58 and L98 are different in solution from that in the structure. Excluding these two residues from the fit resulted in a major improvement in correlation for all structures and overall best result (Q=0.166) for the 1KX5 H2B structure (Fig. 3.6b). Sidechain rotamer orientation can be determined using on residual dipolar couplings[58]. We therefore tested various rotamer conformations of I58 and L98, with all tested rotamers improving the Q-factor compared to 1kx5 rotamer conformations (Table S3.5 and fig. S3.7). For I58 the best fitting rotamer (Table S3.4 rotamer 1) resulted in a Q-factor (Q=0.165) comparable to the fit excluding I58 and L98. We suggest that I58 adopts this rotamer conformation in solution. For L98 none of tested rotamers led to a satisfactory improvement in Q-factor compared to the fit excluding I58 and L98.

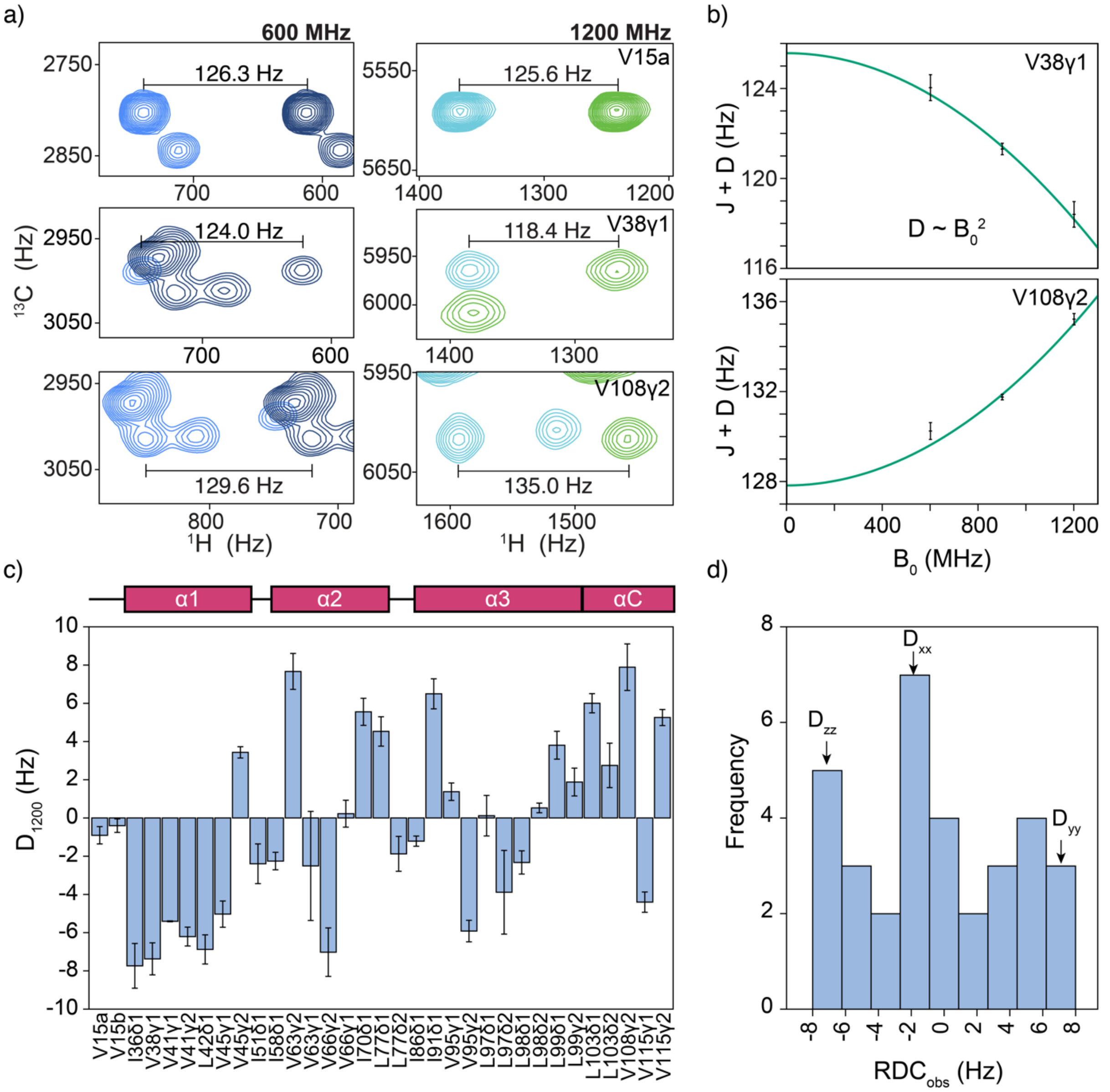

Figure 3.5: Substantial magnetic field induced alignment of nucleosomes at 28.2 T. a) Zooms of IPAP methyl-TROSY spectra recorded at 600 (14.1 T) and 1200 MHz (28.2 T) showing the ^{1}H-^{13}C J+D splitting. The spectra with either upfield or downfield doublet component are shown in different colors. Size of the splitting is indicated. b) Experimental field-dependent J+D values and best fits for two selected residues. Full results are in Table S3.2 and S3.3. c) Extracted ^{1}H-^{13}C fiRDC at 1200 MHz for H2B ILV methyl groups in the nucleosome. The secondary structure of H2B is indicated in top of the figure. d) Histogram of the observed fiRDCs at 1200 MHz. The distribution suggests a relatively high rhombicity of the alignment tensor.

As the order parameter *S* is unknown for the methyl groups, determination of the alignment tensor and correlation with the structure was done assuming a uniform value *S* for all core methyl groups. We thus conclude that the L98 methyl groups have substantially different dynamics compared to the other core methyl groups. Since the order parameter S samples motions up to the microsecond time scale and thus includes motions occurring on time scales slower than the molecular tumbling, relaxation experiments are not sufficient to determine S as those sample only motions up to the molecular tumbling. Thus, the true value for S can only be determined from detailed analysis of RDCs obtained in independent alignment conditions[59–61], which is beyond the scope of this chapter. Yet, the high-quality correspondence of the observed RDCs to the H2B structure indicates that the order parameter S for the other methyl groups is indeed rather uniform.

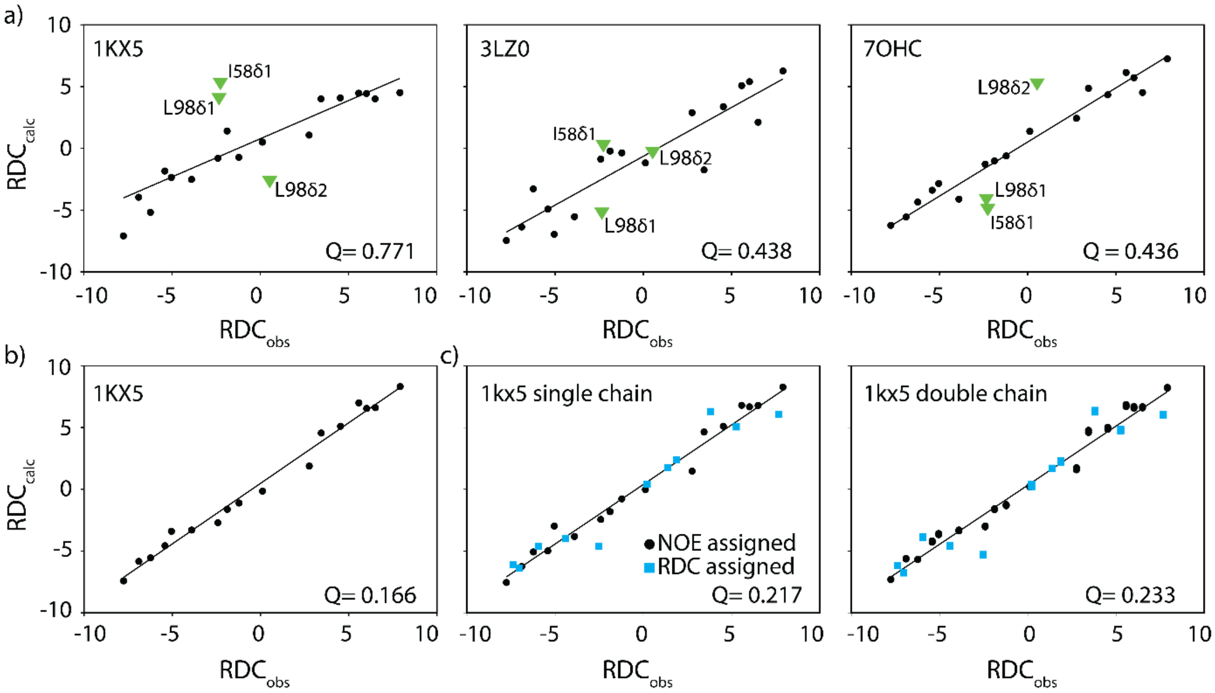

Figure 3.6: Correlation between experimentally observed and calculated RDCs. RDCs were fit using the indicated structures of H2B in the nucleosome. a) Correlation plots for three structures based on all stereo-specifically assigned residues using NOE data. RDCs for residues I58 and L98 are highlighted. b) Correlation plot excluding I58 and L98 from the fit improves correlation significantly, indicating the solution rotamers for I58 and L98 are different from that in the crystal. c) Fit in b with NOE and Chemical shift assigned resonances is used to assign residues without known stereochemistry. A correlation plot using both NOE and RDC assigned resonances calculated using a single H2B chain from 1kx5 (left) or both H2B chains (right) show a good correlation (I58 and L98 excluded).

Determination of stereospecific assignments from fiRDCs

We then reasoned that the predicted RDCs could be used to obtain the stereospecificity of the 6 LV residues (12 methyl groups) for which we could measure a fiRDC but did not have stereospecific assignments. Comparing the experimental fiRDC to the predicted RDC for either the δ1/γ1 or δ2/γ2 methyl group, we could obtain stereospecific assignments for all 6 residues (Table S3.7). Fitting all 29 fiRDCs from methyl with stereospecific assignment (but excluding I58 and L98) to the 1KX5 H2B structure resulted in an excellent correlation (Q = 0.217) (Fig. 3.6c). We also tested the feasibility of assigning the stereochemistry if no previous stereochemistry assignments were available as might be the case for other proteins. Assuming only the stereospecificity of the Ile methyl is known (based on the labeling scheme), 12 out of 14 LV residues could be stereo-specifically assigned after fitting the Ile fiRDCs to the H2B structure (I58 excluded, 5 fiRDCs in total used for the fit). Including chemical shift-based prediction[38], stereo-specific assignments for 4 Leu could be obtained and in total 12 fiRDCs were used to determine the fit to the H2B structure. Based on the predicted fiRDCs of this fit, again all remaining LV residues could be assigned stereo-specifically, expect for L98 and V41. For L98 neither assignment option gave a good fit, and for V41 both options gave equally good fits. Together, these results show that fiRDCs at ultra-high field are very valuable to aid NOE and chemical shift-based stereo-specific assignment and are potentially also a useful source of information for automated assignment programs.

Estimation of linker DNA conformation from fiRDCs

Having established that the experimental fiRDCs agree well to the H2B structure, we next wondered whether the fiRDCs could also be used to determine the linker DNA conformation. Linker DNA has been observed with DNA ends bound to the core, detached from the core, or transiently wrap and unwrap from the nucleosome core[62–66]. Additionally, opening of the linkers has been described to occur symmetrically and non-symmetrically[67–69]. The (average) linker DNA conformation in solution can be derived from the fiRDCs, as the extracted alignment tensor can be directly converted into the magnetic susceptibility tensor, which is turn determined mostly by the DNA in the nucleosome. We constructed models of nucleosome with linker DNA in closed or various open states and calculated the $\Delta\chi_{mol}$ from these structures. While the anisotropy of the $\Delta\chi_{mol}$ tensor is not much affected by the conformation of the linker DNA, it is clear from the models that there is strong impact on the rhombicity of the tensor (Fig 3.7a and table S3.6). The rhombicity is predicted to be highest when the linker DNA extend parallel in the same direction from the nucleosome core particle and decreases upon opening or closing the DNA (Fig. 3.7a). Thus, comparison of experimental and calculated rhombicity should give a good indication of the average linker DNA conformation.

To determine the $\Delta\chi_{mol}$ tensor from the experimental fiRDCs we first extended our analysis from using a single to both H2B copies in the nucleosome. Fits to either copy are of similar quality and result in similar orientation of the alignment tensor principle axis frame (PAS) with respect to the molecular frame (Fig. 3.7b). Indeed, the observation of a single fiRDC for each H2B methyl indicates that the PAS is oriented along the symmetry axis of the nucleosome, as also predicted from the calculated $\Delta\chi_{mol}$ based on the structure (Fig. 3.7a). Fitting the experimental fiRDCs to both symmetry related H2B copies simultaneously results in a very good correlation between observed and predicted RDCs, although Q factor is slightly higher than for the single chain fit (Q= 0.233 vs. 0.217). The alignment tensor from this fit was converted into the magnetic susceptibility tensor to compare against the structure predicted $\Delta\chi_{mol}$ tensors (Fig. 3.7c). The PAS of the experimental tensor is oriented along the dyad, with the $\Delta\chi_{zz}$ component along the super helical axis and the $\Delta\chi_{xx}$ component perpendicular, in good agreement with orientation of the predicted tensors. The fitted tensor anisotropy is about 60% of the calculated value, reflecting the impact of methyl groups dynamics which scale the fiRDCs by the order parameter *S*. While DNA dynamics (transient wrapping and unwrapping of the DNA from the histone core) could in principle also scale the alignment tensor and the reduce the fiRDCs, this is less likely to be responsible as the different nucleosome models have all similar anisotropies. Furthermore, FRET measurements have indicated that wrapping/unwrapping occurs at millisecond time scale which is too slow to scale the alignment tensor.

The rhombicity of the $\Delta\chi_{mol}$ tensor could be determined with reasonable precision from the RDC (0.351 ± 0.03) (Fig. 3.7c). This is substantially lower than the maximal rhombicity for the 'straight linker' model and could thus reflect an either more closed or more open structure. As the lowest rhombicity for a compacted linker DNA conformation was predicted to be 0.48, the experimental data suggest that the linker DNA confirmation is rather open. A model with 20 bp unwrapped on both sides from the core particle result in the same rhombicity as experimental (Fig. 3.7a) suggesting that this represents the time averaged conformation under our conditions. Single molecule FRET measurements have shown that presence of linker DNA increases opening of nucleosomes, in particular under low ionic strength conditions such as here, suggesting that electrostatic repulsion between the linkers is a dominant factor[70]. Furthermore, the data also indicate that the average linker DNA conformation is symmetric as any asymmetry in linker DNA unwrapping would result in a very different orientation of the PAS (Figure 5). This is in contrast to recent MD study that indicated that linker DNA in 601-nucleosome has intrinsically asymmetric dynamics[69]. It could be that at the longer time scales sampled by the experimental fiRDCs the linkers behave symmetrical, but not at shorter time scale probed by the MD simulations. It could also be that the asymmetries in DNA dynamics are too subtle to significantly affect the magnetic susceptibility tensor and are thus not picked up in our experiment.

Overall, the high similarity between the $\Delta\chi_{mol}$ tensor extracted from the experimental fiRDCs and that predicted based on structure indicates that fiRDCs will be an extremely useful tool to study linker DNA related nucleosome dynamics, such as in remodeling. Also, fiRDCs may be very valuable to determine structures of nucleosome-protein complexes, where it can complement binding site information from chemical shift perturbations and add orientational information.

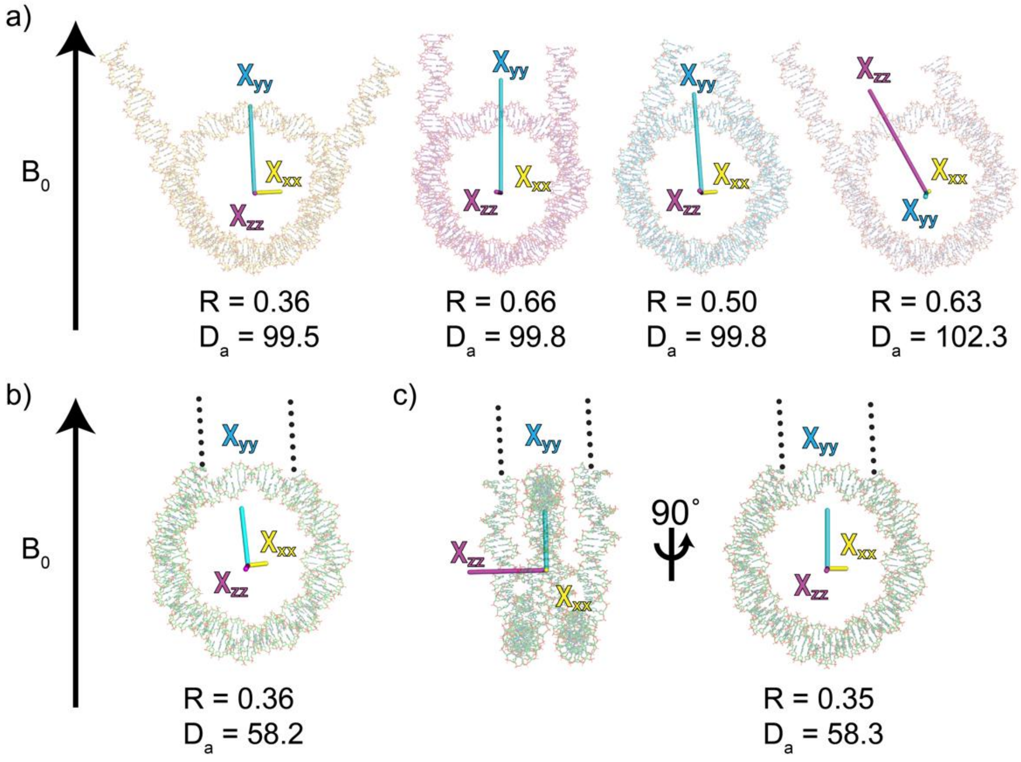

Figure 3.7: Experimental fiRDCs match an open DNA linker conformation. a) Predicted magnetic susceptibility tensors for 3lz0 with differently modeled linker DNA. From left to right: open, straight, closed, and asymmetric linker DNA. b+c) Observed magnetic susceptibility tensor from the single (b) and double (c) H2B chain fit on 1kx5 nucleosome core particle. Dotted lines represent linker DNA. For each conformation the anisotropy (Da 10^{-27} J T^{-2}) is given.

Conclusion

The advent of higher magnetic fields in the form of the 1.2 GHz NMR machine have brought many promising opportunities to the playing field. With the higher field we observe increased resolution for both ^{1}H and ^{13}C, allowing us to visualize asymmetries inside chain conformation between the two histone copies of the symmetric nucleosome complex. At higher field we observe increased methyl CSA, effectively increases ^{13}C transverse relaxation rates by 20% at 1200 compared to 900 MHz. Additionally, a substantial magnetic field induced alignments of nucleosomes occurs at 1.2 GHz. The fiRDCs observed for the nucleosome strongly correlate with fiRDCs predicted for known nucleosome structures and were used to stereospecificity assign nearly all methyl resonances which were not assignable using conventional NOESY experiments. Finally, we used fiRDCs to predict an on average open conformation of linker DNA under our conditions. Recently methyltransferases were applied to methylate nucleosomal DNA and used as NMR probes[39]. As nucleosomal DNA is challenging to study, combination of these type of labeling approaches and fiRDCs can be used to give structural insights in the orientations and dynamics of nucleosomal DNA. The use of fiRDCs is not restricted to nucleosomes but will be applicable to any protein that has a magnetic field induced alignment and will improve with the advancement of field strength.

References

1. Huang, C., Rossi, P., Saio, T. & Kalodimos, C. G. Structural basis for the antifolding activity of a molecular chaperone. *Nature* **537**, 202–206 (2016).

2. Gelis, I. *et al.* Structural Basis for Signal-Sequence Recognition by the Translocase Motor SecA as Determined by NMR. *Cell* **131**, 756–769 (2007).

3. Pervushin, K., Riek, R., Wider, G. & Wüthrich, K. Attenuated T2 relaxation by mutual cancellation of dipole-dipole coupling and chemical shift anisotropy indicates an avenue to NMR structures of very large biological macromolecules in solution. *Proc. Natl. Acad. Sci. U. S. A.* **94**, 12366–12371 (1997).

4. Fiaux, J., Bertelsen, E. B., Horwich, A. L. & Wüthrich, K. NMR analysis of a 900K GroEL-GroES complex. *Nature* **418**, 207–211 (2002).

5. Sprangers, R. & Kay, L. E. Quantitative dynamics and binding studies of the 20S proteasome by NMR. *Nature* **445**, 618–622 (2007).

6. Tugarinov, V., Hwang, P. M., Ollerenshaw, J. E. & Kay, L. E. Cross-correlated relaxation enhanced 1H-13C NMR spectroscopy of methyl groups in very high molecular weight proteins and protein complexes. *J. Am. Chem. Soc.* **125**, 10420–10428 (2003).

7. Tugarinov, V., Choy, W. Y., Orekhov, V. Y. & Kay, L. E. Solution NMR-derived global fold of a monomeric 82-kDa enzyme. *Proc. Natl. Acad. Sci. U. S. A.* **102**, 622–627 (2005).

8. Robson, S. A. *et al.* Mixed pyruvate labeling enables backbone resonance assignment of large proteins using a single experiment. *Nat. Commun.* **9**, 2–3 (2018).

9. Arthanari, H., Takeuchi, K., Dubey, A. & Wagner, G. Emerging solution NMR methods to illuminate the structural and dynamic properties of proteins. *Curr. Opin. Struct. Biol.* **58**, 294–304 (2019).

10. Schütz, S. & Sprangers, R. Methyl TROSY spectroscopy: A versatile NMR approach to study challenging biological systems. *Prog. Nucl. Magn. Reson. Spectrosc.* **116**, 56–84 (2020).

11. Luchinat, E., Barbieri, L., Cremonini, M. & Banci, L. Protein in-cell NMR spectroscopy at 1.2 GHz. *J. Biomol. NMR* **75**, 97–107 (2021).

12. Nimerovsky, E. *et al.* Proton detected solid-state nmr of membrane proteins at 28 tesla (1.2 ghz) and 100 khz magic-angle spinning. *Biomolecules* **11**, (2021).

13. Ollerenshaw, J. E., Tugarinov, V. & Kay, L. E. Methyl TROSY: Explanation and experimental verification. *Magn. Reson. Chem.* **41**, 843–852 (2003).

14. Tugarinov, V., Scheurer, C., Brüschweiler, R. & Kay, L. E. Estimates of methyl 13C and 1H CSA values (Δσ) in proteins from cross-correlated spin relaxation. *J. Biomol. NMR* **30**, 397–406 (2004).

15. Bolik-Coulon, N., Cousin, S. F., Kadeřávek, P., Dumez, J. N. & Ferrage, F. Understanding the methyl-TROSY effect over a wide range of magnetic fields. *J. Chem. Phys.* **150**, (2019).

16. Schanda, P. & Brutscher, B. Very fast two-dimensional NMR spectroscopy for real-time investigation of dynamic events in proteins on the time scale of seconds. *J. Am. Chem. Soc.* **127**, 8014–8015 (2005).

17. Amero, C. *et al.* Fast Two-Dimensional NMR Spectroscopy of High Molecular Weight Protein Assemblies. *J. Am. Chem. Soc.* **131**, 3448–3449 (2009).

18. Maret, G., Schickfus, M. V., Mayer, A. & Dransfeld, K. Orientation of Nucleic Acids in High Magnetic Fields. *Phys. Rev. Lett.* **35**, 397–400 (1975).

19. Bastiaan, E. W. & MacLean, C. Molecular Orientation in High-Field High-Resolution NMR. in *NMR at Very High Field* **25**, 17–43 (Springer Berlin Heidelberg, 1990).

20. Brandes, R. & Kearns, D. R. Magnetic ordering of DNA liquid crystals. *Biochemistry* **25**, 5890–5895 (1986).

21. Kung, H. C., Wang, K. Y., Goljer, I. & Bolton, P. H. Magnetic Alignment of Duplex and Quadruplex DNAs. *J. Magn. Reson. Ser. B* **109**, 323–325 (1995).

22. Tjandra, N., Omichinski, J. G., Gronenborn, A. M., Clore, G. M. & Bax, A. Use of dipolar 1H–15N and 1H–13C couplings in the structure determination of magnetically oriented macromolecules in solution. *Nat. Struct. Biol.* **4**, 732–738 (1997).

23. Zhang, Q., Throolin, R., Pitt, S. W., Serganov, A. & Al-Hashimi, H. M. Probing motions between equivalent RNA domains using magnetic field induced residual dipolar couplings: Accounting for correlations between motions and alignment. *J. Am. Chem. Soc.* **125**, 10530–10531 (2003).

24. Cromsigt, J., Van Buuren, B., Schleucher, J. & Wijmenga, S. Resonance Assignment and Structure Determination for RNA. in *Methods in Enzymology* **338**, 371–399 (2002).

25. Wu, B. *et al.* Global structure of a DNA three-way junction by solution NMR: Towards prediction of 3H fold. *Nucleic Acids Res.* **32**, 3228–3239 (2004).

26. Tjandra, N. & Bax, A. Measurement of Dipolar Contributions to 1 J CH Splittings from Magnetic-Field Dependence of J Modulation in Two-Dimensional NMR Spectra. *J. Magn. Reson.* **124**, 512–515 (1997).

27. Vavřinská, A. *et al.* Impact of nucleic acid self-alignment in a strong magnetic field on the interpretation of indirect spin-spin interactions. *J. Biomol. NMR* **64**, 53–62 (2016).

28. Bryce, D. L., Boisbouvier, J. & Bax, A. Experimental and theoretical determination of nucleic acid magnetic susceptibility: Importance for the study of dynamics by field-induced residual dipolar couplings. *J. Am. Chem. Soc.* **126**, 10820–10821 (2004).

29. Giassa, I. C. *et al.* HERMES – A Software Tool for the Prediction and Analysis of Magnetic-Field-Induced Residual Dipolar Couplings in Nucleic Acids. *Chempluschem* **85**, 2177–2185 (2020).

30. Marley, J., Lu, M. & Bracken, C. A method for efficient isotopic labeling of recombinant proteins. 71–75 (2001).

31. Klinker, H., Haas, C., Harrer, N., Becker, P. B. & Mueller-Planitz, F. Rapid purification of recombinant histones. *PLoS One* **9**, (2014).

32. Lowary, P. . & Widom, J. New DNA sequence rules for high affinity binding to histone octamer and sequence-directed nucleosome positioning. *J. Mol. Biol.* **276**, 19–42 (1998).

33. Dyer, P. N. *et al.* Reconstitution of Nucleosome Core Particles from Recombinant Histones and DNA. *Methods Enzymol.* **375**, 23–44 (2003).

34. Lee, W., Tonelli, M. & Markley, J. L. NMRFAM-SPARKY: Enhanced software for biomolecular NMR spectroscopy. *Bioinformatics* **31**, 1325–1327 (2015).

35. Kato, H. *et al.* Architecture of the high mobility group nucleosomal protein 2-nucleosome complex as revealed by methyl-based NMR. *Proc. Natl. Acad. Sci.* **108**, 12283–12288 (2011).

36. Pritišanac, I. *et al.* Automatic Assignment of Methyl-NMR Spectra of Supramolecular Machines Using Graph Theory. *J. Am. Chem. Soc.* **139**, 9523–9533 (2017).

37. Davey, C. A., Sargent, D. F., Luger, K., Maeder, A. W. & Richmond, T. J. Solvent mediated interactions in the structure of the nucleosome core particle at 1.9 A resolution. *J. Mol. Biol.* **319**, 1097–1113 (2002).

38. Hansen, D. F., Neudecker, P., Vallurupalli, P., Mulder, F. A. A. & Kay, L. E. Determination of Leu Side-Chain Conformations in Excited Protein States by NMR Relaxation Dispersion. *J. Am. Chem. Soc.* **132**, 42–43 (2010).

39. Abramov, G., Velyvis, A., Rennella, E., Wong, L. E. & Kay, L. E. A methyl-TROSY approach for NMR studies of high-molecular-weight DNA with application to the nucleosome core particle. *Proc. Natl. Acad. Sci. U. S. A.* **117**, 12836–12846 (2020).

40. Korzhnev, D. M., Kloiber, K., Kanelis, V., Tugarinov, V. & Kay, L. E. Probing Slow Dynamics in High Molecular Weight Proteins by Methyl-TROSY NMR Spectroscopy: Application to a 723-Residue Enzyme. *J. Am. Chem. Soc.* **126**, 3964–3973 (2004).

41. Delaglio, F. *et al.* NMRPipe: A multidimensional spectral processing system based on UNIX pipes. *J. Biomol. NMR* **6**, 277–293 (1995).

42. Ahlner, A., Carlsson, M., Jonsson, B. H. & Lundström, P. PINT: A software for integration of peak volumes and extraction of relaxation rates. *J. Biomol. NMR* **56**, 191–202 (2013).

43. Sprangers, R. & Kay, L. E. Probing supramolecular structure from measurement of methyl 1H-13C residual dipolar couplings. *J. Am. Chem. Soc.* **129**, 12668–12669 (2007).

44. Williams, T. & Kelley, C. Gnuplot: an interactive plotting program. (2011). Available at: http://gnuplot.info.

45. Vasudevan, D., Chua, E. Y. D. & Davey, C. A. Crystal Structures of Nucleosome Core Particles Containing the '601' Strong Positioning Sequence. *J. Mol. Biol.* **403**, 1–10 (2010).

46. Wang, H., Xiong, L. & Cramer, P. Structures and implications of TBP–nucleosome complexes. *Proc. Natl. Acad. Sci. U. S. A.* **118**, 1–7 (2021).

47. Zweckstetter, M. & Bax, A. Evaluation of uncertainty in alignment tensors obtained from

dipolar couplings. *J. Biomol. NMR* **23**, 127–137 (2002).

48. Lu, X. J. & Olson, W. K. 3DNA: A software package for the analysis, rebuilding and visualization of three-dimensional nucleic acid structures. *Nucleic Acids Res.* **31**, 5108–5121 (2003).

49. Van Nuland, R. *et al.* Nucleosomal DNA binding drives the recognition of H3K36-methylated nucleosomes by the PSIP1-PWWP domain. *Epigenetics and Chromatin* **6**, 1 (2013).

50. Zhang, H., Eerland, J., Horn, V., Schellevis, R. & van Ingen, H. Mapping the electrostatic potential of the nucleosome acidic patch. *Sci. Rep.* **11**, 1–11 (2021).

51. Xiang, S. Q. *et al.* Site-Specific Studies of Nucleosome Interactions by Solid-State NMR Spectroscopy. *Angew. Chemie - Int. Ed.* **57**, 4571–4575 (2018).

52. Sinha, K. K., Gross, J. D. & Narlikar, G. J. Distortion of histone octamer core promotes nucleosome mobilization by a chromatin remodeler. *Science (80-.).* **355**, (2017).

53. Schanda, P., Kupĉe, E. & Brutscher, B. SOFAST-HMQC experiments for recording two-dimensional deteronuclear correlation spectra of proteins within a few seconds. *J. Biomol. NMR* **33**, 199–211 (2005).

54. Vuister, G. W., Wang, A. C. & Bax, A. Measurement of three-bond nitrogen-carbon J couplings in proteins uniformly enriched in nitrogen-15 and carbon-13. *J. Am. Chem. Soc.* **115**, 5334–5335 (1993).

55. Shi, X., Prasanna, C., Soman, A., Pervushin, K. & Nordenskiöld, L. Dynamic networks observed in the nucleosome core particles couple the histone globular domains with DNA. *Commun. Biol.* **3**, 1–11 (2020).

56. Mattiroli, F. *et al.* Structure of histone-based chromatin in Archaea. *Science (80-.).* **357**, 609–612 (2017).

57. Henneman, B. *et al.* Mechanical and structural properties of archaeal hypernucleosomes. *Nucleic Acids Res.* **49**, 4338–4349 (2021).

58. Chou, J. J. & Bax, A. Protein Side-Chain Rotamers from Dipolar Couplings in a Liquid Crystalline Phase. *J. Am. Chem. Soc.* **123**, 3844–3845 (2001).

59. Meiler, J., Prompers, J. J., Peti, W., Griesinger, C. & Brüschweiler, R. Model-free approach to the dynamic interpretation of residual dipolar couplings in globular proteins. *J. Am. Chem. Soc.* **123**, 6098–6107 (2001).

60. Peti, W., Meiler, J., Brüschweiler, R. & Griesinger, C. Model-free analysis of protein backbone motion from residual dipolar couplings. *J. Am. Chem. Soc.* **124**, 5822–5833 (2002).

61. Lakomek, N. A., Carlomagno, T., Becker, S., Griesinger, C. & Meiler, J. A Thorough Dynamic Interpretation of Residual Dipolar Couplings in Ubiquitin. *J. Biomol. NMR* **34**, 101–115 (2006).

62. Li, G. & Widom, J. Nucleosomes facilitate their own invasion. *Nat. Struct. Mol. Biol.* **11**, 763–769 (2004).

63. Li, G., Levitus, M., Bustamante, C. & Widom, J. Rapid spontaneous accessibility of nucleosomal DNA. *Nat. Struct. Mol. Biol.* **12**, 46–53 (2005).

64. Gansen, A. *et al.* High precision FRET studies reveal reversible transitions in nucleosomes between microseconds and minutes. *Nat. Commun.* **9**, 1–13 (2018).

65. North, J. A. *et al.* Regulation of the nucleosome unwrapping rate controls DNA accessibility. *Nucleic Acids Res.* **40**, 10215–10227 (2012).

66. Kono, H. & Ishida, H. Nucleosome unwrapping and unstacking. *Curr. Opin. Struct. Biol.* **64**, 119–125 (2020).

67. Ngo, T. T. M. & Ha, T. Nucleosomes undergo slow spontaneous gaping. *Nucleic Acids Res.* **43**, 3964–3971 (2015).

68. Chen, Y. *et al.* Asymmetric unwrapping of nucleosomal DNA propagates asymmetric opening and dissociation of the histone core. *Proc. Natl. Acad. Sci. U. S. A.* **114**, 334–339 (2017).

69. Huertas, J. & Cojocaru, V. Breaths, Twists, and Turns of Atomistic Nucleosomes. *J. Mol. Biol.* **433**, 166744 (2021).

70. Buning, R., Kropff, W., Martens, K. & van Noort, J. spFRET reveals changes in nucleosome breathing by neighboring nucleosomes. *J. Phys. Condens. Matter* **27**, 064103 (2015).

Supplemental information:

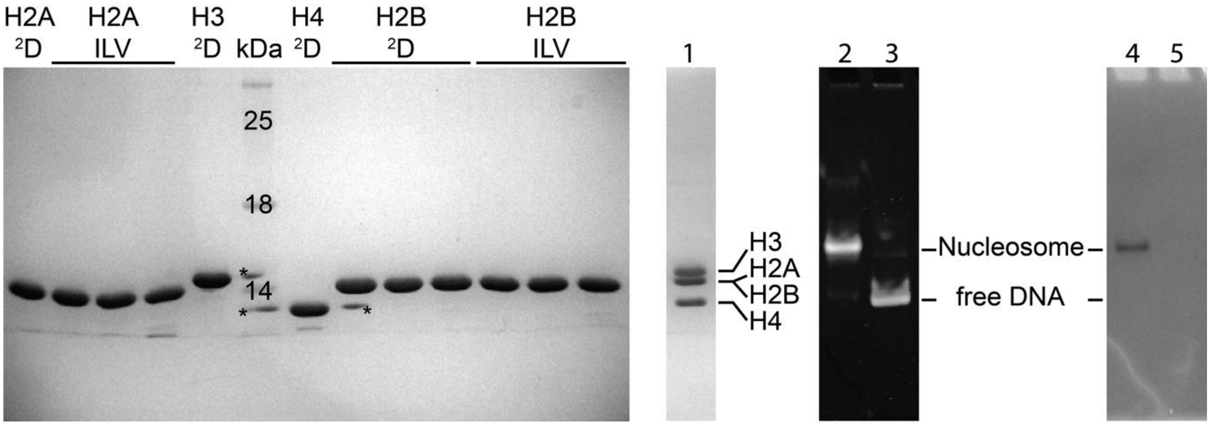
H2A
²D
H2A
ILV
H3
²D
kDa
H4
²D
H2B
²D
H2B
ILV
25
18
14
*
*
*
1
2
3
4
5
H3
H2A
H2B
H4
Nucleosome
free DNA

Figure S3.1: Nucleosome reconstitution. Purified histones (left gel), with stars indicating overflow from neighboring well. 15% SDS page nucleosome (1), 5% native GelRed stain of H2B ILV labeled nucleosome (2) and 167 base pair 601 DNA (3), coomassie stain H2B ILV labeled nucleosome (4) and 167 base pair 601 DNA (5).

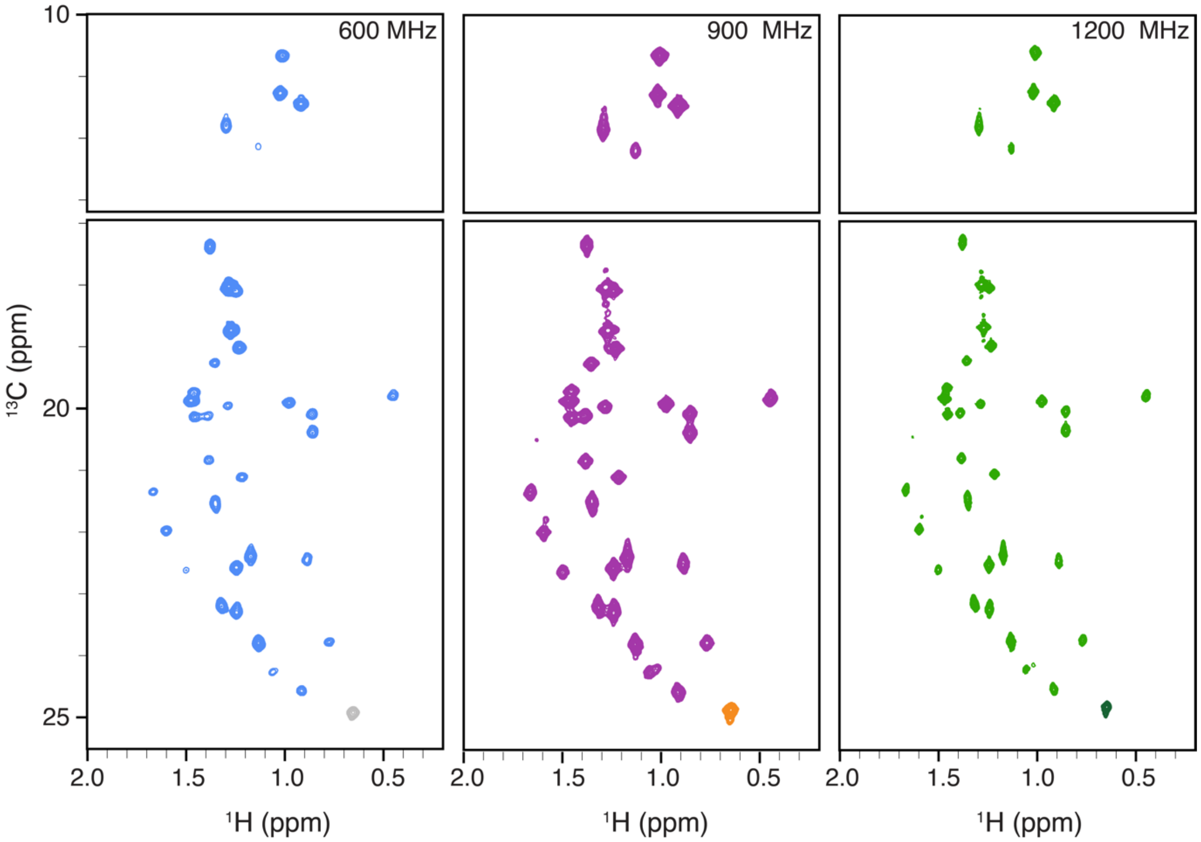

Figure S3.2: H2B ILV methyl resonances. Nucleosome spectra recorded with SOFAST-methyl TROSY HMQC experiments at 600, 900 and 1200 MHz. Signal threshold is set to compare intensities between different field strengths.

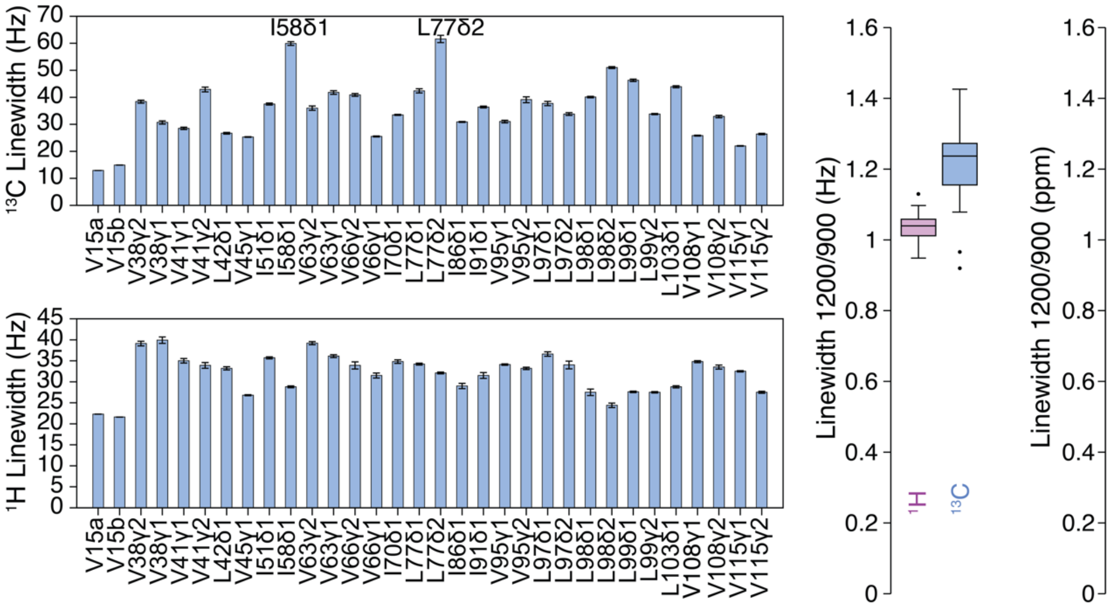

Figure S3.3: Nucleosome methyl group linewidths at 1200 MHz. Linewidths for ^{13}C (top left) and ^{1}H (bottom left) With the two broadest peaks marked for the ^{13}C linewidth. Average ^{1}H and ^{13}C linewidths are shown in Hz and ppm on the right.

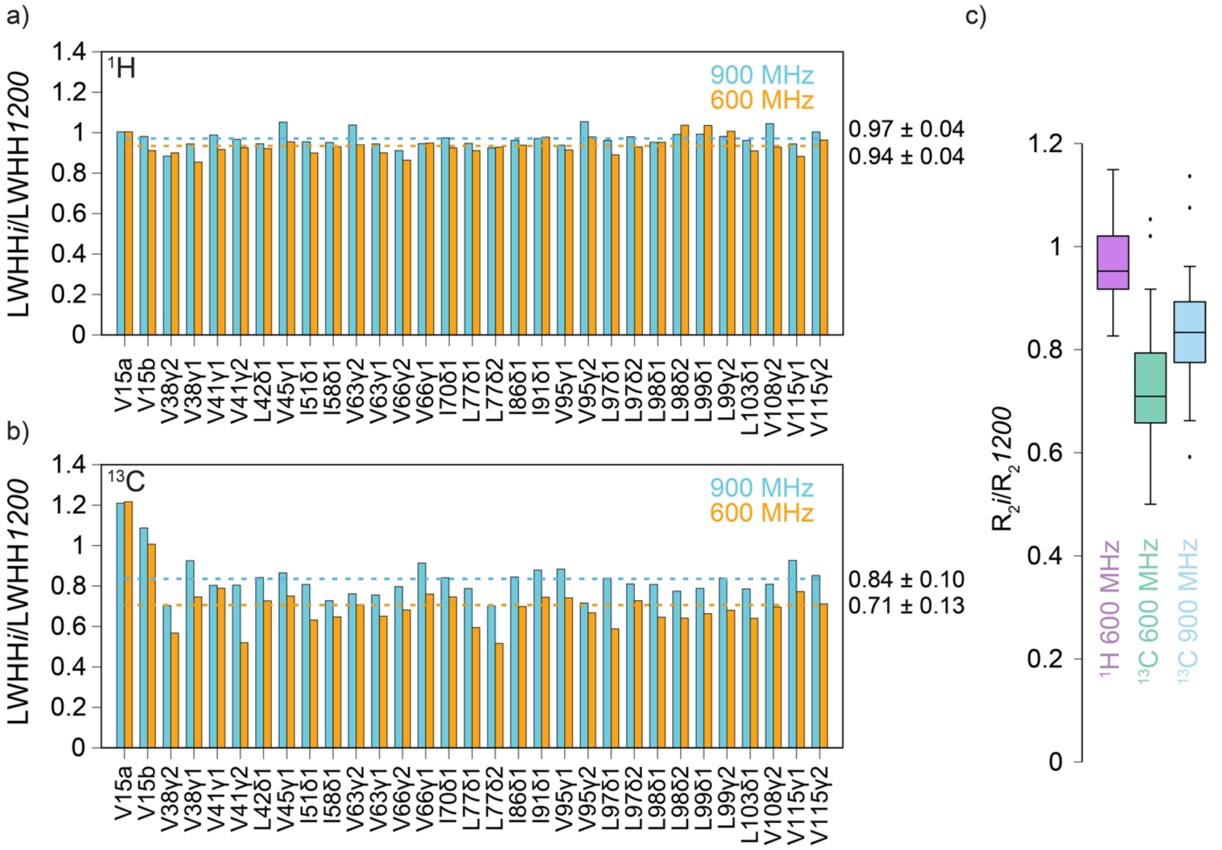

Figure S3.4: Smaller ^{13}C linewidths (Hz) at lower field. a) For the nucleosome all residues show a similar ^{1}H linewidth independent of magnetic field strength. b) While for flexible tail residues ^{13}C linewidth (Hz) become sharper at high field, nucleosome core residue signals broaden with increasing magnetic field. c) Average ratio of R_2 at given field strength compared to R_2 at 1200 MHz.

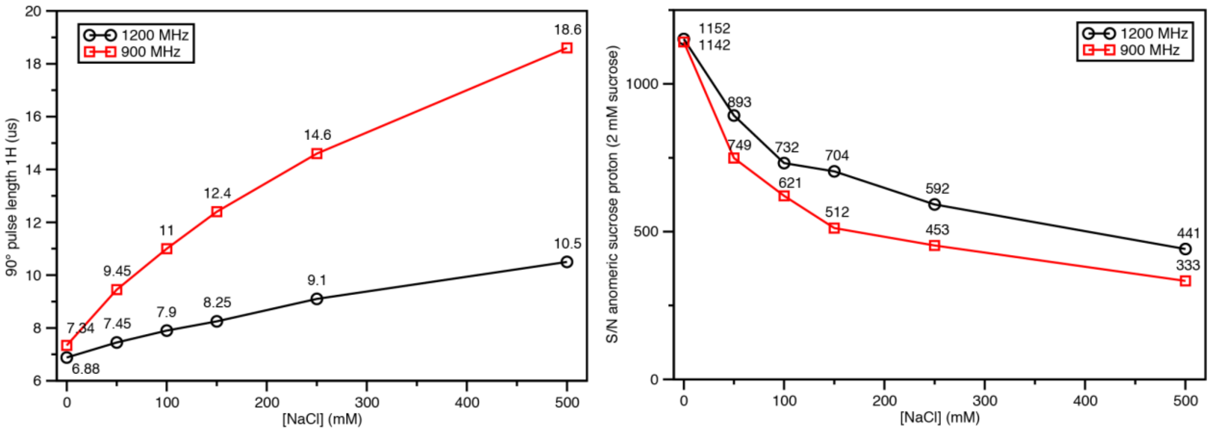

Figure S3.5: Sucrose sensitivity measurements at 900 and 1200 MHZ spectrometer. Both 900 and 1200MHz signal to noise decreases with higher salts but decreases slower on 1200MHz.

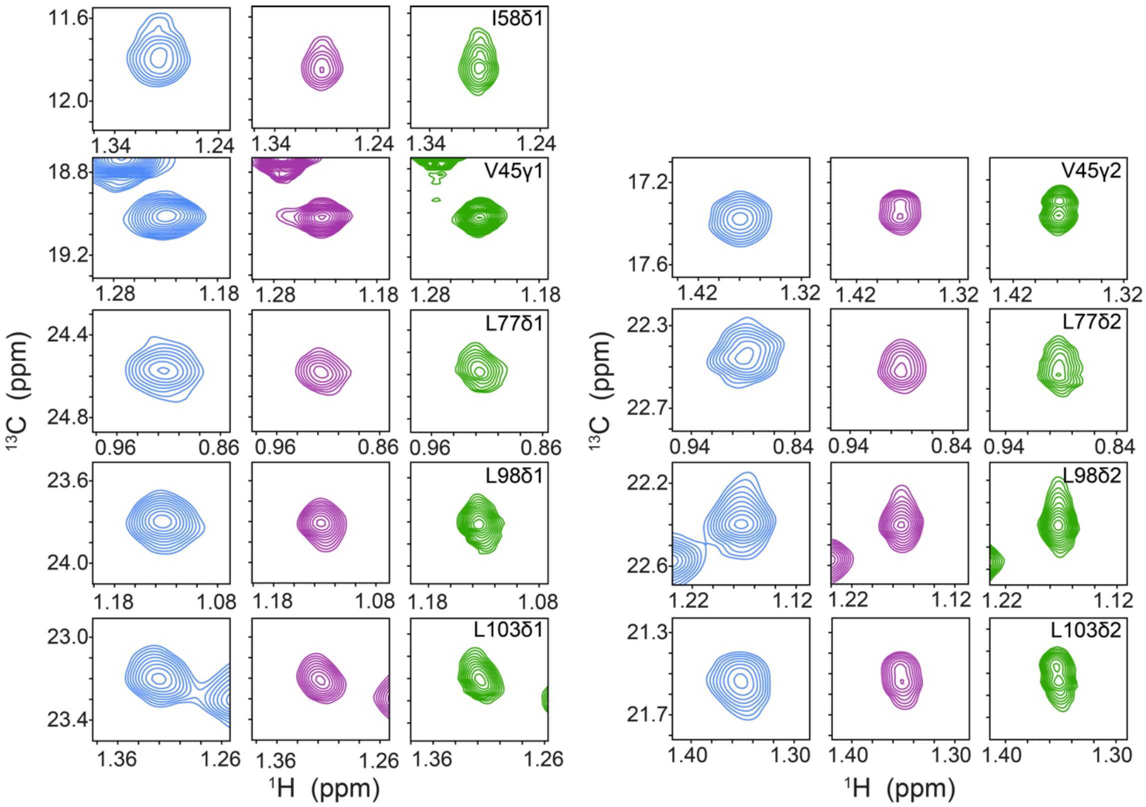

Figure S3.6: Nucleosome H2B ILV resonance split or broadened peak shapes. Resonances for V45γ2 and L103δ2 show peak doubling. Resonances for I58δ1, L77, L98 and L103δ1 show peak broadening in the ^{13}C dimension and L98δ1 and L103δ1 show additional broadening in the ^{1}H dimension.

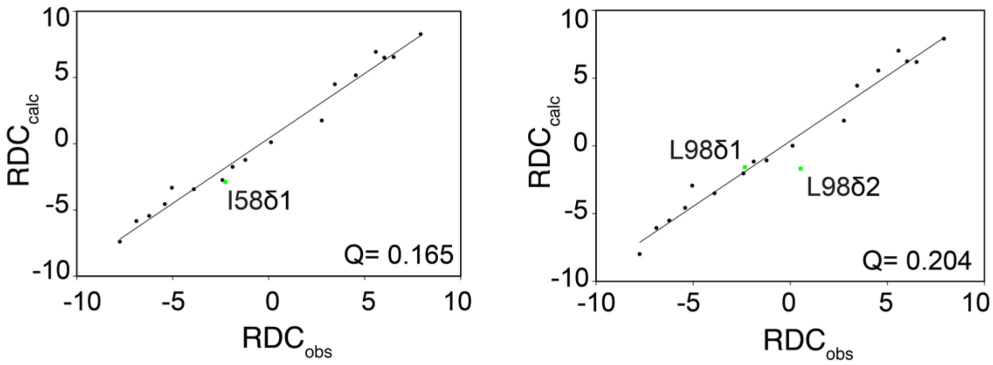

Figure S3.7: Best fitting alternative rotamer orientations I58 and L98. Residue I58 shows a good correlation using 1kx5 with rotamer 1 for I58 (left). Residue I58 shows an improved correlation using 1kx5 with rotamer 5 for L98 (right).

Table S3.1: Xenopus laevis Nucleosome pdb structures used for rotamer analysis.

pdb code	Resolution (Å)	Methode
1AOI	2.80	X-ray
1KX3	2.00	X-ray
1KX4	2.60	X-ray
1KX5	1.94	X-ray
2NZD	2.65	X-ray
3LJA	2.75	X-ray
3LZ0	2.50	X-ray
3LZ1	2.50	X-ray
3REH	2.50	X-ray
3REJ	2.55	X-ray
3UTB	2.20	X-ray
6PX1	3.30	EM
6WZ5	2.20	EM
7KBD	3.38	EM
7KBE	3.50	EM
7KTQ	3.30	EM
7OHC	2.50	EM
3UTA	2.07	X-ray
3UT9	2.20	X-ray
5F99	2.63	X-ray
2FJ7	3.20	X-ray

Table S3.2: Carbon coupled peak splitting. Peak splitting (Δ) at 600, 900 and 1200 MHz due to carbon coupling are reported in Hz for nucleosome H2B ILV methyl groups.

residue	methyl	Δ_{600}	$\sigma_{S,600}$	Δ_{900}	$\sigma_{S,900}$	Δ_{1200}	$\sigma_{S,1200}$
V15	a	126.55	0.05	125.63	0.01	125.34	0.02
V15	b	126.26	0.04	125.84	0.01	125.74	0.02
I36	δ1	125.45	0.79	122.25	0.24	119.19	0.56
V38	γ1	124.28	0.58	121.31	0.25	118.40	0.57
V41	γ1	125.70	0.39	123.87	0.15	121.49	0.29
V41	γ2	124.94	0.43	122.84	0.16	120.28	0.35
L42	δ1	123.49	0.39	120.86	0.14	118.07	0.27
V45	γ1	125.91	0.14	123.56	0.05	121.55	0.09
V45	γ2	126.50	0.21	127.62	0.08	129.23	0.19
I51	δ1	125.24	0.27	123.75	0.10	123.03	0.21
I58	δ1	125.70	0.27	124.89	0.12	124.08	0.27
V63	γ2	127.19	0.55	130.28	0.23	133.29	0.53
V63	γ1	125.89	0.43	122.80	0.18	120.62	0.42
V66	γ2	125.70	0.30	122.77	0.12	120.17	0.30
V66	γ1	126.43	0.27	125.93	0.09	126.23	0.17
I70	δ1	127.02	0.22	128.28	0.08	130.93	0.15
L77	δ1	125.77	0.41	126.71	0.18	129.00	0.43
L77	δ2	124.53	0.39	123.70	0.17	123.25	0.43
I86	δ1	125.35	0.17	124.72	0.06	124.27	0.12
I91	δ1	127.51	0.29	128.75	0.10	131.83	0.19
V95	γ1	126.75	0.45	126.99	0.15	127.72	0.28
V95	γ2	125.27	0.69	123.75	0.24	120.98	0.52
L97	δ1	125.17	0.46	124.80	0.20	125.26	0.46
L97	δ2	124.57	0.38	122.24	0.15	121.26	0.30
L98	δ1	124.22	0.15	123.37	0.06	122.55	0.12
L98	δ2	124.82	0.16	124.87	0.06	125.18	0.12
L99	δ1	125.64	0.24	126.53	0.08	128.41	0.16
L99	δ2	124.87	0.17	125.23	0.06	126.27	0.12
L103	δ1	126.21	0.22	127.86	0.08	130.66	0.17
L103	δ2	126.26	0.22	126.63	0.08	128.21	0.18
V108	γ2	129.45	0.41	131.23	0.14	135.04	0.28
V115	γ1	125.81	0.16	124.18	0.05	122.39	0.10
V115	γ2	127.39	0.27	128.90	0.08	131.31	0.14

Table S3.3: Fitting of nucleosome RDC at 1200 MHz. J_{CH} and RDC of H2B ILV labeled nucleosomes are fit with fit parameters and errors reported in Hz.

residue	methyl	J_{CH}	σ_{JCH}	c_{rdc} (10^{-6})	σ_{crdc} (10^{-6})	fiRDC	σ_{fiRDC}
V15	a	126.20	0.32	-0.63	0.32	-0.91	0.46
V15	b	126.10	0.25	-0.28	0.25	-0.40	0.35
I36	δ1	126.72	0.74	-5.39	0.82	-7.76	1.18
V38	γ1	125.57	0.52	-5.13	0.58	-7.39	0.84
V41	γ1	126.92	0.02	-3.77	0.02	-5.42	0.02
V41	γ2	126.40	0.31	-4.32	0.34	-6.23	0.49
L42	δ1	124.83	0.50	-4.79	0.53	-6.90	0.76
V45	γ1	126.48	0.46	-3.50	0.48	-5.05	0.69
V45	γ2	125.71	0.18	2.39	0.21	3.44	0.30
I51	δ1	125.22	0.67	-1.67	0.72	-2.41	1.04
I58	δ1	126.22	0.28	-1.57	0.32	-2.26	0.46
V63	γ2	125.84	0.58	5.34	0.65	7.69	0.94
V63	γ1	123.89	1.75	-1.75	1.99	-2.52	2.86
V66	γ2	126.87	0.77	-4.89	0.88	-7.04	1.27
V66	γ1	125.89	0.47	0.15	0.49	0.22	0.71
I70	δ1	125.23	0.47	3.87	0.49	5.57	0.71
L77	δ1	124.24	0.47	3.15	0.54	4.54	0.77
L77	δ2	124.87	0.55	-1.31	0.64	-1.88	0.92
I86	δ1	125.44	0.17	-0.84	0.19	-1.22	0.27
I91	δ1	125.18	0.52	4.52	0.55	6.51	0.79
V95	γ1	126.27	0.30	0.96	0.32	1.38	0.46
V95	γ2	127.03	0.36	-4.12	0.39	-5.94	0.56
L97	δ1	124.86	0.65	0.08	0.74	0.12	1.06
L97	δ2	124.70	1.40	-2.71	1.52	-3.90	2.19
L98	δ1	124.75	0.38	-1.62	0.42	-2.34	0.61
L98	δ2	124.60	0.16	0.37	0.18	0.53	0.25
L99	δ1	124.47	0.48	2.65	0.51	3.82	0.73
L99	δ2	124.26	0.48	1.31	0.51	1.88	0.73
L103	δ1	124.53	0.32	4.18	0.35	6.02	0.51
L103	δ2	125.20	0.74	1.91	0.81	2.76	1.17
V108	γ2	126.91	0.79	5.49	0.85	7.91	1.22
V115	γ1	126.72	0.35	-3.07	0.37	-4.42	0.53
V115	γ2	125.98	0.28	3.66	0.29	5.27	0.42

Table S3.4: Alternative rotamer scores I58 and L98. Q-scores calculated for 1kx5 and alternative rotamer conformations for residue I58 and L98. Top part contains RDCs for I58 and L98 where I58 and L98 are not used to determine the fit. Bottom part contains RDCs where I58 or L98 are used as input for the fitting. Lower Q-scores indicate a better fit for rotamers with rotation angles chi1 and chi2. Difference between predicted and observed RDCs is given by *Δ*RDC $\delta 1$ and *Δ*RDC $\delta 2$ for the $\delta 1$ and $\delta 2$ methyl groups. Residue I58 has a low *Δ*RDC for rotamer 1 indicating a good rotamer orientation. Residue L98 has a low *Δ*RDC $\delta 1$ but high *Δ*RDC $\delta 2$ for rotamer 5 indicating that this rotamer is not yet optimal.

Residue	rotamer	Qscore	χ_1	χ_2	*Δ*RDC $\delta 1$	*Δ*RDC $\delta 2$
I58	1kx5	0.629	-57.747	-60.222	9.0061	-
	1	0.167	-67.49	168.721	0.8862	-
	2	0.565	-63.798	-62.007	10.9017	-
L98	1kx5	0.563	-178.393	77.514	7.8581	3.6325
	1	0.259	-65.807	174.701	2.328	3.5788
	2	0.456	-176.776	60.264	6.9872	5.4286
	3	0.342	-89.898	50.281	1.6173	6.0666
	4	0.294	-153.615	-176.808	2.9115	4.2273
	5	0.222	-84.215	-55.973	1.587	2.8359
Recalculated fit						
I58	1	0.165	-67.49	168.721	0.6192	-
L98	5	0.204	-84.215	-55.973	0.7688	2.2026

Table S3.5: Stereochemistry assignments based on RDC, Sider and transferred peaks. Final stereochemistry is given together with the observed RDC. Predicted RDC based on a subset of only isoleucine or isoleucine and sider predicted leucine or all known stereochemistry. Input for predictions is indicated in gray. Confidence of stereochemistry assignment is given for less than 2 σ (dark green) and less than 4 σ (light green). When no assignment was possible values are indicated in red for more than 4 σ, or yellow if no assignment because two RDC's are too close to each other (less than one σ difference).

residue	methyl	RDC$_{\text{observed}}$	σ (hz)	RDC$_{\text{Pred}}$ ile	RDC$_{\text{Pred}}$ ile+leu	RDC$_{\text{Pred}}$ transfered
I36	δ1	-7.76	1.18	-7.76	-7.37	-7.42
I51	δ1	-2.41	1.04	-2.42	-2.22	-2.72
I58	δ1	-2.26	0.46	8.35	8.88	9.26
I70	δ1	5.57	0.71	5.57	6.65	6.99
I86	δ1	-1.22	0.27	-1.21	-0.76	-1.12
I91	δ1	6.51	0.79	6.50	6.44	6.61
L42	δ1	-6.90	0.76	-6.71	-6.09	-5.83
L42	δ2	-		1.82	1.76	1.78
L77	δ1	4.54	0.77	5.26	5.07	5.11
L77	δ2	-1.88	0.92	-2.33	-1.72	-1.63
L97	δ1	0.12	1.06	2.82	-0.05	-0.14
L97	δ2	-3.90	2.19	-5.83	-3.69	-3.30
L98	δ1	-2.34	0.61	6.84	7.52	7.84
L98	δ2	0.53	0.25	-6.44	-4.97	-4.58
L99	δ1	3.82	0.73	4.76	6.12	6.51
L99	δ2	1.88	0.73	2.20	2.24	2.22
L103	δ1	6.02	0.51	6.70	6.35	6.54
L103	δ2	2.76	1.17	-0.77	1.50	1.89
V38	γ1	-7.39	0.84	-4.42	-5.93	-6.33
V38	γ2	-	-	4.40	4.61	4.68
V41	γ1	-5.42	0.02	-4.70	-4.88	-4.57
V41	γ2	-6.23	0.49	-3.89	-4.86	-5.56
V45	γ1	-5.05	0.69	-2.08	-2.76	-3.40
V45	γ2	3.44	0.30	4.91	4.40	4.54
V63	γ1	7.69	0.94	7.98	5.91	5.92
V63	γ2	-2.52	2.86	-4.38	-4.45	-5.10
V66	γ1	-7.04	1.27	-5.31	-6.21	-6.76
V66	γ2	0.22	0.71	0.17	0.36	0.30
V95	γ1	1.38	0.46	4.41	1.72	1.51
V95	γ2	-5.94	0.56	-5.15	-4.45	-4.08
V108	γ1	-	-	-2.90	-2.63	-3.18
V108	γ2	7.91	1.22	7.32	7.96	8.31
V115	γ1	-4.42	0.53	-2.51	-3.80	-4.48
V115	γ2	5.27	0.42	4.45	4.77	4.83

Table S3.6: RDC fit and model scores.

Measured	Q-score	Da (10^{-4})	Dr (10^{-4})	R
1xk5 chain D	0.771	0.92	0.46	0.504
3lz0 chain H	0.438	-1.12	-0.61	0.547
7ohc chain D	0.436	-0.95	-0.46	0.486
1xk5 -I58,L98	0.166	-1.17	-0.43	0.364
3lz0 -I58,L98	0.414	-1.15	-0.67	0.579
7ohc -I58,L98	0.203	-1.09	-0.42	0.386
assigned				
1kx5 single chain	0.217	-1.17	-0.42	0.355
1kx5 both chains	0.233	-1.17	-0.40	0.345
Predicted				
closed	-	-	-	0.501
straight	-	-	-	0.662
open	-	-	-	0.357
assymetric	-	-	-	0.630

Table S3.7: *Xenopus laevis* H2B ILV nucleosome assignment. Nucleosome residue and stereospecific assignment for Xl. ILV labeled nucleosomal H2B. Notations a and b indicate an unknown stereospecific assignment.

Residue	group	^{13}C (ppm)	^{1}H (ppm)
V15	a	20.988	0.961
V15	b	20.286	0.973
I36	δ1	14.439	0.82
V38	γ2	21.98	1.151
V38	γ1	22.21	0.977
V41	γ1	21.528	1.047
V41	γ2	23.627	1.356
L42	δ1	23.364	0.907
L42	δ2	26.525	0.745
L42*	δ2	26.457	0.712
V45	γ1	21.286	0.921
V45	γ2	19.624	1.069
I51	δ1	12.896	0.699
I58	δ1	14.124	0.985
V63	γ2	22.375	1.083
V63	γ1	22.102	0.139
V66	γ2	22.651	0.544
V66	γ1	22.177	0.667
I70	δ1	13.727	0.606
L77	δ1	26.866	0.605
L77	δ2	24.757	0.584
I86	δ1	13.539	0.709
I91	δ1	7.133	0.338
V95	γ1	23.105	1.075
V95	γ2	24.918	1.192
L97	δ1	26.057	0.46
L97	δ2	22.33	0.546
L98	δ1	26.076	0.824
L98	δ2	24.654	0.863
L99	γ1	25.559	0.933
L99	γ2	24.826	0.934
L103	δ1	25.484	1.007
L103	δ2	23.755	1.043
V108	γ1	20.343	0.933
V108	γ2	22.408	1.145
V115	γ1	22.125	1.163
V115	γ2	24.26	1.289

4

Methyl-TROSY NMR observation of ionic strength dependent nucleosome clustering

Based on the manuscript: **Lobbia, V. R.** & van Ingen, H. Methyl-TROSY NMR observation of ionic strength dependent nucleosome clustering. *in preparation*

Abstract

Chromatin plays a vital role in expressing, replicating, and repairing DNA. The compaction of chromatin influences these processes by changing available binding sites for related proteins. How strongly chromatin is compacted is influenced by the concentration of Na^+, K^+ and Mg^{2+} ions. This study investigates which ions give the highest quality nucleosome NMR spectra and observe ionic strength dependent changes to nucleosomes structure and compaction. We applied nuclear magnetic resonance to study nucleosomes with mono- and divalent ions using a methyl labeling approach. An increase from 25 to 75 mM in ionic strength resulted in a more than 50% decrease in core residue signals but did not decrease the tail residue signal. Na^+ ions decreased spectral quality more than K^+ ions. The signal loss is not caused by precipitation, the presence of µs-ms dynamics, or the presence of exchange broadening and point to an increase in effective size of the nucleosome particle due to tail DNA interactions between nucleosome particles. We estimate that nucleosomes cluster with 2-3 nucleosomes at 50 mM NaCl or 75 mM KCl. Additionally, we identify a specific binding site for Mn^{2+} on the acidic patch and identify the H2B tail to interact with nucleosomal DNA. To improve spectral quality, we recommend the use of KCl instead of NaCl for NMR studies of the nucleosome and suggest Mn^{2+} titrations as a viable tool to study histone tail dynamics.

Introduction

Chromatin is a vital structure in eukaryotes as it compacts DNA and thus performs an important role in regulating DNA expression, replication, and repair. Chromatin interacts with a wide array of proteins and study of these interactions is key to understanding regulation of chromatin function [1–4]. Variations in chromatin compaction and chromatin modifications alter how proteins interact with the DNA and locally or globally change the outcome of DNA expression, replication, and repair. As the smallest unit of chromatin, the nucleosome is formed by wrapping 147 base pairs (bp) of DNA around two copies of each of the four histones proteins: H2A, H2B, H3 and H4. The nucleosome consists of a globular core, and flexible tails. The globular core consists of the structured parts of the histones and DNA, while the flexible tails consist of the N-terminal ends of the histones and the C-terminus of H2A.

Large advancements have been made in the last couple decades to study both chromatin and the nucleosome in silico, in vitro, and in vivo. One of these advancements is the development of methyl TROSY (Transverse relaxation-optimized spectroscopy) solution NMR[5]. For a long time, solution NMR had been limited by the increased relaxation in large systems, resulting in a poor signal. Methyl TROSY NMR allows for the selection of more optimal relaxation pathways which has been successfully applied to study protein complexes up to 1 MDa [1,6,7], including the nucleosome with binding partners[1,2,8–10]. The methyl TROSY approach is applied in combination with a specific methyl labeling approach, where only a single methyl group is labeled while the rest of the protein is deuterated to further reduce negative contributions to relaxation.

While this approach results in spectra of superior quality[1,11] under low ionic concentrations (~25mM), we and others[2,8–10,12] have noticed that this quality rapidly degrades when higher ionic strengths are applied. Factors that could contribute to reduced quality of the NMR signal are ionic strength induced conformational changes or a change in rotational correlation time (τ_c) due to intermolecular interactions between nucleosomes. A change in dynamics in the µs-ms range could occur when the nucleosomal DNA or the core opens and behaves more dynamically. Salt induced nucleosome opening is suggested to have a stepwise process: first the interactions between the H2A-H2B dimer and H3-H4 tetramer are weakened, and then the DNA unwraps[13,14]. The weakening of interactions between the different components of the nucleosome suggests that increased ionic strength could increase dynamics within the nucleosome by weakening electrostatic interactions. Additionally, dynamic regions have been reported in the nucleosome core where nucleosome dynamics were required for the ATPase remodeler ISWI to function[2]. In several cases either monovalent or divalent ions need to be present for nucleosome binding partners to have a stable binding or enzymatic activity[15].

Nucleosomes can compact and form higher order structures either through inter-nucleosome contacts or with the help of other proteins such as H1 or HP1[4]. Inter-nucleosome contacts can occur through interactions between either the globular core and the flexible tails, the globular core and DNA or the flexible tails and DNA. The acidic patch can bind N-terminal H4 tail of the nucleosome and is thought to play an important role in the formation of higher order nucleosome structures[16,17]. Similar observations have been made with the H3 nucleosome tail[18,19]. In compacted nucleosome arrays both H3 and H4 tails were found to remain mobile[20,21] and can potentially still interact with other binding partners. Histone tails are important for the wrapping of the nucleosome DNA ends and influence nucleosome stability and compaction[14,22–24].

A factor influencing nucleosome compaction is the concentration of monovalent and divalent cations, which can cause higher order compaction of nucleosomes[25–27]. Monovalent cations efficiently compact nucleosome arrays. While earlier reports did not indicate that they compact mononucleosomes to a more dense phase[28], more recent reports show compaction is possible under physiological ionic concentrations if there is a sufficiently high concentration of mononucleosomes[29]. A monovalent cation concentration above 500 mM can promote unwrapping of DNA from the nucleosome core and dissociation of the nucleosome core[14,30,31]. Between 100-500 mM monovalent cations can cause unwrapping of DNA ends[32–34] and increased accessibility of histone tails[35–37], while keeping the mononucleosomes in an soluble non-crystalline phase[38]. At low concentration of monovalent cations DNA ends and tails are thought to be bound to the nucleosome core[39,40], with ion concentrations depending on the DNA length[37]. Under these conditions nucleosomes will repel each other through a net negative electrostatic charge because not enough ions are present to shield the negative charge between the DNA of two nucleosomes[41] .

Divalent cations compact both arrays and mononucleosomes, with higher efficiency for arrays[26,42]. Divalent cations behave differently in combination with different monovalent salts. When Magnesium is used to compact nucleosome arrays, sodium will improve compaction while potassium either decrease or reverts part of the compaction[27]. Without magnesium both sodium and potassium ions cause compaction of arrays. This highlights the importance of the buffer conditions used in studying nucleosomes, as the absence or different concentration of an ion can influence the experimental outcome. Applying physiological buffer to study nucleosomes with cytosol and nucleoplasm mimicking ionic concentrations (10 mM Na^+, 100-150 mM K^+ and 0.5-10 mM Mg^{2+})[43,44] can be applied to reduce biases. However, these ionic concentrations might interfere with some methods used to study nucleosomes and chromatin.

In this study, we quantify the effects of both monovalent and divalent cations on the *Xenopus laevis* (*Xl.*) nucleosome NMR spectral quality and related parameters. We chose to observe histone H2B in the nucleosome because this residue has multiple isoleucine, leucine and valine (ILV) residues in the interaction dimer tetramer interface. We observe improved NMR signal intensity for KCl compared to NaCl at comparable concentrations. Manganese titrations identify specific binding sites on DNA near H2B residue I36 and on the acidic patch. Manganese titrations indicate the H2B tail to be bound to nucleosomal DNA. We therefore recommend using KCl instead of NaCl for NMR studies with nucleosomes and suggest Mn^{2+} as an alternative way to study binding of nucleosome tails to DNA.

Materials and Methods

DNA and histone expression and purification and nucleosome reconstitution

Production and purification of histones and DNA, and reconstitution of nucleosomes were performed as described in chapter 3.

Reconstitution of H2A-H2B dimers

Dimers were refolded as described in Dyer et al[45]. In brief, histones were mixed in equimolar ratio in denaturing buffer (7 M urea, 50 mM Tris, 100 mM NaCl, pH 7.5). This mixture was then dialyzed to high salt buffer (2 M NaCl, 10 mM Tris, 1 mM EDTA) at 4 °C and purified using gel filtration (S200) to obtain pure dimers. Dimers were dialyzed against either NaPi or KPi NMR buffer containing either 20 mM KPi or 20mM NaPi, pH 6.2 and 0.01% NaN_3, 100% D_2O, ionic strength (I) = 25 mM.

Solubility assay

Solubility of nucleosomes was screened at different concentrations of nucleosomes and different salts (NaCl or KCl) using optical absorbance (A_{260}). Nucleosomes in NMR buffer were adjusted to the desired salt concentration using NMR buffer containing either NaCl or KCl. Samples were mixed and incubated at RT for 1h, spun at 17.000 x g to remove precipitates and then measured. The supernatant was mixed with DNA loading dye and tested on 5% native gels (acryl-bisacrylamide 59:1, 0.2 x TBE buffer) and run in 0.2 x TBE buffer (18 mM Tris-Borate, 0.4 mM EDTA, pH 8.3) to confirm the presence of intact nucleosomes. Native gels were pre-run at 120V for 1 hour and then run with samples at 120V for an hour. Gels were first stained with GelRed to stain DNA and then Coomassie to stain proteins.

Thermal shift assay

Nucleosomes melting curves were measured at a concentration of 1 µM and 10x Sypro Orange in NaPi NMR buffer with varying salt concentrations (0, 50,100,150, 200, 250 mM NaCl) using a Bio-Rad MyiQ single color real-time PCR detection system. A gradient temperature from 25 to 95°C was used with 0.5°C decree steps and 20 second waiting time per step. Fluorescence was recorded using 485 nm excitation and 575 nm emission and analyzed using Bio-Rad MyiQ 2.0 software. The software was used to determine the melting temperature by calculating the derivative of the melting curve and obtaining the first inflection point of the curve (first state transition).

Resonance assignment of Xl. H2B ILV methyl groups in H2A-H2B dimer

Initial assignments of ILV methyl group resonances in the *Xenopus laevis (Xl.)* H2B in the H2A-H2B dimer were based on assignment transfer from the available assignments of the Xl. nucleosome H2B chemical shifts (chapter 3). To confirm and complete the assignment 3D methyl-TROSY (h)CCH NOESY were recorded with acquisition times t_1, max 8 ms, t_2, max 8 ms and t_3, max 67 ms, total measurement time 3 days, and with 200 ms NOESY mixing time on nucleosome sample with ILV-labeled H2B. Assignments were made using MAGMA 1.2.3[46] and verified manually by comparing the experimental NOE network to the methyl-methyl distances in the 1KX5 nucleosome crystal structure[47].

Salt effect and relaxation NMR experiments

All NMR experiments were recorded on an Avance III 600 MHz spectrometer with 5 mm room-temperature probe. Nucleosomes were measured at 85 μM nucleosomes with NaCl, 90 μM with KCl, and 76 μM with MnCl2. Titrations with H2A-H2B dimers were performed in KPi NMR buffer at 324 μM with stepwise additions of MnCl2 (0-1mM) at 25°C. Salt effects were measured by recording SOFAST methyl-TROSY HMQC spectra of nucleosome in NaPi NMR buffer with stepwise addition of NaCl (0-100mM) at 25 and 45°C. Nucleosomes were then buffer exchanged to KPi NMR buffer to remove Na+ ions and titrated with stepwise additions of KCl (0-100mM) at 25 and 45°C. Finally, nucleosomes were buffer exchanged to KPi NMR buffer and titrated with stepwise addition of MnCl2 (0-1mM) at 45°C.

To measure R_2 rates, nucleosomes in NaPi NMR buffer at either 0 or 25 mM NaCl were measured at 45 °C using methyl TROSY CPMG relaxation dispersion experiments to obtain single quantum 1H rates and methyl TROSY CPMG relaxation dispersion experiments centered at either Ile of Val/Leu residues to obtain multiple quantum ^{1}H,^{13}C R_2 rates[48]. For each experiment, the total time of the CPMG element was set to have 60% of the signal remaining (Trelax = 10 ms). All spectra were processed using NMRPIPE (version 10.6) using one times zero filling, forward linear prediction in the indirect dimension and cosine-squared window functions. R_2 experiments were further analyzed using PINT[49] to integrate line shapes and calculate R_2 values. Solvent accessible surface area (SASA) was calculated based on 1kx5 using POPScomp[50], with the parameters of atomistic resolution and a solvent radius set to 1.4 Å.

HydroNMR calculation correlation times

Multiple nucleosome structures and complexes were obtained from the PDB with either bound or open DNA ends (Table S1). All non-histone proteins were removed when complexes with a binding partner were used. For 1kx5 all histone tails were removed using pymol to generate a tail-less nucleosome model, to match the other structures and to remove bias from a single histone tail conformation on the calculated correlation time. For 3lz0 nucleosomes with longer DNA ends with 10 additional base pairs on both ends were generated. Additional DNA was generated using 3DNA and added to the model using pymol. For several pdb structures obtained using X-ray crystallography, crystal symmetry was used to create di-nucleosome and tri-nucleosome models with nucleosomes having acidic patch-H4 tail interactions. All structures and models were analyzed using HydroNMR (nsig: -1, viscosity 0.892 cP for 25 °C and 0.597 cP for 45 °C) to estimate correlation times at 25 or 45 °C.

Results and discussion

Nucleosomes remain soluble and stable at elevated ionic strength

Nucleosomes used for this study were reconstituted in vitro from perdeuterated Xenopus laevis (Xl.) histones with ILV-labeled histone H2B and a 167 bp DNA fragment corresponding to the Widom 601 strong positioning sequence[51]. We screened nucleosome solubility up to 300mM NaCl (Fig. 4.1a) and at varying nucleosome concentrations including concentrations used in NMR experiments (Fig. 4.1b) by measuring DNA concentration after rigorous centrifugation. These screens did not show a decrease in solubility, in agreement with other works[29,52]. However, nucleosome melting temperature of the first state transition decreased by 4 °C at higher ionic strength, suggesting a decrease in nucleosome stability (Fig. 4.1a and S4.1).

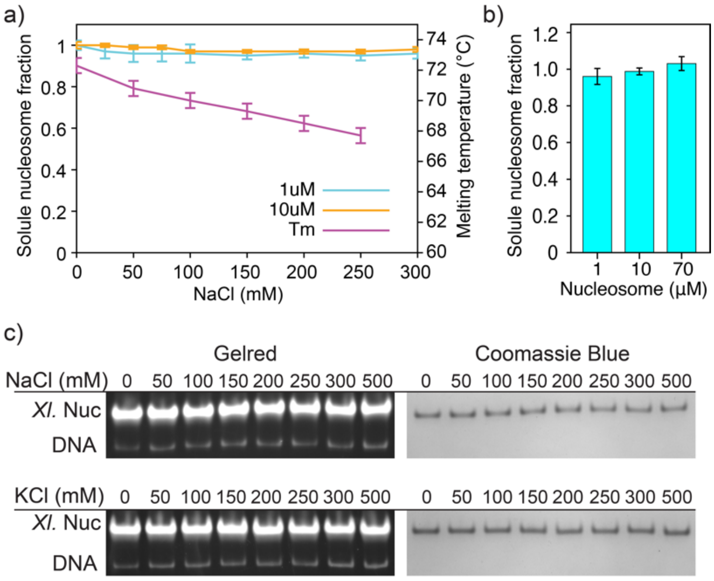

Figure 4.1: Nucleosomes remain soluble and stable over a large range of salt concentrations. a) Solubility and stability of nucleosomes as function of salt concentration. Soluble nucleosome fraction was determined over a range of salt concentrations showing no decrease of nucleosomes in the soluble fraction (n=3). Nucleosomes show a decrease in thermal stability upon addition of NaCl indicated by the drop in melting temperature (n=3). b) Nucleosome solubility at 75 mM NaCl with varying nucleosome concentrations including NMR sample conditions (70 µM, n=3). c) Native PAGE (5%) of nucleosomes at concentrations between 0 and 500 mM NaCl or

KCl shows no indication of disassembly or precipitation upon addition of NaCl or KCl. Gels were stained with GelRed Nucleic Acid Stain for DNA and Coomassie Blue for protein.

This decreased stability is expected as the DNA–histone interactions are mostly electrostatic. Release of soluble DNA due to nucleosome disassembly will give a false indication of nucleosome concentration as DNA has a much larger contribution to A260 absorption than the histones. We therefore also tested nucleosome solubility using native PAGE which can be used to detect both DNA and protein. We detect both nucleosomal DNA and proteins to remain in the soluble fraction without releasing additional free DNA up to the highest tested concentration of 500 mM NaCl or KCl (Fig. 4.1c) and remain folded in a nucleosome sized particle.

Increase in ionic strength decreases nucleosome core NMR signal intensity

Next, we investigated how monovalent salts affect the NMR signal of nucleosomes by performing titrations with nucleosomes and either NaCl or KCl and recording methyl TROSY HMQC experiments. The spectrum of nucleosomal H2B gives a well resolved spectrum for the isoleucine, leucine, and valine (ILV) methyl groups for both the NaPi and KPi NMR buffer at 0 mM salt (Fig S4.2). Assignments for the nucleosomal H2B ILV methyl groups were transferred from data in chapter 3.

At initial low ionic concentrations (I = 25 mM), methyl residues give intense signals for all resonances. The signal intensity of the ILV peaks is severely decreased upon the addition of monovalent ions (Fig. 4.2a and b), specifically, for the nucleosome core residues but not for the histone tail residue (V15). The decreased signal is not due to degradation or precipitation of the nucleosome as it is fully reversible by removing the added ionic strength (Fig. S4.2) and remains soluble (Fig. 4.1). A larger decrease in peak intensity is observed with higher monovalent ions concentrations, lower temperatures and for Na^+ compared to K^+ (Fig. 4.2b). We find that K^+ ions at both 25 and 45 °C have more signal than Na^+ ions at 25 or 45 °C independent of concentration. At 125 mM ionic strength, the nucleosome core has up to 2.7 times the intensity for K^+ compared to Na^+ at 25 °C. Monovalent salts up to 125 mM ionic strength were tested after which measurement times became too long to obtain observable signals within a reasonable timeframe.

An ion specific decrease in signal fit with observations that Na^+ concentration is a higher driving force for nucleosome compaction than K^+ concentration[27]. Na+ has a higher charge density than K^+. Extrapolating the charge density with our findings we hypothesize Li^+ to more detrimental to the NMR signal while Rb^+ or Cs^+ could potentially be less detrimental. Nucleosomes crystals have been observed to bind Rb^+ and Cs^+ ions[53,54] at similar sites as Mn^{2+} and Mg^{2+}. The type and concentration of ions present can change the amount of twist in DNA with a higher twist corresponding with a lower charge density except for Li^+ ions[55,56]. How this translate to the nucleosome structure is not clear yet.

No chemical shift perturbations were observed during titrations making it unlikely conformational changes occurred in the nucleosome core (Fig. 4.2a and S4.3). Additionally, we measured R_2 rates using CPMG relaxation dispersion experiments at 0 and 25 mM NaCl where sufficient signal remained for the experiment. When NaCl concentrations are increased to 25 mM ^{1}H R_2 increased by 1.27 and ^{13}C R_2 increased by 1.25 for the nucleosome H2B globular core residues, while for the tail ^{1}H R_2 decreased by 0.89 and ^{13}C R_2 increased by 1.08 (Fig. 4.2c). These values agree with the observed changes in NMR intensity where the core residue intensities decreases but the flexible tail residue intensities do not. From the relaxation dispersion measurements, we do not observe exchange in the ms-μs timescale for H2B ILV residues in the nucleosome in both the absence and presence of 25mM NaCl (I = 25-50 mM) (Fig. S4.4). Kitevski-LeBlanc et al. report that the nucleosome had μs-ms dynamics in H2B (residues I58, L77, L97, L98, I66) only when the nucleosome was destabilized by mutations in the dimer tetramer interface, but not for wild type nucleosomes (I = 22mM)[11]. Because we do not observe a change in μs-ms dynamics after increasing the ionic strength, we μs-ms dynamics to be the cause of the observed decreased signal intensity. However, our CPMG measurements were recorded with 1 kHz for ^{1}H and 2 kHz for ^{13}C dynamics, and we cannot exclude if there were much faster dynamics present. Some residues have much larger R_2 rates then their neighboring residues suggesting that indeed faster dynamics could be present (Fig. S4.4), but no change is seen increased ionic strength. It is also not possible to exclude dynamics in other parts of the nucleosome as our study focused on H2B.

A decease in NMR signal can be caused by conformational changes or a change in rotational correlation time (τ_c) due to intermolecular sticking. Our data exclude conformational changes in the histone globular core. Two other conformational changes that can occur due to changes in ionic strength are extension of histone tails from the nucleosome core and unwrapping of DNA ends. Histone tails and DNA are known to become more accessible with increased in ionic strength. However, both DNA ends, and histone tails are thought to be bound to the nucleosome core below 50 mM monovalent cations[32–34,36,38]. It is therefore less likely that extension of histone tails or DNA unwrapping are the only cause of the loss of signal.

This leaves an increase of τ_c to explain the loss of signal at increased ionic strength. The τ_c would increase when the viscosity of the buffer increases or the nucleosome starts to behave like a larger particle by interacting. The increased viscosity due to the added ions is negligible for the tested range for all tested ions (less than 0.1%) and therefore needs to be caused by intermolecular interactions.

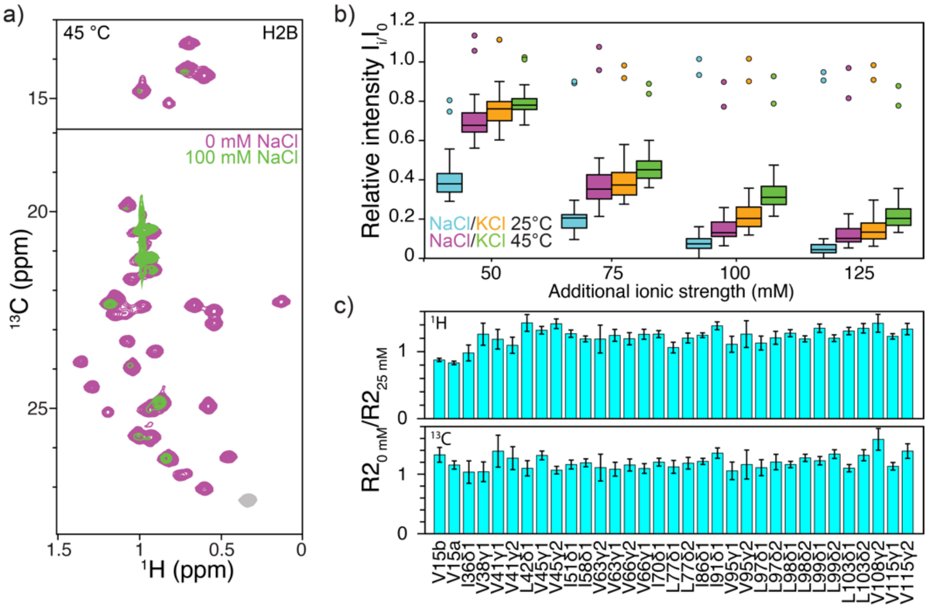

Figure 4.2: Na$^+$ ions cause a stronger decrease in NMR signal then K$^+$ ions. a) Overlay of methyl TROSY spectra at 0 mM and 100 mM NaCl show a decrease of NMR signal at higher ionic strength. b) Relative intensity of nucleosomal H2B ILV signals at varying ionic strength compared to nucleosomes with only NaPi or KPi buffer (I_{buffer} = 25 mM) at their respective temperatures. Addition of NaCl or KCl result in a decrease of NMR signal from H2B core ILV residues (boxes), but not for the H2B tail (circles). c) Ratio for ^{1}H and ^{13}C R_2 between 0 mM and 25 mM added NaCl. The ^{1}H and ^{13}C R_2 for ILV core residues increases upon addition of 25mM NaCl.

The H2A-H2B dimer and DNA remain bound at increased ionic strength

Nucleosomal DNA ends unwrap with increasing concentration of NaCl. Unwrapping of DNA ends is dynamic and ~2-10% nucleosomes are unwrapped between 0.04 and 0.15M NaCl[57]. Unwrapping occurs with a rate k_{12} of 4 s^{-1} and wrapping with a rate k_{21} of 20-90 s^{-1} (I ~ 25 mM)[58]. Nucleosomes have been suggested to unwrap asymmetrically from the side with less flexible DNA preferentially and unwrapping stabilizes the other side[59,60]. Asymmetric opening of the core would be expected to result in multiple chemical shifts if they are not time averaged. We do not find any chemical shift perturbations indicative of release of or binding to the nucleosome core.

To further investigate residue specific effects of monovalent salts on the nucleosome we first wanted to identify which residues can be used as probes to identify if DNA linker ends are unwrapped from the nucleosome and if H2A-H2B dimer remains properly attached to the nucleosome. We compared nucleosome spectra at different temperatures and compared nucleosomal and H2A-H2B dimer spectra to identify these probes.

Intensities of H2B ILV residues in the nucleosome decrease by 80% in overall signal compared to H2B ILV residues in the dimer, scaled for concentration and copies of H2B and the same processing (Fig. 4.3a). Residue V15, which is flexible in both dimer as nucleosome conformation, shows an average drop of 40% in intensity. This can be attributed to the increase of tumbling of the whole molecule due to a tenfold increase of size. It is unlikely that there are any large contribution of other factors contributing as the V15 peak shows no significant shift between the dimer and nucleosome indicating that its chemical environment remained the same (Fig. S4.5). Therefore, we most likely are only observing the unbound fraction of V15 if any is bound. The globular core residues have a larger drop in intensity that the tail (80%) and can be contributed to the tail residue being more mobile and thus being more disconnected from globular core of the nucleosome.

Incorporation of dimer into the nucleosome creates several new interaction surfaces that were previously exposed to the solvent. ILV residues in these regions are I58, L77 and L97 contacting H4 and I36 is near the DNA superhelix 5. Residues I36, I58, L77 and L97 have a strong decrease in intensity with chemical shift perturbations occurring for I58, L77 and L97. While, I36 does not have a large chemical shift difference between dimer and nucleosome it is close to the protonated DNA. This will result in a significant contribution of cross correlated relaxation between I36 and the DNA protons, causing faster relaxation and a lower intensity. Because these residues have large intensity differences and perturbations between a dimer and nucleosome state, I36 will be a good probe to determine if DNA is unwrapping from the histone core, while I58, L77 and L97 are good probes for dimer-H4 interactions.

Similarly, lowering the temperature decreases the signal intensity of residues I36, L77, and L97δ1 more than other residues (Fig. 4.3b). A decrease from 45 to 25 °C does not cause a significant decrease in intensity for the tail residue V15, as is expected since it is dynamic at both temperatures. The decrease in temperature caused an average decrease in intensity of core residues by ~40%. In comparison, intensity of residue I36 decreases by ~75% (Fig. 4.3a, b), indicating a more dynamic interaction with or closer proximity of protons to I36 at a lower temperature. Therefore, at 45 °C the DNA would either need to be more unwrapped or more breathing of DNA near I36 should occur compared to 25 °C.

If we assume that the decrease of residue I36 signal below the average decrease in intensity of the core residues is because of proton-proton cross-relaxation, we can estimate an upper limit to the movement of DNA due to temperature change. The strength of the proton-proton cross-relaxation scales with $1/r^6$ and primarily the closest protons will have the largest effect on the intensity. Using this scaling factor and considering all DNA protons within a range of 10 Å of I36 we determined the average effective DNA-I36 proton distance to be 1.95 ± 0.11 Å (1kx5, 3lz0 and 7ohc). A minimal change of 0.24 ± 0.01 Å is found to be sufficient to change the proton-proton cross-relaxation by 50%. The change in histone DNA distance required to explain the change in intensity in case of DNA proton cross-relaxation is very small and suggests DNA remains bound to the nucleosome core near I36.

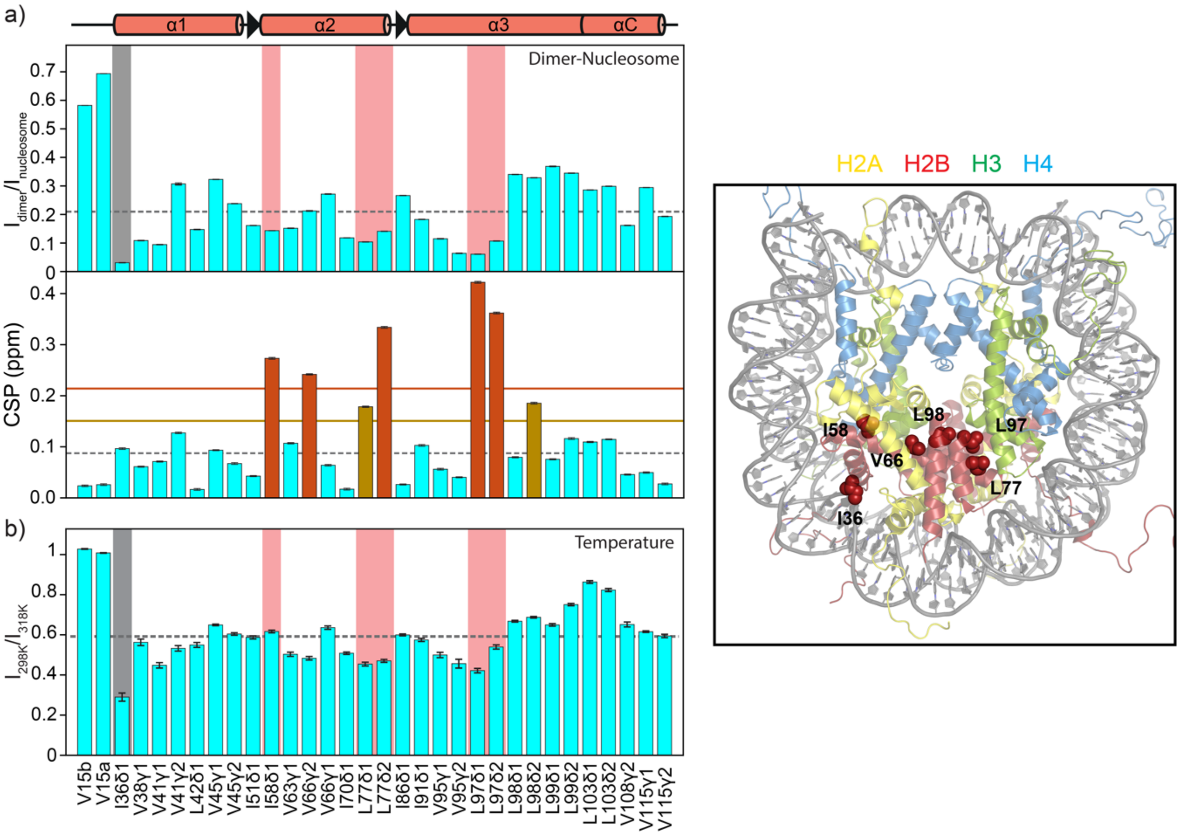

Figure 4.3: H2B probes for nucleosome structure. a) Incorporation of H2A-H2B dimer into a nucleosome show larger loss of signal for core residues compared to tail. Dotted line represents the 10% trimmed mean of intensity loss or chemical shift perturbation (csp) of all residues, the yellow line represents 1 standard deviation form average and the red line two standard deviation from average. b) H2B signal intensity ratio after the temperature is lowered from 45 to 25 °C. Colored background boxes indicated that those residues are in the interaction interface with DNA (gray) and H4 (red). Residues with large chemical shift perturbations are shown on the structure of 1kx5.

Salt titrations show a lower variation in core intensities ratios compared to changes in temperature or incorporation of the H2A-H2B dimer into a nucleosome (Fig. 4.4). Both NaCl and KCl show a similar pattern in intensity changes for all residues (Fig. 4.4a, b). Residues V41γ1 and L97δ1 have the strongest decrease in signal intensity for both NaCl and KCl titrations, while V45γ1 and L98δ1 have the weakest decrease in signal intensity. Visualizing the decrease in intensity on the H2B structure (1kx5) shows that primarily residues in the H2A-H2B dimer handshake motif near the H2A α2 helix exhibits the largest decrease. This indicates that the observed variations occur due to changes in the dimer. Titrations with NaCl or KCl at either 25 and 45 °C do not show any intensity change for residue I36 nor are large differences seen for L77 and L97δ2. This indicates that, within the tested range, increased ionic strength does not result in an increased unwrapping of DNA or the detachment of the H2A-H2B dimer from the nucleosome.

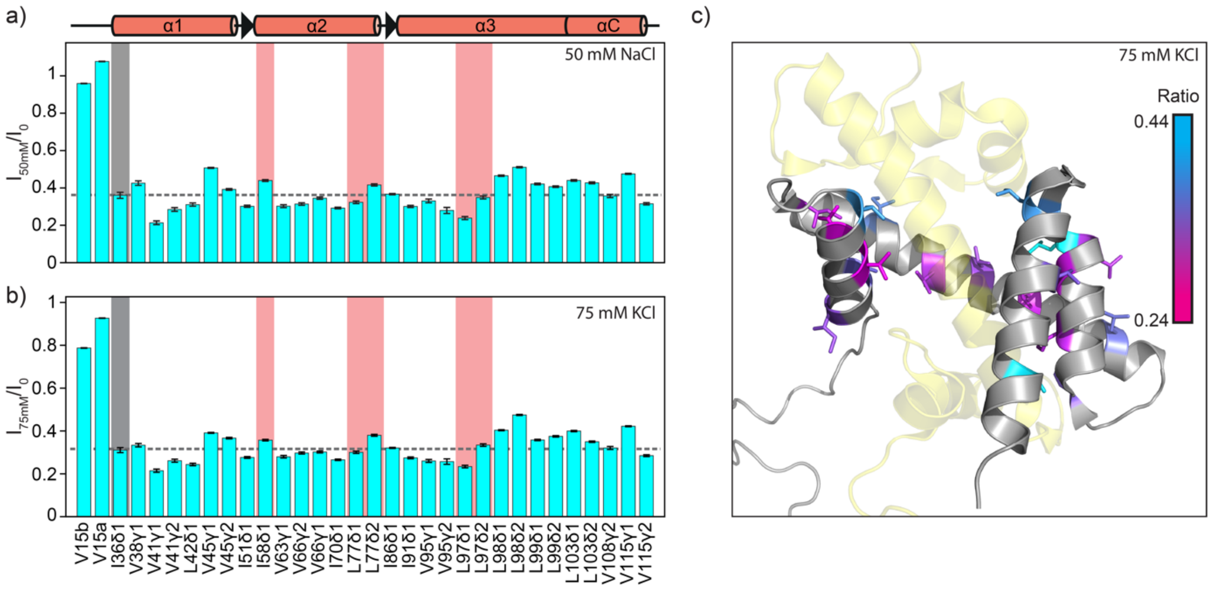

Figure 4.4: Residue specific intensity difference upon adding monovalent salts. Comparison between absence and presence of NaCl (a) and KCl (b) at 45 °C. Intensity ratios for 50 mM NaCl and 75 mM KCl plots are shown as they have a similar drop in overall signal intensity. Colored background boxes indicated that those residues are in the interaction interface with DNA (gray) and H4 (red). c) Intensity ratios for 75 mM KCl are shown on the nucleosomal H2B structure (1kx5) for the globular core, with H2A show in yellow and other histones and DNA not shown. Most of the residues with the strongest decrease in intensity are in the core of the H2A-H2B dimer near the H2A α2-helix.

Nucleosome rotational correlation time increases due to intermolecular interactions

Inter-nucleosome interactions can occur through nucleosome tail and DNA-core interactions[61]. At low ionic strength interactive forces between nucleosomes remain repulsive, with histone tails becoming more extended with increased ionic strength[37] by charge neutralization[62]. These tails could then interact with other nucleosome particles and increase the τ_c. This could explain why Na^+ causes more signal loss than K^+ because Na^+ has a higher charge distribution and could more effectively neutralize the charge[63].

To gain more insight in the reason behind the potential increase in τc we calculated the τc of multiple possible states of the nucleosome (Table S4.1). Specifically, we investigated nucleosomes with and without linker lengths, different unwrapped states of the nucleosome and multimerization of nucleosomes (Table 4.1). Our predicted τ_c of the nucleosome matches with reported τ_c for MNase digested nucleosome core particles (120 ns at 44 °C)[64], nucleosome core particles (194 ns in D_2O at 20 °C)[65] and for nucleosomes with 167 bp DNA (150 ns at 45 °C) (LEK, HVI, unpublished data).

The τ_c calculated at 45 °C is 37% lower than the τc at 25 °C (Table 4.1), which matches with the ~40% average decrease in signal observed for the nucleosome (Fig. 4.3a). The τ_c calculated for the dimer is 88% lower than the τ_c for a nucleosome with 167 bp DNA, which matches with the ~80% average decrease in signal observed between the dimer and nucleosome (Fig. 4.3b).

Two options by which the nucleosome could increase its τ_c are by unwrapping of DNA where the DNA stays rigid and through inter-nucleosomes interactions forming larger particles. The τ_c calculated for nucleosomes with unwrapped DNA ends is higher than wrapped nucleosomes and increases with increased unwrapping DNA ends, while considering the DNA ends rigid and without dynamics. Opening of DNA however is not a rigid event but dynamic[57]. Increasing ionic strength will decrease the persistence length of DNA[66], increasing DNA flexibility. Therefore, the real τ_c will be lower.

We do not expect opening of the nucleosome beyond SHL5 based on I36 intensity. Opening of DNA ends on both sides till ~124 bp is at maximum expected to result in a 30% signal loss based on τ_c, considering rigid opening of the DNA ends. We observe a larger signal loss (> 60%) with increasing ionic strength than is possible based on linker DNA opening. Additionally, we found in chapter 3 that at 45 °C nucleosomal DNA experience unwrapping from the nucleosome a low ionic strength (I = 25 mM). This lowers a possible contribution of DNA unwrapping due to increased ionic strength to the signal loss. Therefore, we exclude DNA unwrapping as the major contribution to the signal loss at higher ionic strength.

The τ_c of interacting nucleosomes is more difficult to predict, because the unspecific interactions that histone tails can form with DNA or the histone core likely result in a network of nucleosomes that are dynamically linked together. To simplify, we considered two (di-) or three (tri-) nucleosomes linked together as is observed in the crystal packing of nucleosomes. Di-nucleosomes have on average a 2.1-fold increase in τ_c while tri-nucleosomes had a 3.6 fold increase (Table 4.1). With a decrease in signal of 61% for nucleosomes with 50 mM NaCl (Fig. 4), we would expect between two and three nucleosomes to interact together (τ_c ~292 ns (closed linker DNA) - ~420 ns (open linker DNA)).

Signal loss for both Na^+ and K^+ ions was observed to be temperature dependent (Fig. 4.2b). Histone tails have been found to remain attached to the nucleosome at temperatures up to 45 °C at low ionic strength, but detach at higher temperatures[67]. It is thus possible that the increased temperature weakens nucleosome-tail interaction, causing less slow tumbling particles to form and results in retaining more signal. This highlights the importance of temperature used for measurements nucleosomes at physiological conditions as their interaction weakens at higher temperature.

Table 4.1: Predicted rotational correlation times (10^{-9} s) for multiple nucleosome states and dimer. Full list in table S4.1

	DNA (bp)	45 °C	25 °C
1kx5 with tails	147	144.6	237.6
Tailless nucleosomes	147	86.5	142.2
Tailless nucleosomes	167	110.1	180.9
DNA open till SHL5	167	172.0	282.6
Two nucleosomes	147	189.9	312.1
Two nucleosomes	167	230.8	379.3
Three nucleosomes	167	392.8	645.6
H2A-H2B dimer	0	13.6	22.3

Manganese ions localize to the DNA and acidic patch

Next, we investigated the effect of divalent ions on the NMR spectrum. Often magnesium ions are added for biochemical assay as they can be required for enzymes to function or are present in the cellular environment. Addition of magnesium ions to nucleosomes causes reversible phase separation and excludes nucleosomes from the dilute phase into a condensed phase[26,68]. With solution NMR we only observe molecules that tumble fast enough and remain within the detection coil of the NMR machine. We expect a decrease of signal because of Mn^{2+} induced phase separation of nucleosomes into a heavier and more viscous condensed phase. Based on the nucleosome concentration of our sample we expect phase separation to become observable from around ~7 mM Mn^{2+} [26]. To observe the interaction of divalent ions below 7mM, we opted to use manganese ions rather than magnesium because these ions will cause a paramagnetic relaxation enhancement (PRE) where it binds. This PRE is strong and will be observable below concentrations of divalent ions that cause phase separation of nucleosomes.

We performed methyl-TROSY experiments while titrating in $MnCl_2$ up to 1 mM where peaks broadened too much to observe peaks properly due to the solvent PRE effect. At 10 μM $MnCl_2$, distinct sites can be identified on the nucleosome with reduced intensities (Fig. 4.5a and S4.6). Residues I36, V45, I58, L103 intensities are decreased, with I36 and L103 being most affected, while other residues have no to minimal intensity change. The high specificity of localization at low concentrations of $MnCl_2$ indicate that these sites have a high affinity to binding manganese ions. Both high affinity binding sites correlate with sites on the nucleosome with a high electronegative charge (chapter 2), with I36 close to DNA and L103 inside the acidic patch (Fig. 4.5d).

Up to 45 binding sites for divalent cations have been reported for the nucleosome core particle[69]. At the tested concentration of 10 μM $MnCl_2$ and 76 μM nucleosome there is a 7.6-fold excess of nucleosomes compared to Mn^{2+} ions. At this ratio we would expect less than one binding site per nucleosome to be occupied and only at a concentration of 3.4 mM MnCl2 (45 * 76 μM nucleosome) enough Mn^{2+} are present for each binding site on the nucleosome. However, we observe for both I36 and L103 approximately 80% reduced signal at 10 μM $MnCl_2$. This reduced signal is higher than expected and means that Mn^{2+} ions are rapidly exchanging between higher affinity binding sites between nucleosomes.

At higher concentrations of $MnCl_2$, additional sites can be observed with intensity loss (Fig. 4.5b). When paramagnetic compounds remain unbound in solution these compounds can quench signals of solvent accessible residues, so called solvent PRE's. We determined the solvent accessible surface area of the nucleosome (1kx5) and compared these with the observed signal loss to determine if the decreased intensity would better fit with a solvent PRE effect or a specific binding (Fig. 4.5b). The ILV residues in the core are buried, while residue V15 in the flexible tail is exposed. Careful investigation of the solvent accessible surface area of the core residues does not reveal a correlation with the intensity loss. We therefore conclude that we are primarily observing specific binding events for the core residues near residue I36, I86 and L103 and not solvent PRE effects. Based on the experiments with nucleosomes we cannot yet conclude if we are observing specific effect or solvent PRE effects for V15 in the histone tail.

Residues V38, V41 and L42 are not besides a negative patch but show intensity loss at higher $MnCl_2$ concentrations. They are near I36 and therefore will be affected by the PRE effect from manganese binding at this site. Similarly, L99 located near the acidic patch has reduced intensity. Residue I86 is not located near a binding site seen at μM $MnCl_2$ and therefore is a new binding site with a lower affinity to bind manganese ions.

To separate the contribution of the DNA and histone core to Mn^{2+} ion binding we compared $MnCl_2$ titrations of both nucleosomes with H2A-H2B dimers (Fig. 4.5c). Titrations with dimers require higher concentrations of Mn^{2+} to have a similar decrease in average intensity compared to the nucleosomes, after accounting for the difference in histone concentration (two copies in the nucleosome, one in the dimer). This difference in affinity makes sense as the DNA is highly negative charged molecule and contains most of the binding sites for Mn^{2+} ions. Therefore, the DNA is important for the recruitment of divalent cations to the nucleosome core. However, inspection of residue specific changes highlights several binding sites that do not require the presence of DNA. Residues I36 and I86 are no longer strongly perturbed indicating that these binding sides require DNA, while the binding site near V45 and L103 does not. Interestingly, a new site of decreased intensity is observed for the H2A-H2B dimer at V115. In the H2A-H2B dimer the H2A-αN helix is disordered where it would form an α helix and interact with the H2B-αC helix in the nucleosome[70,71]. Solution-state NMR structures have a less defined orientation for the H2B αC-helix structure. The higher mobility of the H2B αC helix could influence how V115 interact with Mn^{2+} ions as both residues are in this helix.

Surprisingly, residue V15 in the flexible tail shows an intensity comparable to the average decrease in signal for the H2A-H2B dimer, while it was much lower for the nucleosome. The dependence on DNA indicates that residue V15 needs to be close to DNA. Nucleosome tails are known to be bound to DNA at low salt concentrations and would explain the decreased intensity of V15. For the nucleosome V15 signal decreases and remains low up to the highest tested concentration of 1 mM $MnCl_2$, indicating that the H2B tails remains bound to nucleosomal DNA at these concentrations. Therefore, these low Mn^{2+} concentrations can be used to study the average bound or unbound state of the H2B tail and potentially other histone tails.

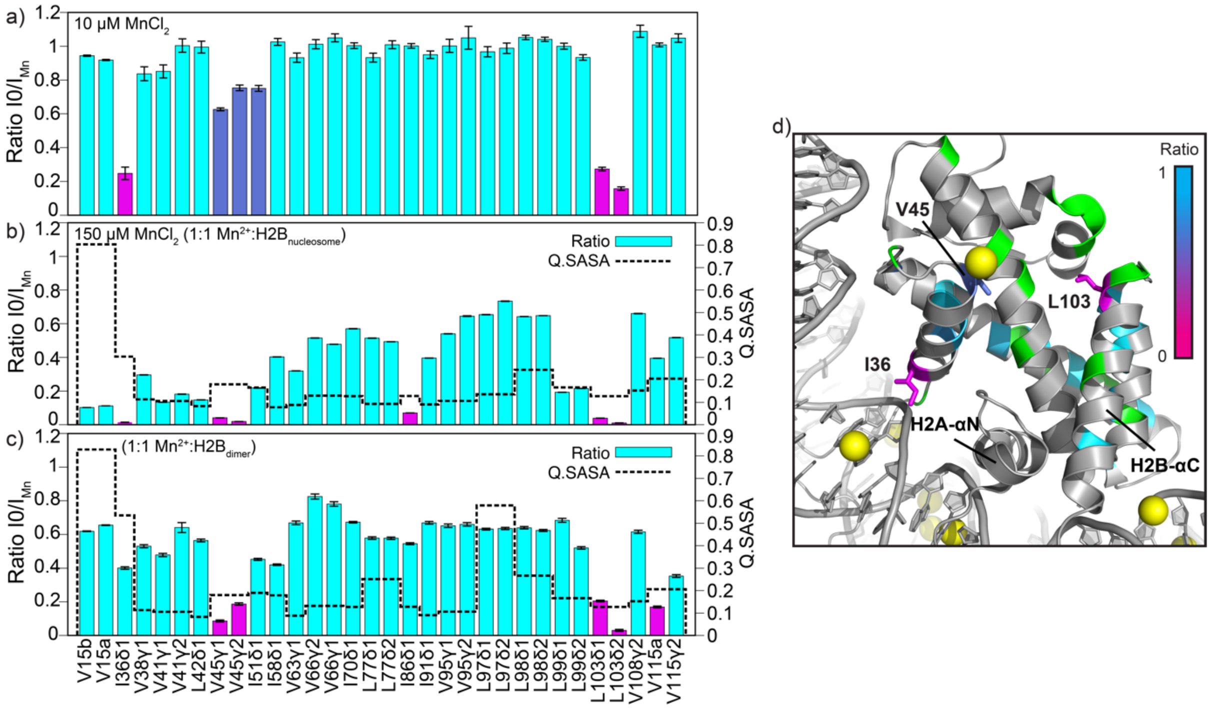

Figure 4.5: Structural validation by Mn^{2+} paramagnetic relaxation enhancement. a) Nucleosomes with non-saturating concentrations of $MnCl_2$, Mn^{2+} ions localize specifically near I36 and L103 (red) with high affinity and thus rapidly exchange between these sides. b) Nucleosome solvent accessible surface area (SASA) at both higher and lower $MnCl_2$ concentrations do not match with losses in peak intensities indicating a specific effect of Mn^{2+} ions rather than a solvent PRE effect. c) H2A-H2B dimer in a 1:1 stoichiometry with $MnCl_2$ is strongly affected at V45, L103 and V115 but not at I36. d) H2A-H2B dimer and DNA from pdb 3LJA highlighted in grey and Mn^{2+} ions bound to the nucleosome shown in yellow. Mn^{2+} ions are positioned close to H2B I36 in the DNA major groove and on top of the alpha helix near H2B V45. Aspartic acid and glutamic acid residues are indicated in green.

Manganese was found to bind with high specificity near I36, L103 and V45 on the nucleosome and at a lower affinity near I86. Nucleosomes can bind various divalent metals like Cu^{2+} at the interface between the two H3 copies or Mn^{2+}, Ni^{2+}, Co^{2+}, Cs^{2+} ,and Rb^{2+} at various sites on both the DNA and nucleosome core[47,53,72,73]. Similarly, a Mg^{2+} ion can bind at the same spot as Mn^{2+} on the H3 α1 helix that makes a crystal contact with the acidic patch on H2A-H2B[74]. The observed binding site near I36 V45, I86 match well with the reported binding sites (Fig. 4.5d). A Mn^{2+} binding site at L103 located in the acidic patch has not been reported. The reported binding sites are derived from crystal structures that form crystal contacts, mostly between the H4 tail and the acidic patch. Therefore, it is not possible for a Mn^{2+} to be present in these structures at the acidic patch. From our data we suggest that the ion positioned above V45 in the crystal structures in solution is positioned on the acidic patch. Localization of Mg^{2+} to the acidic patch will reduce the charge of the acidic patch and might increase the ability to form inter-nucleosome interaction by nucleosomal DNA-histone core interactions[61].

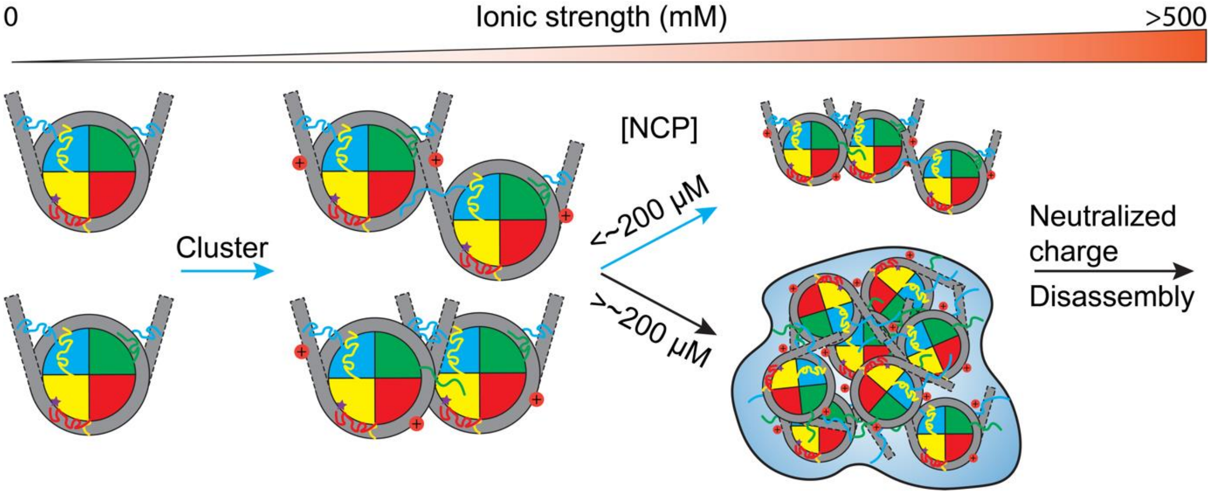

Figure 4.6: Nucleosome compaction by ionic strength. In the absence of or low concentration of ionic strength (25mM) nucleosomes repel each other with nucleosome tails remaining bound to DNA. Within the tested range of 25-125 mM ionic strength DNA-tail interactions are weakened and tails can interact with negatively charged surfaces of other nucleosomes. At nucleosome concentrations of 200 μM or more nucleosomes can form phase separates at an ionic strength around 150 mM. Nucleosomes are depicted with histones H3 (green), H4 (blue), H2A (yellow), H2B (red) and DNA (gray). The purple star indicating residue I36 of H2B near DNA. DNA linker ends are represented as dotted lines to indicate variability in DNA linker end conformation. Blue arrows are suggested to be observed in our NMR experiments.

Chromatin phase separation has been implicated with multiple biologically important processed forming separate compartments[4,75] including a super enhancer region[76] and heterochromatin[9,77,78]. Recent findings show that mononucleosomes can phase separate with 150 mM KCl at 200 μM nucleosomes[29]. While no phase separation occurred at low nucleosome concentration at 150 mM KCl, an increase in optical densities was observed[29]. We suggest this increase in optical density could derive from smaller nucleosome clusters forming and be a step before phase separation. In our study we used

70 μM nucleosomes and therefore do not expect to observe phase separation based on these recent findings. However, we do observe increase in effective particle size and would like to speculate that we could be observing clustering of nucleosomes, a step before a phase separated state. In this model nucleosomes interact with each other through DNA-histone tail interactions until an ionic strength is reached to change the net repulsive interactions to attractive (Fig. 4.6), which is expected to be around 50-150 mM ionic strength depending on linker length[37]. Because DNA tail interactions are unspecific, nucleosomes need to be close enough, through either being linked in an array or with a high enough concentration to compete between own DNA and DNA of a second nucleosome.

Conclusion

Nucleosomes were found to remain soluble and stable at concentration up to at least 70 uM nucleosomes and 125 mM ionic strength. An increase from 25 to 75mM in ionic strength resulted in a more than 50% decrease in core residue NMR signal intensity but did not decrease the tail residue signal. At 125mM ionic strength, the nucleosome core had 2.7 times the intensity for K^+ compared to Na^+ at 25 °C. At these ionic concentrations the H2A-H2B dimer remains bound to the rest of the nucleosome core and DNA remains bound till at least SHL5. Loss of NMR signal is thought to be caused by an increase in rotational correlation time due to inter-nucleosome interactions. Based on the increase of rotational correlation time we expect nucleosomes to form clusters of at least 2-3 nucleosomes at 50 mM NaCl or 75 mM KCl. We believe these clusters to be a first step towards phase separation of nucleosomes. Because the best quality spectra of nucleosomes are obtained with KCl we expect the least amount of clustering to occur with these ions and recommend KCl over NaCl for future NMR studies on the nucleosome. Additionally, manganese ions localize to the DNA near I36 and the acidic patch. Furthermore, we find that at 25 mM ionic strength the H2B histone tail interacts with nucleosomal DNA. As Mn^{2+} was found to report on the binding of H2B nucleosome tail in a nondestructive manner suggest Mn^{2+} as an alternative way to study DNA binding of nucleosome tails.

References

1. Kato, H. et al. Architecture of the high mobility group nucleosomal protein 2-nucleosome complex as revealed by methyl-based NMR. Proc. Natl. Acad. Sci. 108, 12283–12288 (2011).
2. Sinha, K. K., Gross, J. D. & Narlikar, G. J. Distortion of histone octamer core promotes nucleosome mobilization by a chromatin remodeler. Science (80-.). 355, (2017).
3. Fasci, D., Ingen, H. Van, Heck, A. J. R. & Scheltema, R. A. Histone Interaction Landscapes Visualized by Crosslinking Mass Spectrometry in Intact Cell. Mol. Cell. Proteomics 17, 2018–2033 (2018).

4. Lobbia, V. R., Trueba Sanchez, M. C. & van Ingen, H. Beyond the Nucleosome: Nucleosome-Protein Interactions and Higher Order Chromatin Structure. J. Mol. Biol. 433, 166827 (2021).

5. Tugarinov, V., Hwang, P. M., Ollerenshaw, J. E. & Kay, L. E. Cross-correlated relaxation enhanced 1H-13C NMR spectroscopy of methyl groups in very high molecular weight proteins and protein complexes. J. Am. Chem. Soc. 125, 10420–10428 (2003).

6. Sprangers, R. & Kay, L. E. Quantitative dynamics and binding studies of the 20S proteasome by NMR. Nature 445, 618–622 (2007).

7. Gelis, I. et al. Structural Basis for Signal-Sequence Recognition by the Translocase Motor SecA as Determined by NMR. Cell 131, 756–769 (2007).

8. Horn, V. et al. Structural basis of specific H2A K13/K15 ubiquitination by RNF168. Nat. Commun. 10, 1–12 (2019).

9. Sanulli, S. et al. HP1 reshapes nucleosome core to promote phase separation of heterochromatin. Nature 575, 390–394 (2019).

10. Kitevski-Leblanc, J. et al. The rnf168 paralog rnf169 defines a new class of ubiquitylated histone reader involved in the response to dna damage. Elife 6, 1–31 (2017).

11. Kitevski-Leblanc, J. L. et al. Investigating the Dynamics of Destabilized Nucleosomes Using Methyl-TROSY NMR. J. Am. Chem. Soc. 140, 4774–4777 (2018).

12. Morrison, E. A., Bowerman, S., Sylvers, K. L., Wereszczynski, J. & Musselman, C. A. The conformation of the histone H3 tail inhibits association of the BPTF PHD finger with the nucleosome. Elife 7, 1–35 (2018).

13. Böhm, V. et al. Nucleosome accessibility governed by the dimer/tetramer interface. Nucleic Acids Res. 39, 3093–3102 (2011).

14. Toth, K. et al. Histone- and DNA Sequence-Dependent Stability of Nucleosomes Studied by Single-Pair FRET. Cytom. Part A 83A, 839–846 (2013).

15. Andreeva, T. V. et al. Na+and K+Ions Differently Affect Nucleosome Structure, Stability, and Interactions with Proteins. Microsc. Microanal. 1–11 (2021). doi:10.1017/S1431927621013751

16. Dorigo, B., Schalch, T., Bystricky, K. & Richmond, T. J. Chromatin fiber folding: Requirement for the histone H4 N-terminal tail. J. Mol. Biol. 327, 85–96 (2003).

17. Wakamori, M. et al. Intra- and inter-nucleosomal interactions of the histone H4 tail revealed with a human nucleosome core particle with genetically-incorporated H4 tetra-acetylation. Sci. Rep. 5, 1–16 (2015).

18. Zheng, C., Lu, X., Hansen, J. C. & Hayes, J. J. Salt-dependent intra- and internucleosomal interactions of the H3 tail domain in a model oligonucleosomal array. J. Biol. Chem. 280, 33552–33557 (2005).

19. Kan, P.-Y., Lu, X., Hansen, J. C. & Hayes, J. J. The H3 Tail Domain Participates in Multiple Interactions during Folding and Self-Association of Nucleosome Arrays. Mol. Cell. Biol. 27,

2084–2091 (2007).

20. Gao, M. et al. Histone H3 and H4 N-terminal tails in nucleosome arrays at cellular concentrations probed by magic angle spinning NMR spectroscopy. J. Am. Chem. Soc. 135, 15278–15281 (2013).

21. Kato, H., Gruschus, J., Ghirlando, R., Tjandra, N. & Bai, Y. Characterization of the N-terminal tail domain of histone H3 in condensed nucleosome arrays by hydrogen exchange and NMR. J. Am. Chem. Soc. 131, 15104–15105 (2009).

22. Brower-toland, B. et al. Specific Contributions of Histone Tails and their Acetylation to the Mechanical Stability of Nucleosomes. J. Mol. Biol. 346, 135–146 (2005).

23. Iwasaki, W. et al. Contribution of histone N-terminal tails to the structure and stability of nucleosomes. FEBS Open Bio 3, 363–369 (2013).

24. Li, Z. & Kono, H. Distinct Roles of Histone H3 and H2A Tails in Nucleosome Stability. Sci. Rep. 6, 31437 (2016).

25. Widom, J. Physicochemical studies of the folding of the 100 Å nucleosome filament into the 300 Å filament. J. Mol. Biol. 190, 411–424 (1986).

26. De Frutos, M., Raspaud, E., Leforestier, A. & Livolant, F. Aggregation of nucleosomes by divalent cations. Biophys. J. 81, 1127–1132 (2001).

27. Allahverdi, A., Chen, Q., Korolev, N. & Nordenskiöld, L. Chromatin compaction under mixed salt conditions: Opposite effects of sodium and potassium ions on nucleosome array folding. Sci. Rep. 5, (2015).

28. Bass, M. V., Nikitina, T., Norouzi, D., Zhurkin, V. B. & Grigoryev, S. A. Nucleosome spacing periodically modulates nucleosome chain folding and DNA topology in circular nucleosome arrays. J. Biol. Chem. 294, 4233–4246 (2019).

29. Hammonds, E. F. et al. Histone H3 and H4 tails play an important role in nucleosome phase separation. Biophys. Chem. 283, 106767 (2022).

30. Yager, T. D., McMurray, C. T. & van Holde, K. E. Salt-Induced Release of DNA from Nucleosome Core Particles. Biochemistry 28, 2271–2281 (1989).

31. Tokuda, J. M., Pabit, S. A. & Pollack, L. Protein–DNA and ion–DNA interactions revealed through contrast variation SAXS. Biophys. Rev. 8, 139–149 (2016).

32. Chien, F. T. & Van Der Heijden, T. Characterization of nucleosome unwrapping within chromatin fibers using magnetic tweezers. Biophys. J. 107, 373–383 (2014).

33. Gansen, A. et al. High precision FRET studies reveal reversible transitions in nucleosomes between microseconds and minutes. Nat. Commun. 9, 1–13 (2018).

34. Bilokapic, S., Strauss, M. & Halic, M. Histone octamer rearranges to adapt to DNA unwrapping. Nat. Struct. Mol. Biol. 25, 101–108 (2018).

35. Rodriguez, Y., Duan, M., Wyrick, J. J. & Smerdon, M. J. A cassette of basic amino acids in histone H2B regulates nucleosome dynamics and access to DNA damage. J. Biol. Chem. 293,

7376–7386 (2018).

36. Mutskov, V. et al. Persistent Interactions of Core Histone Tails with Nucleosomal DNA following Acetylation and Transcription Factor Binding. Mol. Cell. Biol. 18, 6293–6304 (1998).

37. Mangenot, S., Leforestier, A., Vachette, P., Durand, D. & Livolant, F. Salt-induced conformation and interaction changes of nucleosome core particles. Biophys. J. 82, 345–356 (2002).

38. Livolant, F. et al. Are liquid crystalline properties of nucleosomes involved in chromosome structure and dynamics? Philos. Trans. R. Soc. A Math. Phys. Eng. Sci. 364, 2615–2633 (2006).

39. CARY, P. D., MOSS, T. & BRADBURY, E. M. High-Resolution Proton-Magnetic-Resonance Studies of Chromatin Core Particles. Eur. J. Biochem. 89, 475–482 (1978).

40. Walker, I. O. Differential dissociation of histone tails from core chromatin. Biochemistry 23, 5622–5628 (1984).

41. Clark, D. J. & Kimura, T. Electrostatic mechanism of chromatin folding. J. Mol. Biol. 211, 883–896 (1990).

42. Blacketer, M. J., Feely, S. J. & Shogren-Knaak, M. A. Nucleosome interactions and stability in an ordered nucleosome array model system. J. Biol. Chem. 285, 34597–34607 (2010).

43. Milo, R., Jorgensen, P., Moran, U., Weber, G. & Springer, M. BioNumbers The database of key numbers in molecular and cell biology. Nucleic Acids Res. 38, 750–753 (2009).

44. Palmer, L. G. & Civan, M. M. Distribution of Na+, K+ and Cl- between nucleus and cytoplasm in Chironomus salivary gland cells. J. Membr. Biol. 33, 41–61 (1977).

45. Dyer, P. N. et al. Reconstitution of Nucleosome Core Particles from Recombinant Histones and DNA. Methods Enzymol. 375, 23–44 (2003).

46. Pritišanac, I. et al. Automatic Assignment of Methyl-NMR Spectra of Supramolecular Machines Using Graph Theory. J. Am. Chem. Soc. 139, 9523–9533 (2017).

47. Davey, C. A., Sargent, D. F., Luger, K., Maeder, A. W. & Richmond, T. J. Solvent mediated interactions in the structure of the nucleosome core particle at 1.9 A resolution. J. Mol. Biol. 319, 1097–1113 (2002).

48. Neudecker, P., Lundström, P. & Kay, L. E. Relaxation dispersion NMR spectroscopy as a tool for detailed studies of protein folding. Biophys. J. 96, 2045–2054 (2009).

49. Ahlner, A., Carlsson, M., Jonsson, B. H. & Lundström, P. PINT: A software for integration of peak volumes and extraction of relaxation rates. J. Biomol. NMR 56, 191–202 (2013).

50. Kleinjung, J. & Fraternali, F. POPSCOMP: An automated interaction analysis of biomolecular complexes. Nucleic Acids Res. 33, 342–346 (2005).

51. Lowary, P. . & Widom, J. New DNA sequence rules for high affinity binding to histone octamer and sequence-directed nucleosome positioning. J. Mol. Biol. 276, 19–42 (1998).

52. Gansen, A., Hieb, A. R., Böhm, V., Tóth, K. & Langowski, J. Closing the Gap between Single

Molecule and Bulk FRET Analysis of Nucleosomes. PLoS One 8, (2013).

53. Mohideen, K., Muhammad, R. & Davey, C. A. Perturbations in nucleosome structure from heavy metal association. Nucleic Acids Res. 38, 6301–6311 (2010).

54. Allahverdi, A. et al. The effects of histone H4 tail acetylations on cation-induced chromatin folding and self-association. Nucleic Acids Res. 39, 1680–1691 (2011).

55. Anderson, P. & Bauer, W. Supercoiling in Closed Circular DNA: Dependence upon Ion Type and Concentration. Biochemistry 17, 594–601 (1978).

56. Cruz-León, S. et al. Twisting DNA by salt. Nucleic Acids Res. 50, 5726–5738 (2022).

57. Li, G. & Widom, J. Nucleosomes facilitate their own invasion. Nat. Struct. Mol. Biol. 11, 763–769 (2004).

58. Li, G., Levitus, M., Bustamante, C. & Widom, J. Rapid spontaneous accessibility of nucleosomal DNA. Nat. Struct. Mol. Biol. 12, 46–53 (2005).

59. Ngo, T. T. M., Zhang, Q., Zhou, R., Yodh, J. G. & Ha, T. Asymmetric unwrapping of nucleosomes under tension directed by DNA local flexibility. Cell 160, 1135–1144 (2015).

60. Chen, Y. et al. Asymmetric unwrapping of nucleosomal DNA propagates asymmetric opening and dissociation of the histone core. Proc. Natl. Acad. Sci. U. S. A. 114, 334–339 (2017).

61. Bilokapic, S., Strauss, M. & Halic, M. Cryo-EM of nucleosome core particle interactions in trans. Sci. Rep. 8, 1–8 (2018).

62. Clark, D. J. & Kimura, T. Electrostatic mechanism of chromatin folding. J. Mol. Biol. 211, 883–896 (1990).

63. Huang, S. et al. Poly(1-amino-5-chloroanthraquinone): Highly Selective and Ultrasensitive Fluorescent Chemosensor For Ferric Ion. J. Fluoresc. 23, 621–627 (2013).

64. Feigon, J. & Kearns, D. R. 1 H NMR investigation of the conformational states of DNA in nucleosome core particles. Nucleic Acids Res. 6, 2327–2337 (1979).

65. Brown, D. W., Libertini, L. J. & Small, E. W. Fluorescence Anisotropy Decay of Ethidium Bound to Nucleosome Core Particles. 1. Rotational Diffusion Indicates an Extended Structure at Low Ionic Strength. Biochemistry 30, 5293–5303 (1991).

66. Manning, G. S. Is a Small Number of Charge Neutralizations Sufficient to Bend Nucleosome Core DNA onto Its Superhelical Ramp? J. Am. Chem. Soc. 125, 15087–15092 (2003).

67. Walker, I. O. Differential Dissociation of Histone Tails from Core Chromatin. Biochemistry 23, 5622–5628 (1984).

68. Ohyama, T. New aspects of magnesium function: A key regulator in nucleosome self-assembly, chromatin folding and phase separation. Int. J. Mol. Sci. 20, (2019).

69. Wu, B. & Davey, C. A. Using soft X-Rays for a detailed picture of divalent metal binding in the nucleosome. J. Mol. Biol. 398, 633–640 (2010).

70. Moriwaki, Y. et al. Solution structure of the isolated histone H2A-H2B heterodimer. Sci. Rep.

6, 1–11 (2016).

71. Zhang, H., Eerland, J., Horn, V., Schellevis, R. & van Ingen, H. Mapping the electrostatic potential of the nucleosome acidic patch. Sci. Rep. 11, 1–11 (2021).

72. Attar, N. et al. The histone H3-H4 tetramer is a copper reductase enzyme. Science (80-.). 369, 59–64 (2020).

73. Vasudevan, D., Chua, E. Y. D. & Davey, C. A. Crystal Structures of Nucleosome Core Particles Containing the ‘601’ Strong Positioning Sequence. J. Mol. Biol. 403, 1–10 (2010).

74. Frouws, T. D., Duda, S. C. & Richmond, T. J. X-ray structure of the MMTV-A nucleosome core. Proc. Natl. Acad. Sci. U. S. A. 113, 1214–1219 (2016).

75. Hildebrand, E. M. & Dekker, J. Mechanisms and Functions of Chromosome Compartmentalization. Trends Biochem. Sci. 45, 385–396 (2020).

76. Sabari, B. R. et al. Coactivator condensation at super-enhancers links phase separation and gene control. Science (80-.). 361, (2018).

77. Larson, A. G. et al. Liquid droplet formation by HP1α suggests a role for phase separation in heterochromatin. Nature 547, 236–240 (2017).

78. Strom, A. R. et al. Phase separation drives heterochromatin domain formation. Nature 547, 241–245 (2017).

Supplementary information

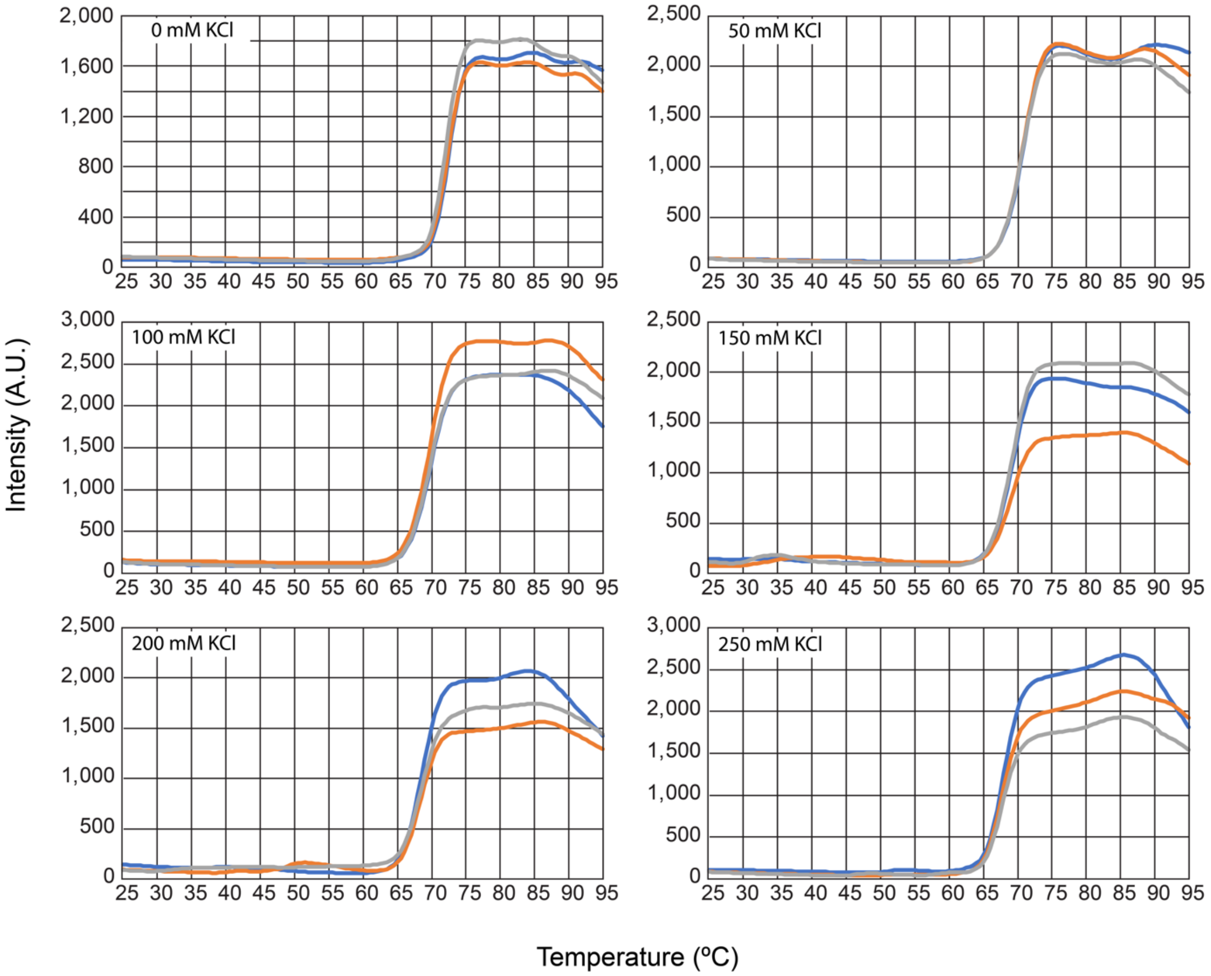

Figure S4.1: Decreased meting temperature of nucleosomes at higher KCl concentrations. The first transition of the melting curves for nucleosomes shifts to lower temperatures with increased ionic concentration. Three replicates were performed for each meting curve indicated in gray, orange and blue.

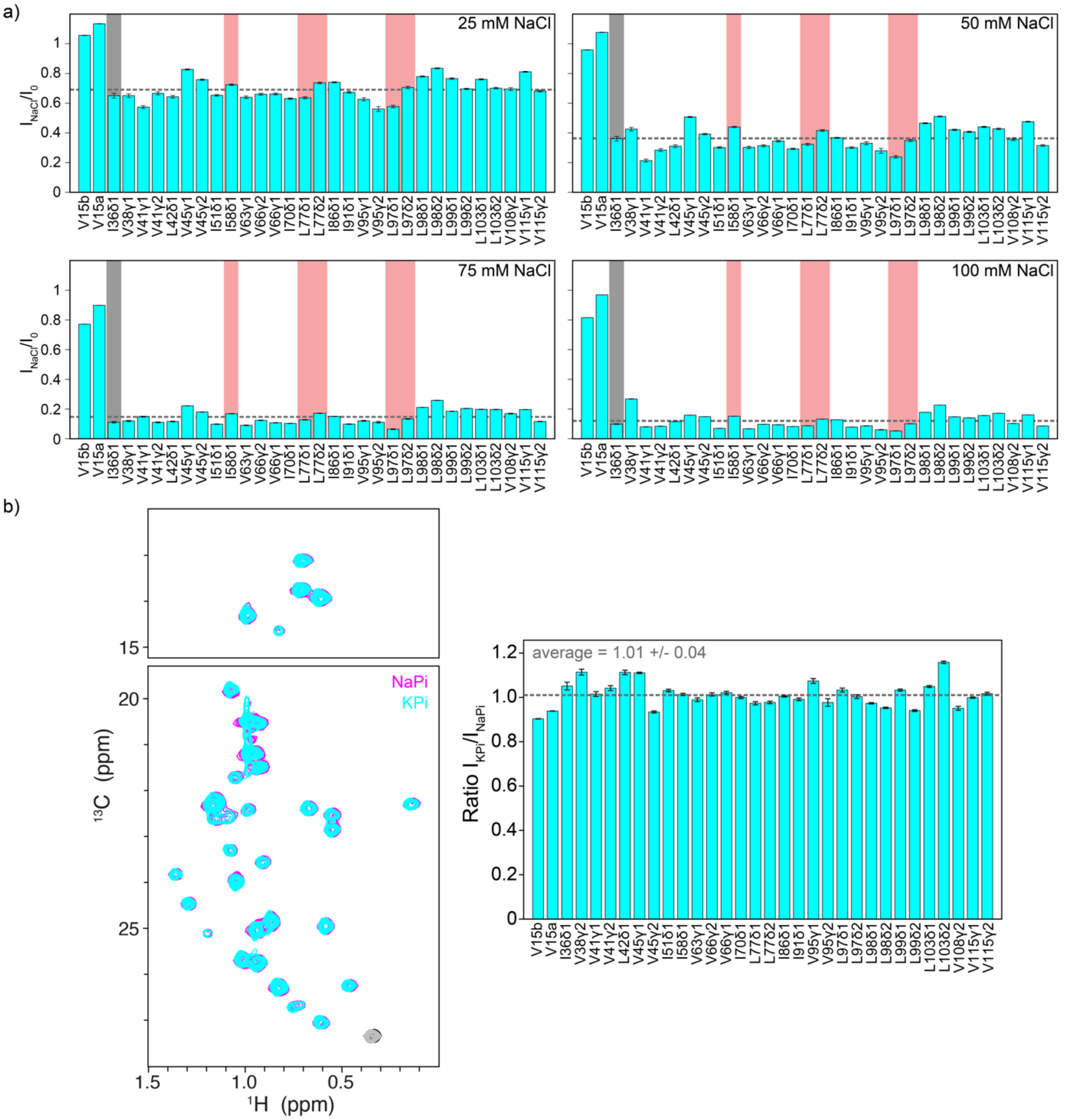

Figure S4.2: NaCl titration and NMR signal intensity returns with lower ionic strength. a) Titration of NaPi buffered nucleosomes with NaCl strongly reduced signal intensity. Colored background boxes indicated that those residues are in the interaction interface with DNA (gray) and H4 (red). b) Buffer exchanging to KPi NMR buffer without added salts results in the return of peak intensities.

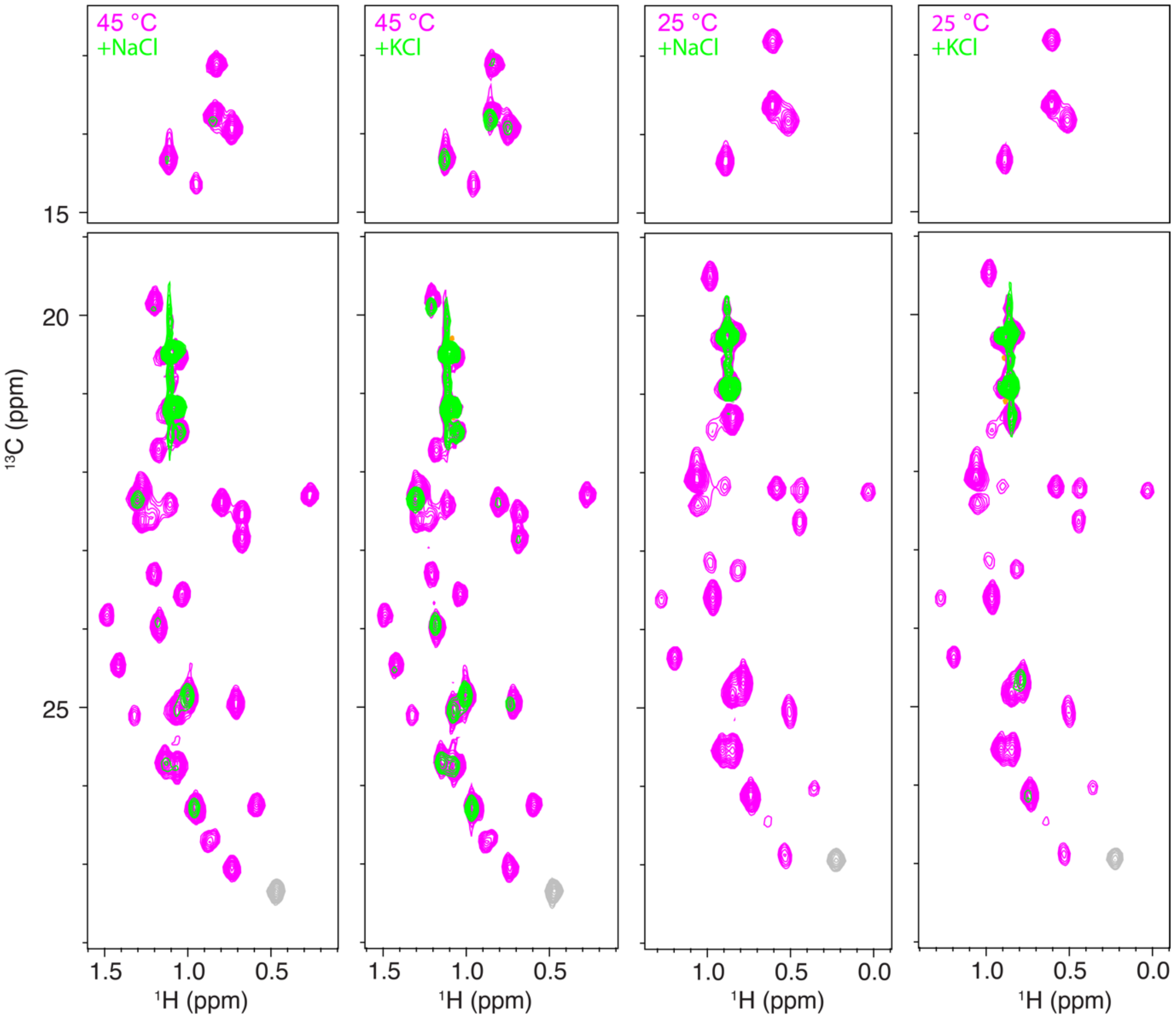

Figure S4.3: Nucleosomes salt titration with varying ions and temperatures. Nucleosomes show a larger NMR signal loss at 25 °C compared to 45 °C and for NaCl compared to KCl.

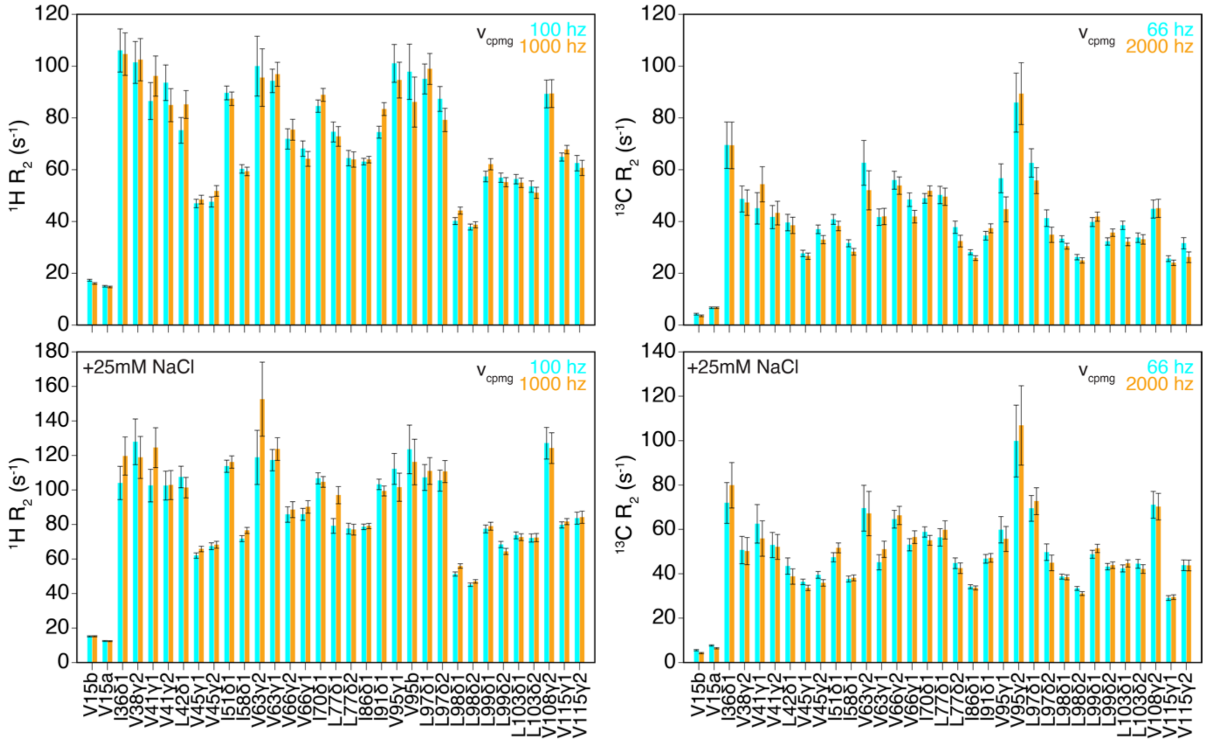

Figure S4.4: ^{1}H and ^{13}C Relaxation dispersion experiments of H2B ILV labeled nucleosomes. R_2 relaxation rates are given for H2B ILV methyl groups at 0 mM (top) and 25 mM NaCl (bottom) for ^{1}H (left) and ^{13}C (right). The nucleosome globular core shows higher relaxation rates than the flexible tail. The nearly identical R_2 rates at lower and higher CPMG rates indicate that these is not exchange in the ms-μs timescale.

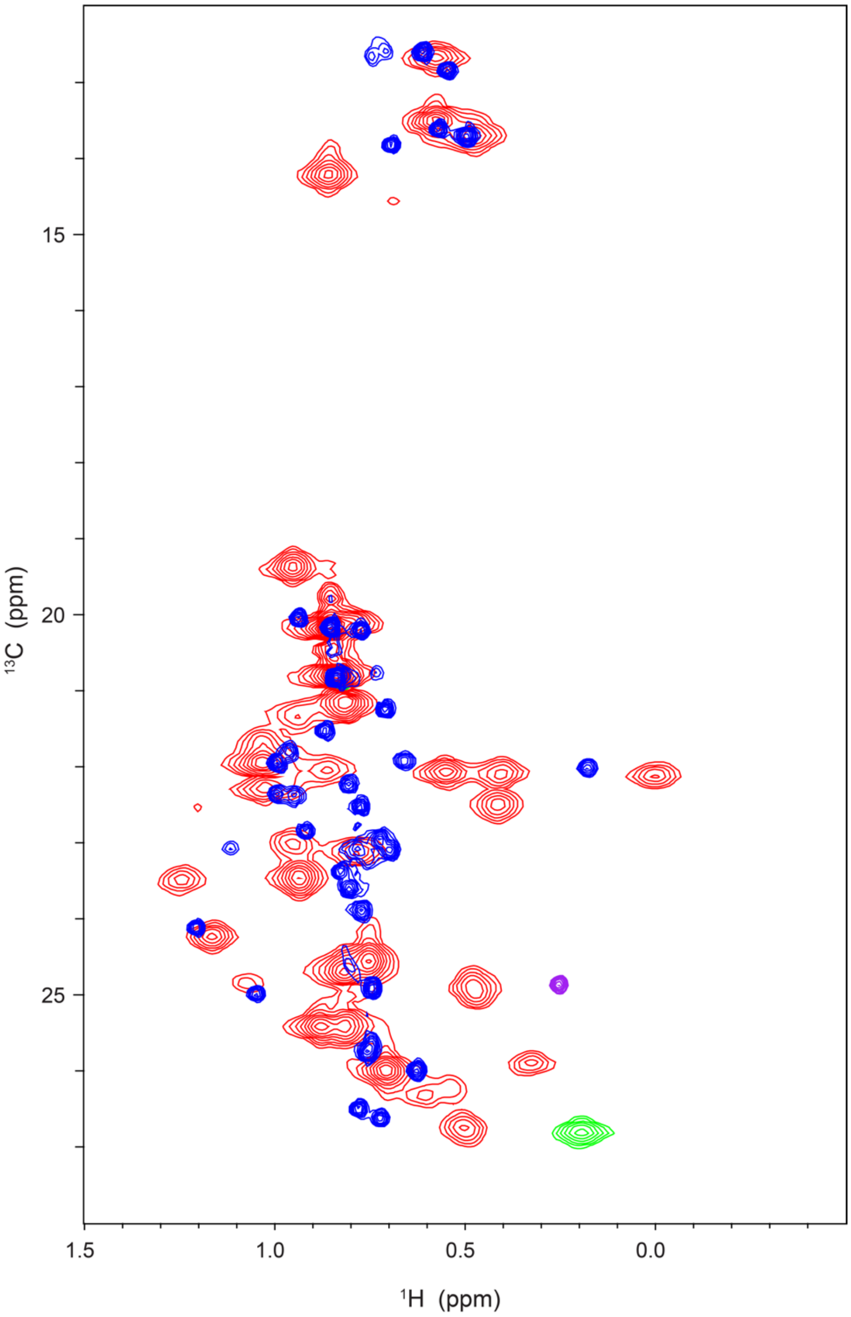

Figure S4.5: Overlay XL dimer and nucleosome. Nucleosomes show a larger spread in chemical shift dispersion than dimers. Peaks of Nucleosomes are considerably broadened compared to dimers.

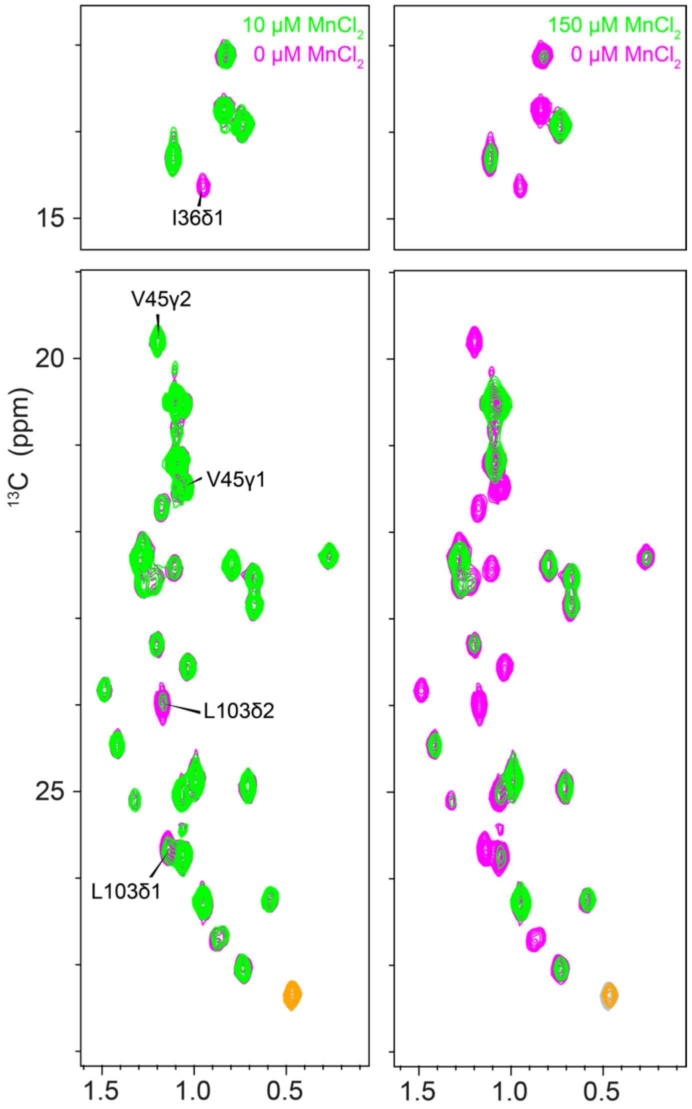

Figure S4.6: Nucleosome MnCl₂ titration spectra. Residues I36, V45 and L103 have the strongest decrease in intensity upon addition of Mn^{2+}.

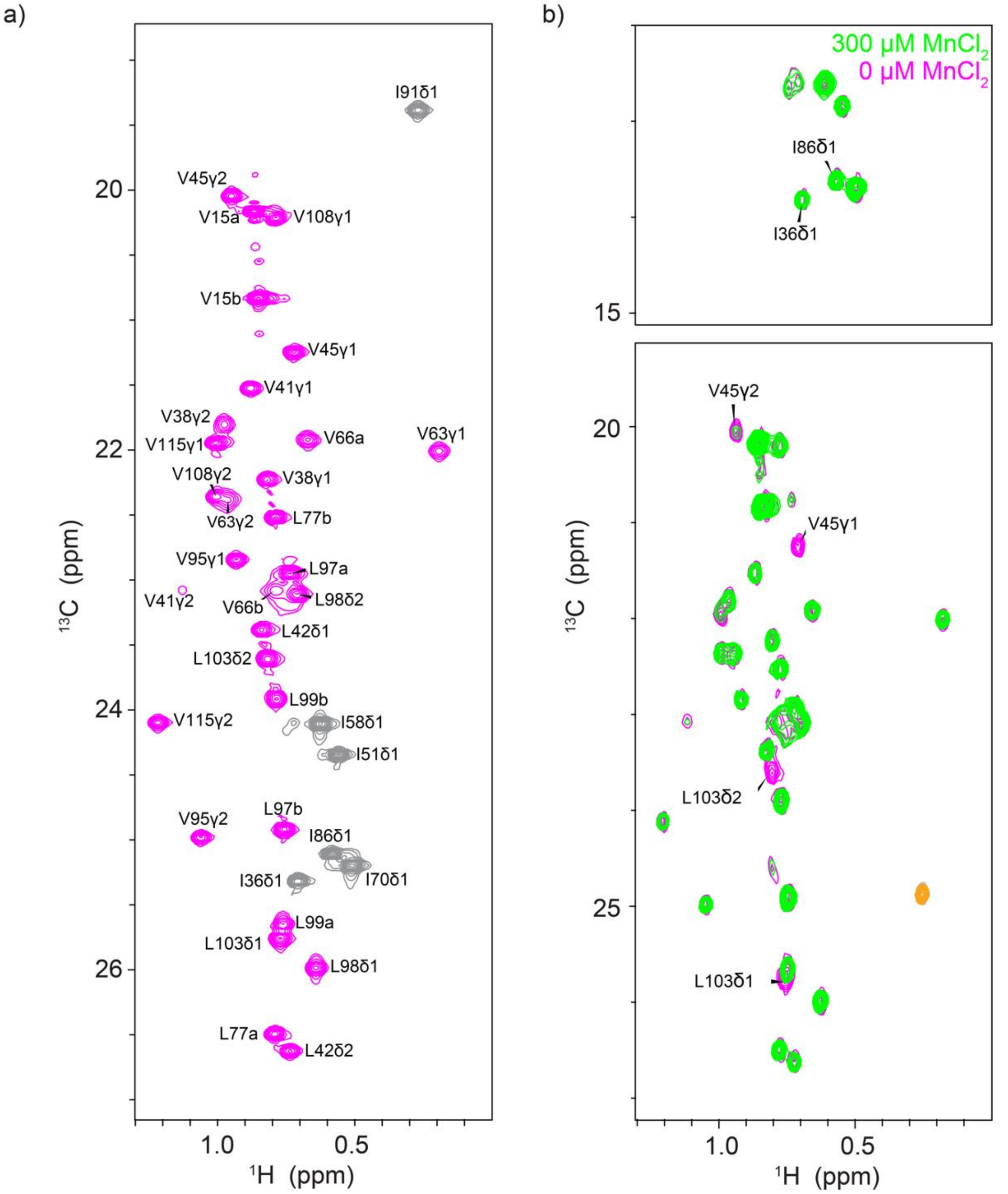

Figure S4.6: H2A-H2B dimer assignment and MnCl₂ titration spectra. Residues V45 and L103 have the strongest decrease in intensity upon addition of Mn^{2+} but not residues I36 and I86.

Table S4.1: Correlation times nucleosomes. Correlation times (10^{-9} s) calculated for different nucleosomes forms. For calculations in HydroNMR tails were assumed to be collapsed on the nucleosome and were removed to obtain tumbling times for only the ridged parts of the complex. Calculations were made assuming opened DNA remained rigid.

	DNA (bp)	45 °C	25 °C	
1kx5 with tails	147	144.6	237.6	
Tailless nucleosomes				
1kx5 tailless	147	86.57	142.3	
2py0	147	90.76	149.2	
3lz0	147	82.69	135.9	
7ohc	145	85.92	141.2	
3lz0 closed*	167	113.7	186.8	
4qlc	166	108.3	177.9	
5wcu	167	108.3	178	
Other conformations DNA				
3lz0 straight*	167	135.8	223.1	Linker DNA parralel opened
3lz0 open*	167	164	269.5	Linker both open till SHL5
6m4d (124 bp DNA)	124	84	138	Linker both sides missing till SHL 5
5o9g_nuc	192	148.1	243.4	All linker one site, open till SHL5
6g01_nuc	177	227.1	373.1	Linker both side open till SHL5
6g01_nuc_red	167	182.8	300.4	Linker both side open till SHL5
6tda_nuc	159	172.2	283	Linker one side other side missing till SHL5
7crq_nuc	166	187.9	308.8	Linker both side open till SHL5
7crr_nuc	167	153.1	251.6	Linker one side open till SHL5
7ea5_nuc	145	108.5	178.3	Linker one side open till SHL5
7k7g_nuc	122	93.2	153.2	DNA one side open till SHL4, other till SHL5
Multiple nucleosomes				
1kx5	147	195.7	321.6	Two nucleosomes
2pyo	147	191.9	315.4	Two nucleosomes
3lz0	147	182.2	299.4	Two nucleosomes
3lz0 closed*	167	244.7	402.1	Two nucleosomes
5wcu	167	216.9	356.4	Two nucleosomes
3lz0 closed*	167	422.3	694	Three nucleosomes

5wcu	167	363.3	597.1	Three nucleosomes
Smaller complexes (3lz0)				
147bp	147	82.69	135.9	
127bp	127	76.96	126.5	
107bp	107	73.85	121.4	
87bp	87	70.88	116.5	
67bp	67	65.37	107.4	
47bp	47	57.44	94.39	
27bp	27	51.94	85.35	
octamer	0	41.42	68.06	
dimer	0	13.6	22.34	
globular dimer	0	9.32	15.32	

*Structures extended with modeled DNA

Table S4.2: Xenopus laevis H2B ILV assignment of H2A-H2B dimer. **R**esidue and stereospecific assignment for Xl. ILV labeled H2B of the H2A-H2B dimer. Notations a and b indicate an unknown stereospecific assignment.

Residue	group	^{13}C (ppm)	^{1}H (ppm)
V15	a	18.182	0.851
V15	b	17.514	0.866
I36	δ1	22.668	0.707
V38	γ2	19.154	0.975
V38	γ1	19.58	0.819
V41	γ1	18.875	0.88
V41	γ2	20.429	1.128
L42	δ1	20.735	0.839
L42	δ2	23.976	0.736
V45	γ1	18.596	0.722
V45	γ2	17.398	0.95
I51	δ1	21.694	0.56
I58	δ1	21.456	0.624
V63	a	19.735	0.965
V63	b	19.358	0.192
V66	a	20.432	0.788
V66	b	19.271	0.671
I70	δ1	22.547	0.51
L77	a	23.846	0.792
L77	b	19.871	0.788
I86	δ1	22.458	0.584
I91	δ1	16.734	0.268
V95	γ1	20.192	0.932
V95	γ2	22.331	1.061
L97	δ1	20.302	0.737
L97	δ2	22.269	0.756
L98	δ1	23.336	0.641
L98	δ2	20.461	0.711
L99	a	23.005	0.76
L99	b	21.266	0.786
L103	δ1	23.107	0.772
L103	δ2	20.958	0.818
V108	γ1	17.563	0.788
V108	γ2	19.708	1.005
V115	γ1	19.294	1.006
V115	γ2	21.447	1.218

5

Conformational dynamics in ISWI and the nucleosome upon their interaction

Based on the manuscript: **Lobbia, V. R.,** van Emmerik, C.L., Trueba Sanchez, M. & van Ingen, H. Methyl-TROSY NMR at 1.2 GHz: exploiting resolution and magnetic field alignment. *in preparation*

Preliminary experiments were performed by Clara van Emmerik. Cloning, production and NMR of ISWI assignment mutants were performed by María Cristina Trueba Sánchez

Abstract

The chromatin remodeler ISWI plays a crucial role in the maintenance of the dynamic chromatin landscape through its ability to alter nucleosome spacing. Nucleosome remodeling by ISWI involves the translocation of DNA over the histone octamer surface, without disassembly of the nucleosome. Despite the enormous progress in the structural characterization of this process in recent years, it remains unclear to what extent conformational changes in the histone proteins play a role in remodeling. In addition, the molecular mechanism of ATPase activation upon nucleosome binding are not fully understood. Here we studied the conformational dynamics of ISWI and the nucleosome-ISWI complex using methyl-TROSY solution NMR spectroscopy. We find that the free enzyme is highly dynamic throughout the protein. Our data indicate that binding of an active ISWI construct induces conformational changes through the histone octamer, affecting histone-DNA and histone-histone contacts. These findings provide strong support for histone plasticity during remodeling to facilitate DNA translocation and further highlight the histone octamer as an allosteric unit.

Introduction

Chromatin remodelers are a family of proteins that are involved in regulation of DNA-templated activities by altering the chromatin landscape. Chromatin remodelers contain an ATPase domain which is required for their function to manipulate nucleosomes. Chromatin remodelers belong to the SF2 superfamily of helicases which have an ATPase domain that is composed of two RecA lobes that each contain a part of an ATP-binding catalytic site. There are four families of remodelers: the SWI/SNF (SWItch/Sucrose Non-Fermentable), INO80, CHD (chromodomain helicase DNA-binding) and ISWI (Imitation SWItch) remodelers. The catalytic ATPase domain is conserved between the different family members while dedicated domains specific to each family regulate activity, for example promoting nucleosome eviction for INO80.

The ISWI family is capable of remodeling nucleosomes into a regularly spaced nucleosome array with approximately 20 base pair (bp) of DNA in between each nucleosome[1]. ISWI consists of five main functional regions, namely the ATPase domain, the NTR (N-terminal region), NegC (negative element at C-terminus), APB (acidic patch binding), and HSS (HAND-SANT-SLIDE) (Fig. 5.1a). The NTR region negatively regulates the ATPase domain, preventing ATP hydrolysis when it is not bound to the nucleosomes[2,3]. In its inactive form the NTR region binds both lobes of the ATPase domain in a conformation where the ATP catalytic regions of both lobes are separated[3,4] (Fig. 5.1b). While DNA only slightly activates ATP hydrolysis, full activation is only observed when the nucleosome is bound, including not only DNA binding but also binding of the H4 tail (Fig. 5.1b). The H4 tail is thought to compete with the L3 loop of the NTR region for a binding site on one of the ATPase lobes and can thus release the NTR[2,3,5–7]. Full activity also requires release of inhibition by NegC, through binding of at least 20 bp free linker DNA by the HSS domain[1,6,8]. The HSS domain is thought to act as a ruler to measure the distance between nucleosomes and thus regulate nucleosome spacing[1]. Lastly the APB motif located just in front of the HSS domain can bind the acidic patch on the nucleosome surface and is required for nucleosomes remodeling[9].

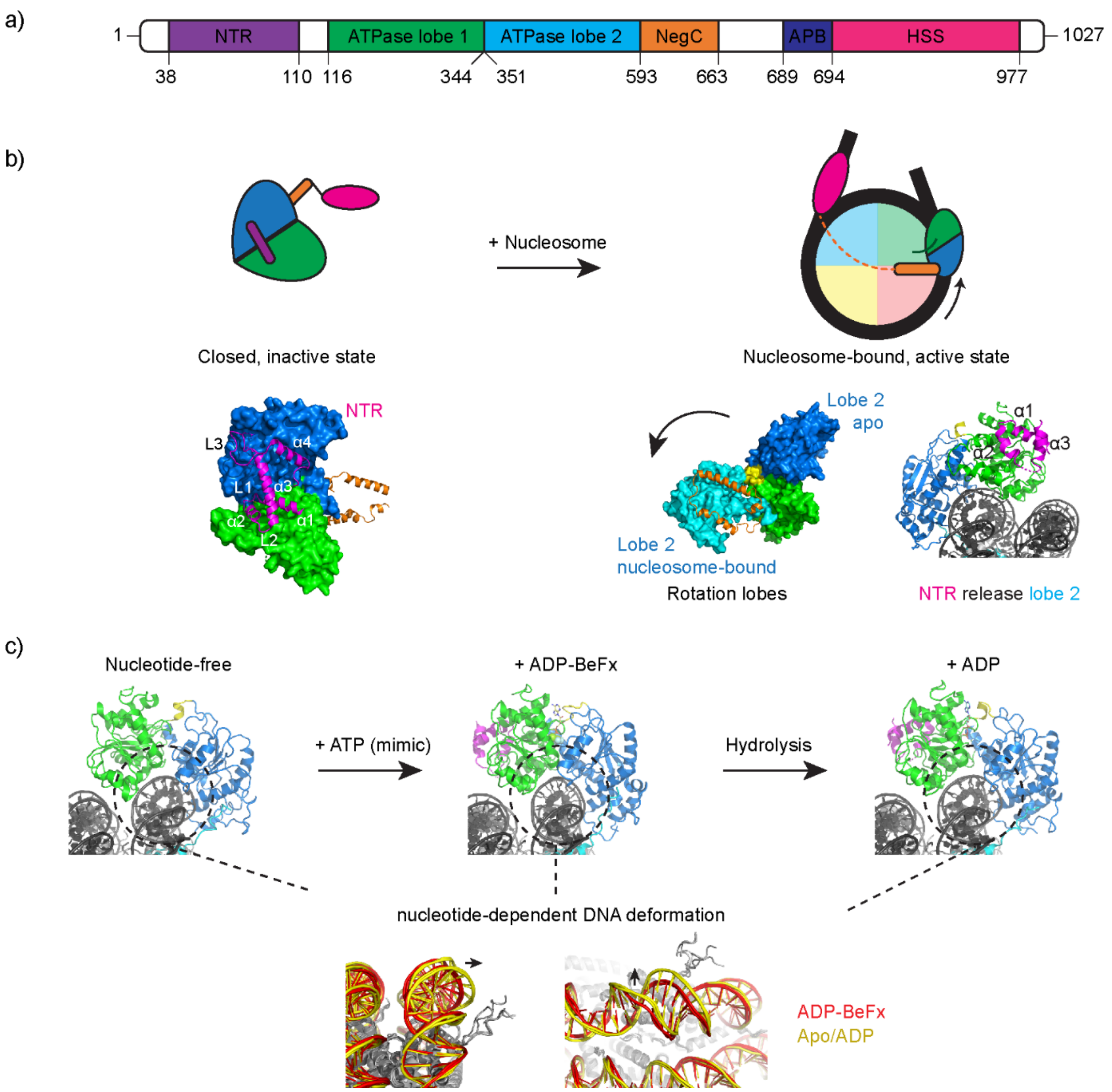
a)
1
NTR
ATPase lobe 1
ATPase lobe 2
NegC
APB
HSS
1027
38
110
116
344
351
593
663
689
694
977
b)
+ Nucleosome
Closed, inactive state
Nucleosome-bound, active state
NTR
L3
α4
L1
α3
α2
α1
L2
Lobe 2
apo
Lobe 2
nucleosome-bound
Rotation lobes
α1
α2
α3
NTR release lobe 2
c)
Nucleotide-free
+ ATP (mimic)
+ ADP-BeFx
Hydrolysis
+ ADP
nucleotide-dependent DNA deformation
ADP-BeFx
Apo/ADP

Figure 5.1. ISWI architecture and proposed remodeling mechanism. (a) Overview of ISWI architecture including residue numbers for *Dm.* ISWI, showing the N-terminal region (NTR), the two ATPase domain lobes, the NegC, the acidic patch binding region (ABP) and the Hand-Sant-Slide (HSS) domain. (b) Overview of ISWI activation upon substrate binding, showing cartoon on top with high-resolution structures below. (right) In the free enzyme, two ATPase lobes are locked in an inactive conformation by the NTR (specifically the L3 loop and α4 helix) preventing ATP hydrolysis. (left) Binding of binding of nucleosomal DNA and the H4-tail by ISWI results in conformational changes: the NTR is released from the lobe 2, allowing the two ATPase lobes to rotate compared to each other, activating the ATP hydrolysis. NegC inhibition to remodeling is released when the HSS domain can bind sufficiently long DNA linkers. (c) Comparison of structures of ISWI ATPase domain in complex with the nucleosome in nucleotide-free, APD-BeF$_x$ and ADP-bound states. Binding of ISWI in apo or ADP bound form causes conformational changes in the nucleosomal DNA at superhelix location (SHL) 2. Binding of ATP-mimic ADP-BeF$_x$ brings the two lobes of the ATPase domain closer together and reduces the conformational change of the DNA.

Over the last few decades, a large quantity of structural information has been obtained by biochemical assays and solving the structures of both free[4,10] and nucleosome bound forms of nucleosome remodelers[11–13]. The remodeling activity of ISWI depends on conformational changes within the protein. First to release autoinhibition and second to execute the remodeling itself. Autoinhibition requires conformational changes of the regulatory domains NegC, NTR and HSS, which often remain unresolved in the available structures. The NTR is structured in its inactive form[4] but becomes unresolved in the nucleosome bound state[11–13](Fig. 5.1b). Fixation (cross-linking) of the nucleosome complex in cryo-electron microscopy (cryo-EM) resolved the first three α-helixes to be bound to lobe 1 of the ATPase domain but the remainder of the NTR remained unresolved. In the free ISWI enzyme, the NegC domain also contains a structured region which was observed to bind lobe 2 of a second ISWI molecule in the crystal pacing[4] (Fig. 5.1b). Crosslinking data suggested however that in solution the NegC domain is bound intra-molecularly to lobe 2[7,14,15]. Similar to ISWI activation, nucleosome remodeling and DNA translocation require conformational changes. The recent structures have shown that binding of ISWI causes deformation in the nucleosomal DNA at its binding site at superhelix (SHL) 2 position[11–13] (Fig. 5.1c). Binding of ISWI with the ATP-mimic ADP-BeF_x, and potentially also ATP, does not induce this deformation of the DNA[11–13]. This DNA deformation is thought to be a mechanism by which the DNA can be translocated along the nucleosome by propagating this displacement along the DNA helix[12].

Despite this tremendous progress key questions still exist on both the activation mechanism and remodeling. The conformation of NegC, the mechanism of NegC inhibition and how local DNA deformation is translated to overall DNA movement is unclear. In addition, there is a debate on the role of conformational changes in the histone proteins of the nucleosome. While the high-resolution cryo-EM structures show no change in the histone octamer structure under the various nucleotide-bound state of the remodeler tested so far, other studies have indicated that the histone octamer is distorted during remodeling and that this plasticity is required for remodeling[13,16–18].

Here we studied the conformational dynamics of *Drosophila melanogaster* (*Dm.*) ISWI and the nucleosome by extensive NMR studies. We made use of an ISWI construct comprising residues 26-648 (75 kDa) that has been characterized as an autonomous remodeler[19]. This construct includes the NTR and NegC regions that inhibit ATPase activity domain in the free state of the enzyme but excludes the HSS domain that contributes to activation, remodeling and regulates the activity to allow nucleosome spacing. We found that NegC residue 643-648 are dispensable for inhibition, suggesting that the NegC operates different than is proposed for the CHD1 remodeler. We further find pervasive dynamics in the apo ISWI enzyme including in the ATPase lobes that may relate to remodeling activity. Our NMR data further indicate that the H4 tail binding mode is nucleotide dependent and sensitive to the NegC.

Importantly, our NMR data provide strong support for large scale conformational changes in the histone octamer upon binding of an active ISWI ATPase construct. Conformational line broadening is observed for residues in both histone-histone and histone-DNA contacts, highlighting the histone octamer as an allosteric unit and supporting the twist diffusion model of DNA translocation.

Results

Residues 643-648 in NegC are dispensable for auto-inhibition.

The crystal structure of ISWI revealed a molecular conformation of NegC in which NegC extends from the ISWI core to bind a second ISWI molecule through a crystal contact[20]. In solution, cross-linking mass-spectrometry (XL-MS) and small-angle X-ray scattering (SAXS) however demonstrated that NegC is packed directly to ISWI core[7,14,15]. This suggested that the ISWI NegC conformation may resemble that observed in CHD1, in which the equivalent region passes over the lobes using a so-called bridge helix to bind lobe1[21]. The data so far indicated the NegC has a structured region from residue 617 to 697 that is involved in the inhibition of the ATPase domain[2,19]. Possibly, ISWI remodelers use a similar mechanism as CHD1 in which NegC binds lobe 2 and spans to lobe 1 locking the ATPase domain in an inactive state[21]. To explore this further, we first constructed a molecular model of ISWI NegC using the CHD1 structure as a template. In this model residues 643 to 648 bind lobe 1, suggesting these residues are key to NegC inhibition (Fig. 5.2a). To test this model, we made deletion mutants where residues after 642 were deleted (ISWI^{642}, residue 26-642) and tested its activity in a remodeling assay, taking the full-length (ISWI^{FL}), the inhibited construct ISWI^{648} (residue 26-648) and a known NegC activated construct (ISWI^{617}, residues 26-617) as control. Remodeling activity was tested on a nucleosome array with 15 nucleosomes, spaced 50bp apart with a AvaI restriction enzyme site centered in between each pair of nucleosomes (Fig. 5.2b). In absence of remodeling, incubation with AvaI will eventually result in complete digestion of the array, resulting in mononucleosomal DNA fragments as digestion product. Upon addition of ISWI, remodeling to 20bp linker DNA length will obscure some of the AvaI restriction sites and thus result in longer digestion products and a decrease of mononucleosomal products. Indeed, incubation with ISWI^{FL} results in formation of longer DNA fragments, with remodeling speed dependent on ISWI concentration (Fig. 5.2c,d): at 30 nM a gradual increase is observed while at 300 nM remodeling occurs rapidly within a few minutes. Removal of the HSS domain in the ISWI^{648} construct impedes the release of NegC inhibition in the ISWI648 construct (Fig. 5.2d,e), resulting in only very slight activity within the time frame, with significant remodeling only occurring after overnight incubation (Fig. 5.1). In contrast, truncation of NegC to residue 593-617 (ISWI^{617}) resulted in remodeling intermediate between ISWI^{648} and ISWI^{FL} (Fig. 5.2d,e), as previously observed[2]. When we tested the ISWI^{642} construct a low remodeling activity was observed, similar to the ISWI^{648} construct (Fig. 5.2d,e). While the truncation increased activity slightly, the data indicates that deletion of residues

642-68 is insufficient to release NegC inhibition. We conclude that residues up to 642 are sufficient to inhibit remodeling activity, suggesting in turn that the ISWI NegC performs a different or additional mode of inhibition distinct from that described for CHD1.

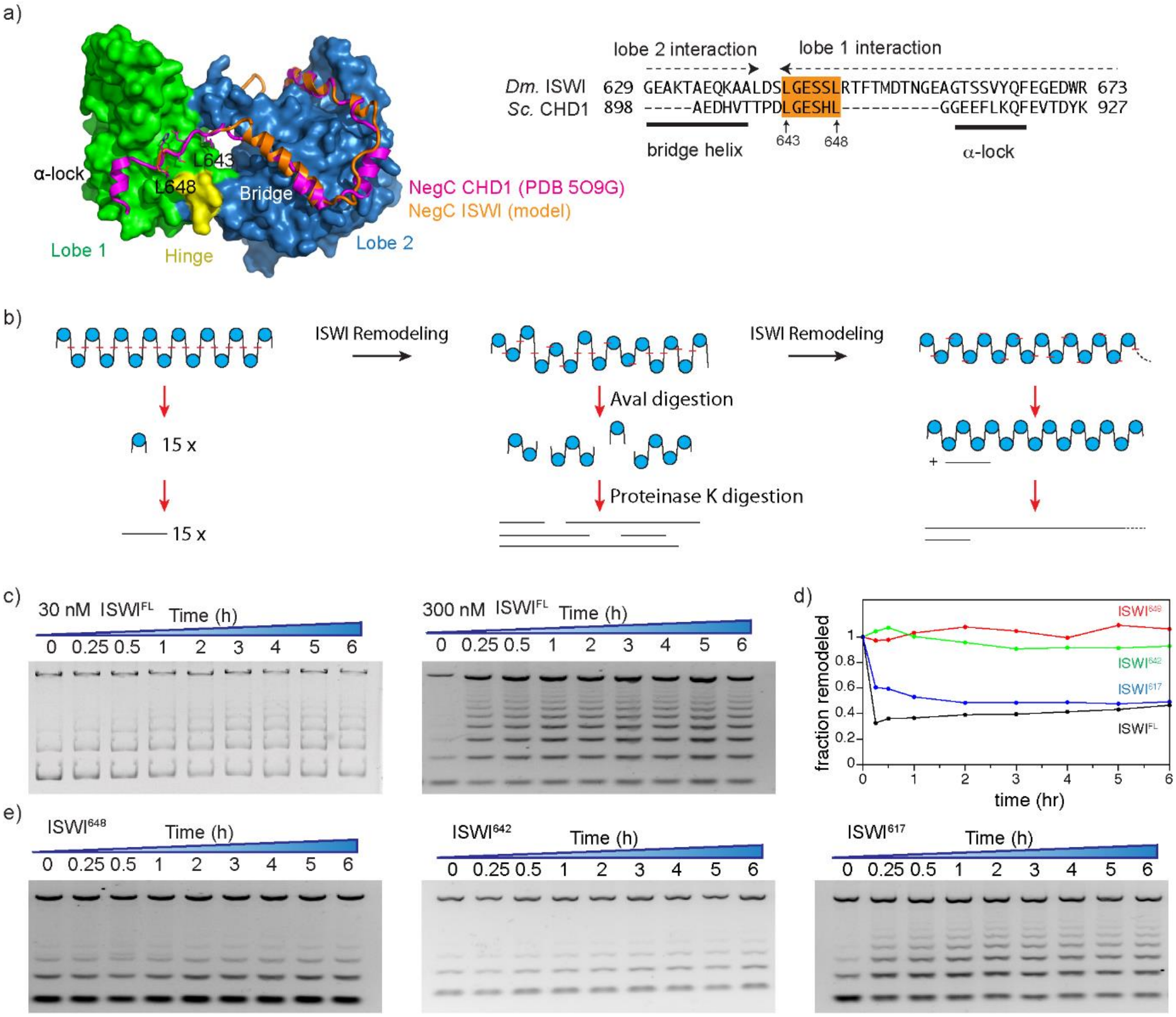
a)
α-lock
L643
L648
Bridge
Lobe 1
Hinge
Lobe 2
NegC CHD1 (PDB 5O9G)
NegC ISWI (model)
lobe 2 interaction
lobe 1 interaction
Dm. ISWI 629 GEAKTAEQKAALDSLGESSLRTFTMDTNGEAGTSSVYQFEGEDWR 673
Sc. CHD1 898 -----AEDHVTTPDLGESHL-----------GGEEFLKQFEVTDYK 927
bridge helix
643
648
α-lock
b)
ISWI Remodeling
ISWI Remodeling
15 x
AvaI digestion
Proteinase K digestion
15 x
+
c)
30 nM ISWI^FL
Time (h)
0 0.25 0.5 1 2 3 4 5 6
300 nM ISWI^FL
Time (h)
0 0.25 0.5 1 2 3 4 5 6
d)
fraction remodeled
0
0.2
0.4
0.6
0.8
1
time (hr)
0 1 2 3 4 5 6
ISWI^648
ISWI^642
ISWI^617
ISWI^FL
e)
ISWI^648
Time (h)
0 0.25 0.5 1 2 3 4 5 6
ISWI^642
Time (h)
0 0.25 0.5 1 2 3 4 5 6
ISWI^617
Time (h)
0 0.25 0.5 1 2 3 4 5 6

Figure 5.2. ISWI NegC residues 643-648 only modestly contribute to inhibition. (a) Molecular model of ISWI NegC based on the CHD1 NegC conformation. Sequence alignment shown on the right. Color coding and selected residues indicated. (b) Overview of the remodeling assay based on restriction of 15x197bp nucleosomal array. Remodeling of the array by ISWI results in protection of the AvaI cut-sites and this an increase in longer DNA fragments, resolved by gel electrophoresis. (c) Gel electrophoresis results for full-length ISWI at 30 nM (left) and 300 nM (right) concentration showing that ISWI is active. Top band is from the unrestricted vector backbone that serves as loading control. Lowest band corresponds to the 197bp DNA fragment. (d) Quantification of the remodeling activity shown in (c) and (e), with fraction remodeled calculated as the intensity of the 197bp DNA fragment, relative to loading control, normalized to 1 at time point 0. Normalization against digestion products obtained in absence of ATP gives similar results. (e) Gel electrophoresis results for indicated truncation mutations of ISWI showing that deletion of residues 643-648 results in slight increase of activity but is insufficient to recover activity to same extent as truncation to residue 617.

Few highly dynamic regions in free ISWI^{648}

To investigate the conformation and dynamics of ISWI in more detail we turned to NMR experiments. The *Dm.* ISWI 26-648 construct, hereafter referred to as ISWI^{648}, could be expressed and purified to sufficient yields and is sufficiently stable to allow NMR studies (Fig. 5.2). We previously reported an NMR study of free ISWI, pointing to the presence of few highly flexible regions within the remodeler (Ch. 4, Thesis Clara van Emmerik[22]). Most of the observed NMR signals could be assigned to specific residues in the protein (see also Ch. 4, Thesis Clara van Emmerik[22]). We here transferred these assignment from an NMR-optimized buffer (20 mM KPi pH 6.8, 100 mM KCl, 1 mM DTT, 0.01% NaN_3, 5% D_2O) to a buffer where ISWI^{648} is more active and more stable (20 mM Tris, pH 7.6, 140 mM KCl, 1 mM $MgCl_2$, 0.1 mM EDTA, 0.01% NaN_3, 5% D_2O) including 1 mM ADP-BeF_x as ATP mimic, resulting in assignment for 38 residues out ~51 observed resonances (Fig. 5.3a). These data show that the terminal 7 residues (642-648) in the NegC region are dynamic with flexibility increasing when progressing towards the C-terminus. This suggests that NegC is stably bound to the ATPase lobes up to residue S641 with the terminal residues either unbound or loosely associated with the ATPase lobes. These observations are in line with activity data that residues 643-648 are dispensable for auto-inhibition (Fig. 2). Furthermore, the data support the structural model in which the NegC region is bound to the core of the protein[23], refining the stably bound NegC region to include residues up to 637.

In addition, clear resonances are observed for residues 31-38, 66-88 in the N-terminal region (NTR), and 387-389 in a loop of lobe 2, indicating these are highly dynamic in the free state. Like NegC, the NTR plays an important role in inhibiting enzyme activity by tethering the two ATPase lobes. In particular, residues 66-88 in the NTR region includes a region that forms a structured α-helix in the crystal structure of *Mt.* ISWI bridging between the two lobes[20] (Fig. 5.3b). The NMR data demonstrate that this bridging element is unstructured and highly dynamic in for Dm. ISWI^{648}, which is likely related to the proline-rich sequence in this region in the *Dm.* enzyme (Fig. 5.3b). Finally, the flexibility of residues 387-388 in loop 2 of lobe 2 may play a role in facilitating binding to H3 when engaged with the nucleosome[11] (Fig. 5.3c). Together these data indicate that ISWI^{648} contains only few highly dynamic and disordered regions which in turn supports a packed conformation of the NTR and NegC together with the ATPase lobe.

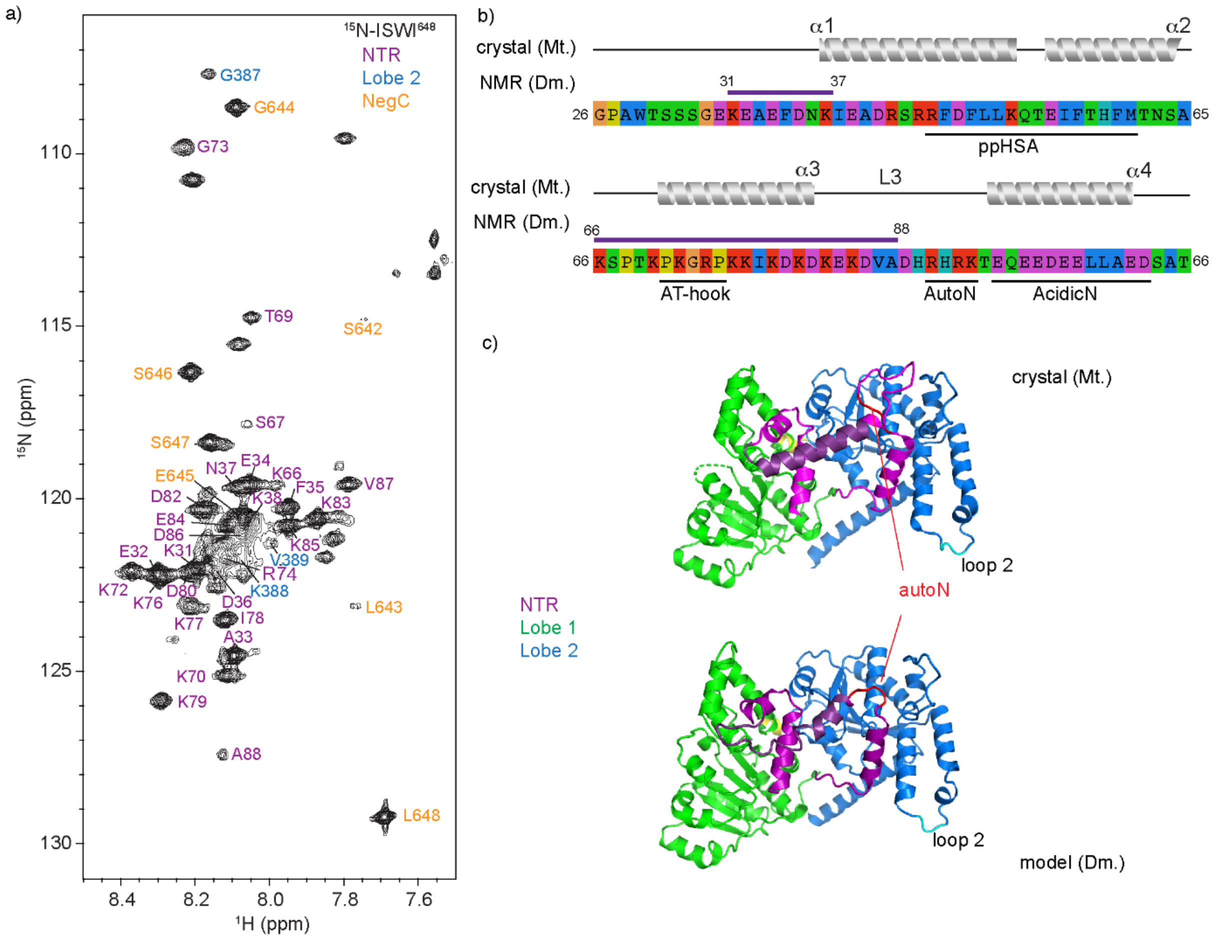

Figure 5.3: NMR detection of highly flexible regions in ISWI^{648}. (a) 2D ^{15}N,^{1}H TROSY NMR spectrum of ^{15}N-labeled ISWI^{648} including assignments color coded according to ISWI region. (b) Amino acid sequence of *Dm*. NTR with corresponding secondary structure in the *Mt*. ISWI crystal structure indicated. The regions observed in NMR are indicated with a purple thick line and are coil/loop regions according to backbone chemical shifts. (c) Structure of the NTR and loop 2 (protrusion or insertion loop) in Lobe 2 in the free Mt. ISWI crystal structure (top) and a *Dm*. ISWI homology model (bottom). Dark colored purple α3-helix in NTR and light blue part of the protrusion loop are highly dynamic coil regions in Dm. ISWI^{648}.

Pervasive slow motions in free ISWI^{648}

To probe the conformational dynamics in ISWI^{648} more thoroughly we resorted to the methyl-TROSY (transverse relaxation optimized spectroscopy) approach[24]. ISWI^{648} was fully deuterated except for the isoleucine δ1 methyl groups which were ^{1}H/^{13}C labeled. ISWI^{648} contains 39 Ile residues that are well distributed, providing probes of conformational dynamics in all functional regions of the protein (Fig. 5.4a,b). The methyl-TROSY spectrum of ISWI^{648} resulted in a mostly well resolved spectrum (Fig. 5.4c and S5.3). Interestingly, at low (5 °C), but not at higher (20 °C) temperature, clear NOE cross-peaks were observed in a 3D NOESY experiment, despite the increased line widths at lower temperature. This suggests that ISWI^{648} is more stably folded at 5 °C compared to 20 °C and we thus carried out further experiments at the lower temperature. At 5 °C, 35 of the 39 expected peaks appear intensely. In total, 15 Ileδ1 assignments could be made based on mutagenesis in combination with comparison of the observed NOE cross-peak pattern to the methyl network in the free ISWI structure, and analysis of the chemical shifts and their perturbations upon mutagenesis and nucleotide binding (see Materials and Methods) (Fig. 5.4c). The assigned methyl groups are distributed across lobe 1, lobe 2 and the NegC (see also Fig. 5.4a,b). Inspection of the peak intensities and line shapes reveals that I380 has very narrow line with and highest peak intensity, indicating that it is increased flexible, in line with its position close to the dynamic loop 2 in lobe 2. Several residues appear broad (e.g I255 and I622) and have lower than average intensities suggestive of the presence of conformational dynamics.

To probe these slow motions more quantitatively we employed a CPMG (Carr-Purcell-Meiboom-Gill) relaxation dispersion experiment. Dispersion of the effective transverse relaxation rate ($R_{2,eff}$) of a certain NMR signal as a function of CPMG pulsing rate occurs when that signal experiences two or more distinct chemical environments that interconvert in the µs-ms time scale[25]. Notably, these experiments are very sensitive to such conformational exchange processes, such that even when a protein exists in an alternate conformation for only a few percent of the time, this may already be detected. Of the 33 peak quantified, 17 exhibit a significant dispersion of $R_{2,eff}$ values ($\chi^2_{\mathrm{red}} > 4$ for a fit to a straight line), indicative of the presence of conformational exchange throughout the protein. Out of the 18 unassigned resonances, 10 show significant dispersion, with $\Delta R_{2,eff}$ ($R_{2,eff}$ at slowest pulsing rate – $R_{2,eff}$ at highest pulsing rate) from 6 up to 70 s^{-1} (Fig. 4d). Only 4 of the unassigned resonance show a good fit to a straight line ($\chi^2_{\mathrm{red}} < 2$ and $\Delta R_{2,eff} < 10$), indicating absence of significant conformational exchange induced line broadening. Of the 15 assigned resonances, 7 show significant dispersion with $\Delta R_{2,eff}$ ranging from 8 to 80 s^{-1} and another 7 show a good fit to a no-exchange model (Fig. 5.4d). The largest exchange contribution occurs for residue I255 and I622. Residue I255 is in the core of lobe 1 and positioned close to the ATP binding pocket while I622 is in the NegC bridge helix in the part that is bound to lobe 2. The conformational heterogeneity at the NegC-lobe 2 interaction is interesting as it suggests that NegC is dynamically bound to lobe 2, which may be important for the release of NegC inhibition upon nucleosome binding. These dynamics may also explain why NegC is generally not observed in any of the recent ISWI cryo-EM structures.

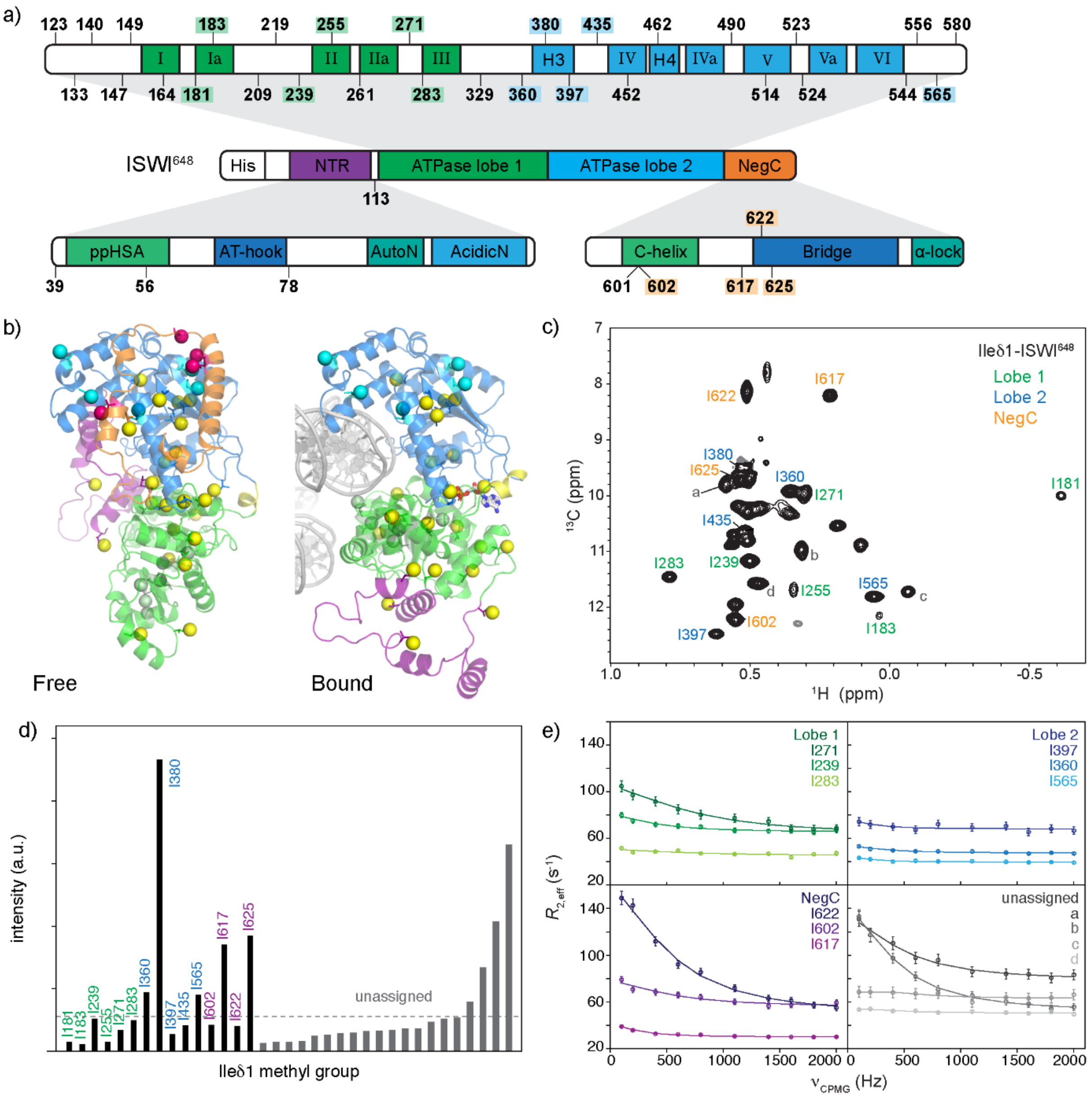

Figure 5.4. Methyl-TROSY NMR of ISWI648 reveals pervasive conformational exchange. (a) Distribution of Ile residues in the amino acid sequence. Numbers indicate position of Ile residues. Assigned residues are indicated with colored background. (b) Distribution of Ile residues in the ISWI^{648} structure in free and nucleosome-bound state (modeled on PDB 6JYL; excluding the NegC for which position is unknown upon nucleosome binding). Unassigned Ile residues shown as yellow spheres, assigned residues indicated with region high-light colors. (c) Methyl-TROSY NMR spectrum of ISWI^{648} with assignments indicated. Peaks labeled a-d are unassigned and highlighted in panel (e). (d) Peak intensities in methyl-TROSY ISWI648 spectrum. (e) Selected ^{13}C,^{1}H MQ CPMG relaxation dispersion profiles showing evidence for significant conformational dynamics in the µs-ms time scale.

Conformational changes in ISWI^{648} NTR and NegC upon nucleosome binding

The auto-inhibition of ISWI is released upon nucleosome binding through large conformational changes involving release of the inhibiting NTR and NegC tethers (see Fig. 5.1). The position and interactions of the NTR and NegC have not been resolved in the ISWI-nucleosome structures obtained so far. We previously found that addition of DNA only to ISWI^{648} results in spectral changes for the NTR that indicate DNA-binding, in particular for its AT-hook (Thesis Clara van Emmerik, Chapter 4[22]). In addition, we then observed that DNA binding induces two conformational states of the flexible C-terminal end of NegC.

We here examined structural changes in NTR and NegC upon activation by addition of nucleosomes to ^{15}N-labeled ISWI^{648} in presence of 1 mM ADP-BeF$_x$ as an ATP-mimic[26]. We further use nucleosomes reconstituted in vitro from *Xenopus laevis (Xl.)* histones with a 167 bp DNA fragment corresponding to the Widom 601 strong positioning sequence[27], i.e. with 10 bp linker DNA at each end. Overall, the peak intensity of most resonances decreased, in line with complex formation (the molecular weight of the ISWI-nucleosome complex is 285 kDa for singly bound ISWI^{648} and 361 kDa for doubly bound ISWI^{648}) (Fig. 5.5). Some resonances, such G387 in the lobe 2 insertion loop disappeared, which is in line with binding of this loop to H3 in the nucleosome complex. Within the NTR, resonances for the N-terminal residues (res. 31-27) as well the residues flanking the ppHSA helix (res. 66-67) showed strongly reduced peak intensity without significant chemical shift perturbations (CSPs) (Fig. 5.5b,c). The reduction of peak intensity indicates the NTR domain is involved in interactions with the nucleosome. The strongest CSPs were observed for residues flanking the AT-hook, while residues R74, K76 and K77 that are part of the AT hook showed no CSP but the largest reduction in peak intensity upon nucleosome binding. For IDR regions involved in interactions such pattern of peak intensity loss for the directly involved region and CPSs for the flanking regions is typical[28]. Moreover, the pattern of CSPs and changes in peak intensity closely mirror those observed earlier upon DNA binding (Thesis Clara van Emmerik, Chapter 4[22]), suggesting the AT-hook in the NTR is bound to the nucleosomal DNA.

Strikingly, residues V87 and A88 that connect to the autoN motif also displayed an increase in peak intensity (up to 3.5x more) indicating an increase in flexibility. Furthermore, several resonances appeared that we could not track during the titration, suggesting that these originate from residues that were rigid within the free enzyme but become highly flexible upon nucleosome binding (Fig. 5.5a). Together, these observations favor the model that upon nucleosome binding, interaction with the H4 tail displaces the autoN motif from lobe 2[2,3,5–7], resulting in release of the NTR tether, DNA binding of the AT-hook and increased flexibility of the autoN and flanking regions.

Upon addition of nucleosome, we also observed gradual appearance of new resonances in the direct proximity of the peaks for NegC residues 646-648. Interestingly, at 2 molar equivalents nucleosomes added, where ISWI should be fully bound, both original and new peaks are present, indicating the presence of two distinct conformations of this flexible part of NegC in the nucleosome bound state. We previously observed the same peak doubling upon DNA-binding with full conversion to the new conformational state upon saturation with H4 tail peptide (Thesis Clara van Emmerik, Chapter 4[22]), suggesting that ISWI^{648} in the current state is not fully engaged with the H4 tail.

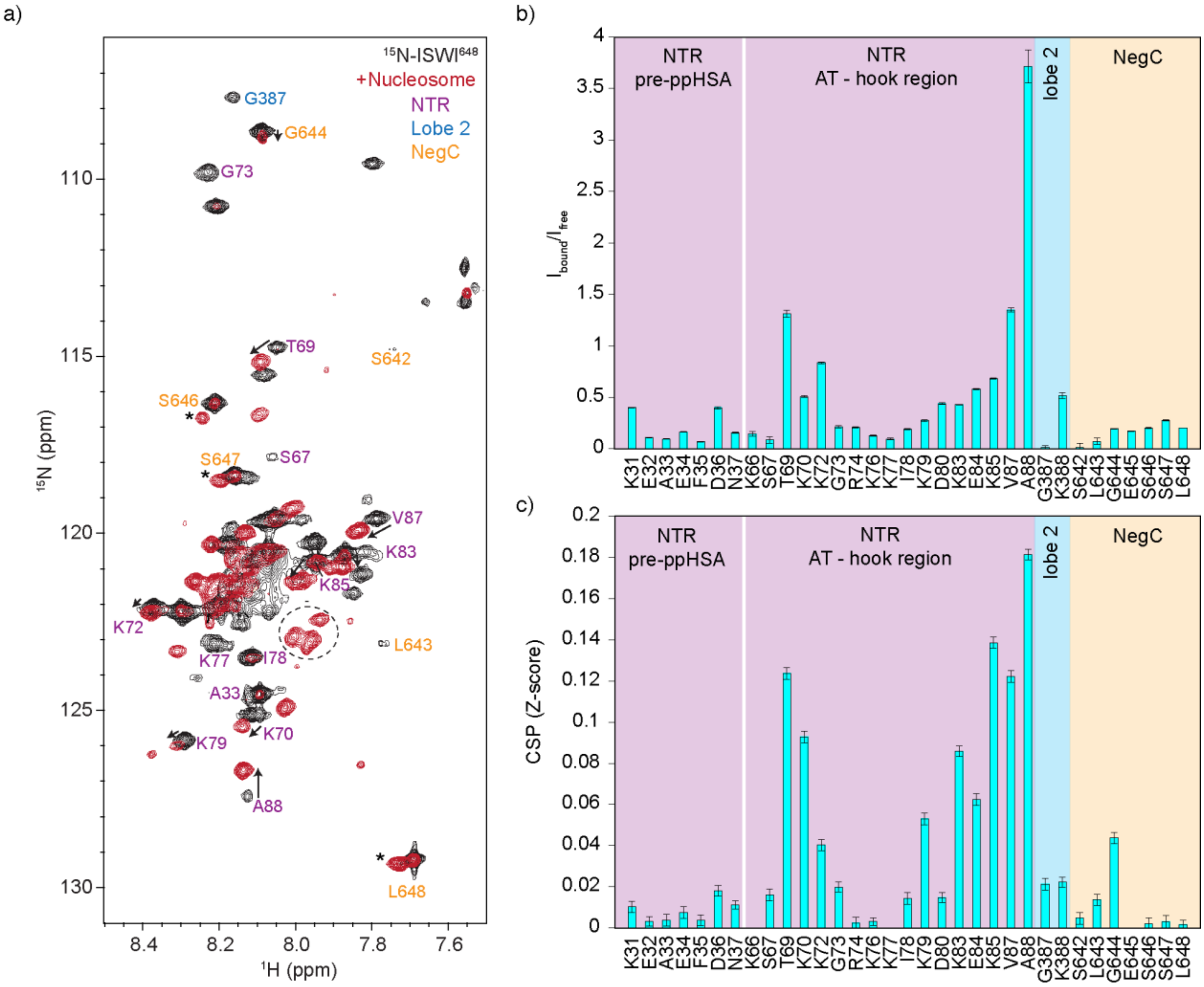

Figure 5.5. Release of NTR and alternative NegC conformation upon nucleosome binding. (a) Overlay of 15N spectra of free and nucleosome bound ISWI. Multiple peaks shift, disappear or show multiple peaks upon binding of nucleosomes. Arrows indicate chemical shift perturbations and stars indicate peak doubling for NegC residues. Dashed area indicates new peaks that become observable in the nucleosome-bound state. (b, c) ISWI peak intensity changes (b) and CSPs (c) upon nucleosome binding, highlighting signal loss in the AT-hook region with significant CSPs for the flanking regions and increase of signal for residues close to the autoN motif.

Conformational changes in ISWI^{648} ATPase lobes upon nucleosome binding

To probe the conformational changes within the ATPase lobes upon nucleosome binding, we returned to the Ileδ1-labeled ISWI and followed spectral changes upon addition of nucleosomes containing fully deuterated histones but protonated DNA in presence of 1 mM ADP-BeF$_x$. We first added ADP and then BeFx to nucleotide-free ISWI^{648} and noted clear chemical shift changes for two unassigned resonances, and residues I181, I183, I255 and I283 which are relatively close to the ATP binding site (Fig. 5.6a).

Interestingly, the addition of BeF_x seemed to stabilize binding as the intensity of several first decreased upon ADP addition and then increase upon addition of BeF_x (see I183 and I255 in Fig. 5.6a). Subsequent addition of nucleosomes up to 1 molar equivalent resulted in rapid loss of peak intensities, consistent with formation of 285 kDa complex (Fig. 5.6b, c). Given that the linewidth in methyl-TROSY experiments is dominated by dipolar interaction between the residual protons[29], the approximate fourfold increase in molecular mass (from 75 to 285 kDa) can be expected to also increase line widths four-fold upon nucleosome binding. With this simple reasoning, we would expect a drop in peak intensity of the square of that increase, or 16x, corresponding to a residual signal that is 6% of the initial intensity. On average the observed signal in the bound state is in this range, with exception of I380, which has significantly higher intensity, indicative of flexibility in the complex.

Consistent with the sparsity of Ileδ1-methyl groups near the DNA binding interface we observed only few, very small chemical shift changes upon binding. Based on the nucleosome bound ISWI model in Figure 5.4b, there is no ISWI methyl residues in direct proximity of the DNA except I239 and I271 in lobe 1 and I397 and I380 in lobe 2 a bit distant from the DNA. Consistent with this model, the strongest CSPs are observed for I239, I271, with most change occurring in the last titration going from 2:1 to 1:1 ISWI to nucleosome ratio. Also notable is the CSP for I255 which is in the central β-sheet of lobe 1. Focusing on the assigned residues in the NegC region, for residues 602, 617 and 622 neither CSPs nor peak doubling or particularly low or high intensities are observed. This indicates that conformational line broadening observed in the free-state is not significantly altered in the nucleosome-bound state, in contrast to the increased conformational heterogeneity for the C-terminal segment 642-648.

Nucleotide-state dependent H4 tail conformation in the ISWI–nucleosome complex

Before examining impact of ISWI on the histone conformation upon nucleosome binding in more detail, we first wanted to verify that ISWI is engaged in its functional binding mode by monitoring H4 tail binding. To also study the histone core, we designed a tailored labeling scheme in which the Leu and Val-methyl groups of H2B and the Ileδ1 methyl goups of H3 were isotope labeled in combination with ^{15}N-labeling of H4, in a fully deuterated background (Fig. 5.7).

Under our conditions, ^{15}N-based spectra of H4 show ~16 peaks of which some are heavily overlapping, corresponding to the highly flexible part of H4 (Fig. 7a). Previous studies showed that residues 1-15 of the H4 N-terminal tail can observed[30]. The $R^{17}H^{18}R^{19}K^{20}$ sequence that is bound by ISWI could not be observed, except upon K16Q mutation to disrupt tight binding to the nucleosomal DNA[30]. Using these data as a reference, we could trace the peaks for residues 3-15 and for R17 in our spectra. In addition, several weak new signals were observed indicating that under conditions (I = 150 mM) the H4 tail is more dynamic and less tightly bound to DNA.

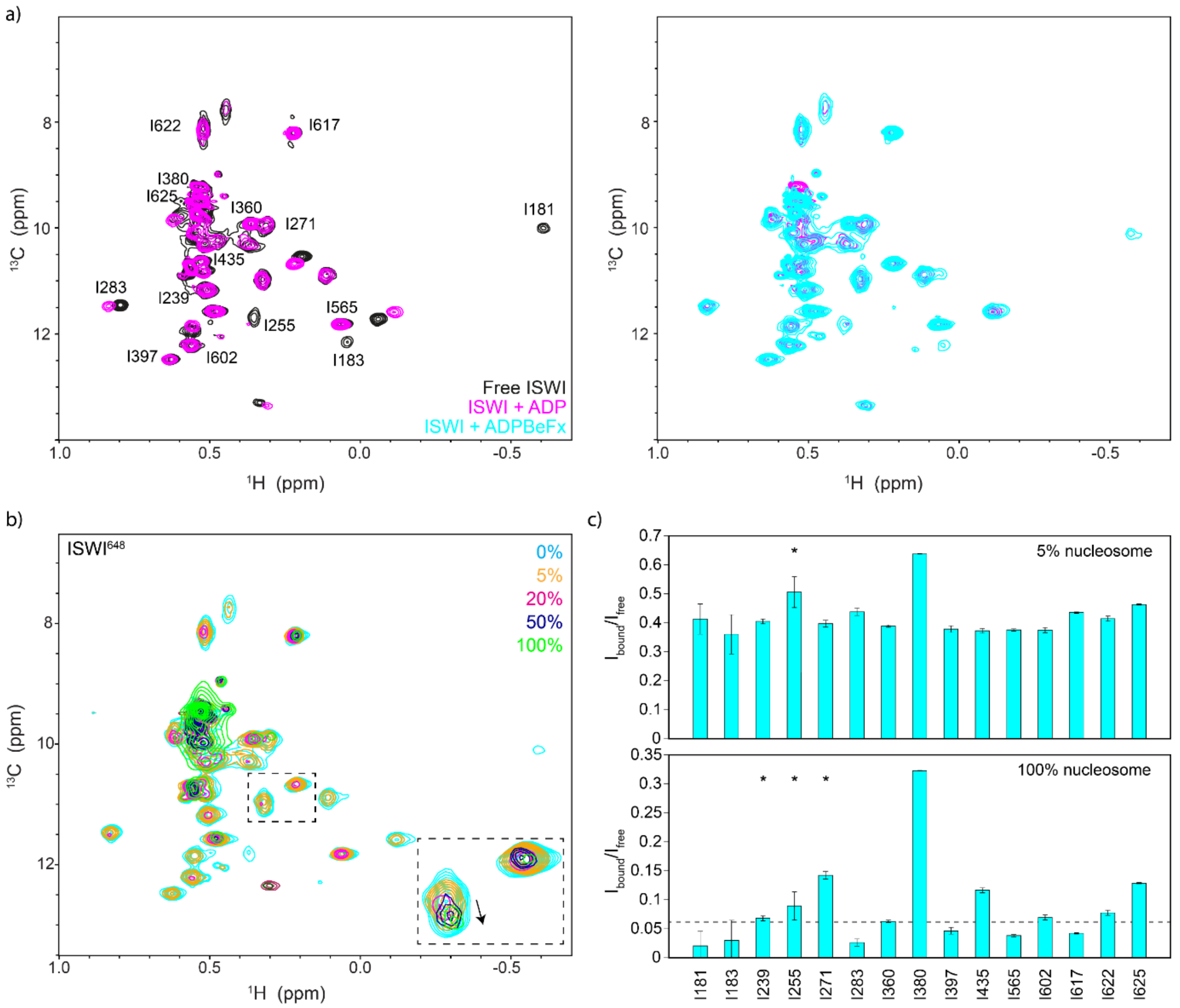

Figure 5.6: Nucleosome binding results in large signal loss for ISWI^{648} Ileδ1 methyl groups without much chemical shift perturbations. (a) ADP and ADP-BeFx addition to free ISWI. Adding ADP to ISWI causes several chemical shift perturbations and a decrease of signal intensity for several peaks. Adding additionally BeFx does not result in extra chemical shift perturbations but results in an increase in signal intensity compared to ISWI with ADP. (b) Overlay of ISWI^{648} methyl-TROSY spectra with increasing amounts of nucleosome (deuterated histones, protonated DNA) up to a 1:1 molar ratio in the presence of ADP-BeFx. The inset shows a zoom on a large CSP for and unassigned residue. (c) Intensity changes for ISWI resonances at 5% and 100% nucleosomes added. Stars indicate residues that have a chemical shift perturbation.

Rather surprisingly, addition of 2 molar equivalent of ISWI^{648} resulted in little changes in the H4 spectrum, except for the appearance of a new peak, labeled 'X' in figure 5.7a. Addition of ISWI^{617} (2 equivalents) and ISWI^{FL} (1 equivalent) confirmed that the appearance of the new peak is not specific to the ISWI construct but is a general feature upon nucleosome binding. This peak must originate from H4 as ISWI is not ^{15}N-labeled in these experiments and moreover did not show any resonances at these chemical shifts in free or bound forms (see Fig. 5.5a). As none of the observed peaks showed a marked decrease in intensity upon ISWI binding, the new peak cannot be result of peak doubling but instead must originate from a H4 residue that was unobservable in the free state. The available ISWI-nucleosome structures show that ISWI binding ‘lifts’ the H4 tail from the nucleosome surface, introducing a hinge around residues V21 and L22. We hypothesize that ISWI binding induces increased flexibility at this hinge and that the new peak is either from V21 or L22. Intriguingly, the H4R17 resonance showed no significant changes in chemical shift or intensity upon addition of the different ISWI constructs, suggesting that H4 tail-binding is centered on residues 18-20 in these conditions and R17 remains flexible.

The recent structures of ISWI-nucleosome complexes[11–13] showed different H4 tail conformations also depending on the nucleotide state of the enzyme. To test whether nucleotide-binding would influence the H4 tail binding mode, we recorded spectra of the H4 tail bound to the different ISWI constructs again but this time in presence of 1 mM ADP-BeFx. Addition of the ATP-mimic resulted in a clear CSP for the new peak X and large drop in intensity for residues L10 and R17. Peak intensity decreased most for the full-length construct. The intensity loss for R17 indicates that nucleotide binding induces a more rigid engagement of the H4 tail. Together these data show that ISWI binds the H4 tail in a nucleotide-dependent manner. Sensitivity to the nucleotide state could be relevant for the remodeling.

Active ISWI ATPase perturbs histone-histone and histone-DNA contacts large scale

Having established that ISWI binds the nucleosome at SHL2 and engages the H4 tail, we next examined the conformational dynamics in the histone core upon ISWI binding. We used nucleosomes with H2B LV-labeled and H3 Ileδ1-labeled. With these ’hybrid’-labeled nucleosomes conformational changes in the histone-DNA interfaces, in particular near the dyad and SHL 4-5 can be monitored, as well changes in histone-histone interfaces near the H3-H3’ interface, within the H3-H4 dimer, in the H2B-H4 interface and within the H2A-H2B dimer including the acidic patch region.

We obtained high-quality methyl-TROSY spectra for these samples (Fig. S6). Assignments for H2B Leu and Val resonances were transferred from Chapter 3 and H3 Ile resonances were transferred from Kato et al.[31]. Although the sensitivity is reduced at the salt concentration used in this study (*I* ~ 150 mM) compared to low-ionic strength conditions (see Chapter 3), the sensitivity and resolution are more than adequate to follow spectral changes in a residue-specific manner. Further experiments showed that the nucleosome-ISWI^{FL} complex remained stable up to but not at more than an equimolar ratio, while addition of two molar equivalents of ISWI^{617} or ISWI^{648} resulted in stable complexes (data not shown).

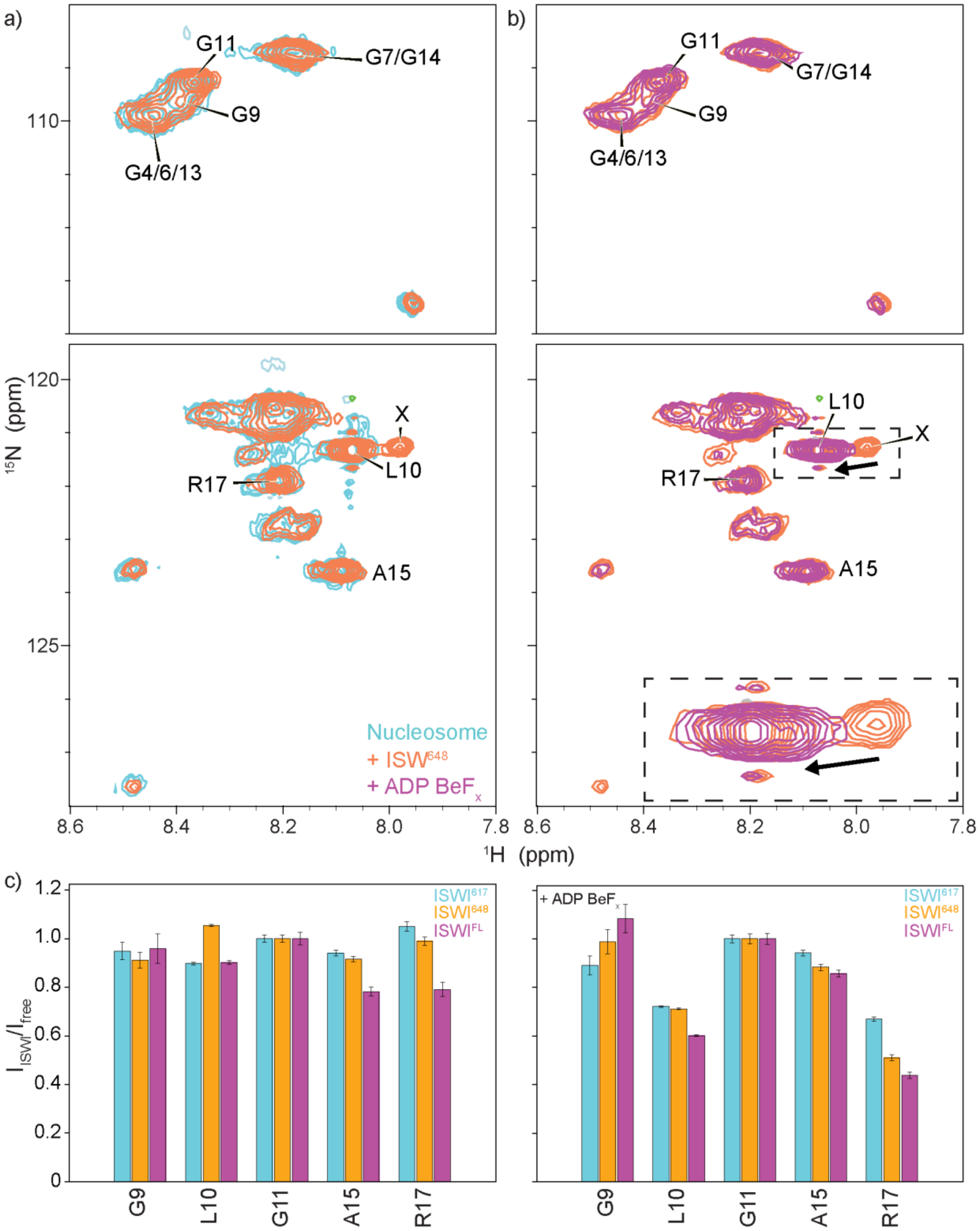

Figure 5.7: ISWI interacts and causes a conformational change in the nucleosome H4 tail. (a) Overlay of 2D ^{15}N,^{1}H-TROSY spectra of nucleosomes with 15N-labeled H4, free after addition of ISWI^{648} showing a new peak appear for the H4 tail (marked ‘X’) in presence ISWI to the nucleosome. (b) 15N spectra of ISWI bound nucleosomes with and without ADP-BeFx show a shift in peak X upon addition of ADP-BeFx, see inset for magnification. (c) Peak intensity ratios between free and bound nucleosomes for ISWI 617, 648 and FL showing no large change in peak intensities. (d) Peak intensity between free and bound nucleosomes in the presence of ADP-BeFx show a decrease of intensity specifically for residue L10 and R17 for all tested ISWI constructs.

In the labeling setup, there are no histone methyl probes close to the DNA at SHL 2, where ISWI binds and induces a DNA bulge in the nucleotide-free and ADP-bound states[11–13]. Still, for many histone methyl groups we observed a clear drop in peak intensity. As was argued before[16], such peak intensity losses are due to increased line broadening due to conformational dynamics within the histone core. In absence of ADP-BeF$_x$, the ISWI constructs generate similar intensity profiles, in particular for ISWI^{617} and ISWI^{FL} (Fig. 5.8 and S5.6). This indicates that the ATPase core in ISWI^{FL} has the same binding mode as in the truncated ISWI^{617}, despite the lack of linker DNA to release NegC based ATPase inhibition via DNA-binding of the HSS domain. Possibly, the HSS domain in ISWI^{FL} is bound to the nucleosomal DNA elsewhere and still able alter NegC conformation as when it would bind linker DNA. Given the similarity in histone peak intensity profile to ISWI^{617} we exclude that the HSS binds near the dyad, SHL 4-5 or near the acidic patch. Both ISWI^{FL} and ISWI^{617} show largest conformational line broadening near SHL5, suggesting conformational changes within the H3-H4 tetramer (Fig. 5.8a,c). Addition of ISWI^{648} resulted in more pronounced peak broadening both within H2A-H2B and H3-H4 throughout the histone core (Fig. 5.8b). This suggests that without the HSS domain, NegC alters the ATPase lobe conformation and nucleosome binding mode, resulting in more conformational strain within the histone octamer.

To understand whether the observed conformational line broadening is related the DNA deformation at SHL2 in the nucleotide-free ISWI-bound state, we next added ATP-mimic ADP-BeF$_x$ to these complexes. In presence of this ATP mimic the ATPase lobe orientation is altered and the DNA deformation at SHL2 is lost, resulting in DNA conformation close to that of the free nucleosome[13,32]. This would suggest that also histone-histone and histone-DNA contacts would be returned to their apo state. An 8.4 Å cryo-EM structure of ADP-BeFx-bound human ISWI isoform Snf2H in complex with the nucleosome suggested however that the helical bundles in H2A-H2B and H3-4H are distorted and conformational heterogeneous[11]. We observed that addition of ADP-BeF$_x$ to the nucleosome-ISWI^{FL} complex increases line broadening for methyl groups in two distinct sites in the histone octamer: H2B residues L77, L97 and L98, which localize near the acidic patch and the H2B-H4 interface and H3 I119 within the H3-H4 tetramer (Fig. 5.8a). This may reflect a difference in binding mode for the auxiliary domains (e.g. the acidic patch binding motif) upon ADP-BeFx binding or may be an indirect effect caused by conformational changes in the histone octamer, as was observed for Snf2H.

The nucleosome-ISWI^{648} complex has fewer changes in peak intensity when ADP-BeF$_x$ is added (Fig. 5.8b). Residues in the H2A-H2B interface increase in intensity. Additionally, residues in the core of H3, not near the nucleosomal DNA, show a decrease in intensity indicating increased conformational heterogeneity within H3-H4. Overall, conformational line broadening occurs throughout the histone octamer, both within H2A-H2B and within H3-H4, largely for the same residues as seen for ISWI^{FL} but to a greater degree.

A dramatic decrease in intensity for select sites in H2A-H2B and H3-H4 are observed for addition of ADP-BeF$_x$ to the nucleosome-ISWI^{617} complex. The largest line broadening effects localize to mostly internal residues within the H2A-H2B, around SHL4, and residues in H3 that are near DNA. Residues within the H3-H4 tetramer are affected to a lesser extent. As ISWI^{617} is an active ATPase motor, more so than ISWI^{648}, these differences in histone octamer conformational line broadening are striking and suggestive of a correlation to ATPase binding mode, i.e. the degree to which an active conformation can be assumed. While rather similar to ISWI^{FL} in the nucleotide-free state, ISWI^{617} induces clearly much more conformational broadening in the nucleotide-bound state. Possibly, the auxiliary ABP and HSS domains in ISWI^{FL} interfere with inducing this particular histone octamer state on this substrate with short linker DNA. Thus, we believe that comparison of the ISWI^{617} vs. ISWI^{648} data gives a clearer indication of the impact of an active vs. inhibited ATPase conformation on histone octamer conformational dynamics. The large-scale line broadening for histone methyl groups upon ISWI^{617} binding in presence of the ATP-mimic ADP-BeF$_x$ provide strong support for the presence of conformational changes within the histone octamer during remodeling and suggest that these may allow concerted translocation of DNA across the octamer surface during remodeling.

Discussion

To what extent conformational changes play a role in nucleosome remodeling remains controversial. High-resolution cryo-EM studies have shown that remodeler binding induces deformation of the nucleosomal DNA without histone deformation[12,13]. An NMR study and a low-resolution cryo-EM structure suggested that the histone core is also deformed in remodeling[11,16], which was further corroborated in an molecular dynamics simulation based on cross-linking study[33]. Here we addressed the question using different constructs of the *Drosophila melanogaster* ISWI ATPase domain to decouple nucleosome movement from motor function. We find that the ATPase domain is an intrinsically dynamic machine that can induce large scale changes in histone-histone and histone-DNA interactions when trapping the ISWI motor in an active conformation.

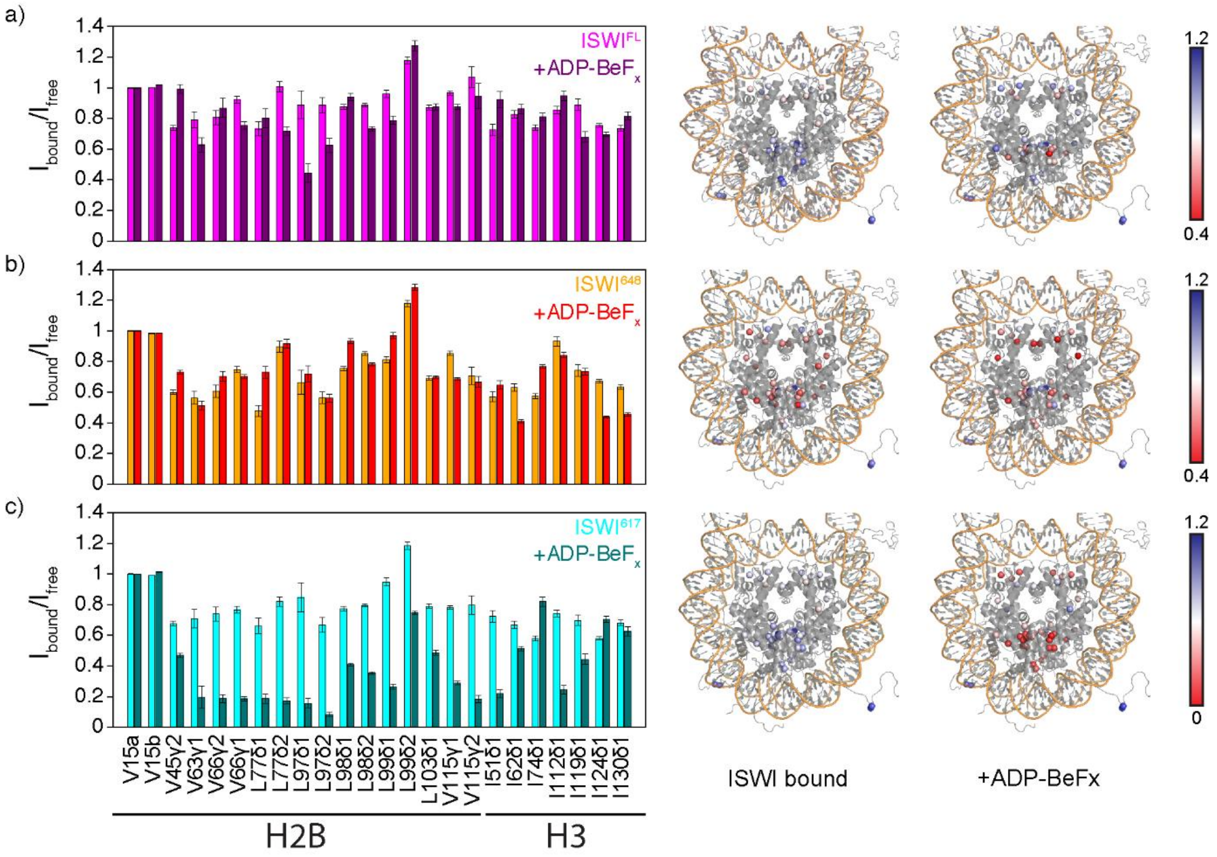

Figure 5.8: Conformational line broadening in histone H2B and H3 upon binding of ISWI. (a-c) Relative methyl group signal intensity in H2B and H3 upon binding of ISWI shown as bar graph for the nucleotide-free and ADP-BeFx-bound state on the left and plotted on the nucleosome structure on the right. Color coding indicated.

The presence of internal motions for so many of the Ile methyl probes in the ISWI ATPase and regulatory NegC domain suggests that intrinsic motions may play a role in the conformational changes during activation and remodeling. The overall low signal-to-noise of the nucleosome-bound ISWI unfortunately precluded more detailed analysis of ISWI dynamics in the bound state.

Our data indicate that the NegC conformation and mechanism of inhibition is different than previously thought. An inhibition mechanism based on a NegC conformation as in CHD1 in which res. 643-648 would bind lobe 1 to lock the lobes together is unlikely, as deletion of these residues only slightly reduced inhibition. This suggests that either the NegC region that binds lobe 1 is between residues 617-642 or that binding of the bridge helix to lobe 1 is sufficient to inhibit the remodeling function.

Recent cryo-EM structures revealed different H4 tail conformations, depending on remodeler protein and nucleotide states, suggestive of a dynamic interaction between ISWI and H4[13]. Also XL-MS and crystallography studies pointed to slightly different region where the H4 tail would bind lobe 2[7,20]. Our data support a rather dynamic H4 tail binding mode. Of the RHRK motif only the HRK sequence seems to be stably bound, with significant flexibility for R17 and residues N-terminal to the ISWI binding site. In presence of the ATP-mimic ADP-BeF$_x$ binding to H4 tail seems to involve a stronger interaction with

R17, in particular for the full-length protein and least for the NegC truncated mutant ISWI^{617}. This suggests that there is coupling between NegC and the ATPase lobe conformation that affects the ability of lobe 2 to bind the H4 tail. Increased rigidification of the bound H4 tail in the ATP-bound state may also provide an additional 'grip' element for the remodeler in the remodeling cycle.

A previous NMR study showed large intensity losses upon binding of the full length human ortholog Snf2H to 167bp ILV-labeled nucleosomes in presence of ADP-BeFx, suggesting significant conformational dynamic and plasticity of the histone octamer[16,17]. Our data provide strong support for a role of conformational changes in the histone octamer upon ISWI binding. Moreover, our data suggests that binding of the ATPase motor domain is sufficient to induce conformational changes and that the extent of these changes is dependent on the presence of NegC and nucleotide-state.

Compared to the Sinha et al study, we find similar effects in H3 when using full-length ISWI under similar conditions but using a different labeling scheme. The intensity changes in our case are somewhat less pronounced than for Snf2H, which could be related to the fact we added 1 equivalent while in the Sinha et al study 2 equivalents were added. In the ADP-BeF$_x$ bound state *Dm.* ISWI induced most changes in the H2B-H4 interface and in the vicinity of the acidic patch. This may be due to an allosteric response of the histone octamer as suggested in the Sinha study and in-line with recent crosslinking study[16,33]. Alternatively, the effect on H2B methyl residues may be caused by the HSS domain as the HSS domain of ISWI has been suggested to be able to release from DNA and bind the acidic patch[9,34].

The largest conformational line broadening for the histones is observed upon binding of the truncated ATPase ISWI^{617} in which the inhibiting part of NegC is deleted, in presence of ADP-BeF$_x$. The affected histone methyl groups are distributed over the entire histone octamer including residues close the DNA, the H2A-H2B acidic patch and the H2B-H4 helical bundle. For a large part this agrees with the location of conformational heterogeneity in the low resolution cryo-EM structure[11]. In this nucleotide state, the ATPase is engaged with DNA at SHL2, bound to the H4 tail, without inducing much distortion in the DNA. Compared to nucleotide free complex, the ATPase lobes are rotated in more compacted conformation in this state. Interestingly, addition of ADP-BeF$_x$ has been shown to be sufficient to induce a single 2 bp translation of the nucleosomal DNA when using full-length enzyme and nucleosomes containing long linker DNAs[11]. In case of ISWI^{648} and ISWI^{617}, such net DNA translocation in presence of ADP-BeF$_X$ is unlikely to occur due to lack of the HSS domain, linker DNA and because of the equal lengths of both DNA ends in our nucleosomes. Also, we would expect the methyl groups close to DNA to recover to the apo-state intensities when the DNA is fully translocated by one base pair and has adopted the same conformation and equivalent histone-DNA contacts. We thus hypothesize that the observed conformational line broadening is due to a continuous interconversion between partly translocated states. The interconversion may due to *i*) dynamic binding of ISWI: the truncated construct have reduced binding affinities compared to the full-length enzyme with reported dissociation constant for ISWI^{648} in the sub-micromolar range (K_D 0.5 µM)[19]; assuming an electrostatically enhanced on-rate (10^8 M^{-1} s^{-1}) the effective life time of the complex ($1/k_{off}$ with k_{off} = K_D x k_{on} = 50 s^{-1}) of ca. 2 ms; *ii*) a change in the conformational energy landscape of the histone octamer upon ISWI binding in which histones have sufficient thermal energy to access higher energy conformational states, as originally proposed in the Sinha study. This may be due to strain induced on the octamer by partial displacement of histone-DNA contacts, although this is not visible in cryo-EM structures. Increased conformational line broadening for the ADP-BeF$_x$-bound active ISWI^{617} construct suggest that the precise ATPase binding mode impacts (indirectly) the histone energy landscape; *iii*) dynamic binding of ADP-BeF$_x$ to ISWI: several cryo-EM structures showed density for ADP but not BeF$_X$ which could indicate a dynamic ISWI-nucleotide complex in which ADP and ADP-BeF$_X$ bound states alternate and thus change ATPase conformation[26]; *iv*) dynamic equilibrium between partly translocated states: in the ADP-bound state ISWI induces a DNA bulge at SHL2 that results in the local translocation of 1 bp of 1 strand. In the nucleotide-free state a similar bulge is induced upon ISWI binding suggesting that there is a similar local translocation of 1 bp of 1 strand. Upon binding of ATP, or in this case ADP-BeF$_x$, the change in lobe conformation and DNA binding mode removes the DNA bulge and this could allow the second strand to catch up resulting in effective translocation of 1 bp, which then could be ‘pushed’ across the dyad region to the exit side via twist diffusion. As in our condition two ATPase motors will be bound at opposite ends of the nucleosome and primed to work in opposite directions this could result in an effective dynamic equilibrium between (partly) translocated states. In this regard, comparison of the peak broadening patterns for ISWI^{648} and ISWI^{617} is particularly intriguing: while the broadening effects are primarily within H3-H4 for the inhibited ISWI^{648}, the effected residues are more distant from ISWI binding site for the active ISWI^{617} construct and include histone-DNA contact around the dyad (SHL 0) and SHL 4. This could mean that conformational changes within the ATPase motor are transmitted via the histone octamer to the histone-DNA interface across the nucleosome to allow concerted translocation of the DNA. More detailed studies are needed to firmly interpret the line broadening effects observed in histones and slow motions detected in ISWI and to relate them to the remodeling reaction.

Conclusions

We presented an NMR study of the conformational dynamics of the nucleosome remodeler ISWI and the nucleosome-ISWI complex. We found that the free ISWI is a highly dynamic enzyme and that the inhibiting elements of the NTR and NegC contain highly flexible elements such that these are not simply rigid ‘locks’ to inhibit the ATPase domain. Binding of ISWI to nucleosome induces large scale conformational changes in the histone octamer both with the H2A-H2B, H3-H4, their interface and the histone-DNA interface, with the precise pattern and strength of effects dependent on nucleotide state and ATPase conformation. Together our work highlights plasticity in the histone octamer and the motor enzyme in chromatin remodeling.

Materials and methods

Molecular modeling of the NegC conformation in free Dm. ISWI

Dm. ISWI models were generated using MODELLER. For free ISWI pdb 5JXR was used as template, for the NegC inhibited state pdb 3MWY was used, for the nucleosome bound state 5X0Y and 5O9G were used. For all models the Dm. ISWI amino acid sequence was aligned with the template sequences. First free ISWI was modelled using 5JXR, modelling the two lobes of the ATPase were modelled separately. These two lobes where then aligned with each of the templates and the connecting loop region was modelled using modeler. To model the NegC the crystal packing in 5JXR was used to obtain the binding motif between the ATPase core (chain A) and the NegC (chain B). The NegC was aligned with each of the models and connected with the ATPase using loop modeling in MODELLER. For the NegC model as in CHD1 the end of the NegC sequence was aligned with the NegC sequence of 3MWY to model the NegC crossing between the two ATPase lobes. The NTR region was modelled based on 5JXR, aligned with each of the models and connected with the rest on the models using loop modeling in MODELLER.

Expression and purification of histone proteins

Perdeuterated *Xl.* histones and ^{15}N,{^{1}H-^{13}C}-ILV histones were expressed and purified as described in chapter 3 in perdeuterated M9 medium in D_2O. For ^{14}N,{^{1}H-^{13}C}-LV H2B, $^{14}NH_4Cl$ was added to the medium and 80 mg/L α-ketoisovalerate (3-(methyl-d_3),4-^{13}C,3-d) sodium salt was added prior to induction. For ^{14}N,{^{1}H-^{13}C}-Ile H3, $^{14}NH_4Cl$ was added to the medium and 60 mg/L α-ketobutyric acid (4-^{13}C,3,3-d_2) was added prior to induction. For perdeuterated ^{15}N H4, $^{15}NH_4Cl$ was added to the medium and no additional precursors were added before induction.

Site directed mutagenesis of ISWI

A pProEX-Htb vector containing the ATPase domain of *Drosophila melanogaster* (*Dm.*) ISWI (residue 26-648, ISWI^{648}) with an N-terminal His$_6$-TEV tag was used as a starting point for new constructs. Constructs were made according to the QuickChange Site-Directed Mutagenesis Kit. Primers were designed to introduce a stop codon in the coding sequence to make the ISWI^{642} (residue 26-642) and ISWI^{617} (residue 26-617) mutants. Primers were designed to mutate isoleucine to leucine residues for residues I147, I263 and I602 for assignment (see Table S5.1). Constructs were made using PCR by mixing 50 ug plasmid with 10 uM primer each, 2 mM dNTPs and homemade Pfu in 50 uL Pfu buffer (20 mM Tris-HCl (pH 8.8 at 25°C), 10 mM $(NH_4)_2SO_4$, 10 mM KCl, 0.1 mg/mL BSA, 0.1% (v/v) Triton X-100, 2 mM $MgSO_4$). After PCR samples were treated with DpnI (10U) for 1 hour at 37°C and then transformed into homemade *Escherichia coli* (*E. coli)* DH5α competent cells and incubated overnight at 37°C. Colonies were picked and grown in LB medium, followed by extraction of the desired plasmid DNA using a MiniPrep kit. All constructs were sequenced to confirm correct incorporation of the mutations.

Expression and purification of ISWI proteins

Full length (ISWI^{FL}), and ISWI constructs were expressed using *E. coli* BL21(DE3) plysS in M9 medium (6 g/L Na_2HPO_4, 3 g/L KH_2PO_4, 0.5 g/L NaCl, 0.5 g/L NH_4Cl, 2 mM $MgSO_4$, 0.1 mM $CaCl_2$, 10 μM $FeCl_2$, 5 g/L unlabeled glucose or 2g/L labeled glucose, 50 mg/L ampicillin, vitamin supplements and trace elements). Cultures were grown at 37°C till an OD_{600} of 0.6-0.8 and then cooled to 18°C before inducing overnight expression using 0.2 mM IPTG. For isotope labeling of ISWI proteins, the M9 medium was adapted with the appropriate isotopically labeled compounds, i.e. ^{15}NH4Cl for ^{15}N labeling and $^{15}NH_4Cl$ together with d-glucose-$^{13}C_6$ in D_2O-based M9 medium for deuterated ^{15}N,^{13}C-ISWI^{648}. To obtain perdeuterated ^{14}N,{^{1}H-^{13}C}-Ile ISWI (Ile ISWI) $^{14}NH_4Cl$, glucose-1,2,3,4,5,6,6-d_7 was added to the D_2O-based M9 medium and 60 mg/L α-ketobutyric acid (4-^{13}C,3,3-d_2) was added prior to induction.

Cells were harvested by centrifugation at 4 krpm for 15min at 4°C and resuspended in ice cold T300 buffer (50 mM Tris, 300 mM NaCl, 0.5mM βME) with lysozyme and protease inhibitor cocktail, then lysed using one freeze-thaw cycle and sonication on ice (6 times 10 s on/10 s off). Soluble protein was collected by centrifugation at 30 krpm for 20 min at 4°C and filtration of the soluble fraction over a 0.45 μm filter. The ISWI protein was purified at 4°C using a 5 mL HisTrap HP column (GE healthcare) in combination with a 5 mL HiTrap Q column (GE healthcare) in 15 mM Tris pH 7.4, 130 mM KOAc, 1 mM βME and using a gradient of 0-400 mM imidazole for elution. Fractions containing ISWI were concentrated using a 30 kDa MWCO centrifugal concentrator at 4°C and directly loaded onto a HiLoad Superdex 200 16/600 gel filtration column equilibrated in 20 mM Hepes, pH 7.6, 200 mM KCl, 0.2mM EDTA, 1 mM βME. The pooled fractions containing ISWI were buffer exchanged to storage buffer (20 mM Tris, pH 7.6, 140 mM KCl, 0.01% NaN_3) at 4°C, falsh-frozen and stored at -80°C until use.

Expression and purification of nucleosomal DNA

A pUC19 plasmid containing 12 x 167 base pair repeats was used to produce 167 base pair 601 Widom DNA[27]. A plasmid containing 15 x 197 base pair repeats was used to produce 15 x 197 base array of 601 Widom DNA. Plasmids were produced using DH5α in 2xYT medium with an overnight culture at 37 °C. Cells were collected by centrifugation at 4 krpm for 10 min at 4°C and resuspended in STET buffer (8% sucrose, 50 mM Tris, pH 8.0, 50 mM EDTA, 1% Triton) to an OD of 30. Cells were lysed using a freeze-thaw cycle and fresh lysozyme (0.3mg/mL) and RNase A (10ug/mL) were added and incubated for 30 minutes. The lysate was then heated till 70°C for 5-10 minutes, then centrifugated at 20 krpm for 10 min and supernatant was collected. A final concentration of 0.19% CTAB (5% Cetrimonium bromide dissolved in 500mM NaCl) was added to the supernatant and incubated for 10 minutes at room temperature and then centrifuged at 20 krpm until all precipitate formed a pellet. Supernatant was removed and the pellet was redissolved in 1.2 M NaCl and then centrifuged at 20 krpm for 5 min. The supernatant was collected, and DNA was precipitated by adding 125 mL absolute ethanol per 50 mL supernatant and centrifuged. The pellet was then washed with 70% ethanol, dried and then resuspended in TE 10/0.1 buffer (10 mM Tris, pH 8.0, 0.1 mM EDTA). The 12 x 167 bp plasmid was digested with ScaI-HF (New England Biolabs) in Cutsmart buffer, while the 15 x 197bp plasmid was digested with EcoRV (New England Biolabs) in NEB 3.1 buffer. Plasmids were purified using a 5 mL Hitrap Q column in TE buffer (10 mM Tris, pH 8.0, 1 mM EDTA) using a 0-1 M NaCl gradient, ethanol precipitated and resuspended in TE buffer to a concentration of ~2.4 mg/mL before storage at -20 °C.

Reconstitution of mononucleosomes

Mononucleosomes were reconstituted as described in Chapter 3. Fully deuterated nucleosomes were made by mixing perdeuterated histones in equimolar ratios to make octamers and then reconstituted with 167 bp 601 DNA. For H2A-ILV labeled nucleosomes the same procedure was followed but using ILV-labeled H2A during octamer refolding. For hybrid nucleosomes, perdeuterated H2A, LV-labeled H2B, Ile-labeled H3 and ^{15}N-labeled H4 (all perdeuterated) were mixed in equimolar ratio to make octamers and then reconstituted on 167 bp 601 DNA.

Reconstitution of nucleosome arrays

Unlabeled histone octamers were refolded as described in Chapter 3. Octamers were mixed with EcoRV digested 15 x 197 bp 601 DNA at a 1:1.25 molar ratio in high salt buffer (10 mM Tris, pH 7.5, 2 M NaCl, 1 mM EDTA) and incubated for 30 minutes at room temperature. The salt concentration was lowered to 1 M NaCl by quickly mixing in low salt buffer (10 mM Tris, pH 7.5, 1 mM EDTA) and incubated for 1 h. The salt concentration was subsequently lowered in steps to 0.8, 0.6 and 0.2 M NaCl using low salt buffer with a 1-hour incubation between each step. The nucleosome array was then concentrated using a 30 kDa MWCO centrifugal concentrator. Nucleosome arrays were purified by adding a final concentration of 5 mM $MgCl_2$ and incubating for 5 minutes to precipitate the arrays. After centrifugation for 5 minutes 15 krpm at room temperature, the upper layer was removed and discarded and the lower layer containing the nucleosome arrays was resuspended in 20 mM Tris pH 7.6, 20 mM EDTA, 200 mM KCl and then buffer exchanged to remodeling buffer (20 mM Tris pH 7.6, 50 mM NaCl, 0.1 mM EDTA, 1 mM $MgCl_2$, 1 mM DTT).

Remodeling activity assay

Remodeling assays were performed with 2 nM nucleosome arrays (equivalent to 30 nM mononucleosome concentration) in remodeling buffer with either 30 or 300 nM of ISWI (full-length, or ISWI^{684}, ISWI^{642} or ISWI^{617} construct). Remodeling was started by adding 1 mM ATP to the samples at 26 °C. Remodeling activity was followed over a time course of 6 hours. Samples were taken at different timepoints by quenching the reaction by adding 1 U FastAP phosphatase (Thermofisher) to 4 μL remodeling reaction. Remodeled arrays were then digested by adding 1 U AvaI restriction enzyme and incubating overnight at 26 °C. AvaI activity was quenched by adding a final concentration of 20 mM EDTA to the sample. Samples were digested with proteinase K at 60 °C for 90 minutes, followed by ethanol precipitation and resuspension in TE buffer. Resuspended samples were then visualized on a 1.6% agarose gel using GelRed (Biotium). Band intensities were quantified using Fiji[35]. The bottom 197bp band corresponding to mononucleosomes for each sample was normalized for using the top band (control competitor DNA).

NMR spectroscopy

All measurements were performed on a 900 MHz Bruker Avance III spectrometer equipped with a TCI cryoprobe. All spectra were processed using Bruker Topspin and analyzed using NMRFAM-Sparky, except where mentioned otherwise. Chemical shift perturbations and peak intensity changes during titration experiments were followed using ^{15}N-^{1}H 2D TROSY HSQC experiments for backbone amide observation or ^{13}C-^{1}H SOFAST methyl-TROSY HMQC experiments for methyl group observation. All NMR spectra were recorded in NMR buffer (20 mM Tris, pH 7.6, 140 mM KCl, 1 mM $MgCl_2$, 0.1 mM EDTA, 0.01% NaN_3, i.e. storage buffer with 1 mM $MgCl_2$ and 0.1 mM EDTA, I = 150 mM) except for the assignment spectra, see below. Methyl-observed experiments were run on samples in NMR buffer with 100% D_2O, whereas NMR buffer with 10% D_2O was used for amide-observed experiments.

Backbone assignment of ISWI^{648}

Backbone assignment of ISWI^{648} was performed at 20 °C using a fractionally deuterated uniformly ^{15}N/^{13}C labeled ISWI^{648} sample at 139 μM in 20 mM KPi pH 6.8, 100 mM KCl, 1 mM DTT, 0.01% NaN_3, 5% D_2O. Using a set of 3D TROSY versions of HNCA, HNCO, HN(CA)CO, HN(CO)CA, HNCACB, HN(CO)CACB experiments 48 H_N,N backbone assignments could be made, comprising most of the strong peaks in the spectrum. Other backbone resonances suffered from too much overlap or low signal intensity for assignment.

Ile-δ1 methyl group assignment of ISWI^{648}

The resonance at –0.6 ppm 1H chemical shift could be assigned to the δ1 methyl of I181, thanks to its unique position in lobe 1 of ISWI. The presence of multiple aromatic sidechains (W250, F275) around I181δ1 can be expected to induce strong ring-current effects that explain its strongly upfield shifted ^{1}H chemical shift. We could further assign residue I283 based on an I283L mutation (Fig. 4). Spectra of the WT and mutant (I147L, I283L and I601L) ISWI^{648} were recorded using ^{13}C-^{1}H SOFAST methyl-TROSY HMQC experiments in 20 mM KPi, pH 7.4, 100 mM KCl, 0.01% NaN_3, 1 mM DTT, 100% D_2O at 20 °C. Mutants were measured at 19.2 μM for I283L, 18.3 μM for I147L and 3.6 μM for I601L. Further assignments were based on the observed NOE cross-peak pattern and the chemical shift perturbations upon mutagenesis and nucleotide binding (Fig. S5.4, S5.5). 3D methyl-TROSY (h)CCH-NOESY with 200 ms mixing time was recorded on a 223 μM Ile-labeled WT ISWI sample in NMR buffer with 100% D_2O at 5 °C. In total, 15 clear and reciprocal NOE cross-peaks could be identified. The observed cross-peak pattern and relative intensities were compared to the Ile-δ1 methyl-methyl distances in the *Dm.* ISWI homology model to derive assignments (Fig. S5.4). Four sets of NOE networks were observed (Fig. S5.5) of which one contained the assigned residue I181 and its neighboring I183, I255, I271, I239, the second matched with most residues affected by the I601L mutation (Fig. S5.4), resulting in the assignment of I380, I397, I565, I602 and the third contained a dense network that could only be assigned to I360, I435, I617, I622, I625 which form a set of closely packed isoleucines. The fourth network was not assignable because to many possible assignments were available. In total 15 Ile-δ1 assignments could be obtained, corresponding to 38% completeness.

Resonance assignment Xl. H2A ILV methyl groups

Initial assignments of the ILV methyl group resonances in *Xenopus leaevis (Xl.)* H2A were based on assignment transfer from the available *Drosophila melanogaster* (*Dm.*) chemical shifts[31]. To confirm and complete the assignments, 3D methyl-TROSY (h)CCH NOESY were recorded with acquisition times $t_{1,max}$ 8 ms, $t_{2,max}$ 8 ms and $t_{3,max}$ 67 ms, total measurement time 3 days, and with 200 (50) ms NOESY mixing time on nucleosome sample with ILV (2MeLV)-labeled H2A. Spectra were processed using forward linear prediction in both indirect dimensions and analyzed using NMRFAM-SPARKY 3.13. Assignments were made using MAGMA 1.2.3[36] and verified manually by comparing the experimental NOE network and to the methyl-methyl distances in the 1KX5 nucleosome crystal structure[37] resulting in 98% assignment. Stereospecific assignments could be transferred from the *Dm*. spectra based on conservation of NOE patterns. Comparison of the Leu ^{13}C δ1 and δ2 chemical shifts and the crystal structure rotamer conformation using the Sider program[38] confirmed the stereospecific assignments for Valine 107 and all Leu residues, except L108, which was too dynamic.

Backbone amide assignment of H4 tail in the nucleosome

Assignments were transferred from previously published assignment of the histone tails[30]. Out of the ~21 observable resonances, 5 could be assigned uniquely and 5 as groups.

Methyl-TROSY relaxation dispersion experiments of Ileδ1-labeled ISWI^{648}

Slow motions on the µs-ms time scale in ISWI were probed using methyl-TROSY ^{13}C,^{1}H multiple quantum CPMG relaxation dispersion experiments on a sample of 223 µM Ileδ1-labeled ISWI^{648} at 5 °C. Spectra recorded at 5 °C have similar spectral quality compared to those recorded at 20 °C but benefit from the increased stability of ISWI^{648} at lower temperatures. The relaxation delay was set to 10 ms and CPMG pulsing rate was varied between 100 and 2000 Hz (10 points in total). Data processing and calculation of the effective transverse relaxation rate ($R_{2,\mathrm{eff}}$) was carried out as described in Chapter 3. Dispersion profiles were fit using the CPMG template of PINT[39] to guide the eye and quantify the magnitude of the dispersion, $\Delta R_{2,\mathrm{eff}}$.

NMR titration experiments of isotope-labeled ISWI^{648}

Changes in the highly dynamic parts of ISWI^{648} upon nucleosome binding were monitored using NMR titration experiments of protonated ^{15}N-labeled ISWI^{648} (200 µM) recorded at 15 °C with 1 mM $MgCl_2$, 1 mM ADP, 1.25 mM $BeSO_4$, 6.25 mM NaF (1 mM ADP-BeF_x) added to the NMR buffer. Comparison of spectra in presence and absence of ADP-BeF_x showed no significant differences. Nucleosomes with deuterated histones were titrated in steps up to a 1:1 ISWI^{648}:nucleosome ratio.

Changes to the methyl group signals of ISWI^{648} upon binding of ADP-BeF_x were followed using NMR titration experiments of Ileδ1-labeled ISWI^{648} (223 µM) recorded at 5 °C in absence and presence of 1 mM ADP Mg / 1 mM BeF_x. Impact of nucleosome binding (in the presence of 1 mM ADP-BeF_x) was monitored by addition of nucleosomes with deuterated histones up to a 1:1 ISWI^{648}:nucleosome ratio.

NMR titration experiments of isotope-labeled nucleosomes

All measurements of labeled nucleosomes were performed at 25 °C. Nucleosomes containing ILV-labeled H2A were titrated under low ionic strength conditions with perdeuterated ISWI^{648} up to a 1:2 nucleosome:ISWI ratio in 20 mM KPi, pH 7.6, 0.01% NaN_3, 100% D_2O. H2A ILV labeled nucleosome were measured at 80 uM for free nucleosomes and 44uM in combination with ISWI.

'Hybrid' nucleosomes containing Ileδ1-labeled H3, LV-labeled H2B and ^{15}N-labeled H4 were measured NMR buffer in their unbound state or with either ISWI^{FL} at 1:1, ISWI^{648} at 1:2 or ISWI^{617} at a 1:2 nucleosome:ISWI ratio. The free nucleosome concentration was 42 µM, and 31 µM in combination with ISWI^{FL}, 45.5 µM in combination with ISWI^{648} and 45 uM in combination with ISWI^{617}. For each sample, measurement of the NH backbone resonances of the H4 tail and methyl resonances of H3 and

H2B was alternated by buffer exchange to NMR buffer in 90% H_2O/10% D_2O or NMR buffer in 100% D_2O. For each sample, spectra were recorded both in absence and in presence of 1 mM ADP-BeF_x.

References

1. Lieleg, C. *et al.* Nucleosome Spacing Generated by ISWI and CHD1 Remodelers Is Constant Regardless of Nucleosome Density. *Mol. Cell. Biol.* **35**, 1588–1605 (2015).
2. Clapier, C. R. & Cairns, B. R. Regulation of ISWI involves inhibitory modules antagonized by nucleosomal epitopes. *Nature* **492**, 280–284 (2012).
3. Racki, L. R. *et al.* The histone H4 tail regulates the conformation of the ATP-binding pocket in the SNF2h chromatin remodeling enzyme. *J. Mol. Biol.* **426**, 2034–2044 (2014).
4. Yan, L., Wang, L., Tian, Y., Xia, X. & Chen, Z. Structure and regulation of the chromatin remodeller ISWI. *Nature* **540**, 466–469 (2016).
5. Clapier, C. R., Längst, G., Corona, D. F. V., Becker, P. B. & Nightingale, K. P. Critical Role for the Histone H4 N Terminus in Nucleosome Remodeling by ISWI. *Mol. Cell. Biol.* **21**, 875–883 (2001).
6. Dang, W., Kagalwala, M. N. & Bartholomew, B. Regulation of ISW2 by Concerted Action of Histone H4 Tail and Extranucleosomal DNA. *Mol. Cell. Biol.* **26**, 7388–7396 (2006).
7. Ludwigsen, J. *et al.* Concerted regulation of ISWI by an autoinhibitory domain and the H4 N-terminal tail. *Elife* **6**, 1–24 (2017).
8. Yamada, K. *et al.* Structure and mechanism of the chromatin remodelling factor ISW1a. *Nature* **472**, 448–453 (2011).
9. Dao, H. T., Dul, B. E., Dann, G. P., Liszczak, G. P. & Muir, T. W. A basic motif anchoring ISWI to nucleosome acidic patch regulates nucleosome spacing. *Nat. Chem. Biol.* **16**, 134–142 (2020).
10. Grüne, T. *et al.* Crystal structure and functional analysis of a nucleosome recognition module of the remodeling factor ISWI. *Mol. Cell* **12**, 449–460 (2003).
11. Armache, J. P. *et al.* Cryo-EM structures of remodeler-nucleosome intermediates suggest allosteric control through the nucleosome. *Elife* **8**, 1–26 (2019).
12. Chittori, S., Hong, J., Bai, Y. & Subramaniam, S. Structure of the primed state of the ATPase domain of chromatin remodeling factor ISWI bound to the nucleosome. *Nucleic Acids Res.* **47**, 9400–9409 (2019).
13. Yan, L., Wu, H., Li, X., Gao, N. & Chen, Z. Structures of the ISWI–nucleosome complex reveal a conserved mechanism of chromatin remodeling. *Nat. Struct. Mol. Biol.* **26**, 258–266 (2019).
14. Forné, I., Ludwigsen, J., Imhof, A., Becker, P. B. & Mueller-Planitz, F. Probing the conformation of the ISWI ATPase domain with genetically encoded photoreactive crosslinkers and mass spectrometry. *Mol. Cell. Proteomics* **11**, 1–11 (2012).
15. Harrer, N. *et al.* Structural Architecture of the Nucleosome Remodeler ISWI Determined from

Cross-Linking, Mass Spectrometry, SAXS, and Modeling. *Structure* **26**, 282-294.e6 (2018).

16. Sinha, K. K., Gross, J. D. & Narlikar, G. J. Distortion of histone octamer core promotes nucleosome mobilization by a chromatin remodeler. *Science (80-.).* **355**, (2017).

17. Gamarra, N. & Narlikar, G. J. Histone dynamics play a critical role in SNF2h-mediated nucleosome sliding. *Nat. Struct. Mol. Biol.* **28**, 548–551 (2021).

18. Li, L., Yan, L. & Chen, Z. Reply to: Histone dynamics play a critical role in SNF2h-mediated nucleosome sliding. *Nat. Struct. Mol. Biol.* **28**, 552–553 (2021).

19. Mueller-Planitz, F., Klinker, H., Ludwigsen, J. & Becker, P. B. The ATPase domain of ISWI is an autonomous nucleosome remodeling machine. *Nat. Struct. Mol. Biol.* **20**, 82–89 (2013).

20. Yan, L., Wang, L., Tian, Y., Xia, X. & Chen, Z. Structure and regulation of the chromatin remodeller ISWI. *Nature* **540**, 466–469 (2016).

21. Hauk, G., McKnight, J. N., Nodelman, I. M. & Bowman, G. D. The Chromodomains of the Chd1 Chromatin Remodeler Regulate DNA Access to the ATPase Motor. *Mol. Cell* **39**, 711–723 (2010).

22. Emmerik, C. van. *Computational, biochemical and NMR-driven structural studies on nucleosomal DNA*.

23. Harrer, N. *et al.* Structural Architecture of the Nucleosome Remodeler ISWI Determined from Cross-Linking, Mass Spectrometry, SAXS, and Modeling. *Structure* **26**, 282-294.e6 (2018).

24. Tugarinov, V., Hwang, P. M., Ollerenshaw, J. E. & Kay, L. E. Cross-correlated relaxation enhanced 1H-13C NMR spectroscopy of methyl groups in very high molecular weight proteins and protein complexes. *J. Am. Chem. Soc.* **125**, 10420–10428 (2003).

25. Korzhnev, D. M., Kloiber, K., Kanelis, V., Tugarinov, V. & Kay, L. E. Probing Slow Dynamics in High Molecular Weight Proteins by Methyl-TROSY NMR Spectroscopy: Application to a 723-Residue Enzyme. *J. Am. Chem. Soc.* **126**, 3964–3973 (2004).

26. Lacabanne, D. *et al.* ATP Analogues for Structural Investigations: Case Studies of a DnaB Helicase and an ABC Transporter. *Molecules* **25**, (2020).

27. Lowary, P. . & Widom, J. New DNA sequence rules for high affinity binding to histone octamer and sequence-directed nucleosome positioning. *J. Mol. Biol.* **276**, 19–42 (1998).

28. Corbeski, I., Dolinar, K., Wienk, H., Boelens, R. & Van Ingen, H. DNA repair factor APLF acts as a H2A-H2B histone chaperone through binding its DNA interaction surface. *Nucleic Acids Res.* **46**, 7138–7152 (2018).

29. Bolik-Coulon, N., Cousin, S. F., Kadeřávek, P., Dumez, J. N. & Ferrage, F. Understanding the methyl-TROSY effect over a wide range of magnetic fields. *J. Chem. Phys.* **150**, (2019).

30. Zhou, B. R. *et al.* Histone H4 K16Q mutation, an acetylation mimic, causes structural disorder of its n-terminal basic patch in the nucleosome. *J. Mol. Biol.* **421**, 30–37 (2012).

31. Kato, H. *et al.* Architecture of the high mobility group nucleosomal protein 2-nucleosome complex as revealed by methyl-based NMR. *Proc. Natl. Acad. Sci.* **108**, 12283–12288 (2011).

32. Chittori, S., Hong, J., Bai, Y. & Subramaniam, S. Structure of the primed state of the ATPase domain of chromatin remodeling factor ISWI bound to the nucleosome. *Nucleic Acids Res.* **47**, 9400–9409 (2019).

33. Hada, A. *et al.* Histone Octamer Structure Is Altered Early in ISW2 ATP-Dependent Nucleosome Remodeling. *Cell Rep.* **28**, 282-294.e6 (2019).

34. Gamarra, N., Johnson, S. L., Trnka, M. J., Burlingame, A. L. & Narlikar, G. J. The nucleosomal acidic patch relieves auto-inhibition by the ISWI remodeler SNF2h. *Elife* **7**, 1–25 (2018).

35. Schindelin, J. *et al.* Fiji: An open-source platform for biological-image analysis. *Nat. Methods* **9**, 676–682 (2012).

36. Pritišanac, I. *et al.* Automatic Assignment of Methyl-NMR Spectra of Supramolecular Machines Using Graph Theory. *J. Am. Chem. Soc.* **139**, 9523–9533 (2017).

37. Davey, C. A., Sargent, D. F., Luger, K., Maeder, A. W. & Richmond, T. J. Solvent mediated interactions in the structure of the nucleosome core particle at 1.9 A resolution. *J. Mol. Biol.* **319**, 1097–1113 (2002).

38. Hansen, D. F., Neudecker, P., Vallurupalli, P., Mulder, F. A. A. & Kay, L. E. Determination of Leu Side-Chain Conformations in Excited Protein States by NMR Relaxation Dispersion. *J. Am. Chem. Soc.* **132**, 42–43 (2010).

39. Ahlner, A., Carlsson, M., Jonsson, B. H. & Lundström, P. PINT: A software for integration of peak volumes and extraction of relaxation rates. *J. Biomol. NMR* **56**, 191–202 (2013).

Supplemental information

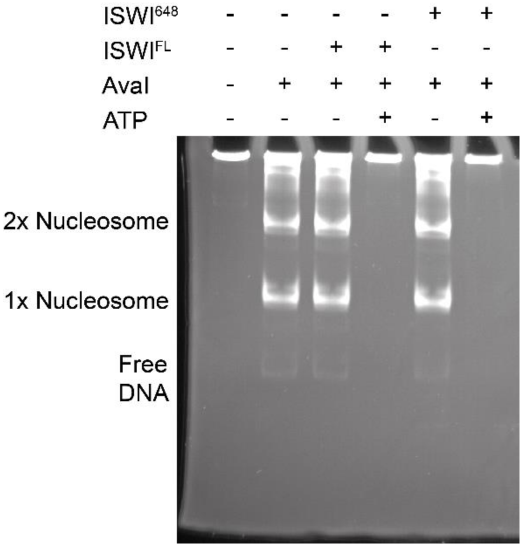
ISWI648 - - - - + +
ISWIFL - - + + - -
AvaI - + + + + +
ATP - - - + - +
2x Nucleosome
1x Nucleosome
Free DNA

Figure S5.1: Prolonged remodeling assay. Prolonged remodeling of ISWI^{FL} or ISWI^{648} (>14h) results in the formation of particles larger than 2 nucleosomes. Indicating remodeling over the available AvaI restriction sites.

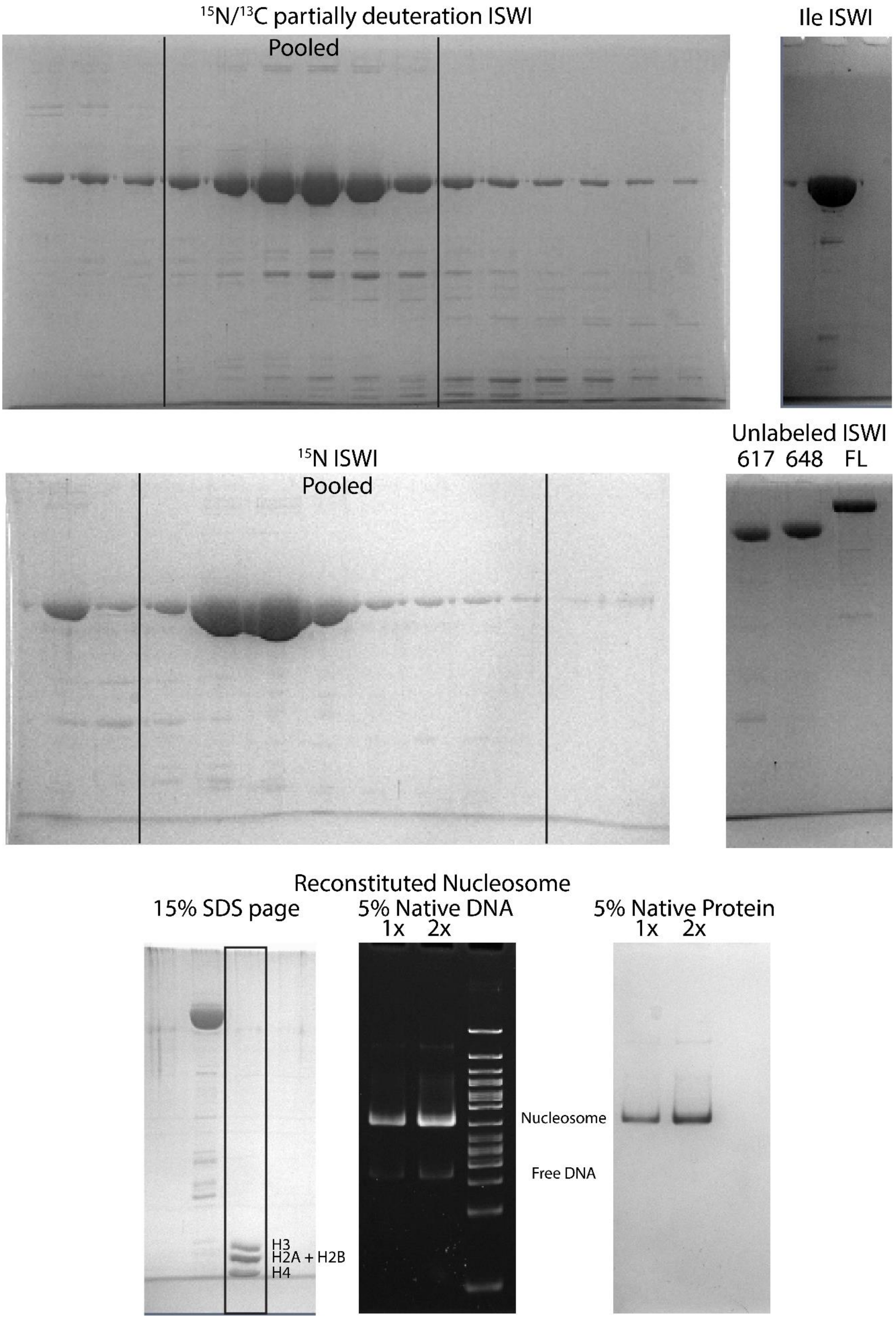
^{15}N/^{13}C partially deuteration ISWI
Pooled
Ile ISWI
^{15}N ISWI
Pooled
Unlabeled ISWI
617 648 FL
Reconstituted Nucleosome
15% SDS page
5% Native DNA
1x 2x
5% Native Protein
1x 2x
Nucleosome
Free DNA
H3
H2A + H2B
H4

Figure S5.2: Purified proteins and complexes used during the different experiments.

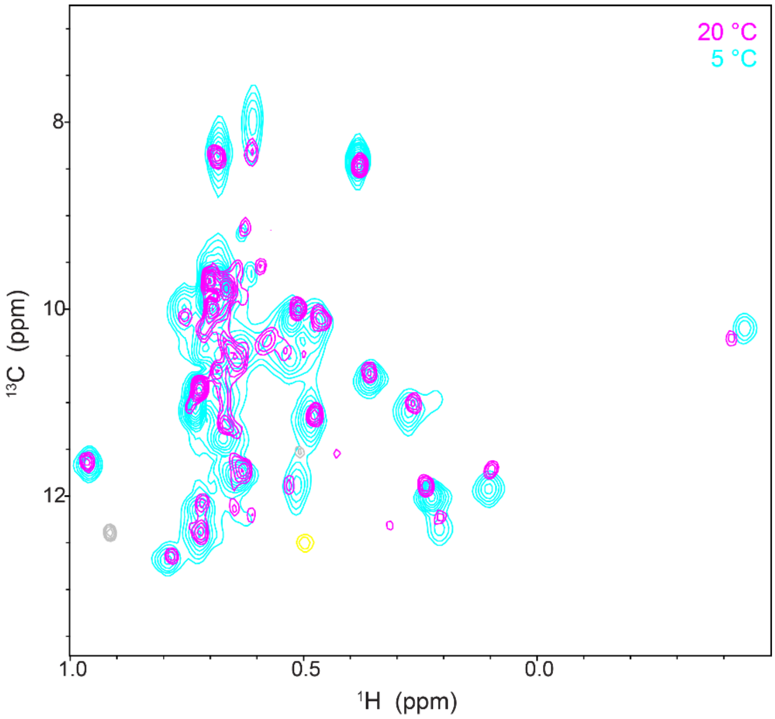

Figure S5.3: Ile ISWI temperature sensitivity. Decrease in temperature from 20 to 5 degrees results in line broadening of all resonances and chemical shift perturbations in several resonances.

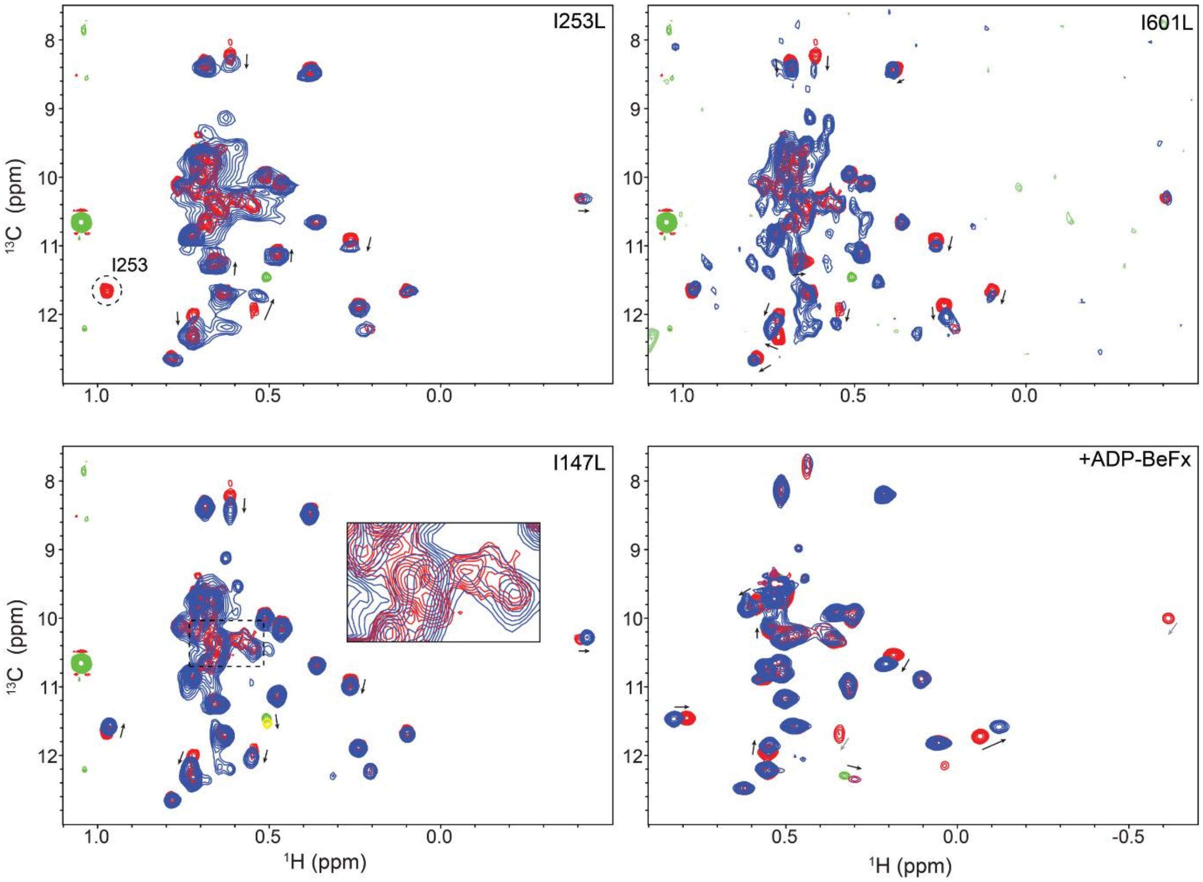

Figure S5.4: ISWI Mutants and ADP-BeFx addition. Mutant I283L has one peak that disappeared and was assigned as I283. Mutants I601L and I147L did not show a clear disappearing peak, potentially due to overlap. All mutant spectra have shifting peaks indicating either their proximity to the mutant or a globular change in the protein. Addition of ADP-BeFx to ISWI results in CSPs for multiple peaks that indicate the ATP binding pocked or changes in the conformation of ISWI.

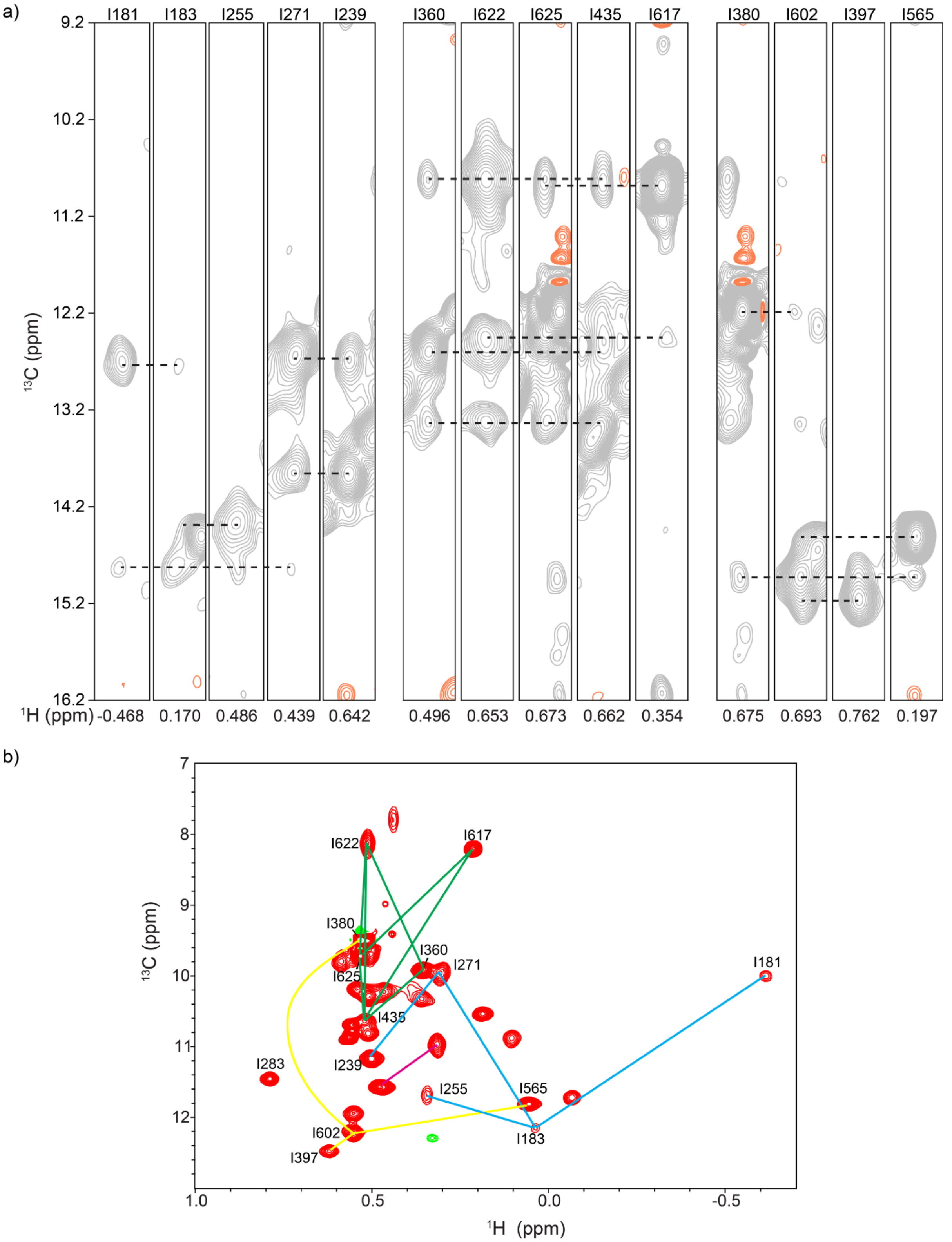

Figure S5.5: NOE strips and NOE networks. a) NOE strips of Ile ISWI648 of the three largest sets of NOE networks. b) NOE networks containing form largest to smallest 5, 5, 4 and two resonances. The three largest networks were assignable, while too many possibilities remain for the smallest network.

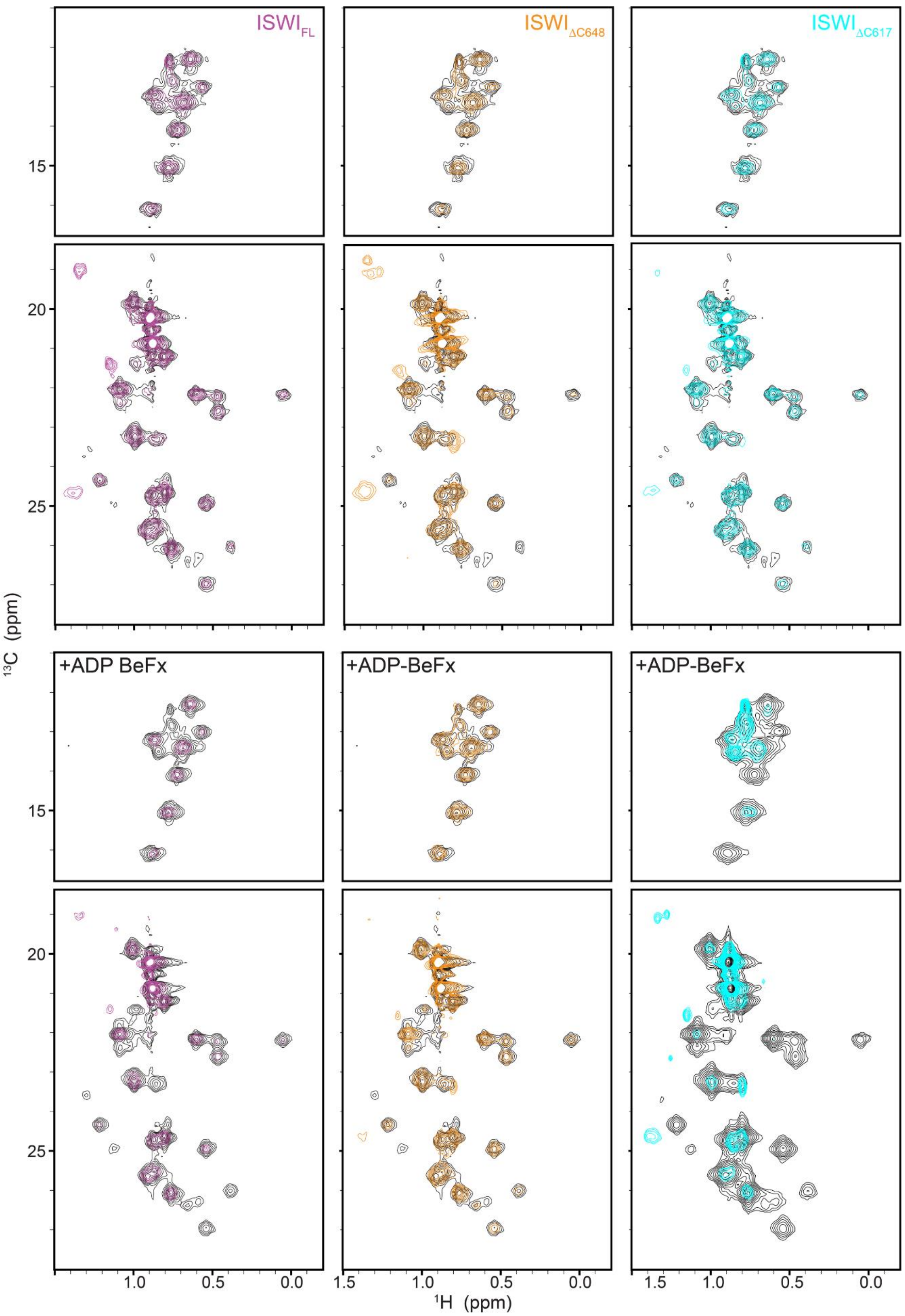

Figure S5.6: Titration of hybrid labeled nucleosomes with ISWI. Nucleosomes labeled on methyl groups of H2B leucine and valine and H3 isoleucine groups was used. Nucleosomes are mixed with the three different ISWI constructs ISWIFL, ISWI648 and ISWI617 in the absence (top) and presence of ADP-BeFx (bottom). Addition of ISWI results in decreased signal intensity but does not result in chemical shift perturbations.

Table S5.1: Primers for ISWI mutants.

Mutation	Sequence (5'-3')
I147L - fw	gatttcgctttacgaaaatggtctcaatggaattctggccg
I147L - rv	cggccagaattccattgagaccattttcgtaaagcgaaatc
I283L - fw	taagaccgctaatcgtctacttctcacgggtactc
I283L - rv	gagtacccgtgagaagtagacgattagcggtctta
I601L - fw	tcagttgaacaaggatgaaatgcttaatttaatccgttttggagcta
I601L - rv	tagctccaaaacggattaaattaagcatttcatccttgttcaactga
deltaC642 - fw	aactctcgcctcaactgtccagtgctgccttttg
deltaC642 - rv	caaaaggcagcactggacagttgaggcgagagtt
deltaC617 - fw	tgtcctcatctcaaatgtctgtctccttagagctga
deltaC617 - rev	tcagctctaaggagacagacatttgagatgaggaca

6

General Discussion

Centuries of dedicated scientists have gone before us to build the foundations to understand the mechanisms of life. They discovered microscopic life and that all living organisms are build up from cells. That these cells are build up by many macromolecules like DNA, RNA and proteins that work together to perform vital functions to sustain and propagate life. That DNA carried the genetic code acting as a blueprint to build these macromolecules. Inevitably they found many mechanisms in place that act as locks and keys to regulate how DNA is processed. In eukaryotes, the prime mechanism is the coating of DNA with proteins, together called chromatin, and as its most basic subunit the nucleosome. This brings us to the current era, the era of epigenetics, where we and others try to understand how the chromatin is regulated so that our DNA blueprint is correctly read. A central question in chromatin biology is how chromatin, DNA binding proteins and chromatin factors work together to regulate all DNA-mediated processes. The underlying molecular mechanisms not only involve interactions between the smallest units, e.g. proteins and the nucleosome, but also the interplay of the complex higher-order organization of chromatin and these molecular interactions. These aspects converge in the case of chromatin remodelers. These enzymes interact with nucleosomes to alter higher-order chromatin structure directly, by reshuffling the position of nucleosomes in the genome.

Various structural techniques have been applied to investigate chromatin biology. One of these techniques, nuclear magnetic resonance (NMR) spectroscopy, is of particular interest as it can capture dynamics information at a molecular level besides structural information. The NMR field has evolved and matured over the years to allow studies of chromatin biology[1]. NMR evolved from a one-dimensional to multi-dimensional experiments permitting the observation and assignment of individual atoms in proteins. Development of relaxation optimized experiments and specific isotopic labeling schemes have pushed the size boundaries of NMR complexes into the mega Dalton range. Finally, the continuous drive towards higher NMR field strengths has increased signal intensity and resolution, giving rise to a more improved and distinguishable signals.

This thesis has examined in detail how the remodeler enzyme ISWI interacts with nucleosomes, explored the relationship between nucleosome interactions and higher-order chromatin structure, and elaborated on approaches to study nucleosome structure and dynamics using high field nuclear magnetic resonance spectroscopy.

Chromatin biology at higher magnetic fields

In **chapter 3** we explored the advantages and disadvantages of ultra-high magnetic fields for methyl-TROSY NMR in context of nucleosome and chromatin research. We approached this project by making a single nucleosome sample with specific isoleucine, leucine and valine methyl-labeling and used this sample to record experiments from 600 MHz till 1.2 GHz. This range gives a good coverage of the field strengths that are currently applied in high field NMR experiments. A first implication of a higher magnetic field is the expected gain in signal sensitivity. Comparing the 3 mm probe setup of the 1.2 GHz with the 5 mm probe setup of the 900 MHz we do not gain sensitivity as observed from the sucrose standard. This lack of sensitivity gain stems inherently from the smaller 3mm probe containing less sample. Continuation of a possible trend to use smaller probes to facilitate higher fields is a conundrum for solution NMR as no additional sensitivity might be gained. Therefore, there should be a focus on overcoming the technological problems of using larger 5mm probes at higher field to keep gaining sensitivity.

At 1.2 GHz the signals from globular core nucleosome are observed to be lower than expected based on a sucrose reference sample. Additionally, R_2 rates increase while R_1 rates remain similar. The increase in R_2 rates matches the increased contribution of chemical shift anisotropy (CSA) relaxation, which scales linearly with the magnetic fields. This raises the question if methyl TROSY experiment using the HMQC will remain the most optimal experiment or if other experiment like the HSQC or HZQC might become more favorable with higher field strengths. Computational comparison of ZQ and DQ experiments indicate that indeed ZQ experiments might become more favorable at higher fields, although at an even higher magnetic field of 55 T (2.3 GHz)[2].

A second implication and advantage of the higher field strength at 1.2 GHz is the increase in resolution. Due to the increase in resolution, split peaks are observed for several residues in the globular core of the nucleosome. This indicates that the nucleosome adopts an asymmetric structure. A likely explanation for this asymmetry could be the asymmetry in the used DNA sequence. Split peaks due to asymmetries have been observed before for residues neighboring the DNA. However, several residues that show peak splitting are located farther from the DNA indicating that differences near DNA could propagate deeper into the core of the nucleosome. We observe a correlation between split peaks a higher variability in rotamer orientation in available nucleosome structures. To investigate these asymmetries further we could study histone dimers or nucleosomes with symmetric DNA at higher fields to uncouple the effect of asymmetric DNA. The asymmetries in the nucleosome could have biological implications. Asymmetric incorporation of histone variants or mutants have shown to influence the directionality and capability of chromatin remodelers[3]. Nucleosomes have also been suggested to have DNA sequence dependent asymmetric DNA opening[4]. The observed asymmetries are more subtle than incorporation of an asymmetric histone variant or asymmetric opening, but this intrinsic asymmetry could potentially influence which of the two faces of the nucleosome a protein wants to interact with higher affinity. It would be interesting to study the nucleosome with varying and native DNA sequences it for instance actively or inactively transcribed sides and determine if similar or even larger asymmetries are observed.

A third implication of the higher magnetic field that we observed is the increased alignment of nucleosomes with the magnetic field. This effect scales with the square of the magnetic field and thus is much larger at 1.2 GHz than at the lower available fields. The magnetic field alignment of nucleosomes give rise to residual dipolar couplings due to the incomplete averaging of the molecular tumbling. These residual dipolar couplings are a valuable tool to obtain structural information on the studied molecule as they depend on the orientation of the molecule to the magnetic field. We were able to apply this information in two use cases. First, we applied the information of the residual dipolar couplings to assign nearly completely the stereochemistry of the leucine and valine methyl rotamers in the nucleosomal H2B leucine and valine residues. This method removed the requirement of specifically single labeled rotamers to assign the stereochemistry, saving precious time and money. Second, we applied the structural information of the residual dipolar couplings to determine the average conformation of the nucleosomal DNA. Currently there is an intense debate on how often DNA ends unwrap from the nucleosome, how long they remain open, how far they open, if they open symmetrically and what the biological implication is of DNA unwrapping. At our measuring conditions, which are at low ionic strength and 45 °C, we observe the DNA ends to be on average unwrapped till approximately superhelix position 5.5, i.e. wrapping of approximately 1.4 instead of 1.7 super helical turns. To correctly interpret these results, we need to compare the experimental conditions with biological relevant conditions, i.e. at 37 ° and an ionic strength of approximately 150 mM. Furthermore, nucleosome opening is likely also dependent on DNA sequences and different for mono-nucleosomes and nucleosomal arrays. A lower temperature would reduce the likelihood of DNA unwrapping, while a higher ionic strength and genomic DNA instead of the high affinity 601 Widom DNA are predicted to increase DNA unwrapping. In **chapter 4** we indeed infer that at a lower temperature the DNA is closer to the histone globular core, but we do not observe additional unwrapping at higher ionic strengths.

Future combination of the RDC measurements with methyl labeling of specific DNA sequences[5] will be very powerful to determine much more directly the DNA conformation, avoiding indirect interpretation via the histone methyl groups RDCs. Potentially this could reveal clearer information on the dynamics of the DNA conformation in relation to the histone core.

Ionic strength induced higher order chromatin organization

As mentioned before the nucleosome and chromatin structure depend on the ionic concentration. Additionally, the NMR signal of nucleosomes was observed to be affected by ionic strengths. In **Chapter 4** we quantified and investigated the effects of ionic strengths on the nucleosome in context of NMR. During this investigation we focused on the monovalent ions Na^+ and K^+ which are prevalent in biological systems and Mn^{2+} as Mg2+ substitute, due to its strong effect on signal intensity because of paramagnetic relaxation enhancement. We applied a methyl labeling to obtain information of both the globular core and flexible tails of the nucleosome through histone H2B. Increasing the ionic strength severely decreased sensitivity. We observe up to almost a 2.7-fold higher NMR sensitivity when K^+ ions are used instead of Na^+ ions for the globular core. This highlights the importance of choice in ion types for NMR experiments when using nucleosomes as the measurement time scales exponentially with the sensitivity. Determining the underlying cause of the sensitivity loss is not trivial. Many of the interaction within and between nucleosomes are governed by electrostatics and therefore will be influenced by changes in ionic strength. Therefore, these changes can result in different DNA or histone tail dynamics or binding affinities between nucleosome particles. Within the range of tested ionic strengths nucleosomes remained intact and do not precipitate from the solution. Additionally, no us-ms dynamics or exchange broadening is observed, suggesting that the loss in sensitivity is caused by an increase in effective particle size. Because nucleosomes remained intact, and no other macromolecules were present, nucleosomes need to interact with each other. Based on the sensitivity loss we calculated a 2 to 3 times increase in particle size from 25 to 75 mM K^+ and larger at higher K^+ concentrations. This suggest that at least 2 to 3 nucleosomes interact with each other, while DNA opening could potentially contribute to a small fraction of the increased particle size. Histone tails and especially the H3 and H4 tails are essential in the higher order compaction of nucleosome arrays. The positively charged histone tails can interact with DNA and because they are dynamic, they could interact with DNA of its own nucleosome or neighbor. In the absence of ions, the histone tails are thought to be collapsed on the DNA of the own nucleosome. An increased ionic strength would weaken the interaction between histone tails and DNA and make them more available to bind DNA or acidic patch of other nucleosomes and form multimers or a network of nucleosomes. With ionic concentrations beyond the tested range, we expect that the charge of the histone tails will be eventually screened and release from DNA. However, nucleosome have an attractive force at elevated ionic strength suggesting other interactions might be involved, i.e. DNA-DNA or DNA-core interactions. Due to these interactions, it is not possible to determine the contribution of the histone tails to the multimerization of nucleosomes with just ionic strength titrations. Future experiments should focus on determining the exact contribution of each of the different components. Contributions of DNA opening can be derived by crosslinking DNA ends to the nucleosome core[6]. Histone tail contributions can be derived by using nucleosomes without histone tails or histone tails without charged residues[7–9]. Combining these experiments will derive the contribution of the other interactions.

Though we do not know the exact contribution of each of the components our data suggest clustering of nucleosomes towards physiological relevant ionic concentrations. A similar phenomenon reported by others is that nucleosomes can be clustered through phase separation, in particular when nucleosomes are present on one DNA strand as in a nucleosomal array. A critical difference between phase separation and the clustering we observe is that with phase separation nucleosomes separate in a dense and dilute phase. This property of phase separation has been proposed to cause specific recruitment or exclusion of proteins from the dense phase and be involved in regulation of heterochromatin formation or RNA transcription. The question remains how the formation of these smaller nucleosome clusters interplay with nucleosome phase separation. Are these clusters a form of pre-phase separation or distinctly different? How relevant are these clusters in-vivo and how do they behave with post translational modifications or proteins like HMGN that are observed to open chromatin?

Besides monovalent ions we also investigated the interaction of the Mn^{2+} ions with nucleosomes to probe divalent ion binding sites. Here we observed specific binding sites of Mn^{2+} ions on the DNA and on the acidic patch. Moreover, we find that at 25 mM ionic strength the H2B tail is binding nucleosomal DNA. While it might not be surprising that histone tails bind nucleosomal DNA at low ionic strength, the fact that we can observe histone tail-DNA binding using Mn^{2+} open options to use Mn^{2+} with nucleosomes to study interaction of other binding partners. The Mn^{2+} ions create a local paramagnetic relaxation enhancement (PRE) and therefore can potentially be used to obtain structural and distance information. The benefit of this method would be that Mn^{2+} is effective at a very low concentration and therefore non-invasive. The different binding affinities of the observed Mn^{2+} binding sites could also be exploited giving PRE on single or multiple sites increasing the amount of information without making an additional sample.

ISWI has a dynamic interaction with the nucleosome

In the previous chapters we investigated the intrinsic properties of the nucleosome and its properties to form higher order structures. In chromatin context these intrinsic properties are complemented with regulatory machinery. One of these regulatory machineries is chromatin remodeling which was addressed in **chapter 5**. We focused on the ISWI chromatin remodeler which plays a crucial role in the maintenance of the dynamic chromatin landscape through its ability to alter nucleosome spacing. ISWI contains sequence elements that inhibit it catalytic activity unless it binds nucleosomes with sufficient linker DNA length. We could decouple ISWI motor function by using constructs containing different lengths of the NegC sequence element.

The NegC is thought to have two large alpha helical regions as observed in the Mt. ISWI structure. The first helix binds on the ATPase near residues I380 which is in the region that can binding H3 during remodeling. Stabilizing the more flexible region of I380 into a conformation as seen in the Mt. ISWI crystal structure or even the presence of the NegC alpha helix itself could potentially form a barrier to

DNA binding. Comparing this binding mode of NegC with nucleosome bound ISWI indeed shows incompatibility of this binding mode with DNA binding as they occupy the same space. For the remodeler CHD1, that also contains a similar NegC domain, the NegC domain bound to two lobes of the ATPases domain together inhibiting its motor function. This conformation with the NegC and other regulatory domains locked the remodeler in a conformation where remodeling was not possible. Because the ISWI and CHD1 NegC have a similar sequence it was suggested that ISWI motor function inhibition works in a similar manner to CHD1 where the NegC locks the two lobes of the ATPase domain together. However, our truncation experiments of the NegC suggested that locking the two lobes might not be required to inhibit ISWI motor function. Deletion of the NegC region which has a similar sequence to the motif in CHD1 that is involved in the binding of one of the lobes does not result in recovery of motor function. Extended truncation of NegC results in motor function recovery and could mean two things: i) The NegC domain can still bind both lobes but in a different part of the sequence. ii) Binding of both lobes of the ATPase is not the main mode of inhibition of ISWI motor function. Crosslinking data for ISWI suggest that until the end of the bridge helix the NegC domain is bound to one lobe and thus large conformational changes would be required to still binding the other lobe. Therefore, inhibition by steric hindrance by the NegC domain to properly bind or cause bulging of DNA seems more likely. However, we still lack structural information of this region to make a conclusion. To confirm deletion mutants of these regions should be made and remodeling activity should be tested.

NMR was used to characterize both ISWI and the nucleosome in free or bound states. We found that free ISWI is highly dynamic, with the regulatory domains containing flexible elements. This flexibility might play a role in the conformational changes that are required during the activation of ISWI remodeling. We were unable to measure dynamics in the nucleosomes bound state due to sensitivity. Most of the interactions withing the complex are interactions with DNA and deuteration of DNA will improve sensitivity due to reduced relaxation. If this does not increase sensitivity enough alternative ways are required to probe dynamics and potentially also structural information in the bound state. Residual dipolar couplings due to magnetic field alignments as discussed in chapter 3 could be a potential solution. Binding of ISWI to the nucleosome will also induce magnetic field alignment of ISWI and produce residual dipolar couplings. These residual dipolar couplings will contain structural and dynamics information and could give information of the orientation and dynamics of the NegC helix. Another approach would be the application of paramagnetic spin labels in the nucleosome that will give distance information[10].

A previous study of the full length human ortholog SNF2H suggested significant conformational dynamic and plasticity of the histone octamer (reference Geeta two paper here with dynamics in the nucleosome with SNF2H). Our data provide strong support for a role of conformational changes in the histone octamer upon ISWI binding. Moreover, our data suggests that binding of the ATPase motor domain is sufficient to induce conformational changes and that the extent of these changes is dependent on the presence of NegC and nucleotide-state. The largest conformational line broadening for the histones is observed upon binding of the truncated ATPase ISWI^{617} in which the inhibiting part of NegC is deleted, in presence of ADP-BeF$_x$. The affected histone methyl groups are distributed over the entire histone octamer including residues close the DNA, the H2A-H2B acidic patch and the H2B-H4 helical bundle. For a large part this agrees with the location of conformational heterogeneity in the low resolution cryo-EM structure[11]. Interestingly, addition of ADP-BeF$_x$ has been shown to be sufficient to induce a single 2 bp translation of the nucleosomal DNA when using full-length enzyme and nucleosomes containing long linker DNAs. We would expect the methyl groups close to DNA to recover to the apo-state intensities when the DNA is fully translocated by one base pair and has adopted the same conformation and equivalent histone-DNA contacts. We thus hypothesize that the observed conformational line broadening is due to a continuous interconversion between partly translocated states.

Comparison of the peak broadening patterns for ISWI^{648} and ISWI^{617} is particularly intriguing: while the broadening effects are primarily within H3-H4 for the inhibited ISWI^{648}, the effected residues are more distant from ISWI binding site for the active ISWI^{617} construct and include histone-DNA contact around the dyad (SHL 0) and SHL 4. This could mean that conformational changes within the ATPase motor are transmitted via the histone octamer to the histone-DNA interface across the nucleosome to allow concerted translocation of the DNA. More detailed studies are needed to firmly interpret the line broadening effects observed in histones and slow motions detected in ISWI and to relate them to the remodeling reaction.

The residual dipolar couplings observed for the nucleosome in chapter 3 could be used to study the nucleosome-ISWI complex as the complex is expected to align with the magnetic field due to the nucleosome and will give structural information on the orientation of the ATPase lobes and regulatory domains. The use of inactive forms ISWI can be used to separate binding events from those caused by active remodeling. Similarly, it would be very interesting to observe the complex with different ATP analogues that simulate different steps in the ATP hydrolysis as this might determine at which step DNA becomes dynamic and translocates. This should be supported with the use of methyl labeled DNA and can be used to follow DNA translocation and binding with ISWI. How the NegC regulates this translocation should be further investigated. The best case would be to obtain structural information in both the free and bound states by for instance Cryo-EM. As this has thus far proven difficult biochemical studies might provide more information on the exact mode of inhibition by NegC. One could truncate the NegC even further to investigate the absolute minimum length. Deletions of regions in NegC can be performed to determine if they might stabilize the loop region that is binds H3 to a conformation that cannot or crosslinking of the NegC with this loop could be performed.

Conclusion

We applied the 1.2 GHz NMR to observe chromatin structure. These high fields open new or better opportunities to study chromatin structure and dynamics. The higher resolution resolves peak splittings between rotamer conformations and magnetic field alignment can be used to study nucleosome DNA orientation. Higher ionic strengths result in the clustering of nucleosome particles even below physiological salt concentrations. We observe the interaction between ISWI and nucleosomes and find that it has a more complicated regulation of its motor function than thought. Finally, we find that ISWI causes dynamics within the nucleosome core during remodeling near DNA binding sites and in the H2A-H2B dimer.

References

1. van Emmerik, C. L. & van Ingen, H. Unspinning chromatin: Revealing the dynamic nucleosome landscape by NMR. *Prog. Nucl. Magn. Reson. Spectrosc.* **110**, 1–19 (2019).
2. Bolik-Coulon, N., Cousin, S. F., Kadeřávek, P., Dumez, J. N. & Ferrage, F. Understanding the methyl-TROSY effect over a wide range of magnetic fields. *J. Chem. Phys.* **150**, (2019).
3. Levendosky, R. F. & Bowman, G. D. Asymmetry between the two acidic patches dictates the direction of nucleosome sliding by the ISWI chromatin remodeler. *Elife* **8**, 1–18 (2019).
4. Mauney, A. W., Tokuda, J. M., Gloss, L. M., Gonzalez, O. & Pollack, L. Local DNA Sequence Controls Asymmetry of DNA Unwrapping from Nucleosome Core Particles. *Biophys. J.* **115**, 773–781 (2018).
5. Abramov, G., Velyvis, A., Rennella, E., Wong, L. E. & Kay, L. E. A methyl-TROSY approach for NMR studies of high-molecular-weight DNA with application to the nucleosome core particle. *Proc. Natl. Acad. Sci. U. S. A.* **117**, 12836–12846 (2020).
6. Pujari, S. S. *et al.* Site-Specific 5-Formyl Cytosine Mediated DNA-Histone Cross-Links: Synthesis and Polymerase Bypass by Human DNA Polymerase η. *Angew. Chemie - Int. Ed.* **60**, 26489–26494 (2021).
7. Hammonds, E. F. *et al.* Histone H3 and H4 tails play an important role in nucleosome phase separation. *Biophys. Chem.* **283**, 106767 (2022).
8. Bertin, A., Renouard, M., Pedersen, J. S., Livolant, F. & Durand, D. H3 and H4 histone tails play a central role in the interactions of recombinant NCPs. *Biophys. J.* **92**, 2633–2645 (2007).
9. Allahverdi, A. *et al.* The effects of histone H4 tail acetylations on cation-induced chromatin folding and self-association. *Nucleic Acids Res.* **39**, 1680–1691 (2011).
10. Kato, H. *et al.* Architecture of the high mobility group nucleosomal protein 2-nucleosome

complex as revealed by methyl-based NMR. *Proc. Natl. Acad. Sci.* **108**, 12283–12288 (2011).

11. Armache, J. P. *et al.* Cryo-EM structures of remodeler-nucleosome intermediates suggest allosteric control through the nucleosome. *Elife* **8**, 1–26 (2019).

English summary

Chromatin is vital to compaction and regulation of the DNA in eukaryotes and is intimately involved in DNA expression, replication, and repair. As one of the cell's biggest polymers, chromatin forms a multi-scale structure consisting of DNA and protein. At the smallest level, the nucleosome forms the repeating unit of chromatin, consisting of two copies of four different histones and around 150 base pair of DNA. A central question in chromatin biology is how chromatin, DNA binding proteins, chromatin factors and environmental factors work together to regulate all DNA-mediated processes. The underlying molecular mechanisms not only involve interactions between the smallest units, e.g. proteins and the nucleosome, but also the interplay of the complex higher-order organization of chromatin and these molecular interactions. These aspects converge in the case of chromatin remodelers. These enzymes interact with nucleosomes to alter higher-order chromatin structure directly, by reshuffling the position of nucleosomes in the genome.

Chapter 1 reviews the basic components of the nucleosome and gives a first glance at factors involved in the higher order organization of chromatin including ionic strength and chromatin remodeling proteins.

In **chapter 2** we expand on this first glance by reviewing nucleosome-protein interactions in higher order chromatin structures. The increasing availability of high-resolution nucleosome-protein structures allowed us to shed more light on how chromatin factors operate in this complex higher order chromatin environment. We analyze the current literature on the interplay between nucleosome-protein interactions and higher-order chromatin structure. We examine in what way nucleosomes-protein interactions can affect and can be affected by chromatin organization at the oligonucleosomal level. In addition, we review the characteristics of nucleosome-protein interactions that can cause phase separation of chromatin.

In **chapter 3** we investigate the effect of the currently highest permanent magnetic field of 28.2 Tesla in the context of chromatin. We investigated the performance of methyl-TROSY NMR at 1.2 GHz, using the nucleosome as a test sample. We find that the increased resolution of the 1.2 GHz system allows to resolve small asymmetries in amino acid sidechain conformation between symmetry-related copies of the histone proteins. Increased CSA relaxation effectively increases ^{13}C transverse relaxation rates by 20% at 1.2 GHz compared to 900 MHz. We further observe significant magnetic field alignment of the nucleosome at 1.2 GHz, giving rise to methyl ^{1}H-^{13}C residual dipolar couplings (RDCs) that can be used for assignment and structural characterization. We show that these histone methyl group RDCs can be used to aid assignment and to determine the overall conformation of the nucleosomal DNA, revealing a significant unwrapping of the DNA from the histone core.

Chromatin compaction is influenced by the concentration of Na^+, K^+ and Mg^{2+} ions. In **chapter 4** we applied nuclear magnetic resonance to study nucleosomes with mono- and divalent ions using a methyl labeling approach. An increase in ionic strength resulted in a decrease in core residue signals but did not decrease the tail residue signal. Na^+ ions decreased spectral quality more than K^+ ions. Our data point to an increase in effective size of the nucleosome particle due to tail DNA interactions between nucleosome particles. We estimate that nucleosomes cluster with 2-3 nucleosomes at 50 mM NaCl or 75 mM KCl. Additionally, we identify a specific binding site for Mn^{2+} on the acidic patch and identify the H2B tail to interact with nucleosomal DNA.

The chromatin remodeler ISWI plays a crucial role in the maintenance of the dynamic chromatin landscape through its ability to alter nucleosome spacing. Nucleosome remodeling by ISWI involves the translocation of DNA over the histone octamer surface, without disassembly of the nucleosome. Despite the enormous progress in the structural characterization of this process in recent years, it remains unclear to what extent conformational changes in the histone proteins play a role in remodeling. In addition, the molecular mechanism of ATPase activation upon nucleosome binding are not fully understood. In **chapter 5** we studied the conformational dynamics of ISWI and the nucleosome-ISWI complex using methyl-TROSY solution NMR spectroscopy. We find that the free enzyme is highly dynamic throughout the protein. Our data indicate that binding of an active ISWI construct to the nucleosome induces conformational changes through the histone octamer, affecting histone-DNA and histone-histone contacts. These findings provide strong support for histone plasticity during remodeling to facilitate DNA translocation and further highlight the histone octamer as an allosteric unit.

In **chapter 6** results from this thesis are highlighted and discussed in a broader context. Our current gaps in knowledge are addressed and future directions are discussed.

Nederlandse samenvatting

Chromatine is essentieel voor het compact maken en reguleren van DNA in eukaryoten en is nauw betrokken in DNA-expressie, replicatie en reparatie. Chromatine, een complex van DNA en eiwit, is één van de cel zijn grootste polymeren en vormt op meerdere niveaus specifieke structuren. Op de kleinste schaal bestaat de repeterende eenheid van chromatine, een nucleosoom, uit twee kopieën van vier verschillende histon-eiwittten en zo'n 150 baseparen DNA. Een centrale vraag in de biologie van chromatine is hoe chromatine, DNA-bindende eiwitten, chromatine factoren en omgevingsfactoren samenwerken om de transcriptie, replicatie, en reparatie van DNA te reguleren. De onderliggende moleculaire mechanismen bestaan niet alleen uit interacties tussen de kleinste eenheden, bijvoorbeeld eiwitten en nucleosomen, maar hangen ook samen met de complexe, hogere-orde organisatie van chromatine. Deze aspecten komen samen in het geval van chromatine remodeler eiwitten. Deze enzymen werken rechtstreeks in op nucleosomen om de hogere orde chromatine structuur te veranderen door bijvoorbeeld de nucleosoom positie te verplaatsen in het genoom.

In **hoofdstuk 1** worden de basiscomponenten van het nucleosoom beschreven en de belangrijkste factoren die betrokken zijn in de hogere-orde organisatie van chromatine inclusief ion-sterkte en chromatine remodeler eiwitten geïntroduceerd.

Hoofdstuk 2 gaat in detail in op de relatie tussen nucleosoom-eiwit interacties en de hogere-orde chromatine structuren, gebruikmakend van het snelgroeiende aantal hoge-resolutie nucleosoom-eiwit structuren. We bekijken op wat voor manier nucleosoom-eiwit interacties een invloed kunnen hebben en beïnvloed kunnen worden door chromatine organisatie op een multi-nucleosoom niveau. Daarnaast bekijken we de eigenschappen van nucleosoom-eiwit interacties die fase-scheiding van chromatine kunnen veroorzaken.

Hoofdstuk 3 beschrijft de prestaties van vloeistof nucleaire magnetische resonantie (NMR) voor grote eiwit-DNA complexen zoals het nucleosoom bij het momenteel hoogste permanente magneetveld (28.2 Tesla/ 1.2 GHz), gebruik makend van specifieke labeling van methyl groepen (methyl_TROSY NMR). Door de toegenomen resolutie van het 1.2 GHz systeem kan een kleine asymmetrie in de aminozuur zijketens conformatie tussen de symmetrie gerelateerde kopieën van de histon eiwitten worden onderscheiden. Toename van relaxatie door de anisotropie van de chemical shift tensor (CSA) zorgt voor een 20% afname in ^{13}C transversale relaxatiestijden op 1.2 GHz in vergelijking met 900 MHz. Verder zien we een significante anisotropie in de oriëntatie van het nucleosoom ten opzichte van het magneetveld ('uitlijning’) op 1.2 GHz. Deze uitlijning zorgt voor residuele dipolaire koppelingen (RDCs) die gebruikt kunnen worden voor toekenningen en structurele karakterisatie. We laten zien dat de RDCs van de histon methyl groepen gebruikt kunnen worden om te helpen met toekenning de NMR-signalen en het bepalen van de algehele conformatie van het nucleosomale DNA. We onthullen daarbij een significante ontvouwing van het DNA van de histon kern.

De compactheid van chromatine wordt beïnvloed door de concentratie van Na^+, K^+ en Mg^{2+} ionen. In **Hoofdstuk 4** bestuderen we het effect van mono- en divalente ionen op NMR-spectra van het nucleosoom. Een toename van ion-sterkte resulteert in een afname in het signaal van residuen in de histone kern, maar niet voor het signaal van het residu in de flexibele histon staart. De signaal-afname is sterker voor Na^+ ionen dan K^+ ionen. Onze data wijzen op een toename van effectieve omvang van het nucleosoom door histon staart-DNA interacties tussen nucleosomen. We schatten dat 2-3 nucleomen groeperen bij 50 mM NaCl of 75 mM KCl. Daarnaast identificeren we een specifieke bindingsplek voor Mn^{2+} op de ‘acidic patch’ van het nucleosoom en vinden dat de H2B staart associeert met nucleosomaal DNA.

De chromatine remodeler ISWI speelt een cruciale rol in het onderhouden van het dynamische chromatine landschap doordat het de afstand tussen nucleosomen kan veranderen. Verplaatsing van nucleosomen door ISWI gebeurt door translocatie van DNA over het oppervlak van de histon kern terwijl DNA en histonen aan elkaar gebonden blijven. Ondanks de enorme ontwikkeling in de structurele karakterisatie van dit proces in de afgelopen jaren blijft het onduidelijk in wat voor mate conformatieveranderingen in de histon eiwitten een rol spelen in remodeling. Daarnaast begrijpen we de mechanismen van de ATPase activatie tijdens nucleosoom binding nog niet volledig. In **hoofdstuk 5** bestuderen we de conformationele dynamica van ISWI en het nucleosoom-ISWI complex door middel van methyl-TROSY NMR-spectroscopie. We vinden dat het vrije eiwit sterk dynamisch is, door heel het eiwit. Onze data geven aan dat de binding van een actief ISWI-construct aan het nucleosome conformatieveranderingen induceert in de histon kern en daarbij histon-DNA en histon-histon contactpunten beïnvloed. Deze bevindingen ondersteunen het idee dat histon-plasticiteit tijdens remodeling DNA-translocatie mogelijk maakt en benadrukken dat de histon kern een allostere eenheid is.

In **hoofdstuk 6** worden resultaten van deze thesis belicht en bediscussieerd in een bredere context. De huidige ontbrekende kennis wordt aangekaart en toekomstig werk wordt bediscussieerd.

Acknowledgement

With these last few pages, I would like to conclude my thesis and thank you all for the amazing and fun years I had during my PhD. I hope to see and hear of all off you in the many years to come.

First and foremost, I would like to thank the person allowing me to have this amazing journey with all of you, Hugo. We had our first conversation by e-mail on the 6th of July 2015, when I was finishing my bachelor and required a mentor for my masters. I then joined your FUNdamentals of NMR course in preparation of a master internship in your group. Afterwards you offered me a PhD position in your group, and gratefully followed you to Utrecht. I am grateful you cheerful and energetic conversations and guidance during all these years.

Marc, thank you for being my promotor during my PhD, giving me access to all the facilities in the NMR group.

Then we arrive at all of you in the "Van Ingen team". Many of us already met before my PhD. I enjoyed all the fun experiences and scientific discussions we had. The many coffee breaks we had at all the different coffee machines throughout the building. The team outings we had to the escape room, the zoo, glow in the dark golf and painting. Velten, thank you for sharing many of your amazing and interesting stories with us during the coffee breaks. Clara, thank you for all the support you have given me when I first started on the ISWI project and thank you for taking the lead in organizing our Rotterdam outing. Heyi, thank you for being able to write my name wrong even after doing my master internship with you and starting the tradition of writing everyone's name wrong on the map of our office. This legacy continues to this day with the new members in the office. Thank you, Ivan, for answering my questions and attempting to keep the lab organized and clean. Ulric, thank you for accompanying me during both my internship and PhD as an office mate and friend. It was an enjoyable time and hope to see you again on many occasions in the future. Maria (Incoronata), though your stay with the group was only a short year, it was fun and thanks to you and Francesca I was finally able to learn some particular Italian words. Of course, there were also several students that joined the group during my stay. Christina thank you for helping me on the challenging ISWI project and I wish you good luck with your own PhD. Petrit you are an interesting person and made for a unique experience in the group. Good luck with whatever you will do in the future. And then Aryaa, you joined at a challenging time when all PhD's and postdocs were finishing in Hugo's group. It must be challenging to suddenly lose most of your daily support, but I hope you can use this experience to grow as an independent scientist and wish you the best of luck too.

Then I would like to thank all the other office mates that I had over the years for making a fun and enjoyable environment in the office. Francesca, I had fun with all your “just one more question” and our exchange of plants. Michaela, you were a jolly office mate, and I liked our long conversations about your dog, forest trips and boardgames. We still have to try and challenge that game. Julia, I also enjoyed your company in the office and thanks to you learned a lot about golf and golf competitions without ever having to play a single game. Ingrid, your stay was the shortest of all but by no means forgettable with your stories about your farm at home and happy hardcore. An honorable mention to Rodrigo who entered the office four times during my PhD.

Of course, my work would not have been possible without support of all the staff members. Hans, Andrei, Johan, and Nancy thank you for keeping all NMR equipment operational. Gert, Mark Daniëls and Raymond thank you for your support in the wetlab, answering all my questions during my PhD, giving guidance, and not letting the lab fall into complete chaos and anarchy. Barbara and Geeske thank you for helping with all administrative tasks, welcoming me into the group and trying to bring a bit of color into the gray building. Alexandre thank you for developing many computational tools that were helpfully during my PhD. Markus thank you for explaining solid state NMR theory.

Upon my arrival I was greeted by a wonderful group of PhD and postdocs that nearly felt like a family. Thank you, Alessandra, Cecilia, Miranda, Siddarth, Reinier, Joao, Shengqi, Helena, Barend, John (Yanzhang), Charlotte, Panos, Adrien, Mikael, Jorge, Francesco, and Cunliang for welcoming me so kindly. I had a of fun with our daily conversations, the hunts for a working coffee machine, the walks through the botanical garden, the lab dinners and lab outings.

With the inevitable departure of you all also came a large group of new colleagues to fill the void. Rhythm and Anamika thank you for filling the position of cat enthusiasts that became available after the departure of the crazy cat ladies. Good luck with the final steps of finishing your thesis, Rhythm. And Anamika, never give up, you can do it! Agnes thank you for the beautiful painting. It is still proudly hanging on my wall. David, I enjoyed our time together, playing pool of going for a drink and listening to your stories from Canada. Maik, the man hidden upstairs, thank you for always showing up on cookies and cake days. Adil we already met during my internship, and you even followed me to Utrecht. Al those years have been fun. I wish you the best with your PhD and after. Raj, keep up your good work. Ajit you can do it too and keep track of the fun moments. Amanda I still wonder how Euromar would have been with disco. Good luck with your PhD. Roy, you had only joined the group for a short time near the end of my PhD, but your sheer dedication to you project makes me believe you will have a successful future. Salima, thank you for all the dad jokes and explaining American tv series and politics during lunch. Svetlana may the force be with you.

With the lockdown due to Corona, I have missed contact with many people especially those in the computational group. Siri, thank you for organizing the board game evenings at work before corona they were very fun. Manon you were unfortunate to start and finish during corona and thus we mainly met online during the Haddock course and the few allowed borrels, but I enjoyed your company. Brian and Zuzana both of you are nice people and I would have liked to be able to meet more without corona. Zuzana has my Dutch lunch gone viral? Marco, new recruit of the haddock group, I hope you can enjoy your time without corona and reconnect with all the lab people like it was in the past.

Besides the people in the lab, I would also like thank my D&D friends for keeping me sane during corona time by doing the most insane adventures. I would also like thank my all friends I met during my studies that are still enjoy doing fun stuff together and play games. You guys make it so there is never a boring moment.

Als laatste wil ik nog mijn familie bedanken die er altijd voor mij zijn geweest. Pa, ma, Kim, Sanne, opa, oma en nonna, dankjewel.

For any that I might not have mentioned personally, according to Ulric’s definition I am an old man (more than 25 years), so I can forget things sometimes. For all of you, thank you.

Curriculum Vitae

Vincenzo Lobbia grew up in Delft, the Netherlands, and his secondary education at the Stanislas college Westplantsoen in Delft in 2011. He continued his studies at the Hogeschool van Amsterdam where he studied Forensic research for one year. He then continued his studies at both the University of Delft and the university of Leiden were het completed a Bachelor's degree in Life science and technology and at the Leiden university he completed a Master's degree in Life science and technology. During his Master, he was a research intern at the Leiden university at the Macromolecular Biochemistry section working on the characterization of the "pre-nucleosome". After graduation in 2017, he went to Utrecht university to pursue a PhD in structural biochemistry in the group of dr. Hugo van Ingen.

List of publications

V.R. Lobbia, M.C. Trueba Sanchez, H. van Ingen. Beyond the Nucleosome: Nucleosome-Protein Interactions and Higher Order Chromatin Structure. Journal of Molecular Biolology 433, 166827 (2021).

C.L. van Emmerik, I. Gachulincova, **V.R. Lobbia**, M.A. Daniëls, H.A. Heus, A. Soufi, F.H.T. Nelissen, H. van Ingen. Ramified rolling circle amplification for synthesis of nucleosomal DNA sequences. Analytical Biochemistry 588, (2020).

K. Teles, V. Fernandes, I. Silva, M. Leite, C. Grisolia, **V.R. Lobbia**, H. van Ingen, R. Honorato, P. Lopes-de-Oliveira, W. Treptow, G. Santos. Nucleosome binding peptide presents laudable biophysical and in vivo effects. Biomedicine & Pharmacotherapy 121, 109678 (2020).